Planar Hall Effect Sensors for Biodetection

Rizzi, Giovanni

Publication date:
2014

Document Version
Publisher's PDF, also known as Version of record

DTU Nanotech
Department of Micro- and Nanotechnology

Planar Hall Effect Sensors for Biodetection

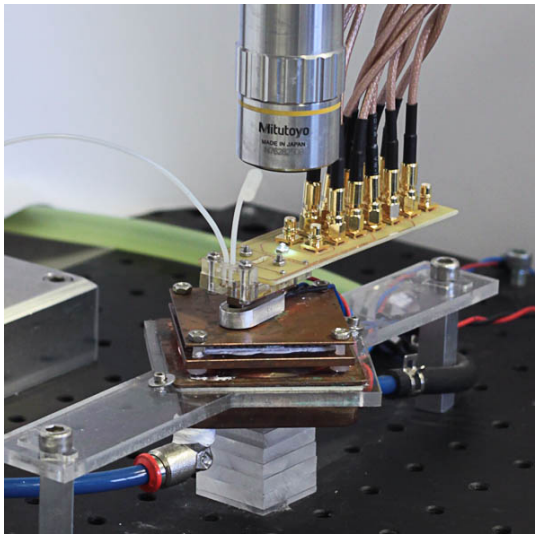

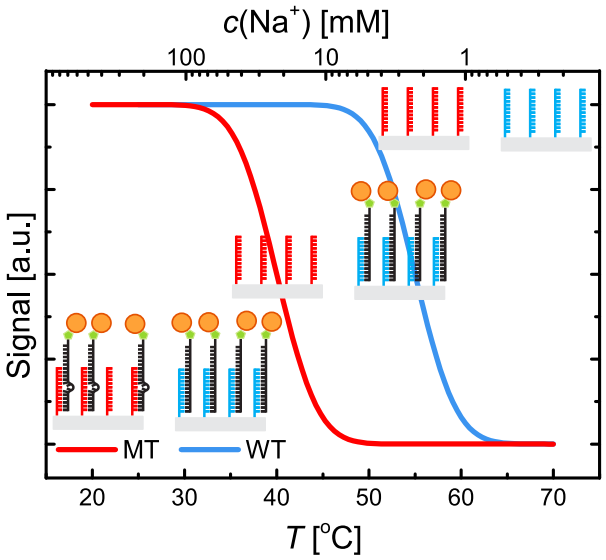

Giovanni Rizzi

Department of Micro- and Nanotechnology
Technical University of Denmark

Ph.D. Thesis, January 29th 2014

Front page picture: (Left) Picture of the sensor setup. The sensor is mounted in the microfluidic system. The sensor baseplate is temperature controlled. A microscope allows for visual inspection of the sensor surface. **(Right)** Denaturation curve measured using magnetic labels. Two sensors are functionalised with wild type (WT) and mutant type (MT) capture probes. After hybridisation, in low stringency condition, target with attached magnetic labels is hybridised to both sensors. Increasing temperature (or decreasing ionic strength) denatures first the mismatched hybrids on the MT probes. At high temperature (low ionic strength) all the hybrids are denatured.

Abstract

The work presented in this thesis contributes to the development of diagnostic tools also suited for use at the point-of-care. These devices may help to spread part of the biochemical analysis work from centralised laboratories to doctors' offices and in some cases to patients' homes. Point-of-care devices can effectively reduce the time for the analysis and the costs that are related to a delay in the diagnosis. Many technologies are available for biosensing devices. In this work, we study and employ magnetic biosensing on magnetoresistive sensors.

For magnetic biodetection magnetic beads are used as labels and planar Hall effect bridge (PHEB) magnetic field sensor as readout for the beads. The choice of magnetic beads as label is motivated by the lack of virtually any magnetic background from biological samples. Moreover, magnetic beads can be manipulated via an external magnetic field and be employed for sample preparation in a lab-on-a-chip device.

The PHEB sensors are formed by four magnetoresistive arms in a Wheatstone bridge geometry. In this thesis two different sensor geometries are used. In the first geometry (PHEB), the magnetic bead signals from the sensor arms are additive. In the second geometry (dPHEB) half of the sensor is used as a local negative reference to subtract the background signal from magnetic beads in suspension. In all applications below, the magnetic beads are magnetised using the magnetic field due to the bias current passed through the sensor, i.e., no external magnetic fields are needed for the measurements.

The two sensor geometries are employed for two different types of biodetection. The PHEB senor is used for volume-based biodetection, where the effective hydrodynamic size of magnetic beads is increased upon binding to the analyte. The change affects the rotation response (Brownian relaxation) of the magnetic beads, which can be measured through magnetic AC susceptometry. The dPHEB sensor is used for surface-based biodetection, where the analytes bind to capture probes immobilised on the sensor surface and allow for ligation of magnetic beads to the sensor surface.

In this thesis, the theoretical PHEB and dPHEB sensor signals are derived. Also, the effects of shape anisotropy on the sensor output are considered. We introduce Brownian relaxation of magnetic beads and chip-based magnetic susceptibility measurements using PHEB magnetic sensors.

The effects of temperature upon the magnetic properties of the sensor stack and signal output are studied. A method is presented to discriminate the reversible and irreversible effects of temperature. It is studied how a low-temperature annealing procedure can mitigate these effects. Experimental results show that it is impossible to avoid irreversible changes in the sensor, and thus we imply the need for a reference to correct for temperature effects in the sensor sensitivity. This reference is necessary whenever a biosensing experiment employs sizeable temperature variations.

PHEB sensors are used to for AC susceptometry measurements for volume-based bioassays. The setup allows to investigate the sensor responce as function of frequency in the range from DC to 5 MHz thus allowing for determining the hydrodynamic size of beads

with nominal diameters from 10 nm to 250 nm and down to a concentration of 64 μg/mL (for 40 nm beads). Beads with a diameter of 80 nm are found to be best suited for biodetection. Time-domain Brownian relaxation measurement are also demonstrated with PHEB sensors. The advantage of the time-domain technique is it lead to faster measurements, but at the cost reduced signal to noise. This method is compared to frequency-domain measurements in detection of biotin-conjugated bovine serum albumin (bBSA) and it is found that both techniques can detect bBSA in the nM range.

Furthermore, frequency-domain measurements are used for the detection of rolling circle amplification (RCA) products. RCA coils with a diameter of ≈ 1 μm are produced by RCA upon recognition of *Vibrio cholerae* and of *Bacillus globigii* spores and detected by incubation with properly functionalised magnetic beads. Binding of the magnetic beads to the RCA coils slow their dynamics, which can be observed as an increase in the hydrodynamic diameter. The assay can detect down to 4 pM of DNA coils and the whole assay can detect down to 500 spores in the starting sample. These figures compare favourably to those obtained using a commercial susceptometer.

Differential PHEB sensors (dPHEBs) are used for a surface-based assay to detect DNA hybridisation in a sandwich assay. Biotinylated DNA target binds to surface tethered capture probes and allows for the ligation of 50 nm streptavidin coated magnetic beads to the sensor surface. The sensor can detect DNA to a concentration of 156 pM upon 60 min hybridisation. The setup is capable of measuring DNA hybridisation in real-time, in a background of suspended magnetic beads. This characteristic is employed in single nucleotide polymorphism (SNP) genotyping, where the denaturation of DNA is monitored in real-time upon washing with a stringency buffer.

The sensor setup includes temperature control and a fluidic system capable of generating both temperature and concentration gradients over the sensor surface. The temperature and buffer concentration can be varied in order to perform denaturation analysis of the DNA hybrids. In this thesis, this kind assay is tested with temperature varying from 20°C to 70°C and Na^+ ionic strength from 400 mM to 4 mM. This demonstrates the flexibility of the presented sensing devices.

Resumé

Arbejdet presenteret i denne afhandling bedrager til udviklingen af diagnostiserings værktøjer der også kan anvendes ved point-of-care. Disse apparater kan bidrage til at udbrede biokemiske analyser fra centraliserede laboratorier til praktiserende læger og i visse tilfælde patienternes hjem. Point-of-care apparater kan effektivt reducere analysetiden og omkostninger relateret til en forsinket diagnose. Mange teknologier er til rådighed for biosensorapparater. I dette arbejde studerer vi og anvender magnetisk biodetektion på magnetoresistive sensorer.

I magnetisk biodetektion bruger vi magnetiske kugler som markører og planar Hall effekt bro (PHEB) magnet feltsensorer til detektion af de magnetiske kugler. Valget af magnetiske kugler som markører er motiveret af at der stort set ikke er noget magnetisk baggrundssignal i biologiske prøver. Ydermere, så kan magnetiske kugler også manipuleres ved brug af ydre magnetfelter og anvendes til prøvepræparation i et lab-on-a-chip apparat.

PHEB sensorerne består af fire magnetoresitive arme i en Wheatstone brogeometri. I denne afhandling vil vi bruge to typer af sensorgeometrier. I den første geometri (PHEB) er signalerne fra magnetiske kugler fra sensorarmene additive. I den anden geometri (dPHEB) bruges halvdelen af sensoren som lokal negativ reference til at kompensere for baggrundssignalet fra magnetiske kugler i væsken over sensoren. I alle anvendelser nedenfor bliver de magnetiske kugler magnetiseret af magnetfeltet fra målestrømmen, der sendes gennem sensoren, dvs. ingen ydre magnetfelter er nødvendige for målingerne.

De to typer af målegeometrier er anvendt i to forskellige analyser. PHEB geometrien anvendes til volumen-baseret biodetektion, hvor ændringen af den hydrodynamiske størrelse af magnetiske kugler ved binding til analyten studeres. Ændringen påvirker rotationsresponset (Brownsk relaksation) af de magnetiske kugler og kan måles ved magnetisk AC susceptometri. dPHEB geometrien anvendes til overflade-baseret biodetektion, hvor analyterne binder til indfangningsprober immobiliseret på sensoroverfladen og muliggør binding af de magnetiske kugler til sensoroverfladen.

I denne afhandling udledes teorien for PHEB og dPHEB sensor signalerne. Ydermere, betragtes effekten af formanisotropi på sensorsignalet. Vi introducerer Brownsk relaksation af magnetiske kugler og chip-baserede magnetiske susceptibilitetsmålinger ved brug af PHEB sensorer.

Effekten af temperatur på de magnetiske egenskaber af sensorfilmen og sensorsignalet studeres. En metode præsenteres til at skelne mellem reversible og irreversible effekter af temperaturen. Det studeres hvordan lav-temperatur annealing can minimere disse effekter. De eksperimentalle resulter viser at det er umuligt helt at undgå irreversible ændringer i sensoren og at der derfor skal korrigeres for disse ved at bruge en reference sensor. En sådan reference er nødvendig i biodetektionseksperimenter, hvor der er betydelige ændringer af temperaturen.

Vi anvender PHEB sensor baseret AC susceptometri til volumen-baseret biodetektion. Den eksperimentelle opstilling gør det muligt at måle sensor signaler som funktion af frekvens i intervallet mellem DC og 5 MHz, hvilket gør det muligt at bestemme den hy-

drodynamiske størrelse for kugler med nominel diameter fra 10 nm til 250 nm i konsentrationer ned til 64 μg/mL (for 40 nm beads). Magnetiske kugler med en diameter på 80 nm findes at være de bedst egnede til biodetektionseksperimenter. Tids-domæne målinger af Brownsk relaksation demonstreres også med PHEB sensor, da denne teknik kan føre til hurtigere målinger, på bekostning af lavere signal til støj forhold. Denne metode sammenlignes med frekvensdomænemålinger for detektion af biotin-konjugeret BSA (Bovine Serum Albumin), bBSA. Begge teknikker kan detektere bBSA i nM området.

Ydermere er Frekvensdomænemålinger anvendt til detektion af rolling circle amplification (RCA) produkter. RCA klumper med en diameter på ≈ 1 μm er fremstillet ved RCA efter genkendelse af *Vibrio cholerae* (VB) og af *Bacillus globigii* sporer og detekteret ved inkubation med korrekt funktionaliserede magnetiske kugler. Binding af de magnetiske kugler til RNA klumperne bremser kuglernes dynamik, hvilket kan observeres som en stigning i den hydrodynamiske diameter. Analysen kan detektere ned til 4 pM af DNA klumper og ned til 500 sporer i udgangsprøven. Disse værdier er sammenlignelige med dem fundet ved brug af et kommercielt susceptometer.

Differentielle PHEB sensorer (dPHEBs) benyttes til overflade-baseret sanwich detektion af DNA hybridisering. Biotinyleret target DNA binder til overflade-bundne indfangningsprober og muliggør derved binding af 50 nm streptavidin-funktionaliserede magnetiske kugler til sensor overfladen. Sensorerne kan detektere DNA ned til en koncentration på 156 pM efter 60 min hybridisering. Opstillingen er i stand til real-tidsmålinger af DNA hybridisering i en baggrund af magnetiske kugler i suspension. Denne egenskab benyttes til SNP (Single nucleotide polymorphism) genotyping, hvor denatureringen af DNA monitoreres i realtid under vask med en stringent buffer.

Sensoropstillingen inkluderer temperaturkontrol og et væskesystem i stand til at generere en ændring af både temperatur og koncentrationen over sensoroverfladen. Temperaturen og bufferkoncentrationen kan varieres således at denatureringsanalyse af DNA hybrider kan foretages. I denne afhandling undersøges denne analysemetode ved temperaturer mellem 20°C og 70°C og Na^+ ionstyrker mellem 400 mM to 4 mM. Dette demonstrerer fleksibiliteten og anvendelsesmulighederne af de præsenterede måleapparater.

Preface

This dissertation is written in order to partial fulfil the requirements for obtaining the PhD degree at the Technical University of Denmark (DTU). The work, on which this thesis is based, has primarily been performed at the Department of Micro– and Nanotechnology (DTU Nanotech) in the period from January 2011 to January 2014. The work has been been supervised by associate professors Mikkel F. Hansen and Martin Dufva.

This project was financed by the Department of Micro– and Nanotechnology. I would like to use this opportunity to thank DTU Nanotech for the financial support.

I would also like to thank all my colleagues of the Magnetic Systems group at DTU Nanotech. In particular Frederik Østerberg who worked shoulder-to-shoulder with me along the project and was of great support and help and also Anders Henriksen for the help provided in correcting this thesis. I would like to acknowledge our collaborators at Uppsala University, in the figures of their respective group leaders, for the technical contribution and preparation of the samples: Professors Mats Nilsson, Peter Svedlindh and Maria Strømme. I would like to thank Professor Per Guldberg, at Kræftens Bekæmpelse, for the fruitful discussions we had.

I thank my family that supported me in all my decisions even when the distance made it more difficult. I would like to thank my old friends in Italy and the new friends I made here in Denmark for the encouragement and affection. I thank my girlfriend, Gosia, that was on my side in the euphoric moments as well as in the more difficult ones.

Finally I would like to thank my two supervisors, Martin Dufva and Mikkel F. Hansen, for the guidance and support they offered me during the last three years.

Giovanni Rizzi
Department of Micro– and Nanotechnology
Technical University of Denmark
January 29th, 2014

Contents

List of Papers

Paper I
G. Rizzi, N. C. Lundtoft,F. W. Østerberg and M. F. Hansen
"Reversible and Irreversible Temperature-induced Changes in Exchange-biased Planar Hall Effect Bridge (PHEB) Magnetic Field Sensors",
Sensors & Transducers Journal **15**, 22 (2012)

Paper II
F. W. Østerberg, G. Rizzi and M. F. Hansen
"On-chip measurements of Brownian relaxation vs. concentration of 40 nm magnetic beads", J. Appl. Phys. **112**, 124512 (2012)

Paper III
F. W. Østerberg, G. Rizzi and M. F. Hansen
"On-chip measurements of Brownian relaxation of magnetic beads with diameters from 10 nm to 250 nm ", J. Appl. Phys. **113**, 154507 (2013)

Paper IV
F. W. Østerberg, G. Rizzi and M. F. Hansen
"On-chip Brownian relaxation measurements of magnetic nanobeads in the time domain", J. Appl. Phys. **113**, 234508 (2013)

Paper V
F. W. Østerberg, G. Rizzi, T. Zardán Gómez de la Torre, M. Strömberg, M. Strømme, P. Svedlindh and M. F. Hansen
"Measurements of Brownian relaxation of magnetic nanobeads using planar Hall effect bridge sensors", Biosens. Bioelectron. **40**, 147-152 (2013)

Paper VI
F. W. Østerberg, G. Rizzi, M. Donolato, R. S. Bejhed, A. Mezger, M. Strömberg, M. Nilsson, M. Strømme, P. Svedlindh and M. F. Hansen
"On-chip detection of rolling circle amplified DNA molecules from *Bacillus globigii* spores and *Vibrio cholerae*", Small (2014)

Paper VII
G. Rizzi, F. W. Østerberg, M. Dufva and M. F. Hansen
"Magnetoresistive sensor for real-time single nucleotide polymorphism genotyping",
Biosens. Bioelectron. **52**, 445 (2014)

Papers not Included in the Thesis

Paper A

A. Persson, R. S. Bejhed, F. W. Østerberg, K. Gunnarsson, H. Nguyen, G. Rizzi, M. F. Hansen, P. Svedlindh
"Modelling and design of planar Hall effect bridge sensors for low-frequency applications", Sensor. Actuat. A-Phys. **189**, 459 (2013)

Paper B

F. W. Østerberg, A. D. Henriksen, G. Rizzi and M. F. Hansen
"Comment on "Planar Hall resistance ring sensor based on NiFe/Cu/IrMn trilayer structure" [J. Appl. Phys. 113, 063903 (2013)]", J. Appl. Phys. **114**, 106101 (2013)

List of Symbols

Symbol	Description	Unit
c	Molar concentration	M
c_m	Denaturation concentration	M
D_h	Hydrodynamic diameter	m
D_nom	Nominal diameter	m
$\tilde{D}_\mathrm{h}$	Median hydrodynamic diameter	m
$\hat{\mathbf{e}}_i$	Unit vector for i-axis	
erf	Error function	
f	Frequency	Hz
f_B	Brownian relaxation frequency	Hz
f_LN	Log-normal distribution	
$\mathbf{H}$	Magnetic field	A/m
H_x	Component of $\mathbf{H}$ along x-axis	A/m
H_y	Component of $\mathbf{H}$ along y-axis	A/m
H_c	Coercivity field	A/m
$\mathbf{H}_\mathrm{De}$	Demagnetisation field	A/m
H_s	Shape anisotropy field	A/m
H_ex	Exchange field	A/m
H_K	Anisotropy field	A/m
H_y^sf	Magnetic self-field	A/m
H_y^b	Magnetic field of beads	A/m
I_x	Bias current	A
I_RMS	RMS value of the AC bias current	A
I_0	Current amplitude DC	A
i	Imaginary unit	
K	Magnetic anisotropy constant	$\mathrm{J/m^3}$
k_B	Boltzmann constant	J/K
l	Length	m
$\mathbf{m}$	Magnetic moment	$\mathrm{Am^2}$
M	Magnetization	A/m
$\mathbf{M}$	Magnetization vector	A/m
$\hat{\mathbf{M}}$	Magnetization unit vector	
M_0	Magnetization at equilibrium	A/m
M_r	Remanent Magnetization	A/m
M_s	Saturation Magnetization	A/m

Symbol	Description	Unit
$\underline{\underline{N}}$	Demagnetisation tensor	
NR	Normalised signal ratio	
R	Resistance	Ω
R_0	Bridge total resistance	Ω
ΔR_n	Resistance variation of n^{th} bridge arm	Ω
R_{offset}	Resistance offset	Ω
S_0	Low-field sensitivity	$(\text{Vm})/\text{A}^2$
S	Low-field sensitivity corrected for shape anisotropy	$(\text{Vm})/\text{A}^2$
S_{R}	Relative signal	
$S_{\text{R,max}}$	Fitting parameter erf	
$S_{\text{R,min}}$	Fitting parameter erf	
SNR	Signal-to-noise ratio	
T	Absolute temperature	K
T	Temperature	°C
T_m	Melting temperature	°C
T_I	DC current period	s
t	Time	s
t_{FM}	Thickness of ferromagnetic layer	m
t	Thickness of magnetic stack	m
U	Total magnetic energy	J
U_{s}	Shape anisotropy energy	J
U_{ex}	Exchange anisotropy energy	J
U_{K}	Uniaxial anisotropy energy	J
U_{Z}	Zeeman energy	J
$\tilde{u}$	Normalised energy density	A/m
V	Volume	m^3
V_{h}	Hydrodynamic volume	m^3
V_x	Bias voltage	V
V_{RMS}	RMS amplitude of the bias voltage	V
V_y	Bridge output voltage	V
V_{pp}	Peak-to-peak amplitude of bridge output voltage	V
V'_{n}	In-phase n^{th} harmonic signal	V
V''_{n}	Out-of-phase n^{th} harmonic signal	V
$V''_{2,\text{corr}}$	V''_2 corrected for offset	V
V_{off}	First harmonic bridge offset	V
$V_{0\text{t}}$	DC signal amplitude	V
V_0	Fitting parameter modified Cole-Cole	V
V_∞	Fitting parameter modified Cole-Cole	V
V_{ave}	Average DC signal	V
V_{diff}	Differential DC signal	V
$V_0(c,T)$	Reference for signal offset	V
ΔV	Signal variation	V
ΔV_{max}	Fitting parameter erf	V
ΔV_{min}	Fitting parameter erf	V

Symbol	Description	Unit
w	Width	m
α	Polydispersity	
α	Bridge arm angle	rad
χ	Magnetic susceptibility	
χ'	In-phase component of complex magnetic susceptibility	
χ''	Out-of-phase component of complex magnetic susceptibility	
χ_0	DC magnetic susceptibility	
χ_∞	High frequency magnetic susceptibility	
η	Dynamic viscosity	kg/(ms)
γ_0	Self-field effects	1/m
γ_1	Effects of beads magnetised by self-field	1/m
$\gamma_{1\mathrm{t}}$	Time-domain γ_1	1/A
$\gamma_{1\mathrm{f}}$	Frequency-domain γ_1	1/m
μ_0	Permeability of free space	Vs/(Am)
ρ	Resistivity	Ωm
$\rho_\parallel$	Resistivity at parallel current density and magnetization	Ωm
$\rho_\perp$	Resistivity at orthogonal current density and magnetization	Ωm
$\Delta\rho$	$\rho_\parallel - \rho_\perp$	Ωm
σ	Lognormal distribution standard deviation	
σ_{ex}	Interface energy per area	$\mathrm{J/m^2}$
σ_T	Fitting parameter erf	°C
σ_c	Fitting parameter erf	
τ_{B}	Brownian relaxation time	s
θ	Magnetization angle	rad

List of Abbreviations

Abbreviation	Description
AC	Alternating current
AMR	Anisotropic magneto resistance
APTS	3-Aminopropyltriethoxysilane
bBSA	Biotinylated bovine serum albumin
BG	Bacillus globigii
BSA	Bovine serum albumin
CEA	Carcinoembryonic antigen
CPU	Central processing unit
DAQ	Data acquisition
DASH	Dynamic allele-specific hybridization
DC	Direct Current
DNA	Deoxyribonucleic acid
dPHEB	Differential planar Hall effect bridge
DTU	Technical Universtity of Denmark
ELISA	Enzyme-linked immunosorbent assay
ERF	Error function
FBAR	Film bulk acoustic resonator
FM	Ferromagnet
FRET	Frequency resonant energy transfer
GA	Glutaraldehyde
GMR	Giant magnetoresistance
HBB	Human beta globin
HRM	High resolution melting
LOD	Limit of detection
MT	Mutant type
MTJ	Magnetic tunnel junction
PBS	Phosphate buffered saline
PC	Personal computer
PCB	Printed circuit board
PCR	Polymerase chain reaction
PDMS	Polydimethylsiloxane
PHE	Planar Hall effect
PHEB	Planar Hall effect bridge
PLA	Proximity ligation assay
PMMA	Polymethylmethacrylate
POC	Point of care

Abbreviation	Description
QCM	Quartz crystal microbalance
RCA	Rolling cyrcle amplification
RMS	Root mean square
SDS	Sodium dodecyl sulfate
SNP	Single nucleotide polymorphism
SPR	Surface plasmon resonance
SQUID	Superconducting quantum interference devic
SSC	Saline-sodiumcitrate
UV	Ultraviolet
VC	Vibrio cholerae
VSM	Vibrating sample magnetometer
WT	Wild type

CHAPTER 1

Introduction

Advances in biosensor technologies will improve medicine and diagnostics. The introduction of automated, compact and cheap diagnostic tools will lead to a change of paradigm in the medical practice. Now the general practitioner relies on central laboratories to analyse patient specimens, with the introduction of point-of-care (POC) diagnostic tools the sample analysis will be diffused into each doctor's office. The main advantage of such configuration is the shorter time required to obtain results of the analysis. This means a shorter time for diagnosis, and the possibility to monitor over an extended period the evolving of the illness and the efficacy of the cure. Moreover, simple to use or highly automated devices can be operated by trained personnel, as is already the case for drug or alcohol abuse tests.

The glucose monitoring for diabetics is an important example of effective application of this approach. The introduction of an electrochemical sensor for rapid monitoring of the blood glucose level allows for precise administration of insulin by the patients [1]. Another common POC device is the pregnancy test lateral flow assay [2]. In this case the wide spread use of the test is due to the reasonable price of the device and the emotional and privacy interests of the user. In both these cases the balance between the benefits and price determines the success of the device.

1.1 Magnetic biodetection

In our approach to biodetection we use magnetic particles as labels, and detect them using a magnetoresistive sensor. The choice of magnetic particles as label for biodetection is driven by the lack of virtually any magnetic signal from biological material. Among the possible readout technologies for magnetic field, magnetoresistive field sensors could be integrated in POC devices due to their small volume. Many of the proposed magnetic biosensing technologies are reviewed by Freitas *et al.*[3], Tamanaha *et al.* [4] and Wang and Li [5].

The development of magnetic sensors for hard disk drives [6] offered a broad range of sensors that were promptly employed for biodetection as well. These include giant magneto resistance (GMR) sensors [7, 8, 9], magnetic tunnel junction (MTJ) sensors [10, 11] and anisotropic magnetoresistive (AMR) sensors [12]. Common to most approaches is the use of an external field source to magnetise the magnetic beads. In this work we will see how, with our sensor, it is possible to avoid the need for an external magnetic field source.

The most promising results in magnetic biosensing have been achieved by the group of Shan X. Wang at Stanford University for protein detection. Gaster *et al.* [13] reported detection of tumor marker carcinoembryonic antigen (CEA) down to a concentration of

5 fM and a dynamic range of 6 orders of magnitude whether in phosphate buffered saline (PBS), in 0.1% bovine serum albumin (BSA) or mouse serum. Their system was also capable of multiplexing 64 sensors [14] and obtain real-time measurements on all the sensors [15, 16]. They demonstrated also a high density biosensor array, with $\simeq$ 1 000 sensors in 1 mm^2 [17] that they employed to study protein interaction and transport. Also notable is the temperature correction of their system [18] and their hand-held version of their magnetic biodetection platform[19].

Two approaches for biodetection were used in the work presented in this thesis. The first, volume-based biodetection, measures the change in the particle diameter given by binding to a target molecule. The second, surface-based biodetection, detects magnetic particles binding to the sensor surface in a sandwich assay, where the target binds to a surface-linked capture probe, and the magnetic particle binds to the target.

1.1.1 Volume-based biodetection

The volume-based biosensing method used in this thesis employs the measurement of hydrodynamic diameter of magnetic beads. When one or multiple magnetic beads bind to an analyte, their hydrodynamic volume increases (Fig. 1.1.a). Connolly and St Pierre [20] proposed to detect the change in the hydrodynamic size through a measurement of the change in the Brownian relaxation of the magnetic beads.

Brownian relaxation is the process in which the magnetic beads in a fluid rotate to align their magnetisation to an external magnetic field [21]. This process is slowed by the viscosity of the fluid and it is characterised by a relaxation frequency. In Section 2.2.3 we will see that at this frequency a maximum is present in the imaginary term χ'' of the complex magnetic susceptibility of the magnetic beads. Figure 1.1.b shows a sketch of χ'' for free beads and beads clustered on an analyte. The presence of the analyte shifts the signal from the peak due to free beads to a peak at lower frequency.

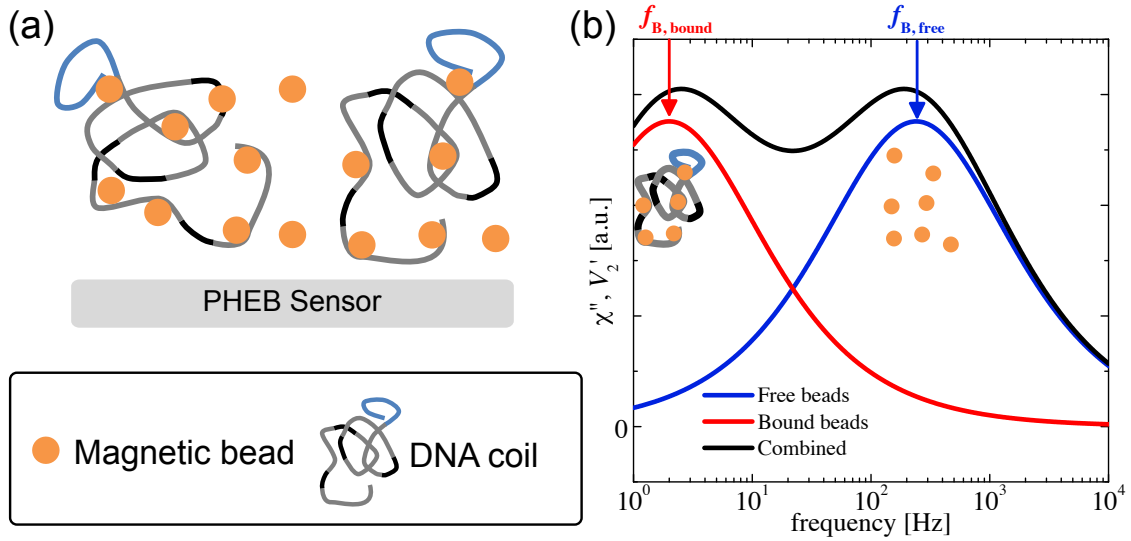

Fig. 1.1: **(a)** Schematic of the volume-based assay. Beads and coils are mixed together. Beads bind to the coils and form cluster that can be detected by magnetic sensors. **(b)** The free magnetic particles relax at a frequency $f_{B,free}$ while the beads-coil cluster at $f_{B,bound}$. Adapted from Paper VI.

Depending on the nature of the analyte, the bead size and their concentration, the

changes in the measured hydrodynamic diameter can be small or large. If the analyte presents a single or multiple binding sites, the bead diameter will be increased directly by the analyte or by formation of bead dimers or clusters.

1.1.1.1 State of the art. Brownian relaxation measurements for biosensing are typically performed using AC susceptometers. Therefore the dynamic magnetic response of the beads is measured when the beads are placed in an alternating magnetic field. The complex magnetic susceptibility χ is measured as a function of the field frequency.

Among magnetic field sensing technologies used for AC susceptometry are: superconducting quantum interference devices (SQUIDs) [22], inductive methods [23, 24, 25], fluxgates [26] and magnetoresistive sensors [27, 28]. SQUIDs offer the highest sensitivity but have a large size (see Fig. 1.2.a) and require cryogenics. Those two aspects make them unsuitable for POC biosensing. Figure 1.2.b shows a picture of a DynoMag AC susceptometer (Imego AB, Sweden). DynoMag is based on inductive measurement of the susceptibility. This equipment is used in Section 5.4 to benchmark our system.

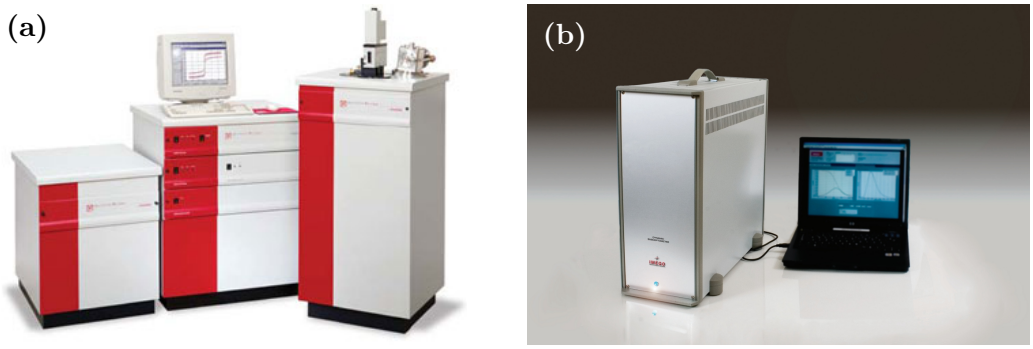

Fig. 1.2: (a) SQUID magnetometer. Comprising cryogenic handling. Source: qdusa.com **(b)** Desktop magnetometer DynoMag(Imego AB, Sweden). Source: imego.com

Miniaturised AC susceptometers have been constructed using commercial AMR barberpole sensors [27, 29] and GMR sensors [30]. These techniques still necessitate an external magnetic field to magnetise the beads, while in our setup it is possible to use the field induced by the current flowing through the sensor to generate the magnetic stimulus [28].

The relaxation of magnetic beads can be also studied in the time-domain[31, 32]. In this case the bead magnetisation is measured while beads rearrange after being aligned by an external magnetic field. The characteristic relaxation time can be measured.

1.1.1.2 Detection of rolling circle amplification (RCA) products. The Brownian relaxation measurements are used in this thesis to detect products of rolling circle amplification (RCA). In an RCA process, the analyte recognition leads to the circularisation of a DNA padlock probe [33]. Since the probe is now a loop of DNA, this can be indefinitely amplified through an isothermal amplification process [34, 35]. The results of this amplification process are coils of DNA, where the same sequence is repeated through all the length. These coils have a diameter of $\simeq 1$ µm. Beads functionalised with the complementary DNA to the amplified sequence can bind to the coils. RCA is an isothermal amplification, when compared to polymerase chain reaction (PCR), it does not require

thermal cycling. The main drawback is that the number of copies in RCA products grows linearly with time, while PCR is an exponential process.

The work in this thesis on detection of RCA coils was carried out in collaboration with the groups of Professors Mats Nilsson, Peter Svedlindh and Maria Strømme from Uppsala University (Sweden). Our collaborators provided us with the samples after RCA amplification that were used for detection in this work. Their previous works on RCA coils detection using a SQUID magnetometer [36] and a DynoMag [25] reported a limit of detection (LOD) on the order of $3 - 4$ pM and a dynamic range of 3 orders of magnitude. Currently their sample preparation is performed in manually in tube, but it can be potentially be performed in a lab-on-a-chip device.

1.1.2 Surface-based biodetection

In surface-based biosensing, the analyte molecules in the sample bind specifically to capture probes tethered to the surface of a substrate. The target is labelled or stained (usually employing fluorescent dyes). The target can be quantified using a fluorescence optical readout system. This is the case for enzyme-linked immunosorbent assay (ELISA) [37] and protein microarrays [38] where the probes are antibodies directed to a specific target antigen. DNA microarrays [39, 40, 41] are also part of this category. In DNA microarray, the probes are oligonucleotides complementary to the sequence of one alternative form (allele) of a gene portion.

For cancer and genetic diagnostics, surface-based DNA assays need to distinguish between DNA sequences differing by a single base, by performing the so called single nucleotide polymorphism (SNP) genotyping. Figure 1.3.a shows a schematic of allele specific hybridisation assay for SNP genotyping as it is performed on a microarray. Two probes specific to the wild type (WT) and mutant type (MT) sequences are used. After hybridisation of a fluorescence labelled target, a stringent washing is used to reduce the unspecific binding. The signal is then read using a fluorescence scanner.

The magnetic approach to surface-based biosensing uses magnetic particles as labels instead of fluorescent dyes. The assay is represented in Fig. 1.3.b. The biotinylated target DNA binds to the capture probes on the sensor surface. The streptavidin coated beads bind to the target through the strong streptavidin-biotin bond.

In our configuration, part of the sensor is used as local negative reference. The signal from the bead suspension is subtracted. Therefore it is possible to measure in a background of unbound target and magnetic beads.

1.1.2.1 State of the art. DNA microarrays with fluorescence end-point detection are the most wide spread method for SNP genotyping. Their approach to the detection is highly multiplexed, with up to 500 000 SNP locations investigated in parallel on the same array (source: illumina.com). Their dynamic range spans to more than five orders of magnitude [41] and they have typically detection limit of $1 - 10$ pM. They rely on big and expensive fluorescence scanners for end-point detection. Non-fluorescence readout method, such as colorimetry enzymatic readout [42, 43] have similar detection limit to fluorescence microarray, but only a dynamic range of one or two orders of magnitude.

While the previous techniques employ an end-point detection, other systems allow for real-time detection of DNA hybridisation and denaturation. Using GMR sensors, Xu *et al.* [44] demonstrated the detection of 10 nM PCR products, by monitoring the binding

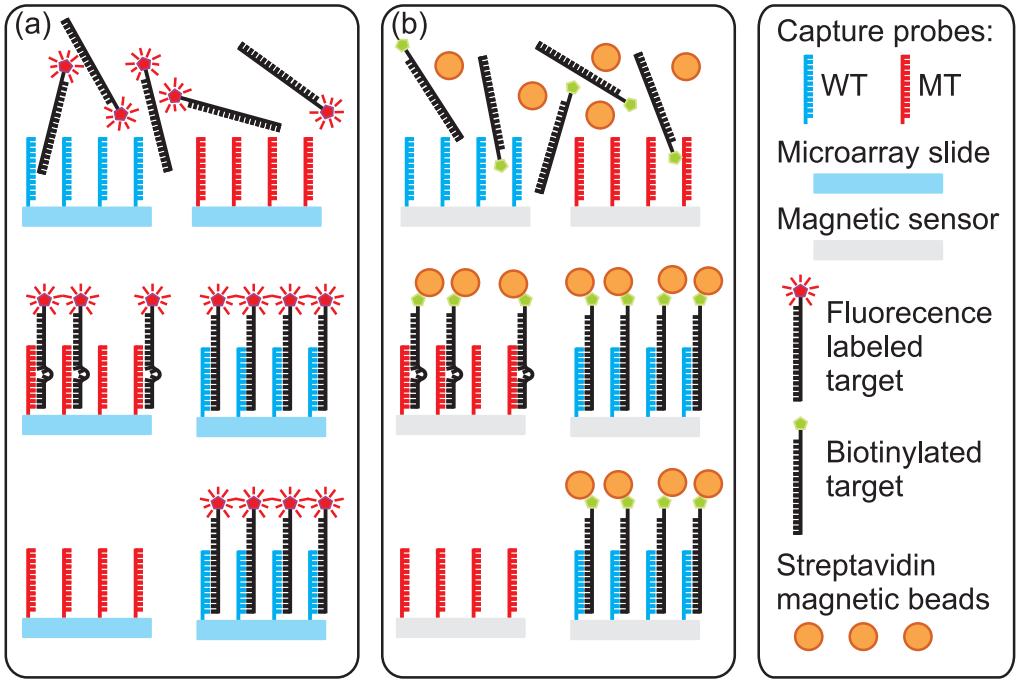

Fig. 1.3: **(a)** Description of microarray assay. Fluorescence labelled target over the microarray slide during hybridisation. After hybridisation high unspecific binding is present. Stringent washing reduces denatures the unspecific duplexes **(b)** Schematics of the surface-based magnetic DNA assay. Biotinylated target is used instead of fluorescence labelled target. Streptavidin coated beads bind to the target and are linked to the sensor surface.

of magnetic particles to a spin valve sensor where DNA target was hybridised outside the measuring system. Other chip based methods include surface plasmon resonance (SPR) [45], quartz crystal microbalance (QCM) [46] and film bulk acoustic resonator (FBAR) [45]. These method do not use a labelling of the targets and have detection limit ~ 1 nM. Their sensitivity is hampered by the unspecific binding of the sample matrix to the sensor surface. Magnetic biodetection however is nominally insensitive to the sample matrix.

1.1.2.2 High-resolution DNA denaturation. The DNA duplex stability depends on the base sequence, the temperature and the ionic strength of the solution [47, 48]. The specificity in a surface-based assay is achieved by washing the substrate in a stringent condition to denature the mismatched duplexes (i.e.: the duplexes in which the two strands differ by a SNP) while retaining intact the perfectly matched duplexes. It is possible to increase specificity of genetic analysis by performing a denaturation curve of the hybrids by sweeping the temperature or the washing ionic strength [49, 50, 51, 52].

Figure 1.4 shows such an assay, at $t = 0$ the target DNA, in low stringency condition, is hybridised to both MT and WT probes. The mismatched hybrids are denatured before the perfectly matched hybrids when increasing the temperature (or decreasing ionic strength). Compared to end-point detection after a single condition washing, the use of a denaturation assay offers at all times the best condition to discriminate the targets [49, 50, 51, 52]. High-resolution melting measurements are usually performed in a thermo-cycler, and are limited in the number of sequences that can be analysed at once. Noticeable is the work of Howell Jobs *et al.* [50] to overcome this limitation. They developed the so called dynamic

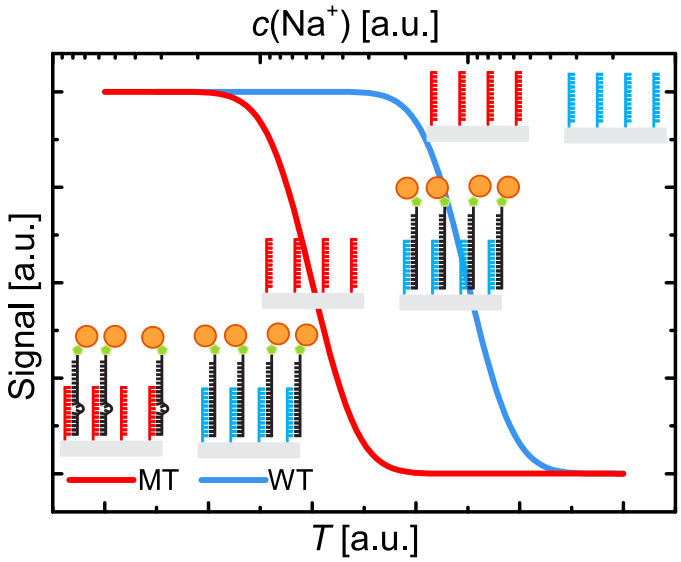

Fig. 1.4: DNA denaturation over magnetic sensor. The mismatched MT probe-target hybrids denature at a lower temperature (or higher concentration $c(Na^+)$) than the perfectly matched hybrids.

allele-specific hybridization (DASH), where multiple hybrids bound on a membrane are denatured using frequency resonant energy transfer (FRET).

1.2 Motivation and outline

The work presented in this thesis, is continuing the work on biodetection on planar Hall effect magnetoresistive sensors by Ejsing *et al.* [12], Damsgaard *et al.* [53, 54] and Dalslet *et al.* [28, 55]. The work on surface-based and volume-based detection was carried in parallel by the author and Frederik Østerberg, respectively. This project was made possible by the improvement in the sensor design by Henriksen *et al.* [56] that increased the sensor sensitivity and paved the way for biodetection.

This thesis aims to investigate the use of planar Hall effect bridge (PHEB) magnetic field sensors for biodetection, their possibilities and limitation for this application. Two different detection method are presented in this work. First, the sensors are used to measure AC susceptibility of magnetic beads. This technique is used to measure the difference in the Brownian relaxation of free beads and beads bound to biological targets. In collaboration with Uppsala University, Brownian relaxation measurements on-chip are used to detect DNA coils from RCA similar to those studied by Strömberg *et al.* [36] and Zardán Gómez de la Torre *et al.* [25] using a SQUID magnetometer and a DynoMag, respectively.

The PHEB sensors, functionalised with surface binding probes, are used to detect DNA hybridisation to the sensor surface. The system is tested on the detection of a single point mutation of the human beta-globin gene using DNA capture probes designed and characterised by Petersen *et al.* [43, 57, 58]. This offers a comparison between our system and the end-point fluorescent detection of microarray. Finally, the sensors are used to measure denaturation of the surface tethered DNA hybrids upon increasing temperature or decreasing Na^+ ions concentration in the solution. This last application employs all

the features of the PHEB sensing to provide a unique approach to perform DNA melting studies using multiple probes on the same chip.

A short description of the thesis structure is given here:

- Chapter 2 introduces the theoretical background about PHEB magnetic field sensor and about detection of magnetic beads on PHEB sensors. The Brownian relaxation of beads is also introduced. The sensor signals are derived for frequency-domain and time-domain measurements of the bead relaxation.

- Chapter 3 presents sensor geometries and fabrication. The chapter describes the measurement setup including microfluidics and electronics. Finally, it gives an overview of all the experimental procedures for sensor characterisation, sensor functionalisation and data treatment.

- Chapter 4 introduces the effects of temperature upon the sensor sensitivity. This study emphasizes the reversible and irreversible changes of the sensor upon temperature cycling. A low-temperature annealing process is investigated to reduce those effects. These results are part of Paper I.

- Chapter 5 investigates the use of PHEB to measure Brownian relaxation of magnetic beads in both frequency-domain and time-domain. First, a broad characterisation of the method is performed, varying bead concentration and diameter. Then, the method is used to detect RCA products (DNA coils) from *Vibrio cholerae* and *Bacillus globigii*. These results are part of Paper II, Paper III, Paper IV, Paper V and Paper VI.

- Chapter 6 investigates the use of PHEB, in a differential geometry, to detect DNA hybridisation to surface bound probes. First, the signal from surface-bound beads is studied using the stronger biotin-streptavidin link as a model. Then DNA hybridisation is performed on-chip and SNPs are detected using a stringent washing. Finally the surface tethered DNA hybrids are denatured using temperature and ionic concentration gradients. These results are part of Paper VII.

- Chapter 7 offers an overview of the possible improvements that can be implemented in PHEB biosensing setup. The chapter also offers an outlook over possible application of the biosensing technology.

CHAPTER 2

Theory

In this chapter the theoretical background to understand the planar Hall effect (PHEB) and differential planar Hall effect (dPHEB) bridge sensors will be given. First the sensor geometries are introduced and their differences in terms of functionality are described. The sensor output is derived in a uniform external field. Then, magnetic bead detection is presented. In PHEB and dPHEB sensor the magnetic beads are magnetised by the field generated by the bias current flowing in the sensor arms. Therefore there is no need for an externally applied magnetic field. This detection technique is also used to measure Brownian relaxation in the time-domain and in the frequency-domain.

2.1 PHEB magnetic field sensor

In this section, the signal output of a PHEB magnetic sensor in an external magnetic sensor will be derived. First, anisotropic magnetoresistance will be introduced for a single segment (or arm) of a bridge sensor. Following, we will analyse PHEB and dPHEB geometries in an external field. The sensor output will be derived from a single domain model of the sensor. We will end the section by explaining how shape anisotropy affects the sensor output.

2.1.1 Anisotropic magnetoresistance

The sensor geometries used in this work are depicted in Fig. 2.1. Both PHEB (Fig. 2.1.a) and dPHEB (Fig. 2.1.b) are formed by four arms of a magnetic stack, exchange biased along the x-direction and arranged in a Wheatstone bridge geometry. Each arm has length l and width w and a stack of thickness t. All the arms have an inclination of $\alpha = \pm\pi/4$. The two geometries differ only in the arrangement of the arm angles.

The magnetic stack used to fabricate the sensors exhibits anisotropic magnetoresistance (AMR). Hence, its resistivity along the magnetisation ($\rho_{\parallel}$) is bigger than the resistivity perpendicular to the magnetisation ($\rho_{\perp}$). The difference between the two resistivities is

$$\Delta\rho = \rho_{\parallel} - \rho_{\perp}. \tag{2.1}$$

To quantify this effect we should keep in mind that $\Delta\rho$ for permalloy ($Ni_{80}Fe_{20}$) is about 2% of the average resistivity [59]. When we consider a single arm of the sensor we work with a slab of magnetoresistive material of length l and width w as in Fig. 2.4. The resistance of an arm depends on the angle α between the arm and the x-axis and upon the angle θ between the magnetisation and the x-axis. If we suppose that the magnetic

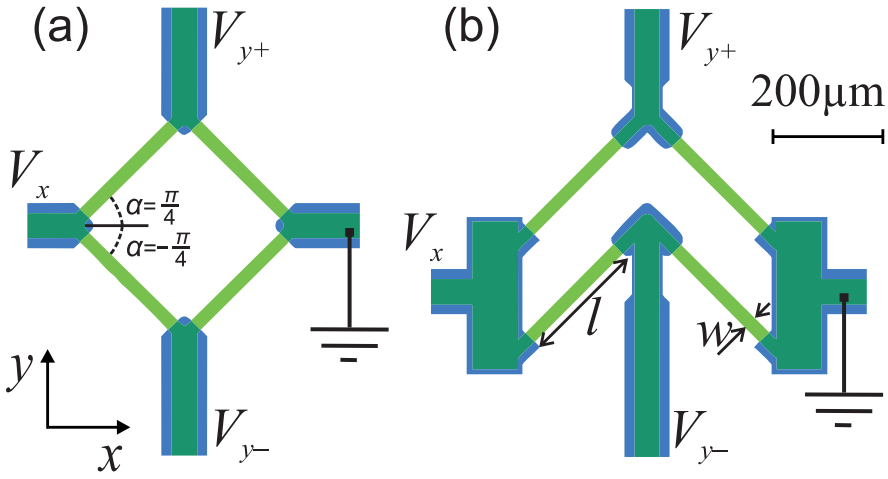

Fig. 2.1: Geometries of the sensors **(a)** PHEB and **(b)** dPHEB. Both sensor bridges are composed by four magnetoresistive elements of width w and thickness t. The bridge arms have an inclination $\alpha = \pm\pi/4$. The sensors are biased with a voltage V_x along the x-axis and the sensor output $V_y = V_{y+} - V_{y-}$ is measured along the y-axis. Adapted from Paper VII.

material has an uniform magnetisation with constant angle θ, the resistance of a single arm is [56]

$$R(\alpha,\theta) = \frac{l}{wt}\left\{\cos^2\alpha\left[\rho_\parallel - \Delta\rho\,\sin^2\theta\right] + \frac{1}{2}\Delta\rho\,\sin(2\alpha)\sin(2\theta) + \sin^2\alpha\left[\rho_\parallel - \Delta\rho\,\cos^2\theta\right]\right\}. \tag{2.2}$$

In our sensor geometries, the angle α can assume the values $\alpha = \pm\pi/4$. The resistance is simplified to the form

$$R(\pm\frac{\pi}{4},\theta) = \frac{l}{wt}\left[\frac{\rho_\parallel + \rho_\perp}{2} \pm \frac{\Delta\rho}{2}\sin(2\theta)\right]. \tag{2.3}$$

In this equation we see that the resistance has a part depending on the angle θ that is linear for small angles. The other part of the resistivity is a constant

$$R_0 = \frac{l}{wt}\frac{\rho_\parallel + \rho_\perp}{2}, \tag{2.4}$$

which is the same for all sensor arms, independently of the sign of the angle α.

2.1.2 Wheatstone bridge output

Although it could be possible to use a single sensor arm as magnetic sensor, we have to notice that R_0 is about fifty times bigger than the AMR component. Moreover R_0 depends on the temperature of the sensor. To avoid the problem caused by this offset, we employed a Wheatstone bridge geometry, that cancels out the constant term of the resistance.

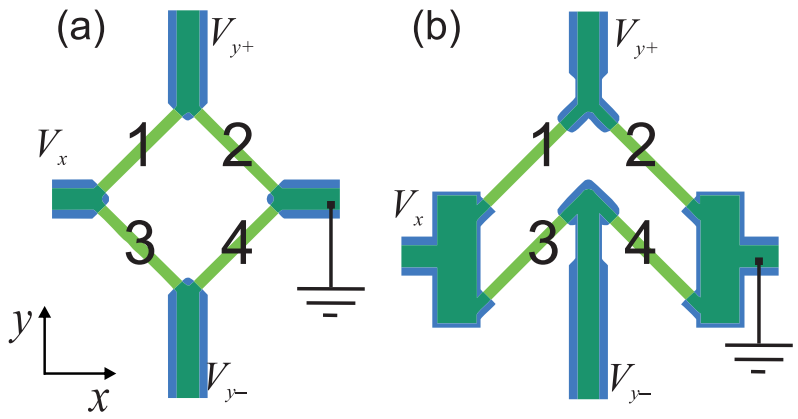

Fig. 2.2: Numbering system used to identify the magnetoresistive arms of the bridges in the **(a)** PHEB and **(b)** dPHEB geometries. Adapted from Paper VII.

Figure 2.2 shows the numbering used to identify the different magnetoresisitve segments forming the PHEB and dPHEB sensor bridges. The Wheatstone bridge output is

$$V_y = V_x \left[\frac{R_3}{R_3 + R_4} - \frac{R_1}{R_1 + R_2} \right]. \tag{2.5}$$

We note that the PHEB geometry in a uniform field fulfils $R_1 + R_2 = R_3 + R_4 = 2R_0$. Hence the total bridge resistance is independent on external field and it is equal to R_0. For the PHEB sensor we can simplify Eq.(2.5) to

$$V_y = \frac{V_x}{2R_0}(R_3 - R_1) = -\frac{V_x}{2R_0}\frac{l}{wt}\Delta\rho\sin(2\theta) = -\frac{V_{\text{pp}}}{2}\sin(2\theta), \tag{2.6}$$

where we defined the peak to peak signal of the bridge as

$$V_{\text{pp}} = \frac{V_x}{R_0}\frac{l}{wt}\Delta\rho. \tag{2.7}$$

From Eq.(2.6) we can see that the bridge output is $V_y = 0$ when $\theta = 0$, it is linear for small angles θ and it reaches maximum (minimum) value $V_y = V_{\text{pp}}/2 (V_y = -V_{\text{pp}}/2)$ when $\theta = -\pi/4\,(\theta = \pi/4)$. This can be easilly understood visually from Fig. 2.3.

In Fig. 2.3.a the magnetisation angle is $\theta = 0$, we see that current is flowing at an angle $\alpha = \pm\pi/4$ in every sensor arm. The resistance of every arm is identical and equal to R_0. The bridge is ideally balanced and there is no voltage output $V_y = 0$. When an external magnetic field changes the magnetisation to an angle $\theta = \pi/4$ as in Fig. 2.3.b, the current flows perpendicular or parallel to the magnetisation vector depending on the sensor arm. The resistivities of the arms are $\rho_\parallel$ and $\rho_\perp$ therefore the bridge is in the condition of maximum asymmetry. Recalling $\rho_\parallel > \rho_\perp$ we see that the bridge output is negative (and therefore minimum). In the last case, in Fig. 2.3.c, the magnetisation angle is $\theta = \pi/2$, this could be the case of a saturating magnetic field in the y-direction. As for the first case, the current flows at 45° with respect to the magnetisation, in all the arms. The resistances of all the arms are identical, the bridge is balanced and therefore the output is $V_y = 0$. The other cases can be obtained by symmetry from these three cases.

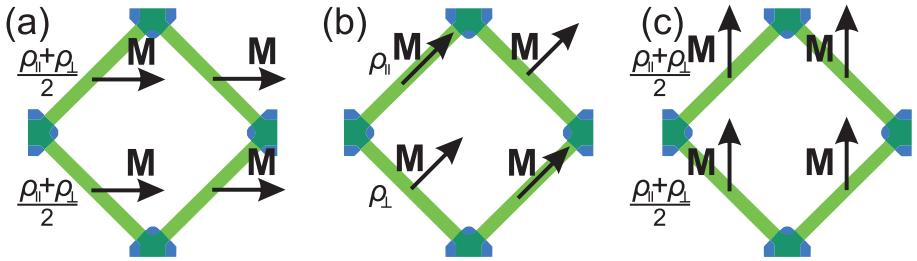

Fig. 2.3: PHEB output in different orientation of the magnetisation. The bias voltage is applied in the x-direction and the output voltage is read in the y-direction. **(a)** In zero external magnetic field, the magnetisation is pinned along the x-axis. The resistance of each arm is identical. The output voltage is zero. **(b)** An external magnetic field orients the magnetisation at an angle $\theta = \pi/4$ respect to the x-axis. The magnetisation is therefore parallel or perpendicular to the arms. The resistances of the arms are as different as possible. The sensor output is minimum. **(c)** A big external field orients the magnetisation parallel to the y-axis. Again the resistances of each arm are identical. The bridge is balanced, $V_y = 0$.

2.1.3 Magnetic energy

In this section the magnetisation angle θ is calculated as a function of the external magnetic field. This function will be used to obtain the sensor output in presence of an external magnetic field.

The material forming the sensing arms of the sensor is a top pinned ferromagnet ($Ni_{80}Fe_{20}$). It means that a preferential direction for the magnetisation was defined by depositing an antiferromagnetic material (here $Mn_{80}Ir_{20}$) over the ferromagnetic layer [60]. We first describe the magnetic energy of the ferromagnetic material. Then, we present an analytical solution for negligible shape anisotropy. In Section 2.1.6, we analyse the realistic case when shape anisotropy is present.

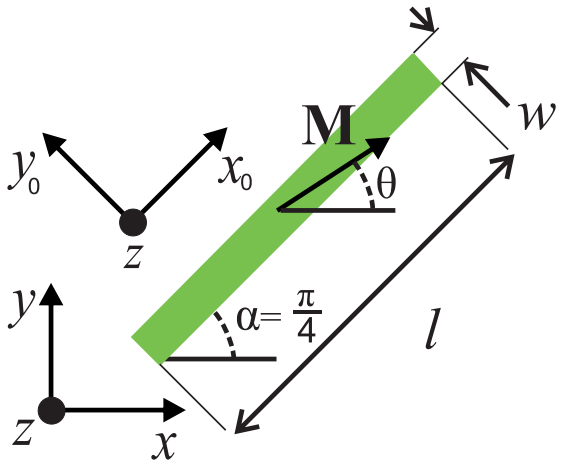

Fig. 2.4: Single segment of magnetic material used for the analysis of the magnetic energy. The magnetisation easy axis and easy direction are in the positive x-axis direction.

Figure 2.4 shows a segment of magnetic stack material, inclined by an angle α to the x-axis and with the magnetisation $\mathbf{M}$ at an angle θ respect to the x-axis. The external field $\mathbf{H} = H_x\hat{\mathbf{e}}_x + H_y\mathbf{e}_y$ is applied in the xy plane. This segment is a generalisation of the geometry of one of the arms of the magnetic sensors. It has a width w and a length l. It is formed by a ferromagnetic layer of thickness t_{FM} top pinned by an antiferromagnetic

layer. We will now analyse the magnetic energy terms for such geometry for a single domain material.

2.1.3.1 Zeeman energy. When a volume V of ferromagnetic material is subject to an external field $\mathbf{H}$ this gives rise to a Zeeman energy

$$U_{\mathrm{Z}} = -\mu_0 V \mathbf{M} \cdot \mathbf{H}, \tag{2.8}$$

where μ_0 is the permeability of free space. This energy term is minimised when the magnetisation is aligned with the external field and it is maximum when they are antiparallel. In our case both the magnetisation and the magnetic field are in the xy plane.

2.1.3.2 Uniaxial anisotropy energy. During deposition of the ferromagnetic material, a preferential axis of magnetisation, named easy-axis, can be defined by applying an external field. The uniaxial anisotropy energy is

$$U_{\mathrm{K}} = -KV \left(\hat{\mathbf{M}} \cdot \hat{\mathbf{e}}_{\mathrm{K}}\right)^2, \tag{2.9}$$

where K is the anisotropy constant, $\hat{\mathbf{M}}$ is the unit vector of the magnetisation and $\hat{\mathbf{e}}_{\mathrm{K}}$ is the unit vector identifying the easy-axis direction. This energy is minimised when the magnetisation is parallel or antiparallel to the easy axis. The uniaxial anisotropy causes the hysteresis in magnetic materials. In our material the easy axis was defined along the positive x-axis so $\hat{\mathbf{e}}_{\mathrm{K}} = \hat{\mathbf{e}}_x$.

2.1.3.3 Exchange anisotropy energy. The exchange biasing with an antiferromagnetic layer defines a preferential direction of magnetisation, named the easy direction. The easy direction is defined during deposition of the antiferromagnetic layer by applying an external magnetic field. The exchange anisotropy energy is

$$U_{\mathrm{ex}} = -\sigma_{\mathrm{ex}} V t_{\mathrm{FM}}^{-1} \left(\hat{\mathbf{M}} \cdot \hat{\mathbf{e}}_{\mathrm{ex}}\right), \tag{2.10}$$

where σ_{ex} is the interface energy per unit area, Vt_{FM}^{-1} is the area of the interface between the ferromagnetic and the antiferromagnetic layer and $\hat{\mathbf{e}}_{\mathrm{ex}}$ is the unit vector identifying the easy direction. This energy is minimised when the magnetisation is aligned with the easy direction. In our case the easy-direction was defined along the positive x-axis such that $\hat{\mathbf{e}}_{\mathrm{ex}} = \hat{\mathbf{e}}_x$.

2.1.3.4 Shape anisotropy energy. Shape anisotropy represents the tendency of the magnetisation to align to the length of the sensor arm, to minimise the magnetic field outside the magnetic material. Shape anisotropy is described by a demagnetisation tensor ($\underline{\underline{N}}$) and a demagnetisation field ($\mathbf{H}_{\mathrm{de}}$) related as

$$\mathbf{H}_{\mathrm{de}} = -\underline{\underline{N}} \cdot \mathbf{M}. \tag{2.11}$$

In a coordinate system (x_α, y_α, z) aligned with the long direction of the slab the tensor $\underline{\underline{N}}$ is diagonalised. The shape anisotropy energy takes this form

$$U_{\mathrm{s}} = -\mu_0 V \mathbf{M} \cdot \mathbf{H}_{\mathrm{de}} = \frac{1}{2}\mu_0 V M_{\mathrm{s}}^2 \sum_{i=x_\alpha,y_\alpha,z} N_i \left(\hat{\mathbf{M}} \cdot \hat{\mathbf{e}}_i\right)^2, \tag{2.12}$$

where $\hat{\mathbf{e}}_i$ are the unit vector in the x_α, y_α, z axis directions and we used $\mathbf{M} = M_\mathrm{s}\hat{\mathbf{M}}$ with M_s saturation magnetisation, that holds true for single domain ferromagnetic materials. Given the geometries of the sensor, where the thickness of the magnetic material is its smallest dimension ($t \ll w < l$), N_z is the largest component of the tensor $\underline{\underline{N}}$. This term confines the magnetisation to be in-plane. We therefore can take into account only the terms $N_{x_\alpha} = N_\parallel$ parallel and $N_{y_\alpha} = N_\perp$ perpendicular to the direction of the slab segment, i.e.: oriented along $\hat{\mathbf{e}}_\alpha$.

2.1.3.5 Total energy. When we sum all the energy term and normalise the total energy U by $\mu_0 M_\mathrm{s} V$, we obtain the normalised energy density

$$\tilde{u} = \frac{U}{\mu_0 M_\mathrm{s} V} \tag{2.13}$$

$$\tilde{u} = -H_x \cos\theta - H_y \sin\theta - H_\mathrm{ex}\cos\theta - \frac{1}{2}H_\mathrm{K}\cos^2\theta - \frac{1}{2}H_\mathrm{s}\cos^2(\alpha-\theta), \tag{2.14}$$

where we used $\mathbf{H} = H_x\hat{\mathbf{e}}_x + H_y\hat{\mathbf{e}}_y$ and only the in-plane terms of the shape anisotropy. We also defined the uniaxial anisotropy field H_K, the exchange anisotropy field H_ex and the shape anisotropy field H_s as

$$H_\mathrm{K} \equiv \frac{2K}{\mu_0 M_\mathrm{s}} \tag{2.15}$$

$$H_\mathrm{ex} \equiv \frac{\sigma_\mathrm{ex}}{t_\mathrm{FM}\mu_0 M_\mathrm{s}} \tag{2.16}$$

$$H_\mathrm{s} \equiv (N_\perp - N_\parallel)M_\mathrm{s}. \tag{2.17}$$

In the next two sections we will work in the simplifying hypothesis that $H_\mathrm{s} = 0$. In this approximation it is possible to obtain a simple analytical formulation for the angle θ for small applied field H_y. The effect of shape anisotropy will be discussed in Section 2.1.6.

2.1.3.6 Magnetisation angle. It is possible to calculate the angle θ through a numerical minimisation of the normalised energy density in Eq.(2.14).

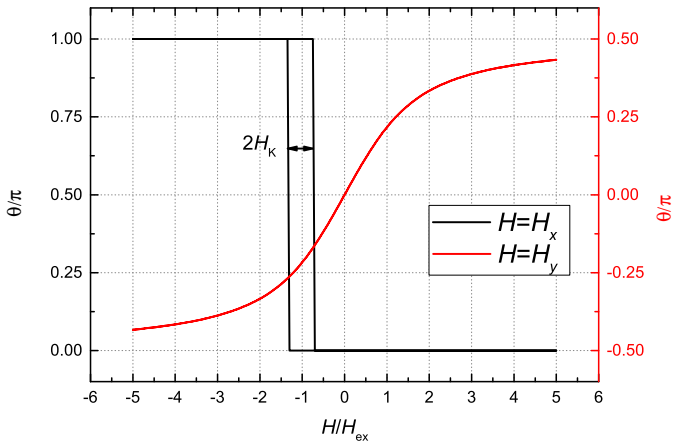

Fig. 2.5: Magnetisation angle θ vs. H_x/H_ex and H_y/H_ex, respectively. The angles were calculated for $H_\mathrm{K} = 0.3H_\mathrm{ex}$. The hysteresis loop is centered in $H_x = H_\mathrm{ex}$ and has amplitude $2H_\mathrm{K}$. For small fields H_y, the angle θ is linear.

Figure 2.5 shows the result of such a minimisation for external field applied in the x and y directions. The calculation was performed for $H_{\mathrm{K}} = 0.3H_{\mathrm{ex}}$ and $H_{\mathrm{s}} = 0$ and sweeping the field in the x-axis and y-axis direction separately. First, we discuss the curve for field applied along the x-direction. When $H_x = 0$ the magnetisation is pinned along the positive x-axis by the combined effect of the uniaxial and exchange anisotropy. When the field is antiparallel to the magnetisation, and it has a magnitude $H_x < -(H_{\mathrm{ex}} + H_{\mathrm{K}})$ the magnetisation flips direction to $\theta = \pi$. When the external field is again increased above $H_x > -(H_{\mathrm{ex}} - H_{\mathrm{K}})$ the exchange anisotropy is the leading energy term and $\theta = 0$. The hysteresis loop opening in the curve is centred at $-H_{\mathrm{ex}}$ and has a width of $2H_{\mathrm{K}}$.

When sweeping H_y the angle θ approaches $-\pi/2$ and $\pi/2$ for high negative and positive fields, respectively. When $H_y = 0$ then $\theta = 0$ and the curve is linear in the low-field region. We also notice that there is no hysteresis loop in the curve. When an arbitrary field is applied, the magnetisation angle will depend mainly on the component of the field in the y-axis direction, as long as the component along the x-axis direction is $|H_x| \ll (H_{\mathrm{K}} + H_{\mathrm{ex}})$. In this condition, and for small angle θ, it is possible to obtain an analytical solution to the minimisation of the normalised magnetic energy density of Eq.(2.14) by deriving and Taylor expanding to first order in θ. The solution is

$$\theta \simeq \frac{H_y}{H_{\mathrm{ex}} + H_{\mathrm{K}}}. \tag{2.18}$$

We see that the angle is linear for low applied field. We also notice that for our sensor the typical value of $\mu_0(H_{\mathrm{K}} + H_{\mathrm{ex}}) \simeq 2$ mT, therefore the condition used to obtain Eq.(2.18) is realistic.

2.1.4 Lock-in amplification

The sensor signals are measured using lock-in amplification. The sensor are biased using a voltage $V_x = \sqrt{2}V_{\mathrm{RMS}} \sin(2\pi ft)$ where V_{RMS} is the root mean square (RMS) amplitude of the voltage and f is the frequency of the wave. The n^{th} harmonic lock-in signal is $V_n = V_n' + \mathrm{i}V_n''$ where V_n' and V_n'' are the in-phase and out-of-phase components, respectively, and can be calculated as

$$V_n' = \frac{\sqrt{2}}{2\pi} \int_0^{2\pi} \sin(2\pi nft) V_y(t) \mathrm{d}(2\pi ft) \tag{2.19}$$

$$V_n'' = \frac{\sqrt{2}}{2\pi} \int_0^{2\pi} \sin(2\pi nft + \frac{\pi}{2}) V_y(t) \mathrm{d}(2\pi ft) \tag{2.20}$$

where $V_y(t)$ is the sensor output.

2.1.5 Bridge geometries

To calculate the output of PHEB and dPHEB sensor geometries we first need the resistance of one of the bridge arms as a function of the external field H_y. Combining Eq.(2.3) and Eq.(2.18) we obtain

$$R(\pm\frac{\pi}{4}, H_y) = \frac{l}{wt}\left[\frac{\rho_{\parallel} + \rho_{\perp}}{2} \pm \Delta\rho \frac{H_y}{H_{\mathrm{ex}} + H_{\mathrm{K}}}\right] \tag{2.21}$$

We can then define the low-field sensitivity.

$$S_0 = -\frac{l}{wt}\Delta\rho \frac{1}{H_{\mathrm{ex}} + H_{\mathrm{K}}}, \tag{2.22}$$

S_0 is defined to be negative. With this definition the arm resistivity becomes

$$R(\pm\frac{\pi}{4}, H_y) = R_0 \mp S_0 H_y. \tag{2.23}$$

As discussed earlier, the resistivity is composed by a constant part and a part that is proportional to the external field H_y. When we arrange four resistor element in a bridge configuration we can cancel out constant term of the resistance R_0.

When we consider the PHEB geometry (Fig. 2.1), the Wheatstone bridge equation Eq.(2.5) can be simplified as

$$V_y = \frac{V_x}{2R_0}(R_3 - R_1) = \frac{V_x}{R_0} S_0 H_y. \tag{2.24}$$

When an AC voltage $V_x = \sqrt{2}V_{\mathrm{RMS}}\sin(2\pi f t)$ is used to bias the sensor, where V_{RMS} is the root mean square (RMS) amplitude of the voltage and f is the frequency, the sensor output due to a uniform applied magnetic field can be measured in the first harmonic lock-in signal output (Eq.(2.20))

$$V_1' = \frac{V_{\mathrm{RMS}}}{R_0} S_0 H_y \tag{2.25}$$

$$V_1'' = 0. \tag{2.26}$$

Here V_1' and V_1'' are the in-phase and out-of-phase first harmonic lock-in signals.

For the dPHEB sensor instead $R_1 = R_3$ and $R_2 = R_4$. Therefore, the bridge is ideally balanced with a voltage output

$$V_y = 0. \tag{2.27}$$

From this it derives also that the first harmonic in-phase signal for the dPHEB is zero. In reality the dPHEB sensors show a small sensitivity to external field. This is around 50 times smaller than the signal from PHEB.

2.1.6 Shape anisotropy effects on low-field sensitivity

As will be discussed further in Chapter 4, the approximation $H_{\mathrm{s}} = 0$ is not realistic for the sensor geometries used in this work. The typical values of the shape anisotropy field measured for PHEB sensors ranges from $\mu_0 H_{\mathrm{s}} = 0.5$ mT to around $\mu_0 H_{\mathrm{s}} = 1$ mT depending on the particular geometry analysed. In this section, we analyse the effects of shape anisotropy on the PHEB sensors. In particular we concentrate on the effects on the low-field sensitivity S_0. Since dPHEB sensors are not sensitive to external field it is not possible to have a direct measurement of low-field sensitivity but we will see in Section 2.2 that S_0 is a key parameter for magnetic bead detection for both PHEB and dPHEB sensors.

The single domain assumption does not hold when shape anisotropy is taken into account. Given the geometry of the sensor, we use an approximation of single domain in each sensor arm. We will have to take into account two possible magnetisation direction, θ_+ for arms with $\alpha = +\pi/4$ and θ_- for $\alpha = -\pi/4$. In this approximation Eq.(2.6) becomes

$$V_y = -\frac{V_{\mathrm{pp}}}{2}\frac{\sin(2\theta_+) + \sin(2\theta_-)}{2}. \tag{2.28}$$

Minimising the normalised magnetic energy in Eq.(2.14), it is possible to obtain the angles θ_+ and θ_- as a function of the external magnetic field. Although there is no simple analytical solution of Eq.(2.14), it is possible to perform a numerical calculation to investigate the effect of the shape anisotropy on the sensor signal. We considered only the presence of an external field in the y-axis direction (H_y). Moreover, the external field H_y, the uniaxial anisotropy field H_K and the shape anisotropy field H_s were normalised by the exchange bias field H_ex to perform a dimensionless analysis. In our simulation we used $H_\mathrm{K} = 0.3H_\mathrm{ex}$ and the external field ranging from $H_y = -5H_\mathrm{ex}$ to $H_y = 5H_\mathrm{ex}$. The results of the numerical minimisation of the magnetic energy are plotted in Fig. 2.6.a for $H_\mathrm{s} = 0$ (green) and for $H_\mathrm{s} = H_\mathrm{ex}$ (blue θ_+ and red θ_-).

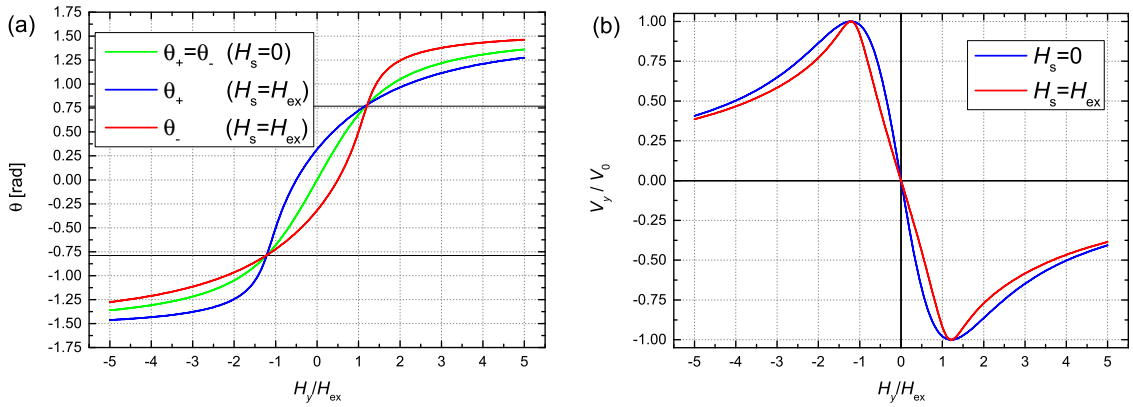

Fig. 2.6: **(a)** Angles θ_+ and θ_- vs. external magnetic field H_y calculated for $H_\mathrm{s} = 0$ (green) and for $H_\mathrm{s} = H_\mathrm{ex}$ (blue and red). **(b)** PHEB sensor output vs. external magnetic field H_y calculated for $H_\mathrm{s} = 0$ and for $H_\mathrm{s} = H_\mathrm{ex}$.

Figure 2.6.a shows the difference between θ_+ and θ_- when $H_\mathrm{s} \neq 0$. In the low-field region the two angles are both non zero, and they have same magnitude and opposed signs. We also notice that the slope of the curve in $H_y = 0$ when $H_\mathrm{s} = 0$ is steeper than for $H_\mathrm{s} = H_\mathrm{ex}$. It is also important to notice that the three curves cross when the angles are $\theta = \pm\pi/4$. For these angle values the sensor output is the highest possible. From this it is directly observed, according to the model, that shape anisotropy do not affect the peak-to-peak value of the sensor signal, as long as $H_\mathrm{s} < 1.5(H_\mathrm{ex} + H_\mathrm{K})$. For this value of H_s an hysteresis loop opens in the angle (data not shown).

The values calculated for the angles θ_+ and θ_- were inserted in Eq.(2.28) to obtain the PHEB output. The PHEB output is plotted in Fig. 2.6 for $H_\mathrm{s} = 0$ (blue) and for $H_\mathrm{s} = H_\mathrm{ex}$ (red). Shape anisotropy does not effect the peak to peak value of the sensor output but narrows the shape of the peaks. Most importantly, the slope for $H_y = 0$, that corresponds to the low-field sensitivity, is reduced. We see that the curve is linear with no offset in the low-field region. Therefore Eq.(2.24) holds true with

$$V_y = \frac{V_x}{R_0} S H_y, \tag{2.29}$$

where S is now the low-field sensitivity corrected for shape anisotropy effects. In Fig. 2.7.a we calculated S (circles) for varying H_s and $H_\mathrm{K} = kH_\mathrm{ex}$, normalised by the corresponding value $S = S_0$ calculated for $H_\mathrm{s} = 0$. We can see that for all the tested values of $k = 0 \rightarrow 0.5$ the behaviour of S is almost identical. The effect of shape anisotropy is to decrease the low-

field sensitivity, reducing it by 25% when $H_s = 0.5(H_{ex} + H_K)$. As we will see in Chapter 4, the investigated values for H_s are realistic for our sensor geometry and composition.

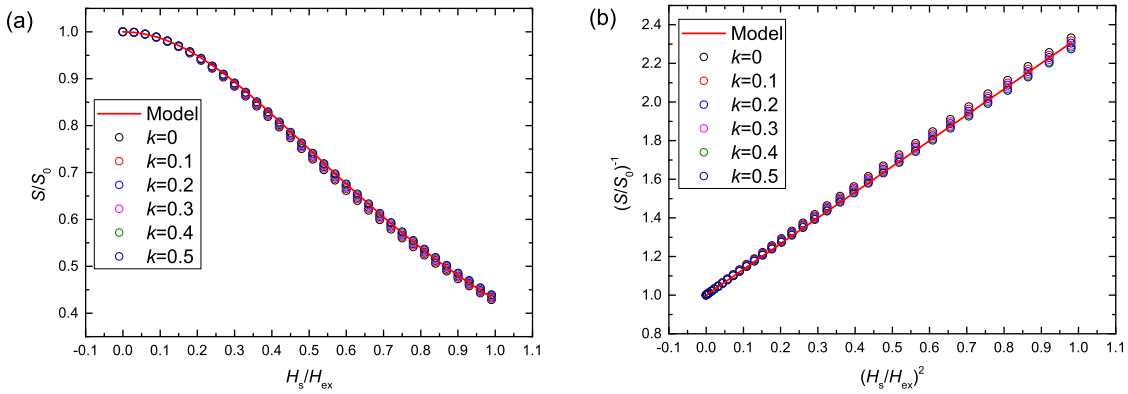

Fig. 2.7: Low-field sensitivity S calculated for $H_K = kH_{ex}$ and normalised by S_0 **(a)** plotted vs. $H_s/(H_{ex}+H_K)$ or **(b)** vs. $[H_s/(H_{ex}+H_K)]^2$ to linearise the sensitivity. The solid lines are the empirical model of Eq.(2.30).

An empirical model for S was proposed starting from the results of Fig. 2.7.a

$$S = 0.75S_0 \left[0.75 + \left(\frac{H_s}{H_{ex} + H_K}\right)^2\right]^{-1}. \tag{2.30}$$

The model is plotted as a solid line in Fig. 2.7. It is seen that the model follows perfectly the calculated points. To validate the model even further the values for $(S/S_0)^{-1}$ are plotted in Fig. 2.7.b vs. $[H_s/(H_{ex} + H_K)]^2$ to linearise the data point.

To summarise, we have found that ideally the shape anisotropy does not affect the peak-to-peak value of the sensor output vs. external field H_y. The main effect of the shape anisotropy is to reduce the low-field sensitivity and to make the peaks in the sensor output vs. field sharper. Since a high sensitivity is critical for detecting magnetic field, the shape anisotropy has to be reduced by using an appropriate sensor design. In particular in this work, the PHEB (and dPHEB) sensors used in Chapter 4 and Chapter 6 were therefore surrounded by the magnetic stack, with a gap of 3 µm. The presence of this surrounding magnetic stack was found to effectively reduce H_s leading to a 60% increase in the sensitivity. In the following paragraphs we will simply consider $H_s = 0$ to determine the sensor response to magnetic beads, knowing that the shape anisotropy will reduce the bead signal with respect to the prediction of the ideal single domain model.

2.2 Sensor response to magnetic beads

2.2.1 Magnetic beads

The magnetic beads can be composed by a variety of different materials and can contain either a single or multiple core particles embedded in different matrices, depending on the application they are developed for. With our magnetoresistive sensors we can detect the dipole field generated by the bead magnetisation $\mathbf{M}$ that is defined as the magnetic moment $\mathbf{m}$ per unit volume V

$$\mathbf{M} = \mathbf{m}/V. \tag{2.31}$$

The magnetisation is related to the magnetic field by

$$\mathbf{M} = \chi \mathbf{H} \tag{2.32}$$

where χ is the magnetic susceptibility. This relation is too simple to describe the different magnetic properties of most real materials. In Fig. 2.8 are sketched the magnetisation of a group of **(a)** ferromagnetic and **(b)** superparamagnetic nanoparticles.

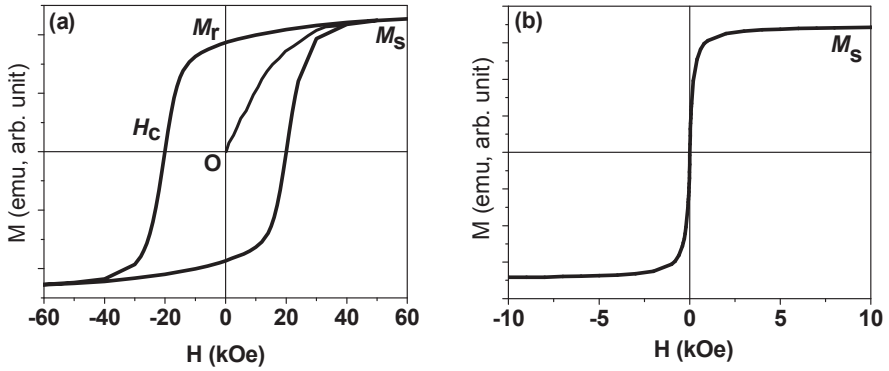

Fig. 2.8: Magnetisation curves for **(a)** ferromagnetic and **(b)** superparamagnetic materials. The quantities defined in the figures are the saturation magnetisation M_s, the remnant magnetisation M_r and the coercive field H_c. Source: Sun [61]

In both cases, the magnetisation of the particles saturate and the value reached by the magnetisation is defined as the saturation magnetisation $\pm M_\mathrm{s}$. The magnetisation of superparamagnetic nanoparticles (Fig. 2.8.b) is linear in the low-field regime and thus follow Eq.(2.32). Opposedly ferromagnetic nanoparticles retain a remnant magnetisation in zero external field M_r. The behaviour depends on material, size and temperature of the magnetic cores of the particles. For example, individual cores of diameter smaller than about 10 nm made of magnetite (Fe_3O_4) will exhibit superparamagnetic behaviour at room temperature.

2.2.2 Self-field bead detection

For both sensor geometries, when no external magnetic field is applied, and for only small variations of the magnetisation angle θ, we have $R_1 + R_2 \simeq R_3 + R_4 \simeq 2R_0$. Therefore the total resistance of the bridge is constant and the current running in each sensor arm is $I = V_x/(2R_0)$.

The current running in the sensor arms generates a magnetic field that can be used to detect magnetic beads. Figure 2.9 shows how. Part of this magnetic field is sensed by the sensor stack (see Paper V). This self induced magnetic field (self-field) is proportional to the current in the sensor arm and has a y component

$$H_y^{\mathrm{sf}} = \frac{\sqrt{2}}{2}\frac{V_x}{2R_0}\gamma_0 \tag{2.33}$$

where γ_0 is a proportionality constant relating the self biasing field to the current in the sensor [62]. The sensor-generated field also magnetises the magnetic beads near the sensor surface. Figure 2.10.a shows the magnetic field over one sensor arm, calculated for a bias

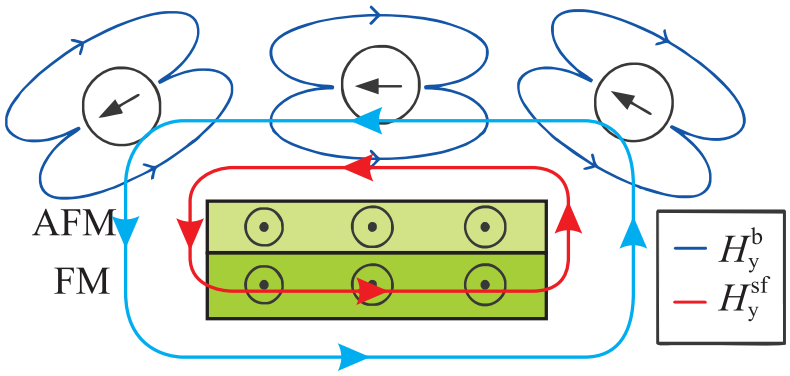

Fig. 2.9: Bead detection in the sensor self-field around a cross-section of one sensor arm. The field generated by the current passing in the sensor stack magnetises the beads. Part of the field is self-induced in the ferromagnetic (FM) layer of the stack and is self-biasing the signal output.

current of 9 mA corresponding to half the RMS value of the total bridge bias current used during the experiments of Chapter 6. We see that the maximum field is found near the edges of the sensor magnetic stack.

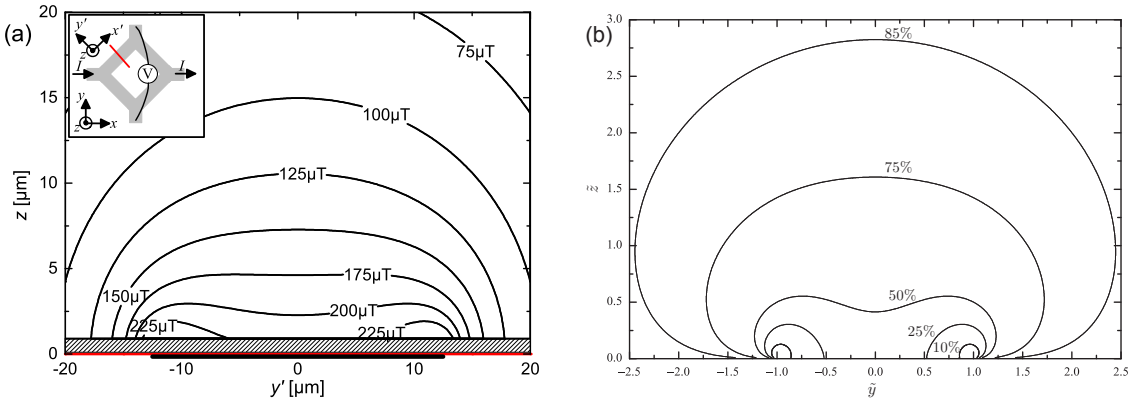

Fig. 2.10: **(a)** Magnitude of the magnetic field H_y^{sf} calculated for a bridge current $I_x = 18$ mA. The thick black line indicates the section of the magnetic sensor, and the hatched rectangle represents the sensor protective coating (thickness $\simeq 1$ μm). In the inset are defined the coordinates for the calculation. Adapted from Paper VII. **(b)** Contour plot of the cumulative bead signal for beads magnetised from the self-field. The dimension is normalised by half the sensor width, i.e.: $\tilde{y} = 2y/w$ and $\tilde{z} = 2z/w$. Distribution of the beads on the plane perpendicular to the current flowing in an arm. Source: Hansen *et al.* [62]

The beads magnetised from the self-field will generate a magnetic field acting back on the sensor. This field will be proportional to the current in the sensor arm and will depend on the amount and distribution of the beads over the sensor arm. The field has the form

$$H_y^b = \frac{\sqrt{2}}{2}\frac{V_x}{2R_0}\gamma_1, \tag{2.34}$$

where the constant γ_1 accounts for the bead spatial distribution. In Hansen *et al.* [62] is proposed an extensive theoretical analysis of the term γ_1. For beads with constant susceptibility this depends on the sensor width, the bead diameter, the bead magnetic susceptibility and the bead number density in the volume over the sensor. Fig. 2.10.b

shows the cumulative bead signal for a homogeneous distribution of beads magnetised from self-field [62]. Due to inhomogeneous self-field, and decay of the dipole field of the beads, 50% of the bead signal is due to beads in the proximity ($z < 0.25w$) of the sensor surface. Moreover it can be shown that $\gamma_1 = 0$ when no beads are present and $\gamma_1 > 0$ in presence of beads.

The total field acting of the sensor due to self-field is

$$H_y = \frac{\sqrt{2}}{2}\frac{V_x}{2R_0}(\gamma_0 + \gamma_1). \tag{2.35}$$

We can combine this result with Eq.(2.23) to obtain the resistance of each sensor arm, when only the self-field is acting on the magnetic beads

$$R(\pm\frac{\pi}{4}, H_y) = R_0 \mp S_0\frac{\sqrt{2}}{4}\frac{V_x}{R_0}(\gamma_0 + \gamma_1). \tag{2.36}$$

To simplify the notation we define the resistance variation in the n^{th} arm as

$$\Delta R_n = \mp S_0\frac{\sqrt{2}}{4}\frac{V_x}{R_0}\left[\gamma_0 + \gamma_1(n)\right], \tag{2.37}$$

where γ_0 depends only on the geometry and is identical for all the sensor arms, while $\gamma_1(n)$ depends on the amount and distribution of beads over each sensor arm. In this simplified notation the arm resistance becomes

$$R_n = R_0 + \Delta R_n. \tag{2.38}$$

The sign of ΔR_n depends on the angle of each arm. For simplicity their signs are summarised in Tab. 2.1.

Tab. 2.1: Sign of the resistance variation ΔR_n due to beads magnetised by self-field, for arm index n and for the two sensor designs.

Arm index (n)	**1**	**2**	**3**	**4**
PHEB	−	+	+	−
dPHEB	−	+	−	+

Expanding Eq.(2.5) we obtain the sensor output

$$V_y = V_x\left[\frac{R_2R_3 - R_1R_4}{(R_1 + R_2)(R_3 + R_4)}\right]. \tag{2.39}$$

We can combine this with Eq.(2.38). Suppressing the terms in ΔR_n of order higher then one we obtain

$$V_y = \frac{V_x}{4R_0}\left(\Delta R_2 + \Delta R_3 - \Delta R_1 - \Delta R_4\right). \tag{2.40}$$

We see that the sensor output depends upon the amount of beads on every arm, and the geometry of the sensor determines how the arm contribution are combined. For the PHEB sensor in particular we find using Tab. 2.1 and Eq.(2.40)

$$V_y^{\text{PHEB}} = \left(\frac{V_x}{R_0}\right)^2 S_0\frac{\sqrt{2}}{4}\left[\gamma_0 + \frac{\gamma_1(1) + \gamma_1(2) + \gamma_1(3) + \gamma_1(4)}{4}\right]. \tag{2.41}$$

Thus, in the PHEB sensor, the bead signals from all the arms are additive. Moreover, the PHEB output has an offset given by the sensor self biasing field. The bead signal is detected without the need of an external magnetic field, and it depends on the bias voltage squared. When the sensor is biased with an AC voltage $V_y = \sqrt{2}V_{\mathrm{RMS}}\sin(2\pi ft)$ at frequency f, the bead signal can be measured by lock-in technique in the second harmonic signal from Eq.(2.20), which is given by

$$V_2' = 0 \tag{2.42}$$

$$V_2'' = -\frac{1}{4}\left(\frac{V_{\mathrm{RMS}}}{R_0}\right)^2 S_0\left[\gamma_0 + \frac{\gamma_1(1)+\gamma_1(2)+\gamma_1(3)+\gamma_1(4)}{4}\right]. \tag{2.43}$$

Since the sensitivity S_0 is negative, V_2'' will be positive and additive for each arm. We also notice that the second harmonic in-phase signal $V_2' = 0$. This holds true when a low bias frequency is used. For higher field frequency, due to Brownian relaxation, the bead magnetisation lag behind the self-field. As we will see in Section 2.2.3 this effect brings an imaginary term in γ_1.

Also for the dPHEB sensor we combine Tab. 2.1 with Eq.(2.40) to find the sensor output

$$V_y^{\mathrm{dPHEB}} = -\left(\frac{V_x}{R_0}\right)^2 S_0\frac{\sqrt{2}}{8}\left[\frac{\gamma_1(1)+\gamma_1(2)}{2} - \frac{\gamma_1(3)+\gamma_1(4)}{2}\right] \tag{2.44}$$

Hence the sensor cancels out the offset signal given by the self-biasing field. Moreover, the signal output of the dPHEB is given by the bead signal from the top half of the sensor, minus the bead signal from the bottom half. When we place capture probes on the top half of the sensor, the second harmonic lock-in signal from Eq.(2.20) becomes

$$V_2' = 0 \tag{2.45}$$

$$V_2'' = -\frac{1}{8}\left(\frac{V_{\mathrm{RMS}}}{R_0}\right)^2 S_0\left(\gamma_{\mathrm{top}} - \gamma_{\mathrm{bottom}}\right) \tag{2.46}$$

with $\gamma_{\mathrm{top}} = [\gamma_1(1)+\gamma_1(2)]/2$ and $\gamma_{\mathrm{bottom}} = [\gamma_1(3)+\gamma_1(4)]/2$. When target and beads can only bind on the upper arms, the bottom arms are subtracting the contribution of beads in suspension, thus behaving as a local reference. This effect is accentuated by the sensitivity of the sensor towards beads near the surface.

The outputs of the PHEB and dPHEB sensors were calculated by means of biasing the sensor with an external voltage. This is the case for sensor driven in parallel as done in Chapter 6. To work with a biasing current I_x instead of a voltage, e.g.: when driving sensors in series, we can remember that the bridge resistance is constant R_0, it follows

$$I_x = \frac{V_x}{R_0} \tag{2.47}$$

$$I_{\mathrm{RMS}} = \frac{V_{\mathrm{RMS}}}{R_0}. \tag{2.48}$$

2.2.3 Brownian relaxation of magnetic beads

When a magnetic bead is placed in an external magnetic field, its magnetic moment will align to the field. Two different processes can take place: the internal magnetisation of the bead can flip or the bead can perform a physical rotation. The first process, the

internal flipping of the magnetic moment, is called Néel relaxation [63] while the second process, the physical rotation of the whole bead is called Brownian relaxation [21]. The dominating relaxation process depends on the magnetic core size, hydrodynamic volume of the particle and temperature of the experiment.

The Néel relaxation of magnetic beads is characterised by the Néel relaxation time [63]

$$\tau_{\mathrm{N}} = \tau_0 \exp\left(\frac{KV}{k_{\mathrm{B}}T}\right), \tag{2.49}$$

where τ_0 is a material dependent constant, K is the magnetic anisotropy constant, V is the volume of the magnetic core and $k_{\mathrm{B}}T$ is the thermal energy.

The Brownian relaxation of magnetic beads in a viscous liquid is characterised by the characteristic Brownian relaxation time [20]

$$\tau_{\mathrm{B}} = \frac{3\eta V_{\mathrm{h}}}{k_{\mathrm{B}}T} = \frac{\pi\eta D_{\mathrm{h}}^3}{2k_{\mathrm{B}}T} \tag{2.50}$$

where η is the viscosity of the liquid, V_{h} is the hydrodynamic volume of the bead and D_{h} is the hydrodynamic diameter of the bead.

The effective relaxation time (τ) is given by

$$\frac{1}{\tau} = \frac{1}{\tau_{\mathrm{N}}} + \frac{1}{\tau_{\mathrm{B}}} \tag{2.51}$$

For the purposes of this work, we will assume that all the magnetic beads used for Brownian relaxation measurements are thermally blocked, i.e.: they have a remnant magnetisation in zero field and the Brownian relaxation dominates over the Néel relaxation.

The hydrodynamic volume of the particles is subject to fabrication uncertainties. The diameter distribution D_{h} is often well described by the log-normal distribution

$$f_{\mathrm{LN}}(D_{\mathrm{h}}; \tilde{D}_{\mathrm{h}}, \sigma)\mathrm{d}D_{\mathrm{h}} = \frac{1}{D_{\mathrm{h}}\sigma\sqrt{2\pi}} \exp\left[-\frac{\left(\ln D_{\mathrm{h}} - \ln \tilde{D}_{\mathrm{h}}\right)^2}{2\sigma^2}\right] \mathrm{d}D_{\mathrm{h}} \tag{2.52}$$

where $\tilde{D}_{\mathrm{h}}$ is the median hydrodynamic diameter and σ is the standard deviation. This size distribution is defined to be volume-weighted, i.e.: $f_{\mathrm{LN}}(D_{\mathrm{h}}; \tilde{D}_{\mathrm{h}}, \sigma)\mathrm{d}D_{\mathrm{h}}$ represents the volume fraction of beads of diameter between D_{h} and $D_{\mathrm{h}} + \mathrm{d}D_{\mathrm{h}}$.

It is possible to obtain information on the Brownian relaxation in both time and frequency domain. In the next section this two cases will be described singularly.

2.2.3.1 Time-domain. Brownian relaxation is measured in the time-domain by biasing a PHEB sensor with a square wave current $I_x(t)$ with amplitude $\pm I_0$ and period T_I. The current through the sensor generates a magnetic self-field (H) proportional to the current $I_x(t)$. Therefore the magnetic beads will be subjected to a field changing direction with a period T_I. When the current and the field switch direction the beads rotate to align to the magnetic field. We define M as the magnetisation of the beads parallel to the field H.

Figure 2.11 shows what happens to the magnetisation M when a bead rotates to align to the field. The current I_x and the field H are synchronous. Before the current switches from $+I_0$ to $-I_0$ the beads are aligned to the field and the magnetisation is $+M_0$.

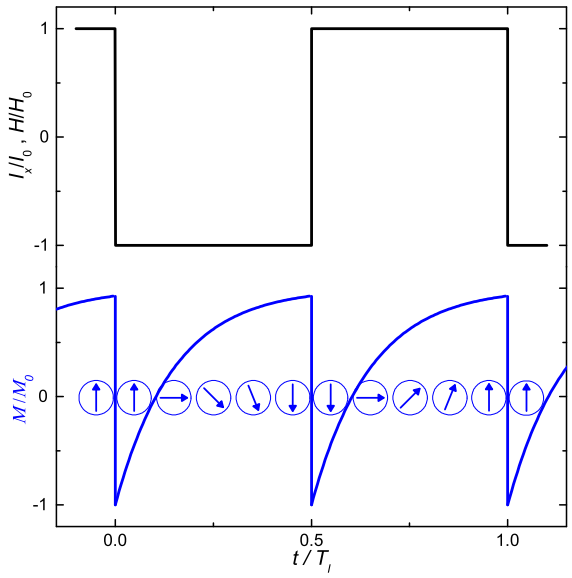

Fig. 2.11: Schematic of beads relaxation in a flipping magnetic field. The field H is generated by, and thus proportional to the bias current I. Before current flipping, the magnetisation M (evaluated in the field direction) is parallel to the field. As the current changes direction, the magnetisation is antiparallel therefore $M = -M_s$. The beads then relax and becomes parallel to the field ($M = M_s$). Adapted from Paper IV.

Immediately after the current switches direction, i.e.: before the beads have enough time to rotate, the magnetisation M is anti-parallel to the field and so $M = -M_0$. During half a period the beads have time to relax and align to the field, therefore before the next current edge $M = +M_0$. Then the process repeats.

The relaxation of the beads is assumed to be described by an exponential decay with time constant τ_B, the Brownian relaxation time.

$$M(t) = M_0 \left[1 - 2\exp\left(-\frac{t}{\tau_B}\right),\right] \tag{2.53}$$

where t is the time after the sign change of the current and the magnetisation goes from $-M_0$ to $+M_0$.

Assuming the external field to be small (nominally zero), we can combine Eq.(2.24) and Eq.(2.41) to obtain the signals $V_+(t)$ (@$+I_0$) and $V_-(t)$ (@$-I_0$) given by

$$V_+(t) = S_0 I_0^2(\gamma_0 + \gamma_{1t} M(t)) + I_0(S_0 H_y + R_{\text{off}}) \tag{2.54}$$

$$V_-(t) = S_0 I_0^2(\gamma_0 + \gamma_{1t} M(t)) - I_0(S_0 H_y + R_{\text{off}}) \tag{2.55}$$

where t is the time from the current switching sign and we have explicitly written the dependence of γ_1 on the magnetisation by introducing $\gamma_1 = \gamma_{1t} M(t)$. We notice that the terms proportional to I_0^2 do not change sign. Therefore we can separate the self-field contribution from the external field and offset contributions by calculating the average and difference of the two measurements at positive and negative currents

$$V_{\text{ave}}(t) = \frac{1}{2}\left[V_+(t) + V_-(t)\right] = S_0 I_0^2(\gamma_0 + \gamma_{1t} M(t)) \tag{2.56}$$

$$V_{\text{diff}}(t) = \frac{1}{2}\left[V_+(t) - V_-(t)\right] = I_0(S_0 H_y + R_{\text{off}}). \tag{2.57}$$

The offset due to γ_0 in Eq.(2.56) can be corrected for using a reference measurement performed without magnetic beads. We see that after this correction V_{ave} is proportional to the time dependent magnetisation. However, V_{diff} depends linearly on the external magnetic field H_y.

To analyse the properties of a solution of beads, we have to integrate the theorical signal of Eq.(2.56) over the volume-weighted log-normal distribution of the hydrodynamic diameters in Eq.(2.52), the result is

$$V_{\text{ave,fit}} = V_{0t} \int_0^\infty \left(1 - 2\exp\left(\frac{-t}{\tau_{\text{B}}(D_{\text{h}})}\right)\right) f_{\text{LN}}(D_{\text{h}}; \tilde{D}_{\text{h}}, \sigma)\mathrm{d}D_{\text{h}} + V_{\text{off}}, \tag{2.58}$$

where we defined $V_{0t} = -S_0 I_0^2 \gamma_{1t} M_0$ as the amplitude of the decay and V_{off} corrects for possible offsets. With this definition V_{0t} is positive and $V_{\text{ave,fit}}$ ranges from V_{0t} ($t = 0$) to $-V_{0t}$ ($t \to \infty$). The free fitting parameters are V_{0t}, $V_{\text{ave,fit}}$, $\tilde{D}_{\text{h}}$ and σ. The last two parameters contain the information on the size distribution.

2.2.3.2 Frequency-domain. The Brownian relaxation can be measured in the frequency domain by placing the magnetic particles in an oscillating magnetic field at frequency f and measuring the complex susceptibility $\chi = \chi' - \mathrm{i}\chi''$ where χ' and χ'' are the in phase and out of phase component of the complex magnetic susceptibility, respectively. The complex magnetic susceptibility is described by the Debye model [64]

$$\chi(f) = \chi' - \mathrm{i}\chi'' = \frac{\chi_0 - \chi_\infty}{1 + (\mathrm{i}f/f_{\text{B}})} + \chi_\infty \tag{2.59}$$

were χ_0 is the DC susceptibility, χ_∞ is the high frequency susceptibility and f_{B} is the Brownian relaxation frequency given by

$$f_{\text{B}} = \frac{1}{2\pi\tau_{\text{B}}} = \frac{k_{\text{B}}T}{6\pi\eta V_{\text{h}}} = \frac{k_{\text{B}}T}{\pi^2\eta D_{\text{h}}^3}. \tag{2.60}$$

For a polydisperse sample, Cole and Cole [65] proposed the empirical model

$$\chi(f) = \chi' - \mathrm{i}\chi'' = \frac{\chi_0 - \chi_\infty}{1 + \left(\mathrm{i}f/f_{\text{B}}(\tilde{D}_{\text{h}})\right)^{(1-\alpha)}} + \chi_\infty, \tag{2.61}$$

for the complex magnetic susceptibility. Here α is a parameter that measures the polydispersity of the sample, it assumes values from 0 to 1, with $\alpha = 0$ for a monodsiperse sample and $\tilde{D}_{\text{h}}$ is the median hydrodynamic diameter of the bead distribution. Although the physical meaning of $\tilde{D}_{\text{h}}$ is similar to that in Eq.(2.52), median of the log-normal distribution, the Cole-Cole model of Eq.(2.61) is not derived from the log-normal distribution. Figure 2.12 shows the theoretical in-phase (a) and out of phase (b) component of the magnetic susceptibility for free beads and for beads with increased diameter (e.g.: because of clustering due to a biological sample).

At low frequencies $f \ll f_{\text{B}}$, the in-phase susceptibility χ' is at the highest level χ_0 and the bead magnetisation is in-phase with the field. Approaching $f = f_{\text{B}}$ the beads start to lag behind the field, the in-phase susceptibility decreases while the out-of-phase susceptibility χ'' increases and reaches it maximum for $f = f_{\text{B}}$. At higher frequencies, $f \gg f_{\text{B}}$ the magnetisation of the beads cannot keep up with the external field therefore

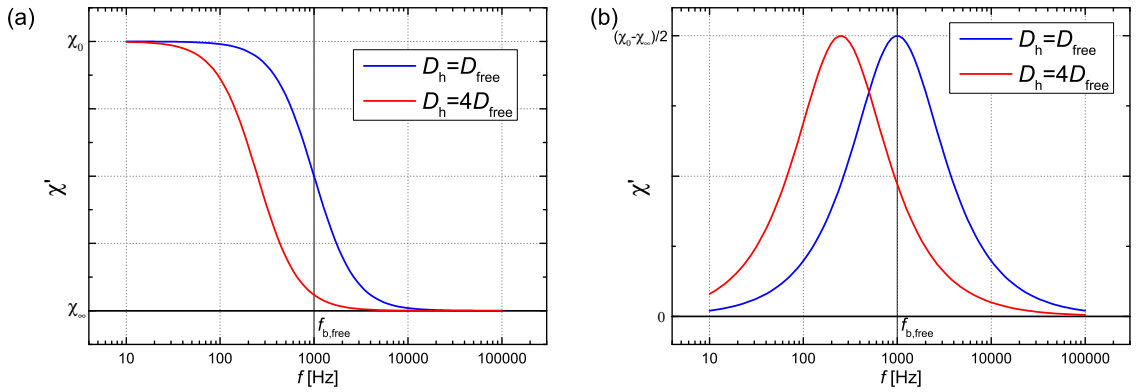

Fig. 2.12: Theoretical **(a)** in-phase and **(b)** out-of-phase complex magnetic susceptibilities calculated for free beads $D_\mathrm{h} = D_\mathrm{free}$ and bead cluster $D_\mathrm{h} = 4D_\mathrm{free}$.

$\chi' = \chi_\infty$ and $\chi'' = 0$. Beads with increased diameter or cluster of beads, $D_h = 4D_\mathrm{free}$ will have a lower relaxation frequency $f_\mathrm{B,bound} < f_\mathrm{B,free}$.

We have previously seen (Eq.(2.43)) that the bead signal can be measured in the second harmonic out-of-phase signal of the PHEB sensor V_2'' when the bead magnetisation is in-phase with the self-field. We can now express explicitly the dependence upon the complex magnetic susceptibility of $\gamma_1 = \gamma_{1f}\chi$. From Eq.(2.41) and Eq.(2.20) we obtain

$$V_2' = -2^{-2} I_\mathrm{RMS}^2 S_0 \gamma_{1f} \chi'' \tag{2.62}$$

$$V_2'' = -2^{-2} I_\mathrm{RMS}^2 S_0 (\gamma_0 + \gamma_{1f}\chi') \tag{2.63}$$

where the out-of-phase magnetic susceptibility χ'' leads to an in-phase second harmonic output V_2'. It is possible to correct the offset due to γ_0 by subtracting a reference measurement with no beads to obtain $V_{2,\mathrm{cor}}$. In this way the in-phase second harmonic signal V_2' is proportional to the out-of-phase susceptibility χ'' and, vice versa, the corrected out-of-phase second harmonic signal is proportional to the in-phase susceptibility χ'. That means that $V_{2,\mathrm{cor}} = V_{2,\mathrm{cor}}' + \mathrm{i}V_2''$ is proportional to $\mathrm{i}\chi = \chi'' + \mathrm{i}\chi'$.

With this correction we can now fit the Cole-Cole model to the second harmonic PHEB signal as

$$V_{2,\mathrm{fit,Cole}} = V_2' + \mathrm{i}V_{2,\mathrm{cor}}'' = \mathrm{i}\frac{V_0 - V_\infty}{1 + \left(\mathrm{i}f/f_\mathrm{B}(\tilde{D}_\mathrm{h})\right)^{(1-\alpha)}} + \mathrm{i}V_\infty, \tag{2.64}$$

where we defined V_0 and V_∞ as

$$V_0 = -2^{-2} I_\mathrm{RMS}^2 S_0 \gamma_{1f} \chi_0 \tag{2.65}$$

$$V_\infty = -2^{-2} I_\mathrm{RMS}^2 S_0 \gamma_{1f} \chi_\infty. \tag{2.66}$$

The free parameters of this model are V_0, V_∞, $\tilde{D}_\mathrm{h}$ and α. It is also possible to use the log-normal distribution of Eq.(2.52) to integrate the complex susceptibility of Eq.(2.59) for distribution of beads. The model in this case becomes

$$V_{2,\mathrm{fit,LN}} = V_2' + \mathrm{i}V_{2,\mathrm{cor}}'' = \int_0^\infty \mathrm{i}\frac{V_0 - V_\infty}{1 + (\mathrm{i}f/f_\mathrm{B}(D_\mathrm{h}))} f_\mathrm{LN}(D_\mathrm{h}; \tilde{D}_\mathrm{h}, \sigma)\mathrm{d}D_\mathrm{h} + \mathrm{i}V_\infty. \tag{2.67}$$

The free parameters of the model are V_0, V_∞, $\tilde{D}_\mathrm{h}$ and σ. This model is of particular interest because offer direct comparison with the parameters obtained by fitting time-domain measurements using Eq.(2.58).

2.3 Summary

In this chapter the PHEB and dPHEB signals were derived. The PHEB voltage output vs. external magnetic field H_y was derived from a model implying single domain of the magnetisation in each sensor arm. This is used in Chapter 4 to characterise the magnetic properties of the sensor stack.

The second harmonic lock-in signal V_2'' was derived. V_2'' is the signal measured for bead detection using the sensor self-field. The self-field signal for dPHEB sensor is used in Chapter 6.

The Brownian relaxation of the magnetic beads was introduced. The second harmonic, frequency depended bead signal measured on PHEB sensor was derived. Two models for this signal were derived, one based on Cole-Cole model and one based on a log-normal distribution of bead diameters. Moreover the time-domain signal for the bead relaxation on PHEB sensor was derived. These three models are used in Chapter 5.

CHAPTER 3

Experimental

This chapter describes the experimental setup and procedures used in this thesis. At the core of the system are the planar Hall effect (PHEB) magnetic sensors. A fluidic system is used to provide electrical contact with the sensor and to define a fluid channel on the sensor surface. The sensor mounting is described in the chapter and includes temperature control capabilities. Finally, the standard procedures used for sensor characterisation, volume-based and surface-based biosensing is described.

3.1 PHEB magnetic field sensors

Some details about the planar Hall effect bridge (PHEB and dPHEB) sensors are presented in this section. First the fabrication procedure for these sensors is described. Then the various sensing geometries used in the experimental work of this thesis are introduced and the sensors are described from a geometrical and functional point of view.

3.1.1 Cleanroom fabrication

The sensor were fabricated as described previously by Henriksen *et al.* [56]. The fabrication was carried on in the clean-room facilities of Danchip at DTU. The substrates used for the fabrication were 4" p-type silicon wafers, with a thermally grown oxide layer of $800 - 1000$ nm. Figure 3.1 shows a schematic of the cross section of a sensor. At the core of the sensor is a top-pinned magnetic stack. Contacts to the magnetic stack were defined in a second lithographic process. Magnetic sensors for biodetection were finally protected by a hybrid organic-inorganic polymer passivation layer. The following sections describe each fabrication step in further detail.

3.1.1.1 Magnetic stack deposition. The top pinned magnetic stack was sputter deposited in a Kurt J. Lesker CSM-18 magnetron sputter system and defined by lift-off. A uniform magnetic field of 20 mT was applied along the x-direction during deposition of the magnetic stack to define easy-axis and easy-direction of magnetisation (see Section 2.1.3). Three different magnetic stacks have been used in the experimental work presented in this thesis. In each section, the used stack composition will be explicitly stated.

The standard stack of (from bottom to top) Ta(3)/ $Ni_{80}Fe_{20}$(30)/ $Mn_{80}Ir_{20}$(20)/ Ta(3) (thicknesses in nm) was used for the work in Chapters 4 and 5. The Ta layers are used to improve adhesion to the substrate oxide and to the electrical contacts. The ferromagnetic $Ni_{80}Fe_{20}$ (Permalloy) layer presents the magnetoresistive properties exploited for the sensor

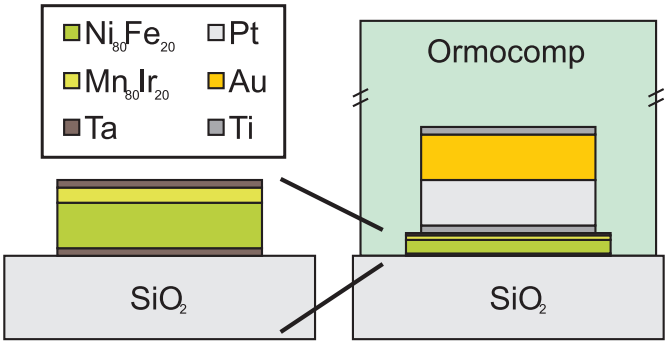

Fig. 3.1: Schematic cross sections of the magnetic stack and of the complete sensor with contacts and protective coating.

function. The antiferromagnetic $Mn_{80}Ir_{20}$ layer exchange couples the magnetisation of the permalloy and so defines the easy-direction of magnetisation.

The second stack was used for the work described in Section 6.4. Its nominal composition was Ta(5)/ $Ni_{80}Fe_{20}$(30)/ $Mn_{80}Ir_{20}$(10)/ Ta(5) (thicknesses in nm). Here a thinner antiferromagnetic layer was used to increase the fraction of the current running through the permalloy layer, thus increasing the magnetoresistivity of the whole stack and decreasing the sensor self-biasing (γ_0).

Finally, for the major part of Chapter 6, a stack of nominal composition Ta(15)/ $Ni_{80}Fe_{20}$(30)/ $Mn_{80}Ir_{20}$(10)/ Ta(5) (thicknesses in nm) was used. Here, we introduced a thicker bottom tantalum layer. The current running in this layer generates in the permalloy a magnetic field opposed to the one generated by the current flowing in the $Mn_{80}Ir_{20}$ layer, thus reducing even further the sensor self-biasing (γ_0).

3.1.1.2 Electrical contacts deposition. The electrical contacts were defined by lift-off in a second lithographic process. The contact stack Ti(10)/ Pt(100)/ Au(100)/ Ti(10) (thicknesses in nm) was deposited by e-beam evaporation after a sputter cleaning process. The contact resistance between magnetic stack and electrical contacts was found to be negligible for this deposition process. This has important consequences for the sensor design (Section 3.1.2).

3.1.1.3 Low-temperature annealing. In Chapter 4 the effects of temperature ramping on the PHEB low-field sensitivity are discussed. To mitigate these effects, a low-temperature annealing process was performed after deposition of the contacts. The wafers were annealed in Kurt J. Lesker CSM-18 magnetron sputter system (same machinery used for magnetic stack deposition). The wafers were heated for 1 hour to 240°C, 280°C and 320°C, respectively. The process took place in vacuum and in a magnetic field 20 mT applied along the positive x-axis direction. The wafers were slowly cooled to room temperature in this condition. Only the sensors analysed in Chapter 4 were subjected to the low-temperature annealing treatment.

3.1.1.4 Protective coating. The sensors were passivated with a layer of Ormocomp® (Micro resist technology GmbH, Berlin, Germany) of thickness 900 nm. Ormocomp® is a hybrid organic-inorganic polymer curable in ultraviolet (UV) light. The polymer was

diluted 1 : 2 in Ma-T 1050 and spin coated on the wafers at 3000 rpm for 60 s. The coating geometry was defined by UV lithography and after development the polymer was hard-baked for 3 hours at 150°C. This was the last and longest exposure to elevated temperature that the sensor magnetic stack encountered before use. Although this was performed in less controlled environment, this heating step was found to produce similar effects to those of low-temperature annealing, on the sensor low-field sensitivity.

3.1.2 Sensor geometries

Two separate mask sets were designed for the sensors used in this thesis. They correspond to two generations in the development of the sensors and will be described one at a time in the next sections. The main differences are (1) the design of the contacts, (2) a change in the aspect ratio l/w that defines sensor resistance and low-field sensitivity and (3) the widespread introduction of magnetic stack material surrounding the sensor. The geometries used are specified in each chapter.

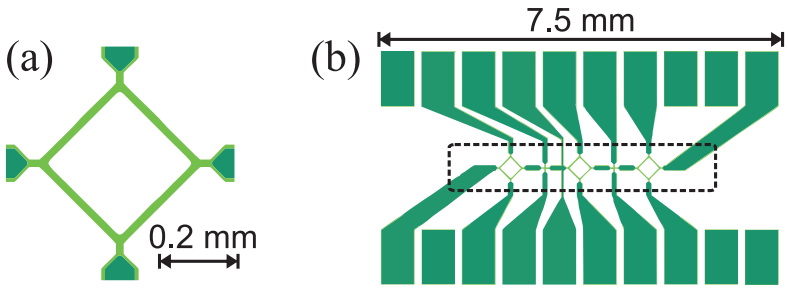

Fig. 3.2: **(a)** First generation PHEB sensor design. Contacts (dark green) do not extend over the sensor stack (light green) on the bridge corners. **(b)** Chip layout. Each chip comprises five sensors. The dashed line outlines the area of the chip surface included in the microfluidic channel.

3.1.2.1 First generation. Figure 3.2.a shows the standard geometry of the PHEB sensor as for the first generation mask. In this design the electrical contacts (dark green) do not extend into the joining points of the bridge arms. In this way the current is injected in the magnetic stack outside the bridge, avoiding the possible unbalancing of the bridge due to contact resistance. This contact geometry does not define clearly the arm length, while the width is $w = 20$ µm. The effect of passing current through the corners of the magnetic stack on the low-field sensitivity was investigated by finite element analysis for a single domain structure. The method showed a response that can be described by the effective aspect ratio $l/w = 14.87$. Figure 3.2.b shows the standard layout of sensors on a chip. Each chip comprises five sensors. The microfluidic setup (see Section 3.2.2.1) defines a microfluidic channel over the sensor surface, in the area delimited by dashed line in Fig. 3.2.b.

3.1.2.2 Second generation. The fabrication procedure ensured a low contact resistance between electrical contact layer and magnetic stack. This allowed for a different geometry, with contacts extending over the bridge corner and defining the sensor arms. Figure 3.3.a shows a detail of a corner of the sensor. The entire geometry of the sensor, for both PHEB and dPHEB are depicted in Fig. 2.1. The length of the sensor arm is $l = 200$ µm and the width $w = 20$ µm, thus the aspect ratio is $l/w = 10$. Figure 3.3.b

shows the layout of the sensors on a single chip. Each chip comprises six sensors. Each sensor can be addressed separately. This allows for driving the sensors in parallel or in series depending on the application requirements. Five sensors on each chip are included inside the microfluidic channel (outlined by the dashed line). One PHEB sensor is included in each chip, outside the microfluidic channel for characterisation purposes.

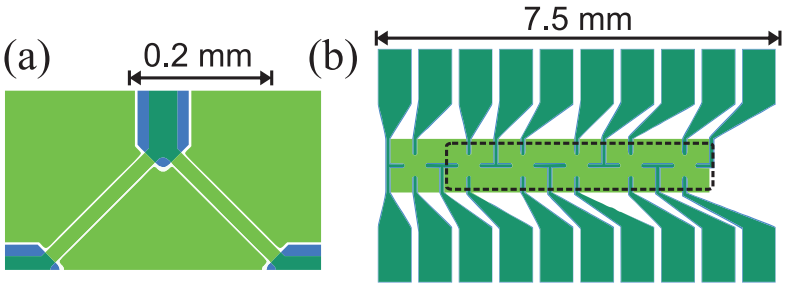

Fig. 3.3: (a) Second generation PHEB sensor design. Contacts (blue) extend over the sensor stack (light green) and over the bridge corners. Sensor stack is surrounding the sensor arms, with a gap of 3 µm **(b)** Chip layout. Each chip comprises six sensors. The dashed line outlines the area of the chip surface included in the microfluidic channel.

3.1.2.3 Reduction of shape anisotropy. To reduce the shape anisotropy, the sensor arms were surrounded by magnetic stack material. Figure 3.3.a shows a close-up of one PHEB bridge angle, where the sensor arm and the surrounding stack are well visible. The gap defining the arms has a width of 3 µm and corresponds to the smallest feature that can be safely defined with the photolithography process employed. The use of surrounding magnetic stack led to a low-field sensitivity increased of 60% due to reduced shape anisotropy.

3.2 Sensor setup and characterization

This section presents the equipment used to characterise the properties of the deposited magnetic stack and to measure the sensor signal. Moreover the components used to control temperature, to handle fluid and to apply external fields are presented.

3.2.1 Magnetic stack characterisation

In this section, the methods to characterise the magnetic and electric properties of the sensor stack are introduced. Only the measurements that are not performed on the sensors themselves but on test structures ad-hoc are described here.

3.2.1.1 VSM. The magnetic properties of the sensor stack, in particular the uniaxial anisotropy field H_K and the exchange anisotropy field H_{ex}, were characterised by measurement of the magnetisation of a 3×3 mm^2 square pad in a sweeping external field. The measurements were performed in a LakeShore model 7407 vibrating sample magnetometer (VSM). The magnetisation was measured by applying a field parallel and perpendicular to the x-axis, that corresponds to the easy-axis for the magnetisation of the top pinned stack.

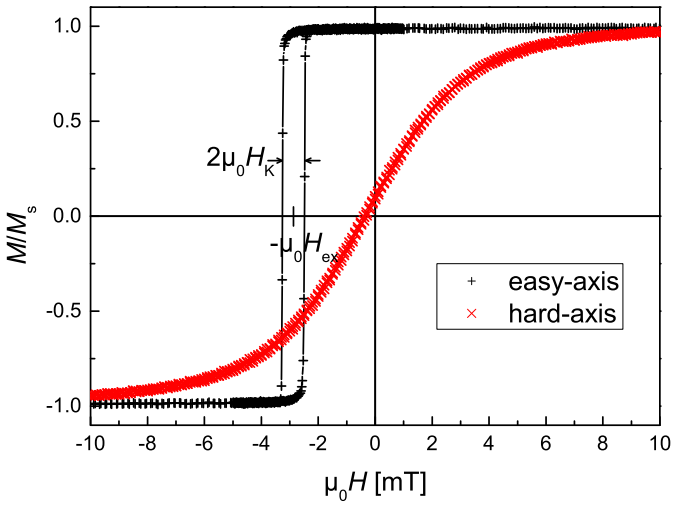

Fig. 3.4: Sample VSM measurement from un-anneald wafer Chapter 4. Magnetisation measured in the field direction when field applied along and perpendicularly to x-axis direction.

Figure 3.4 shows an example of magnetisation curves measured with VSM. These two curves can be compared to the theoretical curve for the magnetisation angle of Fig. 2.5 remembering $\mathbf{M} = M_\mathrm{s}\hat{\mathbf{M}}$. From the hysteresis curve with field aligned to the x-axis, we can obtain $-H_\mathrm{ex}$ as the mid-value of the hysteresis loop and $2H_\mathrm{K}$ as the width of the hysteresis loop. Sweeping the field along the x-direction shows the linear, low-field regime in which the PHEB sensor are employed.

3.2.1.2 Transmission line measurements. A transmission line structure was used to characterise the electrical and magnetoresistive properties of the magnetic stack. Figure 3.5.a shows the geometry used for this measurement. The conducting element had a width $w = 50$ µm. With this geometry, it was possible to measure the resistance of segments as function of the length l.

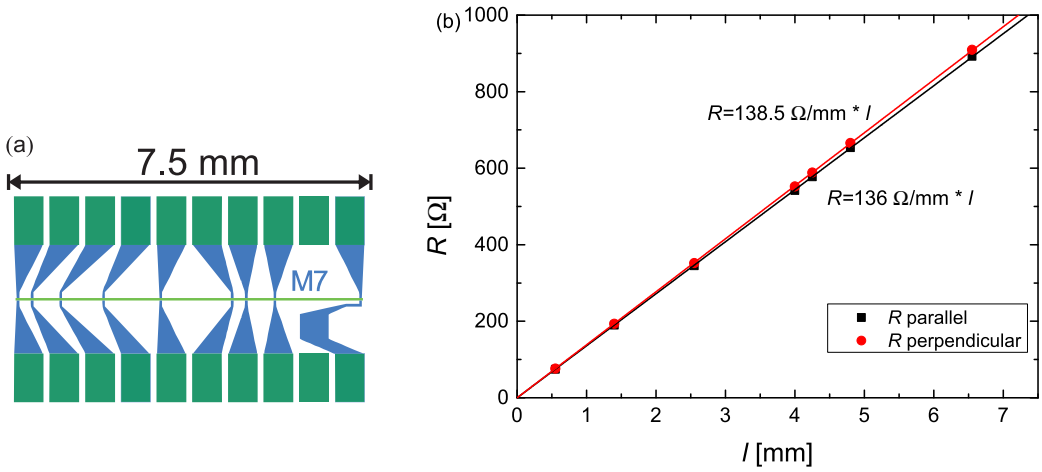

Fig. 3.5: **(a)** Transmission line geometry used for AMR measurement. **(b)** Transmission line resistance vs. segment length. Data measured for un-annealed wafer of Chapter 4. The resistance was measure in a saturating magnetic field applied parallel and perpendicular to the transmission line.

Figure 3.5.b shows the result of four-point measurements of the resistance of segments of varying length. The measurements were performed with a saturating magnetic field applied along and perpendicular to the x-axis, respectively. The parallel and perpendicular sheet resistances $\rho_{\parallel}/t$ and $\rho_{\perp}/t$ can be obtained from the slopes of the linear fits to the points in Fig. 3.5 as follows

$$\frac{\rho_{\parallel,\perp}}{t} = w\frac{\delta R_{\parallel,\perp}}{\delta l} \tag{3.1}$$

The difference between the two sheet resistances is $\Delta\rho/t$ and is a critical parameter for the sensor.

3.2.2 Sensor setup

In this section we describe how the sensor chip is interfaced electrically and connected to a fluid handling system. Figure 3.8.b shows the sensor held in position in a micromachined aluminum well on the copper baseplate. The temperature of the holder is controlled. Figure 3.6 shows, in position, the microfluidic assembly ensuring fluid handling and electrical contacts to the sensor chip. Finally, a microscope is used to verify the condition of the sensor surface.

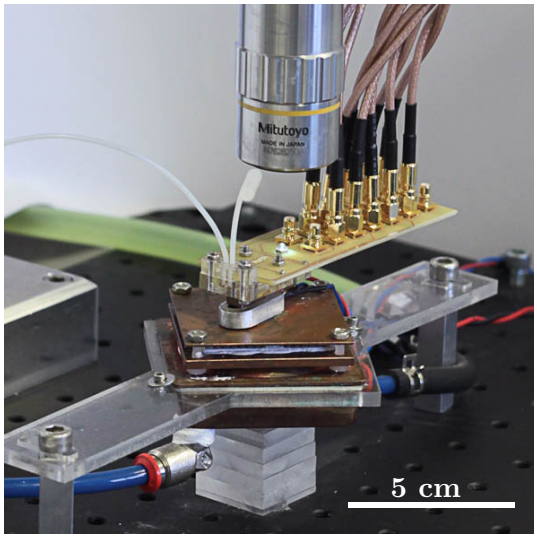

Fig. 3.6: Assembled sensor setup. The sensor is set in place over the copper baseplate. The microfluidic system also provides electrical contacts. A microscope is available for optical inspection of the sensor surface during experiments.

3.2.2.1 Microfluidic and pumping system. Figure 3.7 shows the microfluidic system used to handle sample over the sensor surface. The microfluidc system was micro machined in two layer of polymethylmetacrylate (PMMA) thermally bonded together. The microfluidic channel over the sensor was defined by a polydimethylsiloxane (PDMS) rubber gasket, ensuring a leak-proof coupling between the sensor chip and the microfluidic system. The microfluidic channel defined on the sensor had length 5 mm and width 1 mm. The depth of the channel was varied, depending on the application, from 0.1 mm to 1 mm. The contacts to the chip were ensured by spring loaded pins (POGO-PIN-5.94-1,Emulation Technology Inc., Camarillo, CA, USA). The contact pins were press fitted in

through-holes in the microfluidic system. In this way they ensured connection between the chip and a custom made printed circuit board (PCB). The PCB could be interchanged for the different sensing applications, e.g.: driving sensor in series or parallel. The PCB provided connection to power supply and measuring equipment.

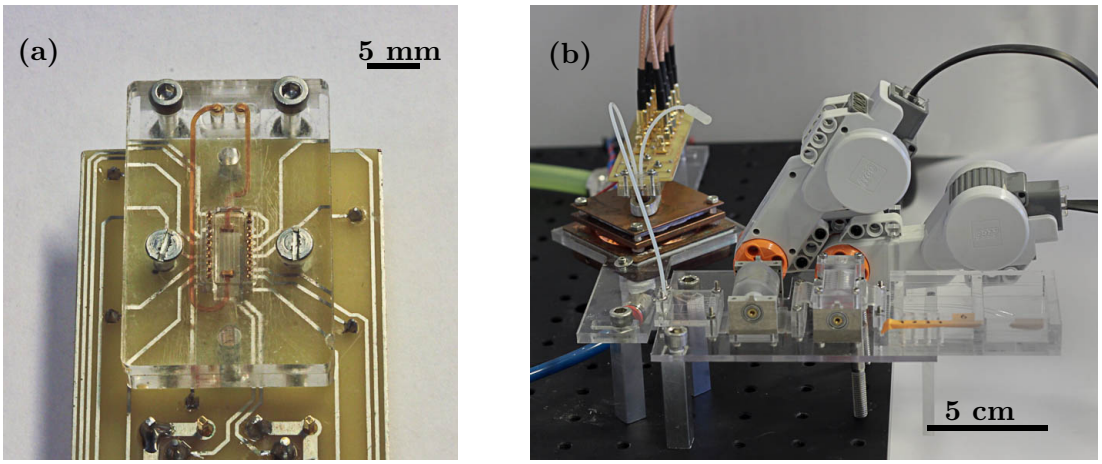

Fig. 3.7: **(a)** Microfluidic system. The system holds in place a PDMS gasket to define microfluidic channel over the sensor. Spring loaded contact pins ensure connection between the sensors and the PCB. **(b)** Pumping system based on design by Sabourin *et al.* [66]. The peristaltic pump is driven by LEGO Mindstorm motors.

Fluid connection to the microfluidic system was ensured by two tubing joints derived from the ones described by Sabourin *et al.* [67, 66].

Two different systems were used for fluid handling. The first (Fig. 3.7.b) was a in-house built system consisting of a peristaltic rotatory pump and a valve [66] that could be driven by LEGO Mindstorm NXT motors and controlled from a PC. This setup could handle 6 samples and ensured a small dead volume. The second system (Fig. 3.8.a) consisted of two syringe pumps whose outputs were mixed into a T-link before the microfluidic system. The flow rates of the two syringe pumps could be controlled via PC. This system was used also to generate concentration gradients, allowing relative dilution as small as 1:1000 (see Section 6.4).

3.2.2.2 Temperature control. The temperature of the sensor baseplate was controlled by the system in Fig. 3.8.b. A Peltier element was used to heat or cool the holder. The bottom side of the Peltier element was kept at room temperature for improved stability using a commercial CPU liquid cooler. The temperature of the sensor baseplate was controlled by a LFI-3751 temperature controller (Wavelength Electronics Inc., MT, USA). The temperature was measured using a PT1000 resistance thermometer or using a thermistor integrated under the sensor baseplate.

3.2.2.3 Real-time measurement. For real time measurement of the binding of magnetic beads to the sensor surface (see Chapter 6) up to five sensors located in the microfluidic channel could be used at once. The sensors output signals were amplified using

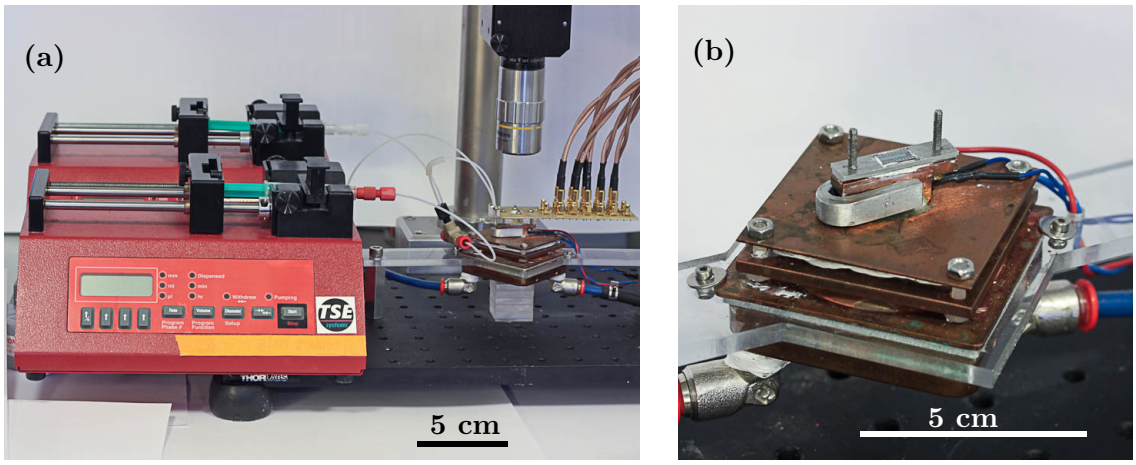

Fig. 3.8: **(a)** Two syringe pumps are connected through a T connection joint to the microfluidic inlet. Controlling the relative flow of the two pumps it is possible to achieve concentration gradients. **(b)** Temperature controlled chip mounting. The chip is positioned in an alignment well in the aluminium plate. The temperature of the holder is controlled by Peltier element and PT1000 thermometer.

five SR552 bipolar pre-amplifiers and measured with five SR830 lock-in amplifiers (both from Stanford Research Systems Inc., Sunnyvale, CA, USA). The sensors were connected in parallel and the voltage was supplied by a commercial audio amplifier driven by the internal wave generator of one of the lock-in amplifiers.

3.2.2.4 Frequency-domain. Two separate methods were used to be able to cover a wide frequency range (see Section 5.1.2.2) when measuring Brownian relaxation in the frequency domain. For the low-frequency range (1 Hz − 50 kHz) the sensor AC bias current was provided by Keithley 6221 AC and DC Current Source (Keithley Instruments, USA). The sensor signal was measured by one SR830 lock-in amplifier. No pre-amplification was used in this case, since it was found to introduce a frequency dependent phase-shift in the sensor signal.

For measurement in the high-frequency range (50 Hz − 5 MHz) the sensor output was measured using an HF2LI lock-in amplifier (Zurich Instruments, Switzerland). The sensor bias current was provided by the amplifier built-in wave generator.

3.2.2.5 Time-domain measurement. To measure bead relaxation in the time domain (see Section 5.2), a NI USB-6281 data acquisition card (DAQ) (National Instruments, USA) was used. The card provided 18 bits of resolution on ±0.1 V input range and 600 kSamples per second. The sensor was biased with a square wave current provided by a Keithley 6221 current source.

3.2.2.6 External magnets and field sweeping. Figure 3.9 shows the two magnets that were used to characterise the sensor signal output when an external field was applied. The magnet frame in Fig. 3.9.a was voltage driven by a Kepco BOP 400-4M power supply (Kepco Inc., NY, USA) and could provide a field in the range ±40 mT. Two commercial Hall probes were placed at the poles of the magnet to measure the magnetic field.

The Helmholtz coils in Fig. 3.9.b were current driven by a Kepco BOP 20-5D power supply and could provide field in the range ±11 mT. The Helmholtz coils generate a

nearly uniform magnetic field in the sensor area but were limited to a single direction, while the magnetic frame could be rotated.

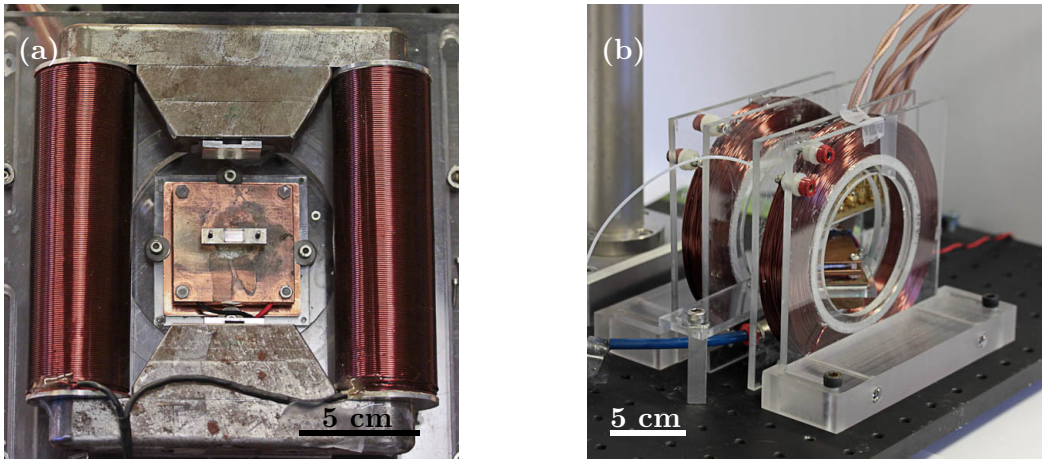

Fig. 3.9: **(a)** Electromagnet frame mounted on the sensor setup. The field is measured by commercial Hall probes positioned in the slots at the poles of the magnet. **(b)** Helmholtz coils mounted around sensor holder. The coils provide nearly uniform magnetic field on the sensor area.

Both electromagnets could be used to characterise the sensor output vs. applied magnetic field. To do so, the sensors were biased with a small current $I_{\mathrm{RMS}} = 1/\sqrt{2}$ mA to avoid heating of the sensor and the external field was swept on the range allowed by the magnet. From theory we know that the first harmonic in-phase PHEB sensor output is

$$V_1' = -\frac{V_{\mathrm{pp}}}{2}\sin(2\theta) + V_{\mathrm{off}}, \tag{3.2}$$

where V_{off} allows for small offsets in the sensor output and we defined the RMS version of

$$V_{\mathrm{pp}} = I_{\mathrm{RMS}}\frac{l}{wt}\Delta\rho. \tag{3.3}$$

The first harmonic sensor output depends on the angle of the magnetisation. In a single domain model, the angle of the magnetisation can be obtained by minimizing numerically Eq.(2.14). This model can be fitted to the field sweep data, the fitting parameters are V_{pp}, V_{off}, H_{K}, H_{ex} and H_{s}. The low-field sensitivity can then be obtained as the slope of the fitted model in the low-field range ± 0.15 mT. This model is used for the experimental work of Chapter 4. The external magnets were used only for characterisation purposes. No external magnetic field is necessary to detect magnetic beads.

3.3 Materials

The materials used for the experimental work of this thesis are reported in this section, with information on the vendors. The critical information is also repeated together with the result, when necessary.

3.3.1 Magnetic beads

Along this thesis a number of different magnetic particles were used. In particular, a broad characterisation of the Brownian relaxation of the beads has been performed to

identify the most suitable bead type to apply to biological assay (see Section 5.1.2.2). Magnetic beads from various producers and with different surface functionalisation were used according to the application. Table 3.1 reports the details about each bead type used in this work.

Tab. 3.1: Magnetic beads used in this thesis. For each bead kind are reported nominal diameter (D_{nom}), type, producer, information about the core of the particle and surface functionalisation. The particle type used will be specified for every application in the respective sections.

D_{nom} [nm]	Type	Producer	Core	Surface group
10	SHP	Ocean Nanotech	Single ($\gamma - Fe_2O_3$)	COOH
25	SHP	Ocean Nanotech	Single (Fe_3O_4)	COOH
40	SHP	Ocean Nanotech	Single (Fe_3O_4)	COOH
50	MicroBeads	Miltenyi		Streptavidin
50	BNF-Starch	Micromod	Multi (Fe_3O_4)	NH_2
80	BNF-Starch	Micromod	Multi (Fe_3O_4)	Streptavidin
80	BNF-Starch	Micromod	Multi (Fe_3O_4)	Plain
130	Nanomag-D	Micromod	Multi (Fe_3O_4)	Plain
250	Nanomag-D	Micromod	Multi (Fe_3O_4)	Plain

The three bead vendors were Ocean Nanotech (AR,USA), Miltenyi Biotech Norden AB (Lund, Sweden) and Micromod Partikeltechnologie GmbH (Rostock, Germany). The magnetic beads could be divided in single-core and multi-core nanoparticles. The first are formed by a single magnetic core, usually coated by a chemical or biochemical active layer. The multi-core particle are formed by a matrix (here starch or dextrane) that binds together the magnetic cores. The multi-core particles are also usually coated with an active surface layer.

The 50 nm Streptavidin MicroBeads (Miltenyi) are the only beads used in Chapter 6. These beads showed (data not shown) a significant in-phase magnetic response up to frequencies of ~ 10 kHz, which indicates that the beads are at least partly superparamagnetic up to these frequencies. Therefore, these beads were found not to be suitable for Brownian relaxation measurements. Measurement on these beads were always performed at 167 Hz to be at a frequency high enough to avoid extensive $1/f$ noise and to ensure high sampling rate (3 samples per second).

Figure 3.10 shows transmission electron microscopy (TEM) pictures of (a) 10 nm, (b) 25 nm and (c) 40 nm Ocean Nanotech SHP magnetic beads (source: oceannanotech.com). The TEM pictures image only the magnetic core of the particle. The cores of the particles in Fig. 3.10.(a,b) are consistent with the nominal diameter given by the manufacturer (the scale was not provided in the image for 40 nm beads). The single core Ocean Nanotech beads of diameter 25 nm and 40 nm are to be thermally blocked in zero applied field. The same assumption could be incorrect for 10 nm beads, where the diameter is on the border for superparamagnetic behaviour.

Figure 3.10.(d) shows a TEM image of one Micromod BNF-Starch 100 nm multi-core bead from Bordelon *et al.*[68] (images were not available in literature for other bead sizes). The TEM image shows the cluster of magnetic cores but cannot detect the embedding starch matrix. The longer dimension of the particle is roughly the nominal diameter but the shape is far from spherical. In this case, the hydrodynamic diameter is an abstraction

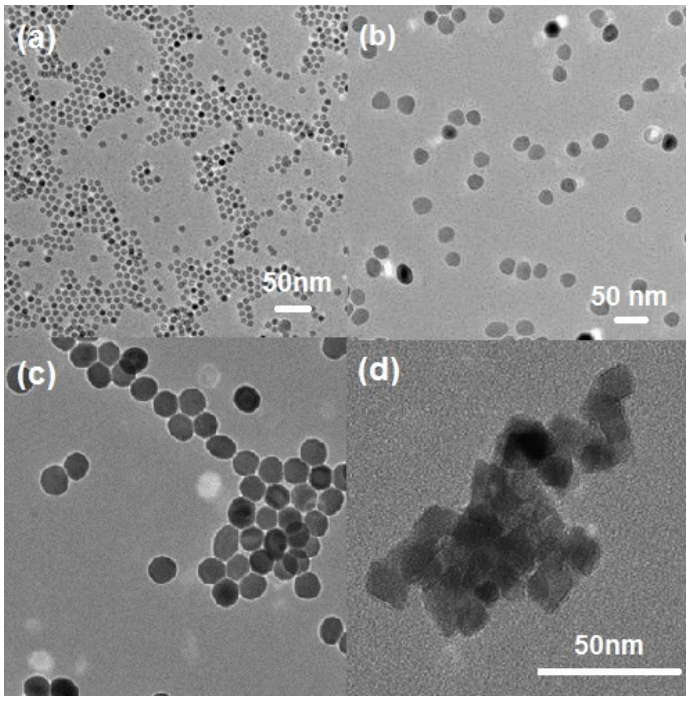

Fig. 3.10: Transmission electron microscope images of: **(a)** Ocean Nanotech 10 nm SHP single core magnetic particles **(b)** Ocean Nanotech 25 nm SHP single core magnetic particles **(c)** Ocean Nanotech 40 nm SHP single core magnetic particles **(d)** Micromod 100 nm BNF-Starch multi core magnetic particles. Sources: oceannanotech.com, Bordelon *et al.* [68].

to characterise the rotational behaviour of the particle in suspension. The multi-core Micromod beads are declared by the producer to be thermally blocked. Therefore we will assume that all those beads follow Brownian relaxation.

3.3.2 Oligonucleotides

In Chapter 6 we will use PHEB sensor to investigate the hybridisation of target DNA to surface-linked DNA probes. For this purpose we used allele-specific probes designed by Petersen *et al.* [57] for SNP genotyping in the human betaglobine (HBB) gene. The DNA probes and target were purchased from DNA Technology A/S (Risskov, Denmark) and their sequences are reported in Tab. 3.2. Two mutation sites were investigated: CD8/9 and CD17. The mutations are underlined in Tab. 3.2. Wild type (WT) and mutant type (MT) probes differ by a single base insertion for CD8/9 and by a single base substitution for CD17.

Biotinylated DNA was used as target, to allow for binding of the streptavidin magnetic beads. WT and MT targets were 120 bases long and included both sequences complementary to the probes. Therefore the MT target included both CD8/9 and CD17 mutations. Moreover a biotinylated DNA probe was used to provide a direct binding site for the beads to the sensor surface. The sequence of the biotinylated probe was chosen to have minimal complementarity to the targets.

These probes and targets were chosen because of the high amount of characterisation information provided by Petersen *et al.* [57, 43, 58]. In their work they analysed SNP detection under varying temperature and washing stringency conditions. In their study,

Tab. 3.2: Sequences of the wid type (*WT*) and mutant type (*MT*) probes and targets for CD8/9 and CD17 mutation sites in the human HBB gene. The point mutation investigated are underlined in both *MT* probes and *MT* target. The probe sequences are colour coded to underline complementary sequences in the target. The target sequences are 120 bases long but only the part complementary to the probe is reported here.

Name	Sequence
Biotinylated	Amino C6-5'-(9xT) TGC GAG CTT CGT ATT ATG GCG -3' TEG Biotin
CD8/9 WT probe	Amino C6-5'-(9xT) G AGG AGA AGT CTG CCG TTA CTG -3'
CD8/9 MT probe	Amino C6-5'-(9xT) G AGG AGA AGGT CTG CCG TTAC -3'
CD17 WT probe	Amino C6-5'-(9xT) CCC TGT GGG GCA AGG TG -3'
CD17 MT probe	Amino C6-5'-(9xT) CCC TGT GGG GCT AGG TGA -3'
WT target	Biotin TEG 5'- [...] TCA CCT TGC CCC ACA GGG CAG TAA CGG CAG ACT TCT CCT CAG [...] -3'
MT target	Biotin TEG 5'- [...] TCA CCT AGC CCC ACA GGG CAG TAA CGG CAG ACCT TCT CCT CAG [...] -3'

the CD8/9 mutation was easier to identify in a broad range of washing conditions, due to the nature of the mutation (base insertion). The CD17 mutation (base substitution), however, showed a more narrow range of optimal washing conditions for positive identification. The two mutation sites were therefore suitable for benchmarking the surface detection capabilities of our sensors.

3.3.3 Reagents

All the reagents used for this work, unless otherwise specified, were purchased from Sigma-Aldrich Denmark ApS (Brøndby, Denmark). Saline-sodiumcitrate (SSC) was purchased from Invitrogen (Auckland, New Zealand).

3.4 Experimental procedure

The experimental procedures used in this thesis are described in this section. First, RCA coil preparation for the Brownian relaxation measurement is presented. Then, the procedures for surface-based hybridisation and denaturation analysis are explained. The surface functionalisation of the sensor is presented, followed by the procedure for hybridisation of the DNA target to the surface-tethered probes. Finally, the denaturation analysis procedures and the data treatment required for those measurements are presented.

3.4.1 Rolling circle amplification

Brownian relaxation measurement performed on the PHEB sensors were applied to the detection *Bacillus globigii* (BG) and *Vibrio cholerae*(VC). The assay detects DNA coils produced by rolling circle amplification (RCA). The technical detail on the preparation of the coils measured in Section 5.4 can be found in the work by Zardán Gómez de la Torre *et al.* [25, 69]. Below, only a minimal explanation about the rolling circle amplification (RCA) process will be given.

Figure 3.11 shows a schematics of the RCA process for *Bacillus globigii* and *Vibrio cholerae*. In both case the goal is to obtain a circularisation of the padlock probe. The loop will be then amplified through RCA. The *Vibrio cholerae* DNA is complementary

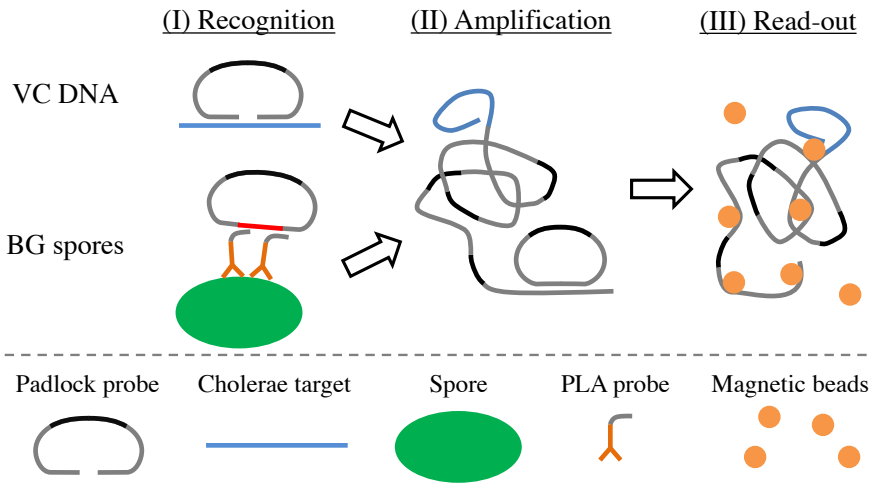

Fig. 3.11: Schematic of the bioassay scheme for the detection of VC DNA and BG bacterial spores. The padlock probe is circularised upon binding to target DNA or two PLA probes. The circular DNA is amplified through RCA. Magnetic beads cluster on the DNA coils. Adapted from Paper VI.

to the detection sequence of the padlock probe. When the probe hybridises to the target DNA, the two extremities are near each other and the probe can be circularised. To detect *Bacillus globigii* a proximity ligation assay (PLA) is employed. PLA utilizes DNA modified antibodies to template circularization of the padlock probe. When two or more PLA probes bind to a target protein, the two extremities of the DNA can be joined. The circular DNA molecules are then copied in an isotermal DNA polymerization reaction (RCA). The DNA template molecule is an endless loop, and thus the process continues until the polymerase dies. This process creates a longer DNA strand (10-100 kbases). Each repetition contains a label sequence that can be used as target for the magnetic beads. These long DNA polymers spontaneously coil into 500-1000 nm diameter blobs of DNA in solution. The beads, functionalised with probes complementary to the amplified sequence, cluster on the coils. The clustering of beads can be detected measuring their Brownian relaxation.

3.4.2 Surface chemistry and probe patterning

To covalently bond DNA probes to the Ormocomp passivation layer of the sensor, a silanisation of the surface was performed, a schematic representation of the binding chemistry can be seen in Fig. 3.12. The steps are: (1) Surface activation for 20 min in 45% H_2O_2 followed by rinsing in MilliQ water and drying in N_2 stream; (2) After washing in acetone the chips were dipped in 10% v/v solution of 3-Aminopropyltriethoxysilane (APTS) in Acetone for 30 min, (3) following rinsing in acetone and drying they were immersed in 5% v/v solution of Glutaraldehyde (GA) in MilliQ water for 30 min; Finally the sensors were rinsed and dried. (4) A solution of 20 µM amino labelled capture probes in 3×saline-sodiumcitrate(SSC) was spotted on the sensor arms using a Nanoplotter with NanoTip (both from GeSim GmbH, Grosserkmannsdorf, Germany) at room temperature and at a controlled humidity of 65%. The probes were incubated overnight on the sensor surface. Prior to use the sensors were rinsed 1×phosphate buffered saline (PBS) then the sensor surface was blocked in a solution of 1 mg/mL of bovine serum albumine (BSA) in 1×PBS

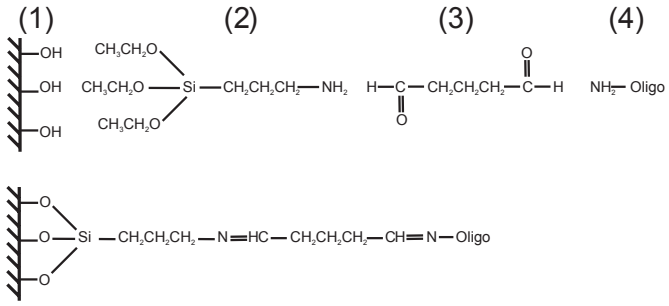

Fig. 3.12: Surface chemistry to bind amino DNA capture probes. (1) Surface OH group (2) APTS (3) GA (4) DNA capture probes.

for 20 min. The sensor was again rinsed in MilliQ water and dried under N_2 stream.

3.4.3 DNA Hybridisation

DNA hybridisation took place on the sensor surface at a temperature of 37°C. The DNA target and beads were injected together on the sensor surface. Before DNA hybridisation, a reference sample of the washing buffer with no targets or beads was measured. The signal from this reference measurement $V_2''(0)$ was then used to correct the second harmonic offset and obtain the signal variation

$$\Delta V_2''(t) = V_2''(t) - V_2''(0). \tag{3.4}$$

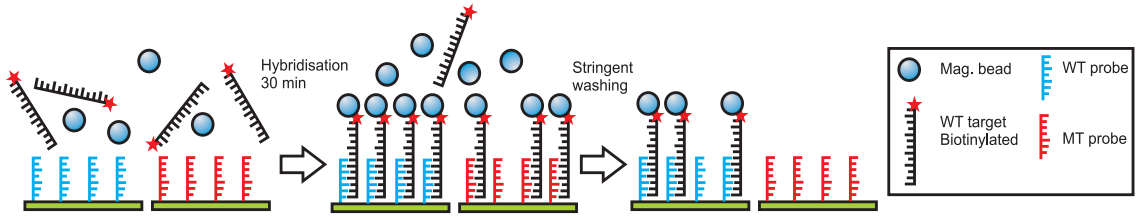

Fig. 3.13: Schematic of an hybridisation assay. Two sensor are functionalised with different probes. After hybridisation at 37°C the sensors are washed and the mismatched hybrids denature. Adapted from Paper VII.

Figure 3.13 shows the flow of an hybridisation experiment for SNP detection. The target diluted in hybridisation buffer was mixed 1:1 v/v with streptavidin coated MicroBeads (Miltenyi). The final volume of the solution 20 µL was injected in the microfluidic system at a flow rate of 30 µL/min using a syringe pump. The sample was injected on the dry sensor, to avoid concentration gradients in the microfluidic channel due to the parabolic flow of the sample.

After injection, the sample was kept stagnant over the sensor surface. The typical hybridisation took place for 30 min (when not otherwise specified). For SNP genotyping hybridisation, this was followed by washing at 37°C with 0.5 × SSC + 0.012% sodium dodecyl sulfate(SDS) for 80 s at a flow rate of 30 µL/min. After washing the system was left stagnant.

3.4.4 Melting curve and stringency gradient

For melting curve and stringency gradient analyses the sensor were prepared with DNA capture probes as in Fig. 3.14. The presence of a positive reference sensor was needed to compensate for the temperature dependency of the low-field sensitivity when ramping in temperature.

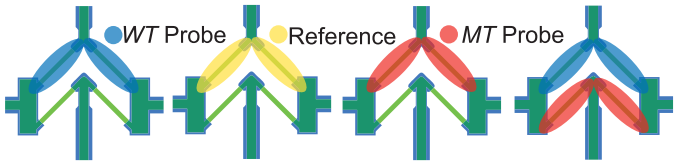

Fig. 3.14: Probe patterning for denaturation studies. Sensor are functionalised with WT, MT and positive reference DNA capture probes. One sensor is functionalised with both MT and WT capture probes

The second harmonic out-of-phase signal was measured during the whole experiment. The signal was a function of the temperature or concentration at the instant at which it was measured. Therefore $V(T,c) = V_2''(t)@(T(t),c(t))$. The hybridisation process was performed as above. After 30 min hybridisation the DNA duplexes were melted in rising temperature or decreasing buffer concentration.

Reference measurements. Reference measurements are taken with no DNA target or beads to compensate for second harmonic offset. The signal from the positive reference sensor was measured during temperature ramping in stagnant washing. The temperature dependent second harmonic offset $V_{0,\mathrm{ref}}(T)$ for the positive reference sensor is used to correct signal during temperature melting of hybrids.

The signal from all the sensors was measured during a concentration gradient at fixed temperature.The concentration dependent second harmonic offset $V_0(c)$ measured for all the sensor was used to correct the signal during concentration denaturation.It was found that, for the investigated temperature and concentration ranges, $V_0(c) \ll V_{0,\mathrm{ref}}(T)$.

Temperature melting of hybrids. For melting curve analysis, after 30 min from sample injection the temperature was decreased to 20°C to inhibit the hybridisation reaction. The sensor was then washed for 80 s at a flow rate of 30 µL/min. The system was left stagnant in washing buffer. The temperature was ramped from 20°C to 70°C and back at a rate 0.1°C/s. The signal from the down-ramping V_{down} was used to correct the second harmonic offset in the up-ramping signal V_{up}. The corrected signal was $\Delta V(T) = V_{\mathrm{up}}(T) - V_{\mathrm{down}}(T)$. The signal from the positive reference sensor was corrected using the reference measurement before hybridisation therefore $\Delta V_{\mathrm{ref}}(T) = V_{\mathrm{ref}}(T) - V_{0,\mathrm{ref}}(T)$

Since the biotin-streptavidin bond is not denatured at the used temperature, the positive reference signal is proportional to the sensitivity. When ramping temperature, the bead signal from other sensor can be normalised by the reference sensor signal to obtain the relative signal (S_{R})

$$S_{\mathrm{R}} = \frac{\Delta V(T)}{\Delta V_{\mathrm{ref}}(T)}. \tag{3.5}$$

Concentration gradient denaturation of hybrids. For concentration gradient denaturation, after 30 min from sample injection, the temperature was set to the desired value. The sensors were then washed with 2 × SSC for 80 s at a flow rate of 30 µL/min. The washing buffer concentration was then varied exponentially from $c(\mathrm{Na}^+) = 400$ mM to $c(\mathrm{Na}^+) = 0.4$ mM in 1200 s. The flow rate during the concentration gradient was 30 µL/min.

The sensor signal were corrected for the second harmonic offset using the reference concentration gradient to obtain $\Delta V(c) = V(c) - V_0(c)$. In this case it was not needed to normalise the signal with the positive reference since the low-field sensitivity is virtually independent on the buffer concentration.

Data analysis. To determine the melting temperature T_m or concentration c_m, the two signals $S_\mathrm{R}(T)$ and $\Delta V(c)$ were fitted with an error function model.

$$S_\mathrm{R}(T) = \frac{1}{2}\left[1 - \mathrm{erf}\left(\frac{T - T_m}{\sigma_T}\right)\right](S_\mathrm{R,max} - S_\mathrm{R,min}) + S_\mathrm{R,min} \tag{3.6}$$

$$\Delta V(c) = \frac{1}{2}\left[1 - \mathrm{erf}\left(\frac{\log(c) - \log(c_m)}{\sigma_c}\right)\right](\Delta V_\mathrm{max} - \Delta V_\mathrm{min}) + \Delta V_\mathrm{min} \tag{3.7}$$

Here the free fitting parameters were T_m, σ_T, $S_\mathrm{R,max}$ and $S_\mathrm{R,min}$ for the temperature ramping. For the concentration gradient, the free fitting parameters were c_m, σ_c, ΔV_max, ΔV_min. The error function is defined as

$$\mathrm{erf}(x) = \frac{2}{\sqrt{\pi}} \int_0^x e^{-k^2}\,\mathrm{d}k. \tag{3.8}$$

CHAPTER 4

Temperature effects in PHEB sensors

In this chapter the effects of temperature on PHEB sensors are investigated. This work expands on previous work from Damsgaard *et al.* [54] on PHE cross sensors. The sensor temperature is known to affect both the AMR ratio and the exchange bias field. These two parameter affect directly the low-field sensitivity S_0 of the PHEB sensor.

We show that fitting a single domain model to the sensor field-sweep proves a reliable tool to study the sensor performance under varying temperature conditions. In this chapter, this technique is used to distinguish reversible and irreversible changes in the sensor properties when exposed to temperatures up to 90°C.

With the aim of performing DNA hybridisation studies (see Chapter 6), and in particular DNA melting curves on-chip, it is of interest how to reduce and compensate the effects given by temperature ramping. Low-temperature annealing was investigated as a possible approach to mitigate these effects. This chapter summarises the results presented in Paper I.

4.1 Experimental

For this characterisation work, four wafers of sensors with the magnetic stack Ta(3)/ $Ni_{80}Fe_{20}$(30)/$Mn_{80}Ir_{20}$(20)/Ta(3) (thickness in nm) were fabricated as described in section 3.1. The sensor fabrication procedure included an heating step at 120°C for 2 min after deposition of the magnetic stack. The sensors used for this study had a geometry with $w = 20$ µm and $l = 280$ µm. The contacts design was such that the bridge corners were active part of the sensing element, therefore the actual geometrical factor for this sensors was found through finite element analysis to be $l/w = 14.87$ [56]. The sensors were surrounded by magnetic stack to reduce demagnetisation effects, with a gap to the sensing elements of 3 µm. After deposition of the contacts the sensors were annealed in vacuum at 240°C, 280°C and 320°C in saturating magnetic field of $\mu_0 H_x = 20$ mT along the x-axis. One wafer was used as un-annealed reference.

The magnetic stack was characterised electrically and magnetically (VSM). The sensor first harmonic in-phase signal (V_1') was characterised by sweeping the external magnetic field $\mu_0 H_y = \pm 20$ mT applied in the y-direction. The field characteristics were measured at temperatures varying from 25°C to 90°C and during repeated temperature cycles (7 hours) at 25°C and 90°C, with 10 min settling time and 8 min to sweep the magnetic field.

4.2 Results

The results of the characterisation of the magnetic stack and of the PHEB sensors are presented in this section. First we go through a validation of the fitting of the sensor characteristics by comparing fitting results to corresponding reference measurements of magnetic properties (VSM) and electrical properties. Subsequently, the effect of varying temperature is analysed and low temperature annealing is tested as a possible resource to mitigate in part these effects. Finally, the effect of repeated exposure to elevate temperature is analysed upon repeated temperature cycling between 25°C and 90°C.

4.2.1 Room temperature measurements

The results of field sweeping at room temperature on the as-deposited sensors are shown in Fig. 4.1 for the wafer annealed at 280°C and the un-annealed reference wafer. The sensor signal, normalised by the bias current I_x, is plotted vs. external magnetic field. Comparing the two curves it is observed that the annealing process increased the sensor low-field sensitivity. This was achieved without changing the peak-to-peak value of the sensor signal, but rather the peak of the sensor were found to be shifted towards lower field values.

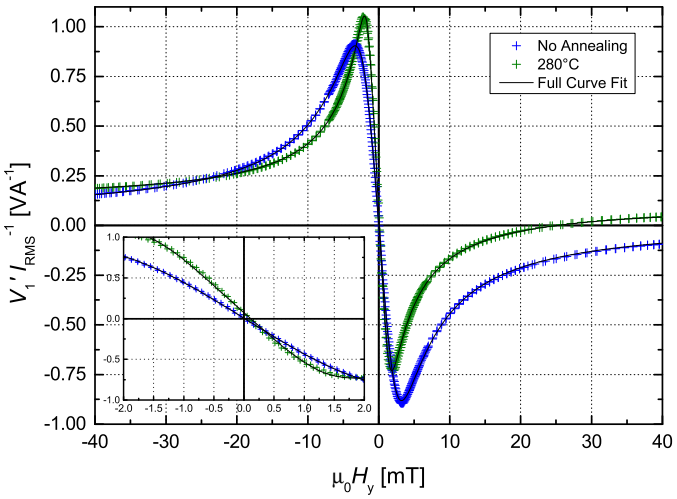

Fig. 4.1: Normalised first harmonic in-phase sensor signal (V_{pp}/I_x vs. external field H_y measured during field sweep of sensors un-annealed and annealed at 280°C. The full lines are fits of the sensor characteristic. Adapted from Paper I.

The solid lines in Fig. 4.1 are least squares fits of the experimental curve as described in Section 3.2.2.6. The shape anisotropy field H_{s} was fixed to the value $\mu_0 H_{\mathrm{s}} = 0.789$ mT obtained from fitting data for all sensor with this parameter free. The fitting of all the sensor responses was of comparable quality as the one in Fig. 4.1. The parameters V_{pp}/I_x, H_{ex} and H_{K} were extracted from fitting and are presented in Tab. 4.1. The low-field sensitivity S_0 was calculated as the slope of the fitted curve in the interval ± 0.15 mT.

The same wafers were characterised through VSM and electrical measurements on a transmission line geometry. In Tab. 4.1 are reported the obtained values of $\mu_0 H_{\mathrm{ex}}$ and $\mu_0 H_{\mathrm{K}}$ from VSM measurement and $\Delta\rho/t$ and AMR from electrical reference. It was possible to compare the quality of the parameters extracted by fitting to the ones measured

Tab. 4.1: Parameters from reference measurement (VSM and electrical) and from fits to sensor field sweeps. All measurements were carried out at 25°C on as-deposited samples. Number in parenthesis are uncertainties obtained from the fitting routine.

	VSM		Electrical ref.		Sensor field sweeps			
Annealing conditions	$\mu_0 H_{ex}$ [mT]	$\mu_0 H_K$ [mT]	$\Delta\rho/t$ [Ω]	AMR [%]	$\mu_0 H_{ex}$ [mT]	$\mu_0 H_K$ [mT]	S_0/μ_0 [V/(AT)]	V_{pp}/I [V/A]
No annealing	2.89(5)	0.39(5)	0.1296(1)	1.88	2.66(1)	0.90(3)	−465	1.779(2)
240°C	2.02(5)	0.41(5)	0.1318(1)	2.03	1.91(1)	0.52(2)	−634	1.785(3)
280°C	1.90(5)	0.50(5)	0.1319(3)	1.95	1.60(1)	0.50(3)	−699	1.764(4)
320°C	1.39(5)	0.46(5)	0.1317(1)	2.03	1.32(1)	0.34(3)	−808	1.768(7)

directly using the other techniques. The measured values for H_{ex} are within the expected variation on a wafer scale. The values for H_K were found comparable for the annealed wafers, but differed by a factor two for the un-annealed wafer.

The low-temperature annealing was found to mainly affect H_{ex}, that decreased steadily with increasing annealing temperature. $\Delta\rho/t$ appeared unvaried, and accordingly V_{pp}/I_x was found similar for all annealing conditions. The result of a decreased exchange bias is reflected in the low-field sensitivity S_0 that increases by almost a factor two for the highest tested annealing temperature.

4.2.2 Temperature dependence and annealing

In this section, the effect of temperature ramping on the sensor sensitivity is tested. To allow for the separation of reversible and irreversible effects caused by heating the sensor, field sweeps were measured at increasingly higher temperature T from 30°C to 90°C. After each elevate temperature measurement, a field sweep was measured at the reference temperature 25°C. First the result from the un-annealed wafer is presented in detail, then the analysis is broadened to the sensors from the annealed wafers.

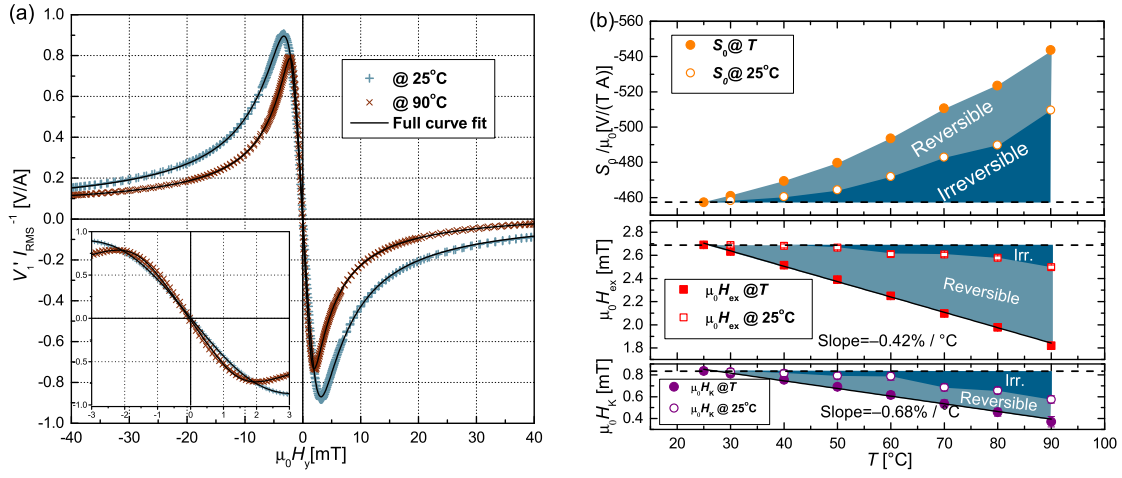

Fig. 4.2: **(a)** First harmonic in-phase signal measured vs. external magnetic field from un-annealed sensor at 25°C and 90°C. Solid lines are least square fit to the single domain model. **(b)** Parameter extracted from the fitting of field-sweep curves. Adapted from Paper I.

Figure 4.2.a shows two field-sweep measurements performed on the un-annealed sensor at 25°C and 90°C. The higher temperature affected the signal in three ways: first the peak

to peak distance decreased, second the peak positions shifted towards lower field, finally the sensitivity increased upon heating. Figure 4.2.b presents in detail the parameter extracted by fitting the field-sweeps with the single domain model. The sweeps were performed at temperature T and subsequently at 25°C. It was found that part of the parameter variation, due to heating, was not reversible upon cooling to the starting temperature. This part of the parameter variation is marked as irreversible in Fig. 4.2 and later on.

The low-field sensitivity increased about 20% when the sensor was heated from 25°C to 90°C. Of this sensitivity variation only half was reversible upon cooling. The values of H_{ex} and H_K decreased approximately linearly with increasing temperature with temperature coefficients of $-0.42\%/°C$ and $-0.68\%/°C$, respectively. The obtained temperature coefficients are in good agreement with those found by Damsgaard *et al.* [54] in a previous study on a similar magnetic stack. For both H_{ex} and H_K a substantial part of the variation was irreversible.

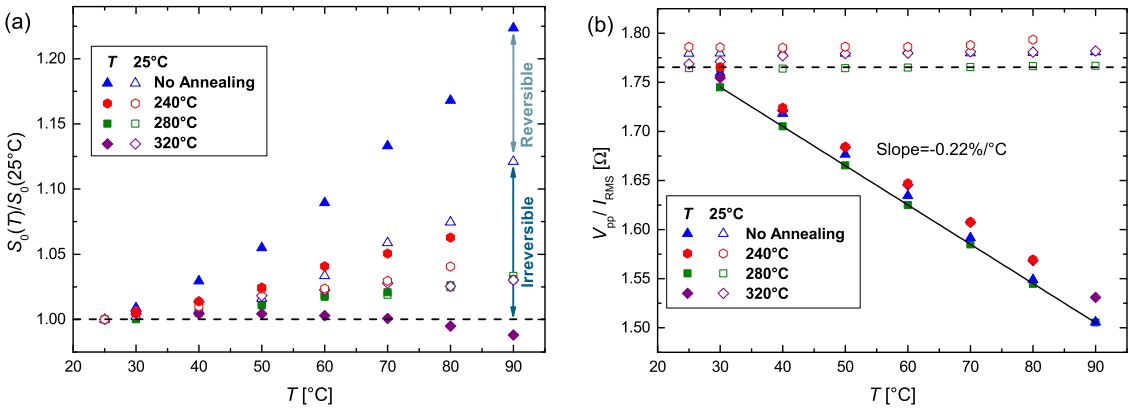

Fig. 4.3: **(a)** Sensor low-field sensitivity normalized by initial sensitivity at 25°C measured at temperature T (filled points) and at reference temperature 25°C (open points). The measurement at 25°C after each exposure to T allows to differentiate reversible and irreversible changes in sensitivity. **(b)** Peak-to-peak voltage V_{pp} measured at temperature T and at reference temperature 25°C. Solid line is a linear fit of the data from the sensor annealed at 280°C. The slope was found to be similar for each annealing condition. Adapted from Paper I.

The same analysis was performed on low-temperature annealed sensors. Figure 4.3 and Fig. 4.4 show the fitting parameters for all the annealing temperatures. Figure 4.3.a shows the values of the low-field sensitivity S_0 normalised by the initial measured value at 25°C. It is possible to make a direct comparison with the data shown before for the un-annealed wafer. Low-temperature annealing decreased the temperature induced variation in all the sensors. The sensitivity of the wafer annealed at 320°C decreased with increasing temperature. For the two highest annealing temperatures the irreversible changes in sensitivity were about 3% at 90°C compared to 12% for the un-annealed wafer.

The normalised peak-to-peak voltage V_{pp}/I_x (Fig. 4.3.a) was found to have only minor inter wafer variation. The parameter decreased linearly with a temperature coefficient of $-0.22\%/°C$ and did not show any irreversible change. This result shows that low temperature annealing does not affect the AMR properties of the magnetic stack.

Figure 4.4.a show the values measured for H_{ex} normalised by the first measurement at 25°C. The exchange bias fields for all annealed wafers are found to decrease linearly with temperature with a coefficient $-0.37\%/°C$. This coefficient is smaller than the coefficient $-0.42\%/°C$ found for the un-annealed wafer. Also the irreversible changes in H_{ex} were

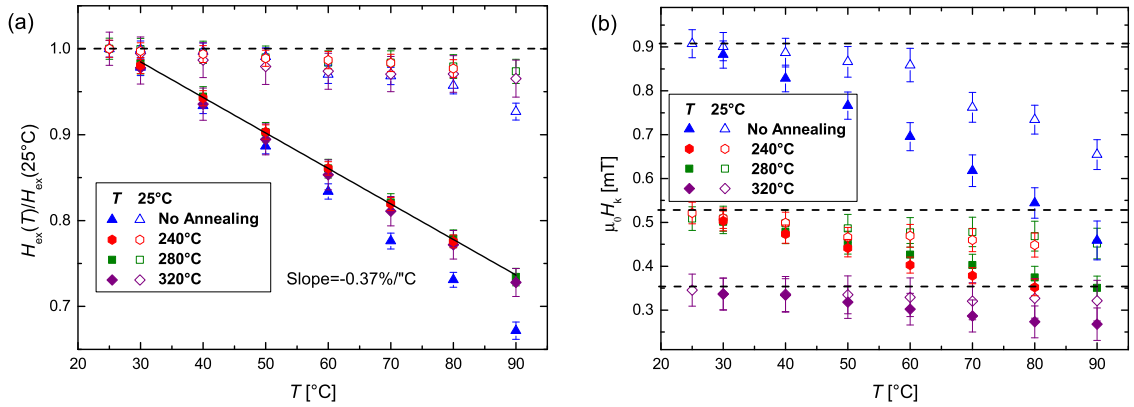

Fig. 4.4: **(a)** Exchange bias field H_{ex} normalised by the initial value at 25°C measured at temperature T (filled points) and at reference temperature 25°C (open points). The measurement at 25°C after each exposure to T allows to differentiate reversible and irreversible changes in H_{ex}. Solid line is a linear fit of the data for the sensor annealed at 280°C. The slope was found to be nearly identical for all the annealed wafers. **(b)** H_K measured at temperature T and at reference temperature 25°C. Error bars are uncertainties obtained from the fitting routine. Adapted from Paper I.

more moderate in the annealed wafers.

Figure 4.4.b shows the values obtained for H_K. The initial value of this parameter decreased with increasing annealing temperature. Compared to un-annealed samples, the reversible and irreversible changes of H_K were more moderate in the annealed samples.

4.2.3 Temperature cycling

Figure 4.5 shows the evolution of the critical parameters S_0, H_{ex} and H_K upon repeated exposure at 90°C vs. time. After each measurement at high temperature, a low temperature reference was acquired at 25°C, therefore only half of the time was spent at 90°C. This study focused only on the sensor annealed at 280°C and the un-annealed reference.

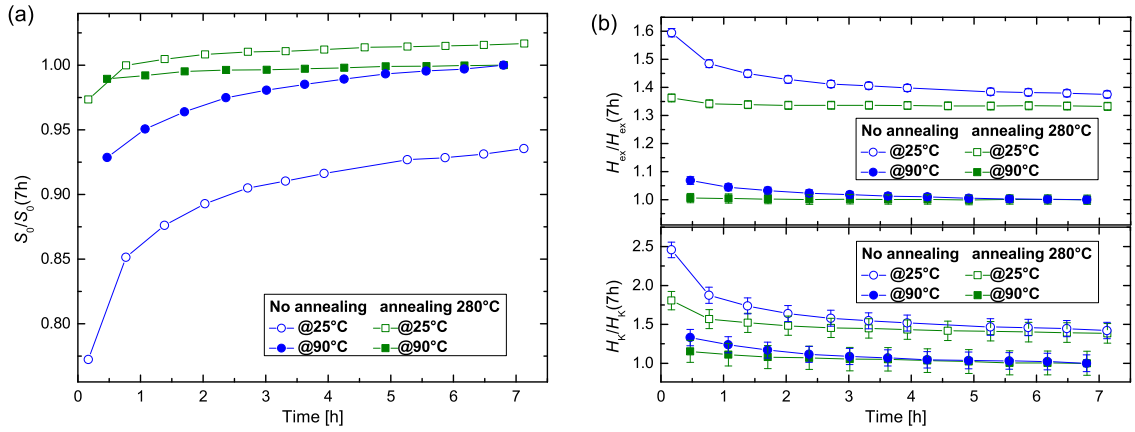

Fig. 4.5: Measurement of the relative value of **(a)** S_0 and **(b)** H_{ex} and H_K as measured vs. time in a cycling temperature for samples un-annealed and annealed at 280°C. A reference at 25°C (open points) was taken after each measurement at high temperature (filled points). Error bars are uncertanties obtained from the fitting routine. Adapted from Paper I.

Figure 4.5.a shows the time evolution of the low-field sensitivity normalised by the final

value reached during the experiment. The un-annealed sensor showed a big change ($> 7\%$) upon the first exposure at high temperature, as seen in the previous set of experiments. S_0 then approached slowly its asymptotic value that was still not reached after 7 h of temperature cycling, and that lead to a total irreversible change of around 20%.

For the annealed sample, the irreversible change of S_0 (25°C) was smaller: less than 5% during the whole experiment and it took place almost entirely during the first high temperature cycle.

Figure 4.5.b shows the effect upon H_{ex} and H_{K}. The asymptotic difference in H_{ex} from 25°C and 90°C for both un-annealed and annealed sensor approached 35%, consistently with what we showed before. For the annealed sample H_{ex} maintained an almost constant value throughout the whole experiment at both temperatures. Opposedly, for the un-annealed sample, the 25°C value of H_{ex} changed strongly with time. Similarly, the change of H_{K} for the annealed wafer is smaller than for the reference un-annealed one.

4.3 Discussion

The single domain model provided excellent fits to the experimental field-sweep. The parameters obtained by fitting are generally in good agreement with the corresponding VSM measurement. It was further possible to compare the V_{pp}/I_x with the electrical reference measurements since $V_{\mathrm{pp}}/I_x = (l/w)(\Delta\rho/t)$ (as seen from Section 2.1). In this case the values measured from field sweeps were 9% smaller than calculated values. This difference is attributed to demagnetisation effects due to sensor geometry that cause the magnetisation of the sensor elements to deviate from the nominal single domain geometry near the edges [70].

The described fitting method allowed us to test the PHEB sensors under a great variety of temperature conditions. Using cyclical heating intercalated with reference measurements at room temperature, we could separate reversible and irreversible changes in the sensors. In our findings $\Delta\rho/t$ was not changed upon annealing and any temperature effects on this were fully reversible. Opposedly H_{ex} and H_{K} showed irreversible changes given by heating. These changes were of reduced magnitude in annealed sample but were still present and took place on a time-scale of several hours. These affect the sensor low-field sensitivity and have to be taken into account in any experiment implementing temperature ramping.

King *et al.* [71] and Geshev *et al.* [72] studied the exchange bias in top pinned ferromagnet by means of Lorentz transmission melectron microscopy [71], cross-sectional TEM and X-ray reflectivity [72]. After annealing in condition comparable with ours, they found no microstructure changes of the interface upon annealing. In particular Geshev *et al.* observed a clear reduction of H_{ex} upon annealing that they attributed to relaxation of frustrated spins in the top antiferromagnetic layer.

Our observation on irreversible changes of H_{ex} indicate a slow, thermically activated process that reduces the exchange bias. Thus our observations are consistent with the above interpretation of a thermal relaxation of frustrated spins in the antiferromagnet.

4.4 Conclusion

In this chapter a method to analyse the magnetic and electrical properties of PHEB magnetoresisitive sensor was presented and validated through comparison with electrical

and VSM reference measurement. The fitting procedure with a single magnetic domain model offer an easy way to obtain the relevant parameters of the PHEB sensor in analysis. This method was employed to study the sensor output in varying temperature.

The analysis of the temperature influence on the sensitivity of the sensor is critical for the following work on biological application of PHEB sensors. DNA hybridisation assays and in particular DNA melting curve analysis involve the use of varying temperature. From this work we saw how temperature cycling affects negatively the sensors, inducing irreversible changes in the low-field sensitivity, on a time scale of several hours. Moreover we saw how low-temperature annealing mitigates but does not resolve the irreversible temperature effects.

As seen in 3.1 the fabrication of the Ormocomp passivation layer requires a hard-baking procedure at 150°C for 3 h. Although this heating was not performed in external magnetic field, it was found to produce similar results to the findings of this chapter. Although effective in reducing irreversible changes, the low-temperature approach do not cancel them completely. Therefore, for actual biosensing a positive reference sensor will be employed to have a quantification of the low-field sensitivity whenever temperature ramping will be necessary.

CHAPTER 5

Volume-based biodetection

Brownian relaxation measurements can be used for biodetection [20] since naked magnetic particles relax faster than particles bound to biomolecules. This approach has been efficiently used to detect DNA coils produced by rolling circle amplification (RCA) using a SQUID magnetometer [36, 73] and more recently with a portable AC susceptometer (DynoMag) operated at room temperature [25, 69, 74, 75] to measure the complex magnetic susceptibility χ of a suspension of magnetic beads. Both techniques are not suitable for a lab-on-chip device, the first requires cryogenic temperature and both are quite bulky equipments. Planar Hall effect bridge (PHEB) sensors can also be used to measure Brownian relaxation and provide a more suitable platform for a readout system, which in the future can be integrated with sample preparation.

In this chapter the PHEB detection method will be presented and validated through measurements in both frequency domain and time domain. These results are part of Paper II, Paper III and Paper IV. A set of magnetic particle of varying diameter will be measured to select the best candidate for biodetection. This is part of Paper III. The detection of bead clustering will be tested with small molecules (biotin conjugated BSA). This is part of Paper IV. Then PHEB detection of RCA products will be compared to DynoMag (Paper V). Finally, the setup will be used for detection of *Vibrio cholerae* (VC) DNA and *Bacillus globigii* (BG) spores, demonstrating the first Brownian relaxation RCA bioassay on a magnetoresisitive platform. These results are part of Paper VI.

5.1 Brownian relaxation in the frequency domain

In this section we will introduce Brownian relaxation measurements in the frequency domain. On a PHEB Brownian relaxation is measured by means of varying the bias current frequency and fitting the in-phase and out-of-phase components of the second harmonic sensor signal to the Cole-Cole model presented in Section 2.2.3. Here the method will be investigated in varying concentration of magnetic beads and with beads of varying diameter. The goals of this work are to validate the measurement and fitting method, to determine the smallest bead concentration detectable and the optimal bead diameter to be used for biosensing. The results of this section were published in Paper II (concentration) and Paper III (diameter).

5.1.1 Experimental

The sensor used for this segment of experimental work, and along the whole chapter, had the nominal stack composition Ta(3)/ $Ni_{80}Fe_{20}$(30)/ $Mn_{80}Ir_{20}$(20)/ Ta(3) (thickness in

nm) on a standard bridge sensor with $l = 280$ µm and $w = 20$ µm.

For the measurements with varying bead concentration the sensor was biased with a current $I_{\mathrm{RMS}} = 14.8$ mA. The signal was measured at 20 frequencies equally distributed on a logarithmic scale from $f = 986.9$ kHz to $f = 37.7$ kHz. Measurements were performed on 40 nm SHP magnetic beads from Ocean Nanotech (AR,USA). The bead concentration was varied from $c = 4$ mg/mL to $c = 16$ µg/mL in a two-fold dilution series. Further details can be found in Paper II.

For the measurements of beads with varying diameter a bias current $I_{\mathrm{RMS}} = 14.1$ mA was used. The beads were measured in frequencies from $f = 5$ MHz to $f = 1.88$ Hz in 39 logarithmic steps. Two different lock-in amplifiers were used to cover the whole frequency range. The bead nominal diameter and producer information are reported in Tab. 5.1. A bead solution $c = 1$ mg/mL in PBS was injected over the sensor for each measurement. Further details can be found in Paper III.

5.1.2 Results

In this section we will present the results of the Brownian relaxation measurements obtained by sweeping the frequency. First, measurements as function of the bead concentration will be presented and later as function of the bead nominal diameter.

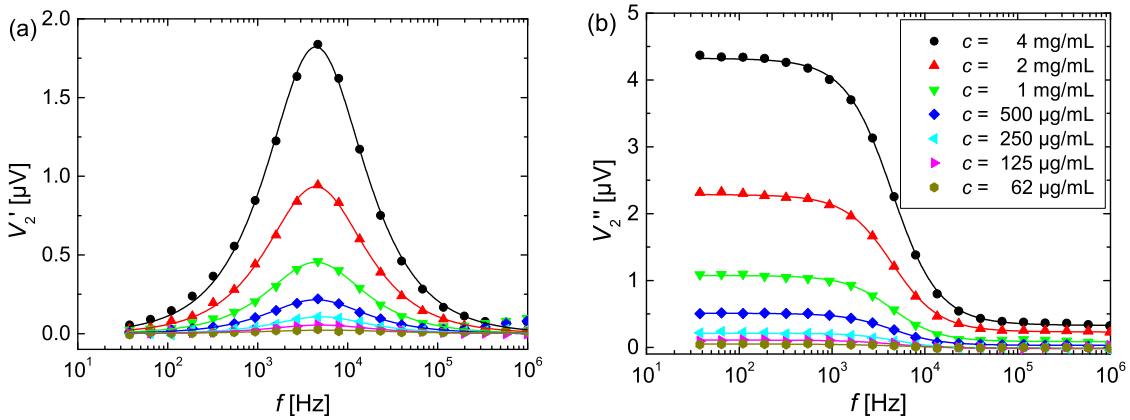

Fig. 5.1: Second harmonic **(a)** in-phase and **(b)** out-of-phase sensor signal vs. bias current frequency. The frequency sweep were measured for decreasing concentration c of 40 nm SHP magnetic beads from Ocean Nanotech. The solid lines are fits of the Cole-Cole model to the data. Adapted from Paper II.

5.1.2.1 Concentration. Figure 5.1 shows (a) the in-phase and (b) the out-of-phase second harmonic signal as a function of the bias current frequency (f) measured 29 min after sample injection into the microfluidic system. At this time, the signal was found to be stable after bead sedimentation (data not shown). The data for concentrations smaller than $c = 62$ µg/mL are not shown in Fig. 5.1 since these were indistinguishable from the $c = 0$ µg/mL reference sample. The solid lines in the plot are fits to the Cole-Cole model (Section 2.2.3). The curve shape was found to be independent of the bead concentration while the amplitude scaled with c. The peak of V_2' (Fig. 5.1.a) was found to scale linearly with bead concentration, with a slope = 460(2) nV/(mg/mL).

Figure 5.2 shows the values of the Brownian relaxation frequency f_{B} obtained by fitting the Cole-Cole model for each frequency, on three consecutive sweeps. The error

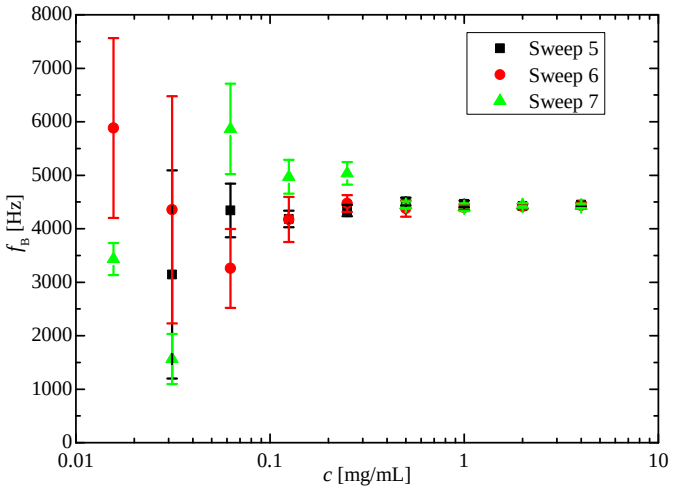

Fig. 5.2: Brownian relaxation frequency obtained by fitting the Cole-Cole model vs. bead concentration c. The value were obtained from three consecutive sweeps. The error bars are uncertainties reported by the fitting routine. Adapted from Paper II.

bars represent the uncertainties reported by the fitting routine. For the four highest concentrations we found $f_B = 4.4(1)$ kHz corresponding to a hydrodynamic diameter of 47(1) nm. For smaller concentrations the average f_B was the same but with higher deviation; for $c = 62$ µg/mL the standard deviation of f_B was found to be 0.8 kHz. The α parameter of the Cole-Cole model was found to be 0.05(1) for the experiments with $c > 62$ µg/mL. For lower concentrations the noise was too high for the model to be fitted reliably to the data.

5.1.2.2 Bead diameter. Figure 5.3 shows the in-phase (a) and out-of-phase (b) second harmonic sensor signal as a function of the bias current frequency (f) measured 20 min after sample injection. The frequency sweeps were measured for six different bead types with nominal diameters ranging from 10 nm to 250 nm. The signal from the frequency sweep was normalised by the maximum value of the curve, to better compare the shape of the curves for different bead types. The solid lines are fits of the Cole-Cole model to the data. The result of the fitting was found to be of high quality for every bead tested. The width of the peaks (in Fig. 5.3) was found to be more narrow for beads with nominal diameter 10 nm, 40 nm and 80 nm indicating that these bead had a more narrow size distribution.

The hydrodynamic diameter $\tilde{D}_h$ and the α parameter obtained by fitting are reported in Tab. 5.1. We see that the obtained values for $\tilde{D}_h$ are all within 25% of the nominal diameter with the only exception being the 250 nm beads.

It was also possible to estimate the peak signal normalised by the bead concentration $V'_{2,\mathrm{peak}}/c$ for all the bead sizes. This parameter is crucial for selecting the most suitable bead type for biosensing applications. It determines the smallest concentration of beads detectable, and therefore the lower limit of the dynamic range for the sensing. The largest beads (250 nm) were found to provide a substantially higher signal per bead. This higher signal could not be explained only by the volume difference, but bead sedimentation probably increased the bead concentration near the surface for bigger beads.

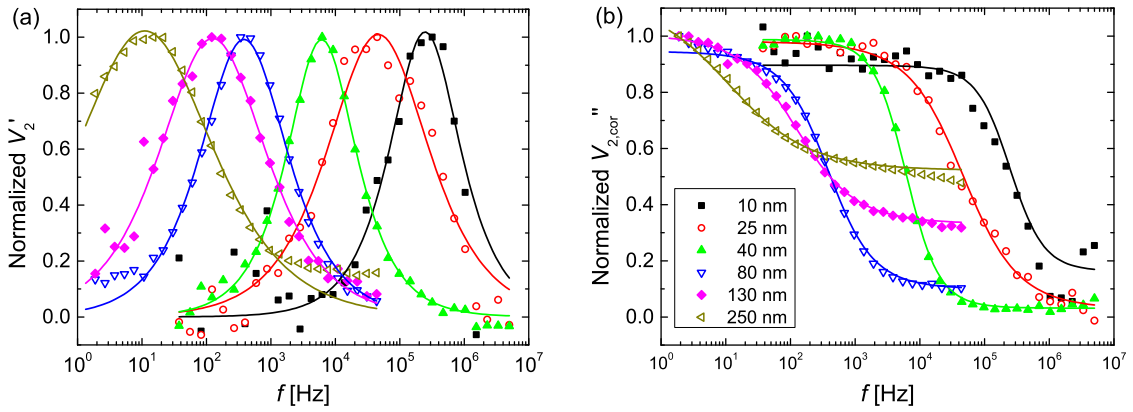

Fig. 5.3: Second harmonic **(a)** in-phase and **(b)** out-of-phase sensor signal vs. bias current frequency. The frequency sweep were measured for varying bead nominal diameter D_{nom}. The solid lines are Cole-Cole fits to the data. Adapted from Paper III.

Tab. 5.1: Values of $\tilde{D}_{\mathrm{h}}$ and α from Cole-Cole fits to the frequency sweeps. The numbers in parenthesis are 95% confidence levels from fitting routine. Last two columns are molar concentration c and peak sensor signal normalised by the bead molar concentration.

D_{nom} [nm]	Type	Producer	$\tilde{D}_{\mathrm{h}}$ [nm]	α	c [nM]	$V'_{2,\mathrm{peak}}/c$ [nV/nM]
10	SHP	Ocean Nanotech	12.4(3)	0.08(5)	860	0.1
25	SHP	Ocean Nanotech	21.6(4)	0.28(2)	58	3.0
40	SHP	Ocean Nanotech	42.4(2)	0.06(1)	14	31.4
80	BNF-Starch	Micromod	107.0(9)	0.20(1)	2.0	602
130	Nanomag-D	Micromod	155(2)	0.31(1)	0.48	622
250	Nanomag-D	Micromod	349(3)	0.43(1)	0.08	17.9×10^3

5.1.3 Discussion

In this section we showed how it is possible to use the PHEB to perform frequency domain measurements of Brownian relaxation of magnetic bead on a vast range of frequencies. Moreover the bead properties (hydrodynamic diameter and polydispersity) can be robustly obtained from fitting to the relaxation model.

From the frequency sweep vs. bead concentration (Fig. 5.1) it is seen that the shape of the measured curve is independent of the bead concentration. The hydrodynamic diameter can be reliably obtained by fitting for concentration as small as $c = 63$ µg/mL corresponding to about 0.9 nM. Lower bead concentration increases the standard deviation of the obtained parameter, due to lower signal-to-noise ratio.

By testing different bead sizes from different producers it was clear that the choice of bead type is important for a volume-based bioassay. By increasing the bead size it is possible to obtain a higher sensitivity with the trade-off of a lower dynamic range. For example, in our system the electrical noise is about 5 nV the 10 nm beads would have a limit of detection higher than 50 nM. Bigger beads would increase this figure, but the sedimentation of these big particle makes them unsuited for biosensing. A good compromise is found in the 80 nm beads that showed a moderate sedimentation and a particularly large signal-per-bead. The theoretical dynamic range for these beads is 6 pM − 2 nM. For these reasons this particular kind of beads will be the choice for the

following work on biosensing.

5.2 Brownian relaxation in the time domain

The Brownian relaxation of magnetic beads can be also studied in the time domain. The self-field direction is inverted when switching the bias current. It is therefore possible to monitor the time it takes for the magnetic beads to realign to the magnetic field. The model for the relaxation of an ensemble of beads was described in section 2.2.3. Measuring in the time domain is faster than sweeping in frequency. A faster sampling of the relaxation can lead to time-resolved measurements.

In this section, the time domain measurement is benchmarked against frequency sweeping on measurements performed on magnetic beads of four different diameters ranging from 40 nm to 250 nm. The results of this section are part of Paper IV.

5.2.1 Experimental

For frequency domain measurements, the sensors were biased by a sine wave with current amplitude $I_{\mathrm{RMS}} = 14.1$ mA. The bias current frequency was varied in 29 logarithmic steps from 43.69 kHz to 1.88 Hz. The data were fitted to the model in Eq.(2.67).

For time domain measurements, the sensors were biased by a square wave with current amplitude $I_x = \pm 14.1$ mA. The half period of the square wave was $T_I = 62.5$ ms corresponding to a frequency of 8Hz. The sensor signal was measured over 192 periods. The measurements were averaged over 500 time intervals, the duration of the averaging intervals was increased logarithmically, starting from the current switching event. The averaged data were used to fit the relaxation model of Eq.(2.58).

The measurements were performed on beads of nominal diameter 40 nm (Ocean Nanotech), 80 nm, 130 nm and 250 nm (Micromod). All bead types were diluted to 1 mg/mL in PBS. Further details can be found in Paper IV.

5.2.2 Results

Figure 5.4.a shows the results of frequency sweeps on beads with different diameters. The solid lines in the plot are the results of least squares fitting of Eq.(2.67) to the data. As for the Cole-Cole model above, the relaxation model matches well the experimental data, except for the high frequency of the 250 nm. Figure 5.4.b reports the bead signal V_{ave} measured vs. time and normalised by the fitting parameter V_{0t}. Solid lines are fits of the relaxation model of Eq.(2.58) to the data.

The parameters obtained for the measuring strategies are summarised in Tab. 5.2. The numbers in parenthesis are uncertainties reported by the least squares curve fits. The values obtained by the two fitting methods, hydrodynamic diameter $\tilde{D}_{\mathrm{h}}$ and logarithmic standard deviation σ of the bead diameter distribution, were found in agreement within experimental uncertainties for beads smaller than 250 nm. For beads with $D_{\mathrm{nom}} = 250$ nm the measurement in both time and frequency domains gave a significantly higher $\tilde{D}_{\mathrm{h}}$.

5.2.3 Discussion

For the beads with nominal diameter smaller than 250 nm the hydrodynamic size and logarithmic standard deviation found by the two measurement methods agree within ex-

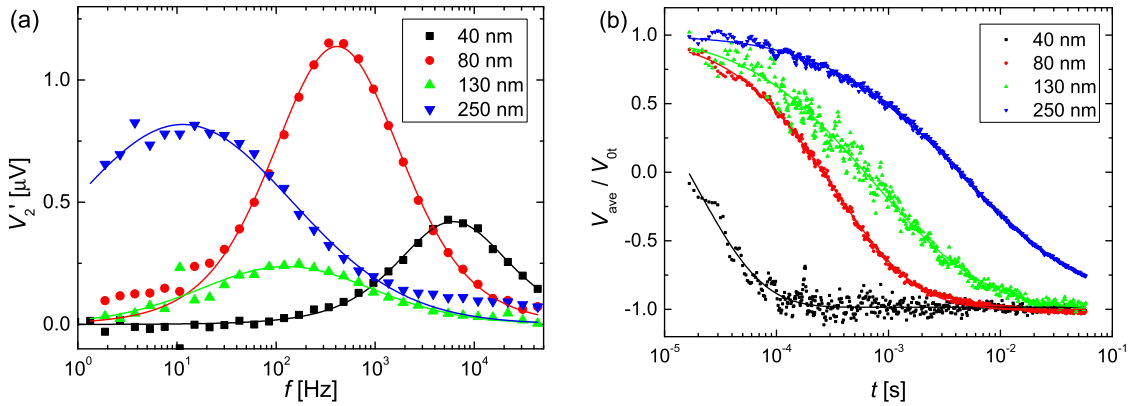

Fig. 5.4: Brownian relaxation measurement performed on beads with varying nominal diameter. **(a)** signal measured vs. frequency. **(b)** signal measured vs. time normalised by the fitting parameter V_{0t}. Solid lines are fit of the relaxation model to the data. Adapted from Paper IV.

Tab. 5.2: Hydrodynamic diameter $\tilde{D}_\mathrm{h}$ and logarithmic standard deviation σ of the bead diameter distribution obtained by fitting time domain and frequency domain data.

	Time domain		Frequency domain	
D_nom [nm]	$\tilde{D}_\mathrm{h}$ [nm]	σ	$\tilde{D}_\mathrm{h}$ [nm]	σ
40	41(2)	0.22(5)	42.5(3)	0.18(2)
80	108(1)	0.35(1)	107(2)	0.32(2)
130	152(2)	0.45(2)	159(4)	0.50(2)
250	299(4)	0.60(1)	350(7)	0.64(2)

perimental uncertainties. The measurement on 40 nm beads are about the limit of what can be resolved in the time domain for this setup. For such a bead size, the relaxation is complete in 100 μs and the time resolution of the data acquisition card (DAQ) is only 1.6 μs, resulting in only 60 measurement points to define the relaxation. Studying at the signal in the time domain it is also clear that the relaxation signal is only a few times higher than the noise. For $D_\mathrm{nom} = 40$ nm the relaxation signal is $V_{0\mathrm{t}} = 1.8$ μV. The sensors have a very low intrinsic thermal noise [76] on the order of 1 nV. Therefore the time domain measurements are now limited by the noise and resolution of the DAQ card. Thus it can be improved by employing low noise signal amplification or sampling on a higher number of cycles.

On the other extreme of the measurement range, the hydrodynamic diameters measured for 250 nm beads with the two techniques differ and the diameter measured in the time domain was smaller then the relative measurement in the frequency domain. Because 250 nm beads had a relaxation time longer then half period of the square wave then for this beads were never completely aligned to the magnetic field. This gave a relatively larger weight to the smaller beads and hence shifts the result for time domain measurement towards smaller diameters. In the frequency domain instead the 250 nm beads did not reach equilibrium during the measurements, due to the long time required for sedimentation. Since the frequency was swept from high to low frequency, sedimentation had the effect of increasing the signal when low frequencies were measured resulting in bigger beads dimensions.

The measurements in the time domain were performed in 24 s compared to the equiv-

alent in the frequency domain that took 1 min 21 s. The use of time domain measurement can pave the way to measurements of the binding kinetics, given the shorter measurement time.

5.3 Detection of small analytes

In this section the detection of biotin conjugated bovine serum albumin (bBSA) will be performed on PHEB sensors, in the time and frequency domains. The streptavidin coated magnetic beads form clusters when bBSA is present in solution. The clustering is detected as an increased hydrodynamic diameter in the relaxation measurements. The results of this section are part of Paper IV.

5.3.1 Experimental

A solution of 80 nm BNF-Starch streptavidin coated magnetic beads (Micromod) was mixed with bBSA to a final bead concentration of 1 mg/mL. Four bBSA concentrations were tested 0 nM, 2.5 nM, 5 nM and 10 nM. To enhance the cluster formation the suspension was placed in a magnetic field (45 mT) for 10 min. Each bBSA has 8-16 biotin molecules, therefore several beads can bind to the same albumine molecule, thus forming beads dimers or clusters. The cluster formation was measured in time and frequency domain with the same condition as in the section above. More details can be found in Paper IV.

5.3.2 Results

Figure 5.5 shows the frequency domain measurements for bead clustering as function of bBSA concentration. The solid lines are fits of Eq.(2.67) to the data. The results of the fitting procedure are reported in Tab. 5.3.

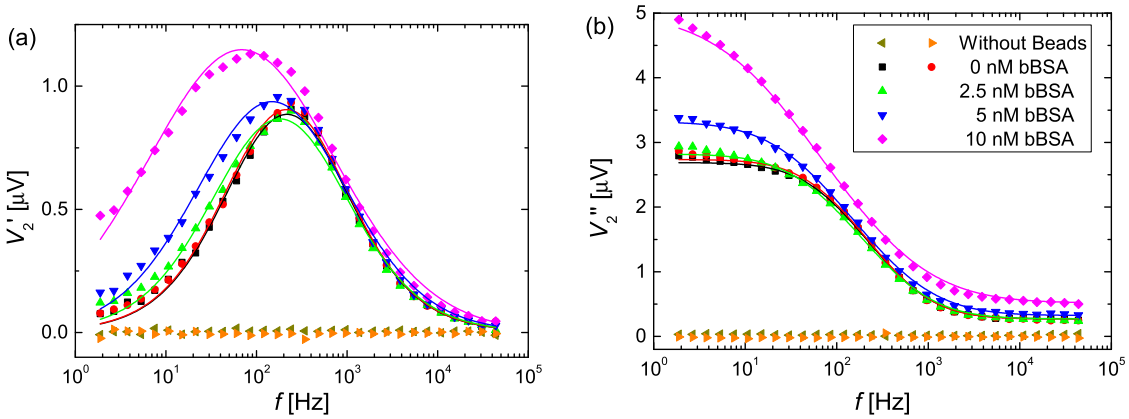

Fig. 5.5: Frequency domain measurement of magnetic bead clustering as function of bBSA concentration. In-phase **(a)** and out-of-phase **(b)** second harmonic signal vs. frequency. Solid lines are fits of Eq.(2.67). Adapted from Paper IV.

The measurements performed on the two samples with no bBSA are highly reproducible and the diameter and logarithmic standard deviation obtained by fitting are identical in

the experimental uncertainty. In the presence of bBSA, the peak of the in-phase second harmonic signal (Fig. 5.5.a) was found to increase in magnitude and shift towards lower frequency. Both $\tilde{D}_\mathrm{h}$ and σ (Tab. 5.3) were found to increase with increasing bBSA concentrations.

In Fig. 5.6.a are shown the result of the same measurements performed in the time domain. The solid lines are fit of Eq.(2.58) to the data. The measurements on the two samples with no bBSA were found to almost coincide. The presence of bBSA caused an increase of the signal amplitude and of the signal slope for $t > 10^{-2}$ s. The parameters obtained from the fitting routine are summarised in Tab. 5.3. The values of $\tilde{D}_\mathrm{h}$ were increasing with bBSA concentration, but no difference was found between 2.5 nM and 5 nM. While the values for σ increased also for those concentration.

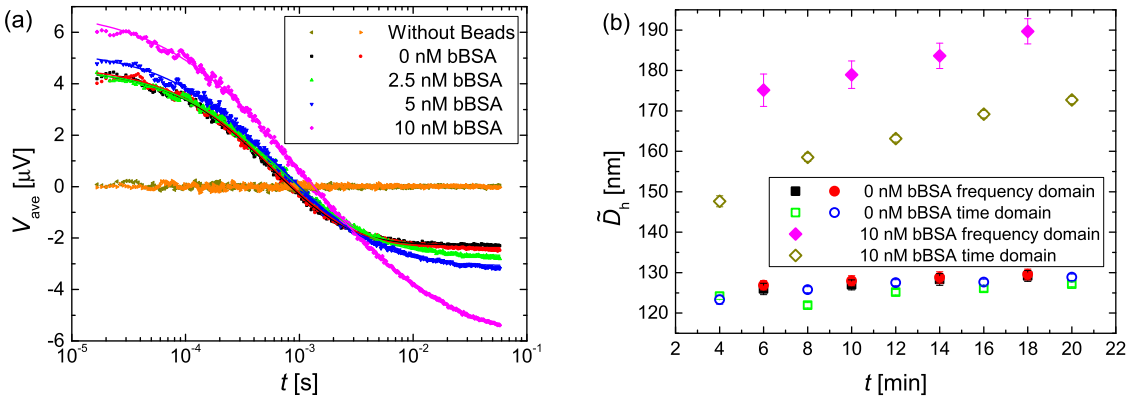

Fig. 5.6: **(a)** Time domain measurement of bead clustering in presence of varying bBSA concentration. Average signal V_ave vs. time. Solid lines are fit of Eq.(2.58). **(b)** Values obtained for the hydrodynamic diameter $\tilde{D}_\mathrm{h}$ for repeated measurements at time t. Measurements for 0 nM and 10 nM bBSA. Error bars are uncertanties reported by the fitting routine. Adapted from Paper IV.

Figure 5.6.b shows the values obtained the hydrodynamic diameter $\tilde{D}_\mathrm{h}$ for repeated measurements at time t. In the reference measurements (no bBSA) the diameter was found to increase slightly with time. When 10 nM bBSA was mixed with the bead solution, the obtained hydrodynamic diameter, from both frequency and time domain measurements, was found to be bigger than without bBSA. Moreover, in this case, the diameter was found to increase faster with time than for the sample without bBSA. Finally, the diameter obtained from frequency domain measurements was found to be bigger than the equivalent time domain result.

Tab. 5.3: Hydrodynamic diameter $\tilde{D}_\mathrm{h}$ and logaritmic standard deviation σ of the bead log-normal diameter distribution obtained from fitting of time domain and frequency domain measurement on magnetic bead mixed with varying bBSA concentration.

	Time domain		Frequency domain	
c_bBSA [nM]	$\tilde{D}_\mathrm{h}$ [nm]	σ	$\tilde{D}_\mathrm{h}$ [nm]	σ
0	127.1(6)	0.31(1)	129(2)	0.34(2)
0	128.9(8)	0.33(1)	130(2)	0.34(2)
2.5	139.9(8)	0.40(1)	137(2)	0.40(3)
5	138.8(8)	0.43(1)	147(3)	0.47(3)
10	172.7(9)	0.62(1)	190(4)	0.65(3)

5.3.3 Discussion

Both measurement methods, in time domain and frequency domain, were found effective in measuring the bead clustering due to the biotin-streptavidin bond. In these preliminary experiments using time domain measurements it was found that this technique was not as sensitive to bBSA as the equivalent relaxation measurement in the frequency domain. This happened because the relaxation of bead cluster was slower than half the period T of the bias current in time domain measurements. Therefore the measurement is more sensitive to smaller bead diameters. Nevertheless this can likely be improved with lower noise electronics and longer measuring time. In this work the time domain measurement took one sixth of the equivalent frequency domain measurement. The speed of this technique can be employed to monitor the kinetics of the binding.

It was also found that in the sample containing bBSA, the hydrodynamic diameter was increasing with time. This is likely caused by cluster sedimentation and the following increase of the ratio of clustered vs. un-clustered magnetic beads near the sensor surface. This is an effect that is not present in other relaxation measurement instrumentations (like Dynomag), but it could be potentially used to improve the sensitivity of PHEB measurements. For example, external magnetic fields could be used to speed up sedimentation and therefore increase the cluster concentration in the sample volume nearest to the sensor.

5.4 Biodetection

In this section the volume based measurement technique is used to detect rolling circle amplification (RCA) products. Beads functionalised with the complementary DNA sequence to the repeating sequence of the amplified DNA coil form clusters and are then detected with relaxation measurements in the frequency domain.

First, a proof of concept of the detection of RCA on PHEB is presented. The method is validated in comparison to the commercial Dynomag system using a synthetic DNA target. These results are part of Paper V. Then, the detection of RCA products from *Bacillus globigii* (BG) spores and *Vibrio cholerae* (VC) will be introduced. The first is demonstrating the system flexibility in quantitative study of coils produced targeting DNA (VC), while the second part of the work test the detection method in a complete assay for the detection of proteins (BG). These final results are part of Paper VI.

5.4.1 Experimental

DNA circularisation was performed through padlock probe recognition of the synthetic DNA target and VC DNA [33]. Similarly, circularisation of the probe DNA was obtained through proximity ligation assay (PLA)[77] to recognise BG. Following circularisation of the probes, RCA process was run for 60 min to obtain coils containing around 1000 replicas of the sequence complementary to the probe and having a diameter of $500 - 1000$nm. Magnetic beads were then conjugated with DNA complementary to repeating sequence in the coil to form bead clusters.

For detection of synthetic DNA target 50 nm beads (Micromod) were mixed with coils to a final concentration of DNA coils $c = 200$ pM. The mixture was then incubated for 30 min at 70°C prior to measurements over PHEB sensor. Another sample with identical number of coils and beads was measured in the DynoMag system for reference. The data from DynoMag and PHEB sensor were normalised by the high frequency values of χ' and

V_2'' respectively , to approximate χ_∞ and V_∞ as described in [25]. Further details can be found in Paper V.

Coils from VC DNA detection were diluted in a two-fold dilution series to a final concentration of coils from $c = 256$ pM to $c = 1$ pM. Detection of BG spores was performed on sample containing from 50000 to 5 spores in a 10 fold dilution series. Therefore the detection of different concentration of BG is tested in a complete assay, including target detection, RCA amplification and Brownian relaxation measurements. The coils were then mixed with 80 nm BNF-Starch beads (Micromod) functionalised with single stranded DNA complementary to the repeated sequence of the coils. The mixture was incubated at 55°C for 30 min. The in-phase second harmonic signal V_2' were normalised by the unweighted average of the measured data value, to take into account variation over time of the amount of beads contributing to the signal. Further details can be found in Paper VI.

5.4.2 Results

First, the validation of the method by comparison of synthetic target DNA detection via PHEB and DynoMag measurements will be presented. Later the PHEB Brownian relaxation measurements of coils from VC DNA and BG spores will be presented.

5.4.2.1 PHEB biodetection of RCA products. Figure 5.7 show the relaxation measurement performed by **(a)** DynoMag and **(b)** PHEB sensor on beads binding to 200 pM RCA coils. Figure 5.7 shows the effect of coils on the relaxation of the beads in (a) Dynomag and (b) PHEB relaxation measurements. In presence of coils the low frequency value of χ' and V_2'' decreased and the peak value χ'' and V_2' decreased. The same relaxation frequencies were obtained for DynoMag and PHEB sensor systems.

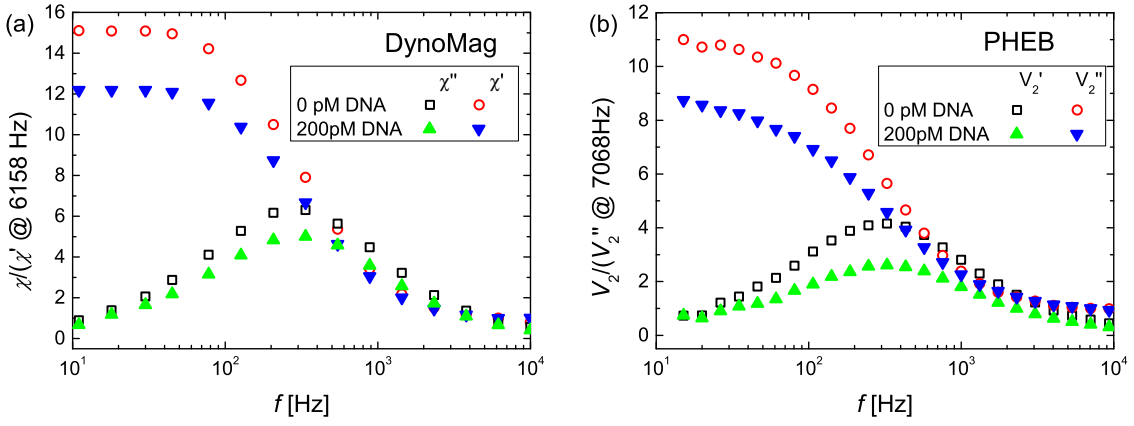

Fig. 5.7: **(a)** DynoMag relaxation measurement on 50 nm beads bound to 200 pM of DNA coils from rolling circle amplification (RCA) and negative reference with no coils. The signals were normalised by the high frequency, in-phase susceptibility χ'_∞. **(b)** PHEB relaxation measurement on identical samples. The signal was normalised by the high frequency out-of-phase signal V_∞. Adapted from Paper V.

5.4.2.2 Detection of *Vibrio cholerae*. Figure 5.8.a shows the second harmonic in-phase signal V_2' normalised by the unweighted signal average vs. sweeping frequency of the bias current. The measurement was performed on a two-fold dilution series of DNA coils formed by VC DNA recognition. The signal was measured 30 min after sample

injection into the microfluidic system. The low frequency signal is due to beads bound to DNA coils and the middle frequency signal is due to the free beads. The signal spectra can therefore be divided into three regions, where the behaviour for different coil concentration varied evidently: at low frequencies ($f < 35$ Hz) the normalised signal increased with coil concentration; at medium frequencies (35 Hz $< f <$ 2.7 KHz) the normalised signal decreased with coil concentration; at high frequency ($f > 2.7$ KHz) the normalised signal increased slightly with coil concentration.

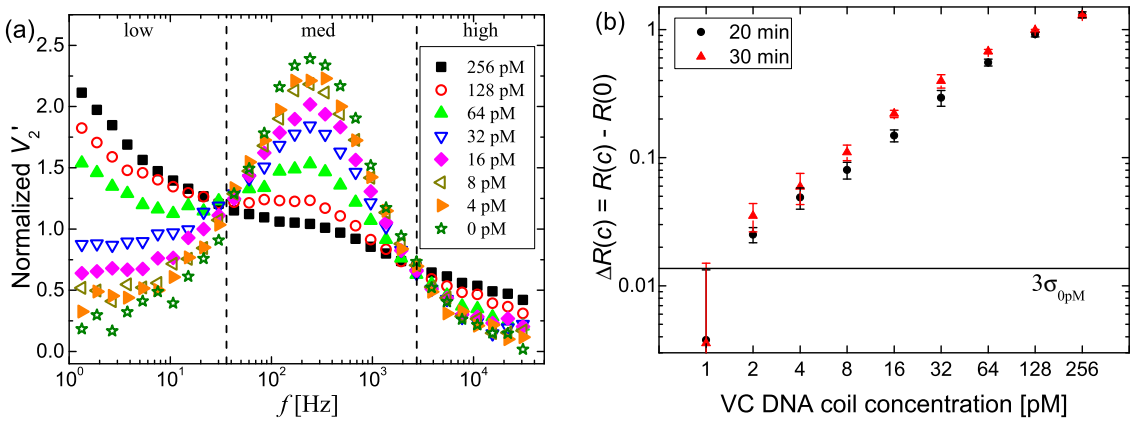

Fig. 5.8: **(a)** Second harmonic in-phase signal V_2' normalised by the unweighted signal average vs. frequency for sample with $c = 4 \rightarrow 256$ pM RCA coils from *Vibrio cholera* (VC) DNA. **(b)** Variation $\Delta R(c)$ of the ratio $R(c)$ between low and medium frequency signals vs. concentration of coils from VC. Ratios measured 20 min and 30 min after sample injection over the sensor. Adapted from Paper VI.

To quantify the coil concentration we calculated the ratio $R(c)$ between the signals at low and medium frequencies. Figure 5.8.b shows $R(c)$ as measured 20 min and 30 min after sample injection. Error bars are standard deviations from $n = 3$ repetition of the experiments in separate days. The horizontal line represents 3 standard deviation ($3\sigma_{0\text{pM}}$) of the negative reference signal, and therefore the smallest detectable signal. $R(c)$ was found to increase with increasing coil concentration. The smallest tested concentration giving a significant signal was found to be $c = 2$ pM while the signal begins to saturate at the highest tested concentration $c = 256$ pM. This gives a dynamic range of about two orders of magnitude and a limit of detection (LOD) of $\simeq 2$ pM. The signal ratio was also found to increase with longer waiting time after injection of the sample.

5.4.2.3 Detection of *Bacillus globigii* spores. This section presents the results obtained for coils produced by proximity ligation assay (PLA) of BG spores and following RCA. The assay was repeated on samples containing from 5 to 50000 spores in a ten-fold dilution series. Therefore this data are the result of a complete assay, and not the quantification of the readout system. Figure 5.9.a shows the normalised spectra and their behaviour followed roughly the same as VC data, with clear splitting of low, medium and high frequencies. Fig. 5.9.b shows the ratio $R(c)$ between the low and medium frequency regions of the spectra calculated for different number of spores. The error bars are standard deviation from $n = 3$ repetition of the experiments. The solid line in Fig. 5.9.b represents three standard deviation ($3\sigma_{0\text{pM}}$) of the negative reference signal. Also in this case LOD was found to decrease with increasing time from sample injection and the sample with 500 spores gave a signal ratio significantly different from the negative reference. The sample

with highest spore number showed saturation of the signal ratio.

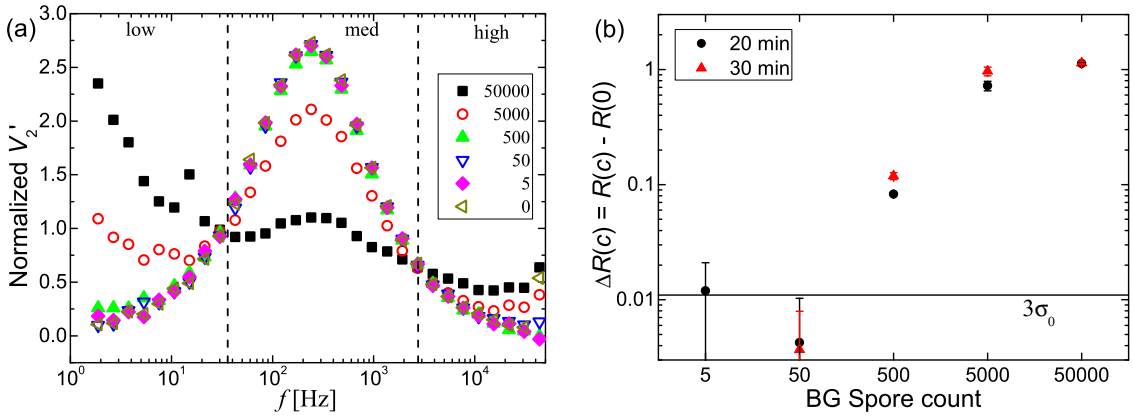

Fig. 5.9: **(a)** Second harmonic in-phase signal V_2' normalised by the unweighted signal average vs. frequency for sample with RCA coils from proximity ligation assay (PLA) of *Bacillus globigii* (BG) spores in starting number from 5 to 50000 spores. **(b)** Variation $\Delta R(c)$ of the ratio $R(c)$ between low and medium frequency signals vs. concentration of coils from BG. Ratios measured 20 min and 30 min after sample injection over the sensor. Adapted from Paper VI.

5.4.3 Discussion

The data from RCA of padlock probes binding to synthetic DNA allowed for comparison between the commercial DynoMag system and PHEB sensors for detection of DNA coils clustering magnetic beads. The clustered nano-beads relax at a frequency on the order of 1 Hz [36]. Therefore the bound magnetic beads are inactive at the investigated frequencies leading to a decreased low frequency value χ' and decreased peak of χ'' [25]. The same behaviour was found for the PHEB results in V_2'' and V_2' respectively.

The normalisation procedure was validated by Zardán Gómez de la Torre *et al.* [25] for the DynoMag system. Their measurement system is measuring the whole sample volume and is not affected by sedimentation. On the other hand, PHEB sensors are mostly sensitive near the sensor surface, therefore the amount of beads contributing to the signal might vary with time. This impacts positively the sensitivity of the assay as the relative coil concentration near the sensor increases upon sedimentation, but it requires a different analysis approach.

The normalisation applied for detection of VC DNA and BG spores uses the unweighted average signal from all the frequencies. With this normalisation it was possible to define three frequency regions in the signal spectra. When the concentration of RCA coils increases, the relative amount of free beads and hence the normalised signal at medium frequencies decreases. Correspondingly the relative amount of bound beads increases, leading to higher low frequency normalised signal. The comparison between this low and medium frequency regions allows us to quantify the concentration of RCA coils.

The PHEB sensor system was capable to detect down to 2 pM of RCA coils from VC, over a range of two orders of magnitude. It should also be noted that LOD and dynamic range can be tuned by varying the magnetic bead concentration. The system was also capable of distinguish as few as 500 BG spores in an assay.

To compare with commercial devices, Zardán Gómez de la Torre *et al.* [25] studied detection of RCA coils from VC DNA using the commercial DynoMag susceptometer.

For that system they found a LOD of 4 pM and similar dynamic range as the PHEB sensor. The same authors also studied RCA coils from BG spores [74] finding a LOD of 500 spores for samples prepared in the same way as in this study. Therefore the magnetoresistive platform was found to offer LOD and dynamic range similar to or even better than the available commercial system. The sensor system has the advantage of being smaller and better suited for integration in a microfluidic setup with sample processing and can measure on a smaller sample volume.

5.5 Conclusion

We have demonstrated that PHEB sensor can be used to measure hydrodynamic diameter of magnetic beads both in the time and frequency domain. Both techniques have been carefully characterised. This allowed us to identify the weak spots of the detection technique. Time domain measurement demonstrated to be of high interest because of the speed of the technique, allowing for almost real-time monitoring of the clustering process.

We compared our technique with one commercially available device (DynoMag) in detecting synthetic target, VC DNA and BG spores. In all cases we were able to obtain result as good as or better than those obtained in DynoMag with a much larger sample volume. This shows that PHEB sensor have the potential to be the platform of choice for Brownian relaxation measurements of RCA products.

CHAPTER 6

Surface-based DNA analysis

The vast majority of systems to detect surface bound DNA employ an end-point reading to detect hybridisation. For example in DNA microarrays hybridisation of DNA target to surface bound probes is followed by washing of unbound targets and only then the fluorescent signal is read into a scanner. This is done because the background fluorescence signal would not allow for a real time readout.

We have seen in Section 2.2.2 that PHEB and dPHEB are mostly sensitive to beads near the sensor surface, and that dPHEB could be used to implement a local reference for subtracting the signal of suspended beads. Our sensors are also capable of measuring with a rate of 3 points/s, allowing for real time monitoring of surface binding of target.

In this chapter we test this hypothesis. First, we use the biotin-streptavidin link as a model binding to compare detection of surface bound beads on PHEB and dPHEB sensors. Then we will test dPHEB capabilities in detecting DNA hybridisation and genotyping single nucleotide polymorphism (SNP) through stringent washing. This result are part of Paper VII.

Then, we use our system to study the denaturation of surface bound DNA targets by means of ramping temperature and ramping stringency of washing buffer. These results are part of ongoing work and are presented here for the first time.

6.1 Sensor response to surface-bound beads

A comparison of PHEB and dPHEB sensor geometries was performed to establish the best configuration for measurement of surface-tethered magnetic beads. The beads were bound to one to four of the sensing arms as depicted in Fig. 6.1. The bead signal was measured both in a background of suspended beads and after washing the unbound beads.

6.1.1 Experimental

The sensors had nominal stack Ta(15)/ $Ni_{80}Fe_{20}$(30)/ $Mn_{80}Ir_{20}$(10)/ Ta(5) (dimension in nm). They were functionalised as described in Section 3.4.2 with biotinylated DNA probes to provide a direct binding site to streptavidin coated magnetic beads. In this section and in this whole chapter the used beads are Streptavidin MicroBeads (Miltenyi Biotec) of nominal diameter 50 nm. Figure 6.2 shows a schematic of the assay. A volume of 15 µL stock solution of beads was injected and incubated for 20 min at room temperature. The sensors were then washed with 1 × PBS at a flow rate 200 µL/min.

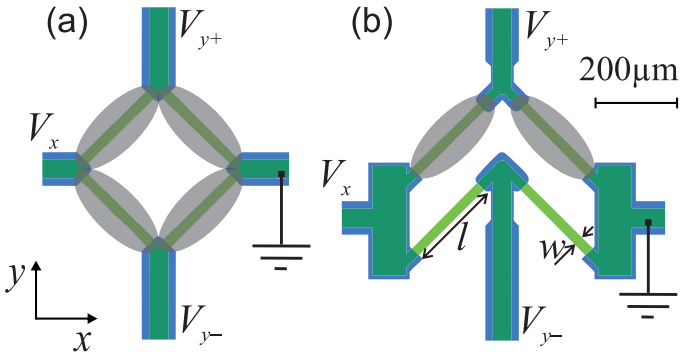

Fig. 6.1: Schematic illustration of the spot position over sensor arms. **(a)** PHEB sensor, up to four sensing arms were functionalised with biotinylated DNA (grey). **(b)** On the dPHEB sensor only the two top arms can be functionalised with biotinylated DNA (grey), the bottom arms are retained as local reference. Both sensor types are inserted in a microfluidic channel (width 1 mm). The injected sample covers the whole sensor surface. Adapted from Paper VII.

6.1.2 Results

The sensor second harmonic out-of-phase signal variation ($\Delta V_2'' = V_2''(t) - V_2''(t=0)$) was measured for both PHEB and dPHEB sensor geometries, with an increasing number of functionalised arms. The signal was measured before and after washing. Before washing, the measurements were carried out in the presence of a suspension of magnetic beads over the sensors. Fig. 6.3 shows $\Delta V_2''$ vs. the number of sensor arms functionalised with biotinylated DNA. For both PHEB (squares) and dPHEB (triangles) geometries the signal increased linearly with the number of functionalised arms in accordance with Eq.(2.43) and Eq.(2.46).

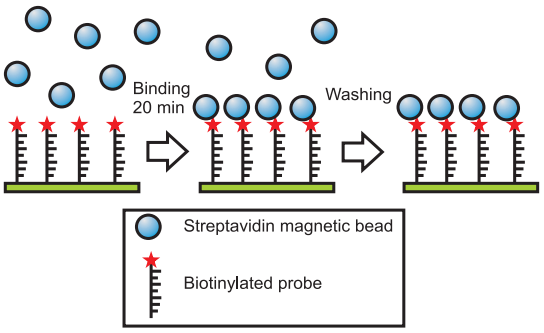

Fig. 6.2: Schematic representation of the direct binding of streptavidin magnetic beads to the sensor surface functionalised with biotinylated DNA probes. The binding was performed for 20 min at room temperature, followed by washing with 1 × PBS. Adapted from Paper VII.

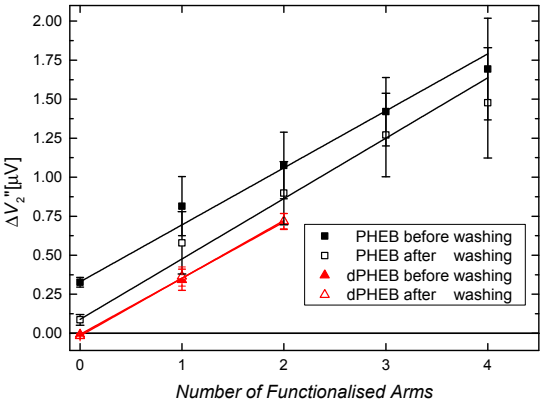

Fig. 6.3: Second harmonic out-of-phase signal variation ($\Delta V_2''$) vs. number of functionalised arms. The signal before washing was measured in a background of suspended magnetic beads. Washing removed all the beads from the fluidic system. Error bars are standard deviation from $n = 3$ repetition of the experiment. Adapted from Paper VII.

The PHEB geometry is sensitive to a suspension of beads, showing a non-zero signal for the non-functionalised sensor (before washing). Washing was found to reduce but not to eliminate this signal. The signal vs. number of functionalised arm before and

after washing was found to be linear with the same slopes for PHEB geometry but with significantly different offsets.

For the dPHEB geometry (triangles in Fig. 6.3) only the two upper sensor arms were functionalised and the bottom arms were used as local reference. In this case no offset was observed and the signal measured before and after washing were perfectly overlapping. The slope was identical to the one of the corresponding PHEB geometry. Finally, the standard deviation from repeated experiments ($n = 3$) on dPHEB geometry was found to be about four times smaller than that observed for PHEB geometry.

6.1.3 Discussion

Using the strong biotin-streptavidin bond it was possible to study the signal from surface-bound beads independently from the washing conditions. This was done for both PHEB and dPHEB geometries and the signal was found, in accordance with theory, to be proportional to the number of functionalised arms. With only two functionalised arms the maximum signal from the dPHEB geometry can reach only half of the equivalent PHEB geometry. However, the PHEB sensor signal is hampered by the effects of the beads in solution and unspecifically bound to the sensor surface giving a non-zero offset that cannot be eliminated by washing. Opposedly, in the dPHEB sensor the two non-functionalised arms are used as local negative reference, resulting in the signal being independent from the bead suspension background. Moreover the dPHEB sensor signal showed a much lower standard deviation than the corresponding PHEB. We speculate that this could be an effect of the proximity of the local reference arm to the sensing arm. This geometrical proximity exposes the two parts of the sensor to nearly identical environmental conditions like bead distribution, temperature and external magnetic field. In this way the *environmental* parameters are effectively cancelled out in the dPHEB sensor. For these reasons, the dPHEB sensor geometry is the choice for surface-based assay and it is used in the rest of this chapter.

6.2 DNA hybridisation assay

In this section the magnetic beads are bound to the sensor surface through hybridisation of biotinylated DNA target to complementary surface bound DNA probes. The target DNA concentration was varied from 40 nM to 0.156 nM to establish the limit of detection of our system. The DNA hybridisation was monitored in real-time, with the presence of target and streptavidin magnetic labels over the sensor surface. This was possible by using the local reference of dPHEB sensors.

6.2.1 Experimental

The sensors had nominal stack Ta(15)/ $Ni_{80}Fe_{20}$(30)/ $Mn_{80}Ir_{20}$(10)/ Ta(5) (dimension in nm). The dPHEB sensors were functionalised as shown in the inset in Fig. 6.5.a with WT probe for CD 8/9 mutation site of HBB gene (probe and target sequences described in Section 3.3.2). Biotinylated WT target was diluted in 2×SSC+0.05%SDS in a five-fold dilution series. The target solution was mixed $1:1\,v/v$ with stock bead solution (streptavidin 50 nm, Milteny), to final DNA concentrations ranging from 0.156 nM to 40 nM .

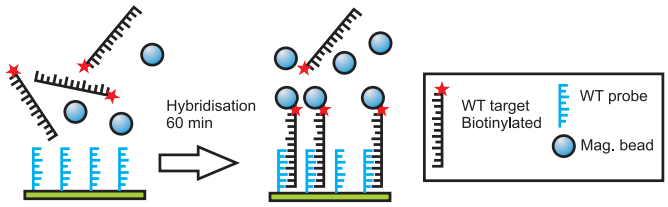

Fig. 6.4: Schematic of the hybridisation assay. Target and magnetic beads are injected over the sensor. During incubation for 60 min at 37°C the biotinylated WT target DNA hybridise to the CD 8/9 WT surface probes. The magnetic beads are bound to the surface through the biotinylated target DNA. Adapted from Paper VII.

The mixture of target and beads was injected over the sensor (Fig. 6.4) and incubated at 37°C for 60 min under stagnant condition. The second harmonic out-of-phase signal variation ($\Delta V_2''$) was measured during the whole incubation period.

6.2.2 Results

Fig. 6.5.a shows the second harmonic out-of-phase signal variation ($\Delta V_2''$) vs. time during incubation of WT target DNA and magnetic beads. The use of a dPHEB sensor allowed for monitoring the hybridisation signal in real-time during the 60 min reaction, in the presence of magnetic particle suspended in the target solution. After sample injection at $t = 0$, $\Delta V_2''$ increased for all investigated concentrations. For the highest concentrations the signal tended to level off for long times. The signal from the sample with no DNA showed small fluctuations around 0 µV with an amplitude of around 3 times the sensor noise. The smallest investigated concentration ($c = 156$ pM) was found to be still discernible from the negative reference.

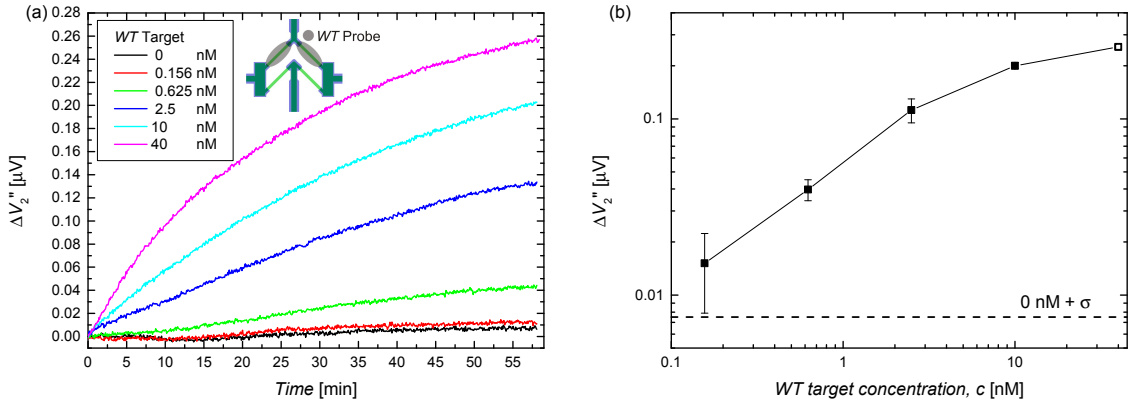

Fig. 6.5: **(a)** Second harmonic out-of-phase signal variation ($\Delta V_2''$) measured vs. time for repeated experiments with varying WT target DNA concentration. **(b)** Final value of $\Delta V_2''$ vs. WT target concentration as measured after 60 min incubation, error bars are standard deviation from repeated experiments ($n = 3$) except for $c = 40$ nM ($n = 1$), dashed line represent the value obtained with negative sample (0 nM) plus one standard deviation. Adapted from Paper VII.

The maximum signal $\Delta V_2''$, measured after 60 min hybridisation, is plotted in Fig. 6.5.b vs. WT target DNA concentration. The error bars are standard deviation from repeated experiments ($n = 3$). The dashed line is the average signal from three experiments with no DNA target ($\Delta V_2'' = 4.5$ nV) plus one standard deviation ($\sigma = 3.1$ nV).

This line represents the threshold level for detection; the smallest tested concentration ($c = 156$ pM) gave a signal significatively higher than this threshold. For the maximum concentration ($c = 40$ nM) the signal level after 60 min of hybridisation reached a value of $\Delta V_2'' = 0.25$ μV, which is about one third of the maximum signal observed for the direct streptavidin-biotin link. This could be the effect of a higher affinity of the streptavidin-biotin bond and of the more complex reaction dynamics when both target and magnetic beads are in suspension.

6.2.3 Discussion

The DNA hybridisation assay with the dPHEB sensor allowed for detection of target DNA with an estimated limit of detection (LOD) of $c = 156$ pM with a dynamic range of two orders of magnitude. DNA hybridisation was monitored in real time, in presence of a suspension of magnetic beads; this was possible by using the local reference of dPHEB sensors. The LOD and dynamic range that we obtained are well suited with the detection of DNA products from amplification process such as polymerase chain reaction (PCR).

The golden standard for DNA detection is at present DNA microarrays. The DNA hybridisation to capture probes tethered on glass substrate is quantified using an end-point fluorescence readout. The detection limit of commercially available microarrays is typically of $1 - 10$ pM and depends on hybridisation time, slide material and capture probes used. Typically the hybridisation time for a microarray experiment is in the range of $8 - 10$ hours, compared to the 60 min of the system presented. A dynamic range of two orders of magnitude is similar to what is found for colorimetric enzymatic assays [42, 43]. This dynamic range is sufficient for SNP detection [43]. The advantages of our method over microarrays and colorimetric detection are the integration of microfluidic system to flexibly control reaction conditions, the integrated voltage readout of the signal and the ability to perform real-time measurements of hybridisation and denaturation in a background of magnetic particles. In the next section we will discuss how real-time detection can be employed to improve SNP genotyping.

Other systems have been proposed for DNA hybridisation assays, in particular Xu *et al.* [44] demonstrated detection of 10 nM of PCR products using magnetic particles as labels for an end-point detection of DNA hybridised to a spin valve sensor.

Other chip based methods were demonstrated to detect hybridisation in real-time, including surface plasmon resonance(SPR) [45], quartz crystal microbalance (QCM) [46] and film bulk acoustic resonators (FBAR) [45]. These method are intrinsically hampered by the unspecific binding of the sample matrices on the sensor surface, limiting the LOD to about 1 nM [45, 46]. Opposedly, there is virtually no magnetic signal from biological samples. Moreover, dPHEB sensors, with their local negative reference, effectively cancel out contribution of unspecifically bound targets and magnetic labels in suspension.

6.3 SNP genotyping

The real time capabilities of dPHEB sensors were tested for SNP detection. The mutations investigated were CD8/9 and CD17 from the *human beta globin* (HBB) gene (Section 3.3.2). These locations were chosen because capture probes for this mutation sites have been subject of previous characterisation using DNA microarray from Petersen *et al.* [58] under varying washing conditions.

6.3.1 Experimental

The dPHEB sensors had nominal stack Ta(15)/ $Ni_{80}Fe_{20}$(30)/ $Mn_{80}Ir_{20}$(10)/ Ta(5) (dimension in nm). Two sensor on the same chip were functionalised with WT and MT capture probes as shown in the inset of Fig. 6.8.a. Two chips were employed to investigate two mutation sites, namely CD8/9 and CD17 (probe and target sequences described in Section 3.3.2). Target DNA was prepared in a 10 nM solution in 1×SSC+0.025%SDS. For the different experiments, 10 µL of solution of WT, MT and 1:1 mixture of WT:MT targets was mixed with 10 µL of stock solution of magnetic beads (streptavidin coated 50 nm, Milteny) and injected on the sensor surface.

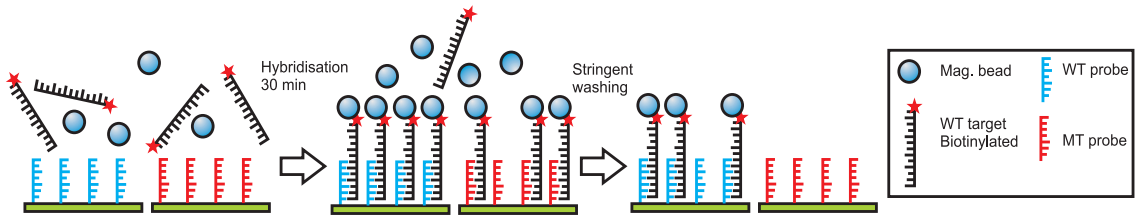

Fig. 6.6: Schematic of the assay employed for SNP detection. The two sensors are functionalised with WT and MT probes respectively. Target and magnetic beads are injected over the sensor and incubated for 30 min at 37°C. The mismatched hybrids are denatured by a stringent washing. Adapted from Paper VII.

Figure 6.6 shows the assay work-flow. Target DNA and magnetic beads were incubated for 30 min at 37°C. After incubation a stringent washing was employed to decrease unspecific binding (i.e.: denature mismatched duplexes). The sensors were washed with 0.05×SSC+0.05%SDS for 80 s at a flow-rate of 30 µL/s and then left stagnant. The signals from the two sensor were then analysed in terms of the normalised ratio of the signals:

$$NR = \frac{\Delta V_2''[WT]}{\Delta V_2''[WT] + \Delta V_2''[MT]} \tag{6.1}$$

Here $\Delta V_2''[WT]$ and $\Delta V_2''[MT]$ are the second harmonic out-of-phase signal variations of the sensors functionalised with WT and MT probes, respectively. This normalised ratio approaches $NR = 1$ when the target-beads complexes are linked only to the WT probes, and $NR = 0$ when they are linked to the MT probes.

6.3.2 Results

Figure 6.7 shows the signal variation $\Delta V_2''$ vs. time for the sensors functionalised with WT and MT probes for the CD8/9 mutation when WT target, MT target and a mixture of WT+MT targets were employed. During hybridisation (in low stringency condition) the hybridisation on the two sensors were found to be identical. Only after washing (higher stringency) the mismatched DNA duplexes (e.g.:WT target on MT probe) were denatured and the different target compositions could be identified.

In Fig. 6.8 results of repeated experiments ($n = 3$), as the ones in Fig. 6.7, are presented in terms of normalized ratio NR for mutation CD8/9 (Fig. 6.8.a) and CD17 (Fig. 6.8.b). Figure 6.9 shows the average of NR from 3 repeated experiment as measured (Fig. 6.9.a) immediately before washing and (Fig. 6.9.b) at the time at which the separation of NR between the target is maximum: 30 min after washing for mutation CD8/9 and 2 min after washing for CD17.

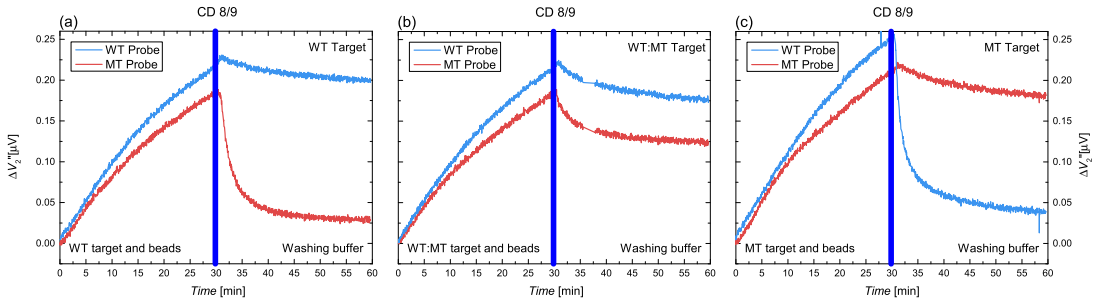

Fig. 6.7: $\Delta V_2''$ vs. time measured on two sensor functionalised with WT and MT capture probe for CD8/9 mutation site. Signal was monitored in real-time during hybridisation of **(a)** WT,**(b)** 1:1 mixture of WT:MT and (**c**) WT targets and subsequent washing and denaturation of mismatched hybrids in higher stringency. Adapted from Paper VII.

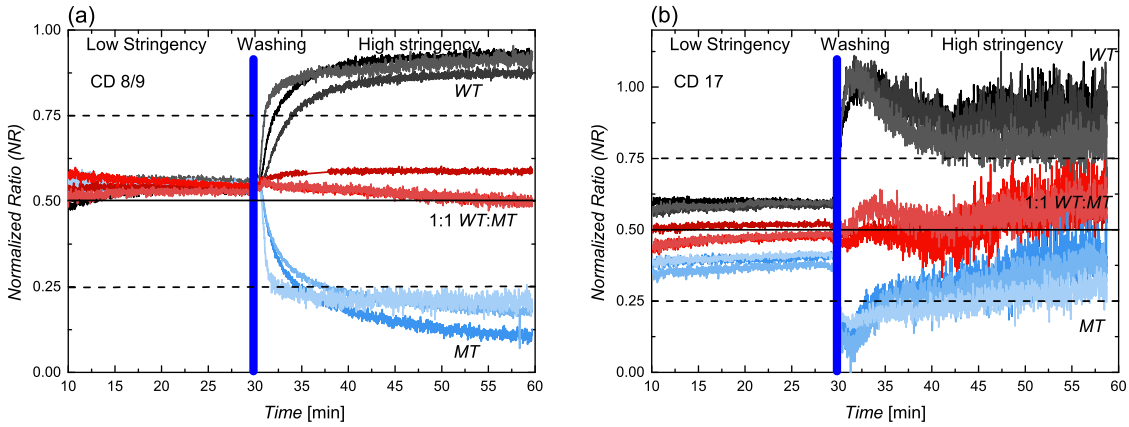

Fig. 6.8: Normalised ratio of the sensor signal variation (NR) vs. time for **(a)** CD8/9 and **(b)** CD17 mutation sites. The signal was measured during hybridisation and following washing. Three target compositions were tested, namely WT target, MT target and 1:1 mixture of WT:MT targets. Each experiment was replicated $n = 3$ times. Adapted from Paper VII.

During hybridisation ($t < 30$ min in Fig. 6.8), NR was found to approach $NR = 0.5$ for all target combinations, corresponding to identical hybridisation on WT and MT capture probes, due to the low stringency condition. For CD8/9 we found $NR \simeq 0.54$ for all target compositions (Fig. 6.8.a and Fig. 6.9.a). For CD17, during hybridisation (Fig. 6.8.b and Fig. 6.9.a), the three targets differed slightly during hybridisation and we found $NR = 0.591(6)$ (WT target), $NR = 0.49(2)$ (1:1 WT:MT target) and $NR = 0.39(2)$ (MT target). After washing, the stringency was higher and the mismatched duplexes denatured at a faster rate compared to the perfect matched counterparts. In particular, for mutation CD8/9 NR values stabilized in 10 min after washing to values above 0.8 and below 0.2 for WT and MT targets, respectively (Fig. 6.8.a and Fig. 6.9.b). For CD17, the maximum separation of the values of NR for the different targets was reached 2 min after washing. For longer times, the signals from both MT and WT capture probes vanished, increasing therefore the standard deviation of NR for longer times (Fig. 6.8).

Figure 6.9.b shows the average values of NR for $n = 3$ repetition of the experiments for each target composition, as measured 30 min (CD8/9) and 2 min (CD17) after washing. The dashed lines $NR = 0.25$ and $NR = 0.75$ mark the threshold values chosen for the differentiation of the target composition. The choice of time after washing, in combina-

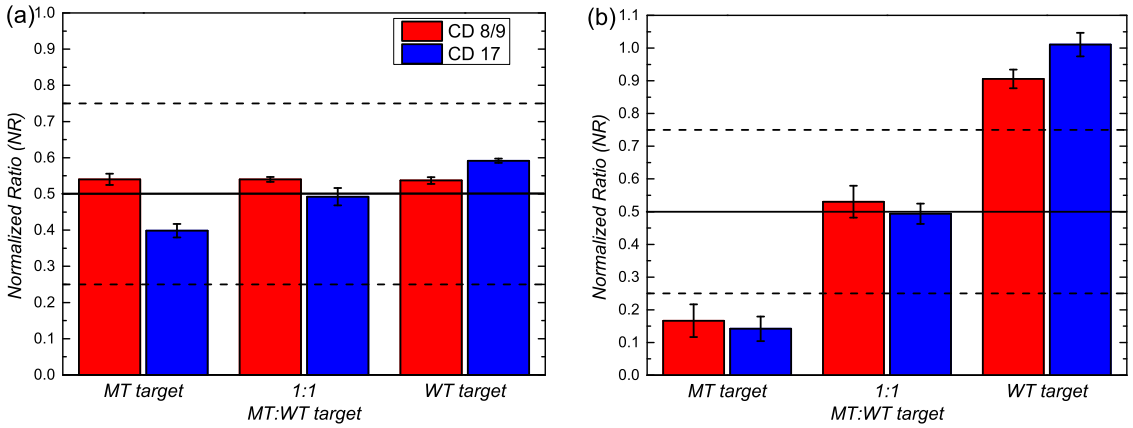

Fig. 6.9: Normalised ratio of sensor signal (*NR*) measured for the different target ratios. The sensor were functionalised with capture probes for CD8/9 (red) and CD17 (blue) mutation sites. Signals were measured after **(a)** 30 min incubation and **(b)** 30 min (CD8/9) or 2 min (CD17) after washing in stringent buffer. The error bars are standard deviation from $n = 3$ repetitions of the experiments. Adapted from Paper VII.

tion with the threshold used, allowed us to identify correctly the sample target in every experiment.

6.3.3 Discussion

The dPHEB sensors were tested for their capability of detecting SNP employing a stringent washing. The washing buffer used (0.05×SSC+0.05%SDS) allowed for discrimination of both mutation sites. Petersen *et al.* [58] tested the influence of washing stringency for genotyping this mutations. In their findings, the working range of washing stringency for mutation CD8/9 include the condition used here. For the CD17 mutation, higher stringency was found to give lower reproducibility of *NR* due to signal loss, in agreement with what we found here. While the signal for CD8/9 reaches a stationary state after washing that allows for target genotyping, for CD17, at this stringency, both matched and mismatched duplexes were denatured in less than 10 min after washing. With such a rapid signal loss, an end-point detection (like in a microarray) would have failed to genotype the SNP. In this work we used the real time data obtained from dPHEB measurements to genotype CD17 mutation in a stringency higher than the optimal one identified by Petersen *et al.* [58]. It was possible to determine the time at which the signal for the various targets differed the most. For the CD8/9 mutation in this washing condition this corresponded to the stationary state after washing (reached in around 10 min), for the CD17 mutation the highest separation was seen after just 2 min from washing. Moreover, the real-time data can be used, in future studies, to obtain kinetic data and for optimising SNP genotyping. This information can be used both for speeding up the readout of this assay, and in general to optimise probe design for standard microarray assays.

6.4 DNA denaturation in stringency and temperature gradients

The possibility of measuring real-time signal, combined with the microfluidic sample handling and temperature control system integrated in our setup paved the way for hybridisation measurement in varying stringency and temperature conditions. In this section the denaturation of target-capture probe hybrids will be driven by either increasing temperature or decreasing Na^+ ionic concentration of the washing buffer. The obtained melting curve and ionic concentration denaturation were performed under varying combined temperature and concentration conditions, to find the most favourable experimental conditions. This work on the characterisation of denaturation profile is in preparation of future work, where these two techniques will be used to enhance SNP genotyping.

6.4.1 Experimental

This work was performed on sensor with nominal stack Ta(5)/ $Ni_{80}Fe_{20}$(30)/ $Mn_{80}Ir_{10}$(20)/ Ta(5) (thicknesses in nm). To characterise the reproducibility of measured denaturation curve in temperature and stringency gradients, three sensors on the same chip were functionalised as in Fig. 6.10. The central sensor was functionalised with a reference biotinylated probe and two sensors were functionalised with the WT and MT capture probes for the CD17 mutation. A fourth sensor was functionalised with WT and MT capture probes on the top and bottom halves of the sensor respectively, to take full advantage of the differential capabilities of the dPHEB sensors.

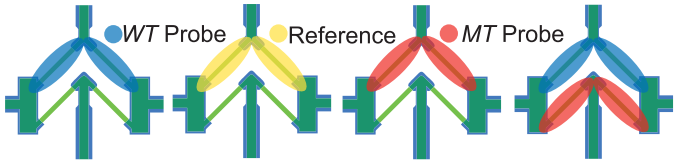

Fig. 6.10: Probe patterning for denaturation studies. Sensor are functionalised with WT, MT and positive reference DNA capture probes. One sensor is functionalised with both MT and WT capture probes

Biotinylated target was diluted and mixed with streptavidin coated magnetic label (50 nm, Milteny) to a final target concentration of 5 nM in 2×SSC ($c(Na^+)$ = 400 mM) hybridisation buffer. The sample was incubated in the sensor microfluidic system at 37°C for 30 min. For temperature ramping the chip was first washed at 20°C for 80 s at a flow rate of 30 µL/min with diluted SSC washing buffer to a final $c(Na^+)$ = 10 mM or 2 mM. The temperature was then ramped from 20°C to 70°C at 0.1°C/s and backwards. For ionic concentration denaturation, the chip was washed with 2×SSC ($c(Na^+)$ = 400 mM) at 30°C or 40°C. The buffer concentration was then varied exponentially from $c(Na^+)$ = 400 mM to $c(Na^+)$ = 0.4 mM in 1200 s.

6.4.2 Results

In this section the results of the various experimental approaches to denaturation in ionic concentration and temperature gradients will be presented. The two paragraphs contain the validation of the method for temperature and ionic concentration profiles respectively; for this denaturation of WT target and CD8/9 capture probes were used as a test case.

6.4.2.1 Ramping temperature. Ramping temperature from 20°C to 70°C was employed to measure melting curve on-chip. The melting was performed in two different Na^+ ion concentrations, $c(Na^+) = 10$ mM or 2 mM. The results of the experiments are shown in Fig. 6.11.

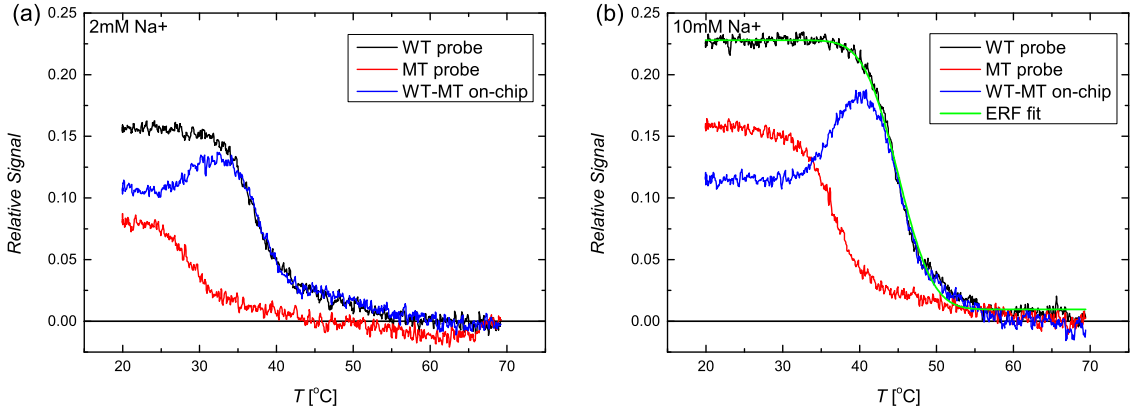

Fig. 6.11: Melting curve for WT target on CD8/9 capture probes performed at **(a)** $c(Na^+) = 2$ mM and **(b)** $c(Na^+) = 10$ mM. Signals from perfectly matched WT target-WT probe duplexes (black), mismatched WT target- MT probe duplexes (red) and differential signal between matched and mismatches duplexes (blue) measured on-chip. In green is plotted the result of error function fit to the data.

The signals before temperature ramping were higher when washing with a higher ionic strength buffer (Fig. 6.11.b), indicating a partial loss of surface bound target for both WT and MT sensors. The relative signal showed a steady value at low temperature and a clear inflexion point with the loss of all the signal. The melting profile obtained in this way could be fitted with the error function (ERF) in Eq.(3.7) as described in Section 3.4.4 to extract the melting temperature T_m. An example of the quality of the fitting can be seen in Fig. 6.11.b for the sensor functionalised with WT probe. The other fits were of comparable quality. The mismatched duplexes (WT-MT target-probe) showed a smaller T_m than the perfectly matched counterpart and in general the melting temperatures are lower at higher stringency ($c(Na^+) = 2$ mM). Three repetitions of each experiment were performed to test reproducibility. The results of these are summed up in Tab. 6.1, the numbers in parenthesis are standard deviations ($n = 3$). From the values of the standard deviations in Tab. 6.1 we see that the difference between melting temperatures $\Delta T_m = T_m^{WT} - T_m^{MT}$ was more reproducible than the absolute value of T_m, with $\sigma(\Delta T_m) = 0.5$°C and $\sigma(T_m) \simeq 2.5$°C for $c(Na^+) = 2$ mM. Since only the temperature of the sensor was controlled in our setup, this variation of absolute values of T_m may be attributed to environmental changes of the temperature of the washing buffers employed.

,

6.4.2.2 Ramping ionic concentration. An exponential ramping of the washing buffer concentration from $c(Na^+) = 400$ mM to $c(Na^+) = 0.4$ mM was employed to denature the DNA hybrids at a constant temperature. Two temperatures were tested 30°C and 40°C. The results of the ionic concentration denaturation experiments are shown in Fig. 6.12. The results are presented for decreasing ionic concentration to resemble a melting curve and the actual time evolution of the signal.

The signal from both perfectly matched (WT-WT target-probe) and mismatched (WT-

Tab. 6.1: Fitting parameter T_m and $\log(c)$ as obtained from ERF fitting of the denaturation profiles. The difference from WT and MT probes are calculated for each dataset. The numbers in parenthesis are standard deviation from $n = 3$ repetitions of each denaturing condition.

T[°C]	c[mM]	WT sensor	MT sensor	$\lvert WT - MT \rvert$
$20 \rightarrow 70$	2	$T_m = 38(2)$°C	$T_m = 29(2)$°C	$\Delta T_m = 8.9(5)$°C
$20 \rightarrow 70$	10	$T_m = 43(1)$°C	$T_m = 35(1)$°C	$\Delta T_m = 7.7(2)$°C
30	$400 \rightarrow 0.4$	$\log(c_m) = 0.17(8)$	$\log(c_m) = 0.80(4)$	$\Delta \log(c_m) = 0.62(6)$
40	$400 \rightarrow 0.4$	$\log(c_m) = 0.76(2)$	$\log(c_m) = 1.20(5)$	$\Delta \log(c_m) = 0.45(5)$

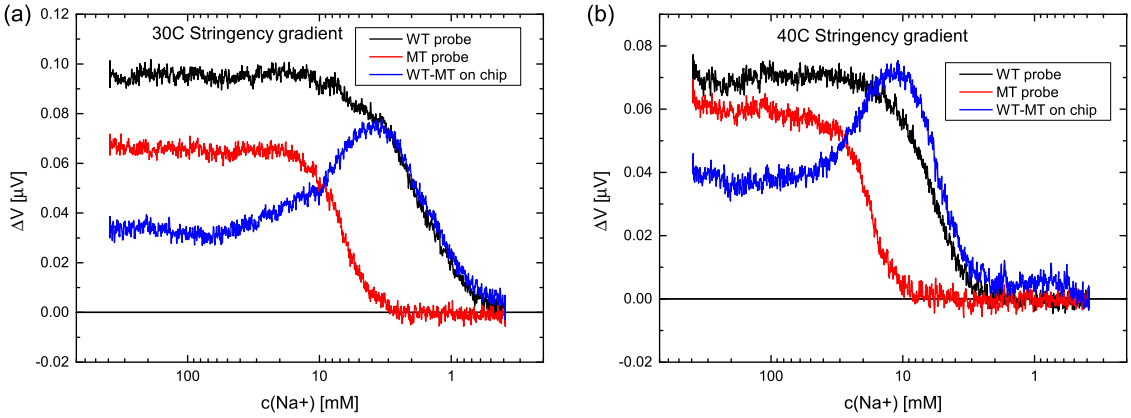

Fig. 6.12: Ionic concentration denaturation of WT target bound to CD8/9 capture probes performed at **(a)** $T = 30$°C and **(b)** $T = 40$°C. On x-axis the concentration is mapped logarithmically and decreasing, to reflect the time evolution of the experiment. Signals from perfectly matched WT target-WT probe duplexes (black), mismatched WT target-MT probe duplexes (red) and differential signal between matched and mismatches duplexes (blue) measured on-chip.

MT target-probe) hybrids was found to be constant for a wide range of high concentrations. At a concentration c_m the signal decreased fast and became null. The matched hybrids were found to denature at a lower concentration and in general c_m was found to be higher at higher temperature (40°C). The signals could be fitted with an ERF to obtain the denaturing concentration in terms of $\log(c_m)$. The parameter of interest to distinguish matched and mismatched duplexes is $\Delta \log(c_m) = |\log(c_m^{WT}) - \log(c_m^{MT})|$. The denaturation experiments were repeated $n = 3$ times and the results are summed up in Tab. 6.1. The values in parenthesis are standard deviations. Using the ionic concentration profile the obtained values of $\log(c_m)$ and $\Delta(\log(c_m))$ had similar standard deviation $\sigma(\log(c_m)) \simeq 0.05$, showing a high reproducibility of the stringency conditions between experiments.

6.4.3 Discussion

The dPHEB sensors were used to perform melting curve and ionic concentration denaturation measurement in continuous variation of temperature and buffer stringency. Both approaches were tested in our on-chip system and allowed us to measure reliably T_m and c_m for surface-bound hybrids. The temperature gradient method demonstrated a high reproducibility in the difference between melting temperatures ($\sigma(\Delta T_m) = 0.2$°C) but lacked of reproducibility on the absolute values of T_m. The ionic concentration profile

technique instead showed similar reproducibility for absolute values of $\log(c_m)$ and differential value $\Delta\log(c_m)$. The two methods can be directly compared in terms of signal to noise ratio (*SNR*) of the ΔT_m and $\Delta\log(c_m)$ defined as $SNR = \Delta T_m/\sigma(\Delta T_m)$ and $SNR = \Delta\log(c_m)/\sigma(\Delta\log(c_m))$. These parameters tell how good the resolution of the system is in distinguishing a single point mutation. For the temperature denaturation the best conditions are at $c = 10$ mM giving $SNR \simeq 40$ and for the ionic concentration denaturation both conditions gave similar resolution with $SNR \simeq 10$. Although the temperature gradient assay has the highest *SNR* it has to be kept in mind that this requires the use of a positive reference signal, and moreover that working at a single temperature greatly simplifies the assay.

Although the resolution and reproducibility of these techniques are lower than the state-of-the-art high resolution melting (HRM) in tube, the magnetoresistive sensing provide an integrated and unique platform for denaturation analysis of surface tethered DNA duplexes. Moreover, it is possible for these sensors to work with multiple probes in a single experiment, using multiple sensors with different functionalisation. Finally, the limit in resolution could be improved by optimising sensor geometry and experimental conditions.

6.5 Conclusion

In this chapter we applied the PHEB and dPHEB sensors to detection of magnetic particles bound to the surface of the sensor. The dPHEB sensors were found to give the most reproducible signal upon binding of magnetic beads on the surface. Their local reference was effective in cancelling the background of beads in solution. They are therefore the choice for detection of surface bound beads.

For this system DNA had a LOD of $c = 156$ pM with a dynamic range of two orders of magnitude. This was reached with a hybridisation time of only 1 h.

The dPHEB is capable of measuring the bound beads in real time. This characteristic was employed to genotype two SNP in our target. The real time approach was found superior to standard end-point detection since it could provide reliable results also in less than optimal washing conditions.

Finally, the system was used to perform DNA denaturation on chip. The signal of bound DNA was measured in ramping temperature and ramping stringency of the washing buffer. In this way the system proved flexibility in controlling experimental condition and the ability to measure the denaturation in real-time. In particular, we notice that the denaturation in a gradient of buffer stringency is a novel approach that was possible thanks to the unique characteristics of our magnetic system.

CHAPTER 7

Conclusion and Outlook

The application of PHEB magnetic field sensors to biosensing was investigated in this thesis. We performed measurements of magnetic beads without the need for external magnetic field sources, but using the field induced by the sensor bias current. We derived the sensor signal for the additive PHEB geometry and the differential dPHEB geometries.

We characterised the magnetic sensors for effects induced by heating up to 90°C. We were able to separate reversible and irreversible effects of heating on the magnetic properties of the sensor stack by fitting our theoretical model to the sensor signal vs. magnetic field. We tested a low-temperature annealing procedure that decreased the temperature induced irreversible effect by almost 60%.

We demonstrated the use of PHEB sensors on measurements Brownian relaxation of magnetic beads in both frequency and time domains. Measurements of Brownian relaxation allowed us to extract reliably bead diameter at concentrations down to 16 µg/mL for 40 nm beads. The setup could measure Brownian relaxation from DC to 1 MHz and on beads with hydrodynamic diameters ranging from 10 nm to 250 nm. We identified problems in the measurement given by sedimentation over time of magnetic beads. In our setup the beads near the surface give higher output, therefore bead sedimentation makes the signal increase over time.

We have demonstrated time-domain bead relaxation measurements using PHEB sensors. This technique offers faster sampling rate, paving the way for real-time monitoring of the experiments. We applied both techniques to detect bBSA in the nM range.

Frequency domain measurements were used to detect RCA products (DNA coils) from detection of *Vibrio cholerae* (VC) DNA by padlock probe recognition and *Bacillus globigii* (BG) spores by proximity ligation assay (PLA). We demonstrated a LOD for such assay of 4 pM of coils (VC) and of 500 spores (BG).

We applied the differential geometry of the dPHEB to measure surface-bound magnetic beads. We characterised this sensing scheme using the biotin-streptavidin link. Doing so we demonstrated that the differential sensor, with its local reference arms, cancel accurately the contribution of background solution beads and beads unspecifically bound to the surface. We applied the dPHEB geometry for the detection of DNA in a hybridisation assay. We demonstrated a LOD of 156 pM DNA target upon one hour of hybridisation. We notice that this LOD is far from the optical microarray capabilities, although in a microarray the hybridisation is typically run for several hours. We used the real-time detection on our dPHEB sensor to perform single nucleotide polymorphism (SNP) genotyping, obtaining perfect discrimination of the target also under non optimal washing conditions.

We employed the unique features of our setup (real-time detection, temperature con-

trol, microfluidic) to perform on-chip DNA denaturation assays. We denatured DNA hybrids in ramping temperature and decreasing ionic strength. We assessed the reproducibility of this kind of assay, and proposed improvements for this approach.

In the following section we address some of the weaknesses of PHEB biosensing proposing step to achieve better and more reliable sensing. We also speculate on possible applications of our sensing scheme.

7.1 Outlook

During this project we had the opportunity to upgrade our system setup to improve the measurement method, the sensor fabrication and design. Nevertheless, due to the restricted amount of time and prioritisation of some goals, it was not possible to test and implement all the ideas we had. This section describes some of the future improvements that could be tested in our biosensing setup. Possible applications of our sensing method are proposed here. First, the general modification of the sensor are presented. Later the applications and improvements are divided between the volume-based and surface-based sensing methods.

7.1.1 Improved sensor signal

Sensor stack. The sensor geometry has been subject of active development during this project. Opposedly, the sensor stack has been modified only marginally, as discussed in Section 3.1. The low-field sensitivity of the PHEB sensors can be increased by reducing the exchange anisotropy field H_{ex} as we have obtained by low-temperature annealing. Another way is to modify the stack composition and employ a *buffer* layer between ferromagnetic and antiferromagnetic layers in the sensor stack [78]. Hung *et al.* [79] report a 80% reduction of the exchange bias upon introduction of 0.12 nm in the magnetic stack Ta(3)/NiFe(10)/Cu(0.12)/IrMn(10)/Ta(3) (thicknesses in nm). This reduction of H_{ex} would lead to a three fold increase in the low-field sensitivity of our sensor.

Protective coating. Section 2.2.2 shows how the sensor is mostly sensitive to the beads near the sensor surface. In this work we used a protective coating of ~ 900 nm of Ormocomp to passivate the sensors. The thickness of the protective coating could be further decreased to increase the bead signal.

Preamplification. The PHEB sensors have a low intrinsic noise [76], nevertheless some of the experiment presented in this thesis are limited by the signal-to-noise ratio of our measurement setup. Preamplifiers were used successfully in Chapter 6 to increase the signal to noise ratio. The same thing could not be done for Brownian relaxation measurements since the preamplifiers introduced a frequency dependent phase shift in the signal. Preamplifiers should be designed ad-hoc for this application.

7.1.2 Volume based biodetection

Magnetic manipulation. We saw in Section 5.4 that volume-based biodetection is slowed by sedimentation of magnetic beads. The signal from bead clusters keep increasing over time. It could be possible to accelerate this process by applying an external magnetic field gradient.

High-throughput analysis. The mechanisation of most laboratory activities and in particular the introduction of lab robots have allowed for high-throughput analysis in biochemical laboratories. Figure 7.1 shows one of such laboratory robot. Multiple pipettes work in parallel on all the well of a microtiter plate.

Fig. 7.1: Laboratory robot. Multiple pipettes work in parallel on the wells of a microtiter plate. Source: drugdiscoveryopinion.com

PHEB sensor could be used as readout method in such an automatised system. PHEB sensors do not require external magnetic field for Brownian relaxation measurements. Moreover, we demonstrated fast measurement in the time domain, using simple electronics. A single PHEB sensor could be fabricated in stick geometry of a size compatible with the wells of a microtiter plate. PHEB sensor could easily be integrated with existing high throughput analysis hardware.

RCA integration. The PHEB sensor setup already includes temperature control and a microfluidic system. The hybridisation of coils and capture probes on the labels could be easily performed on the chip to decrease the assay time. The following step would be to integrate the RCA in the microfluidic setup itself. RCA is an isothermal amplification and therefore does not require thermal cycling. Several examples of RCA integrated in a microfluidic system are presented in literature[80, 81, 82].

7.1.3 Surface based bioetection

Multiplexing. The surface based biodetection on dPHEB sensors demonstrated the capabilities to perform SNP detection and denaturation curve analysis using multiple probes on a single chip. Our long term goal is to apply this sensing technologies on cancer detection. Figure 7.2 shows schematically the envisioned setup. The assay should be based on patient specimen that can be obtained with non-invasive method [83]. The assay can integrate both genetic and epigenetic analysis of cancer markers.

The dPHEB chip design today comprises only five available sensors in the microfluidic system. To measure the signal from all the sensors, five lock-in amplifiers are needed at

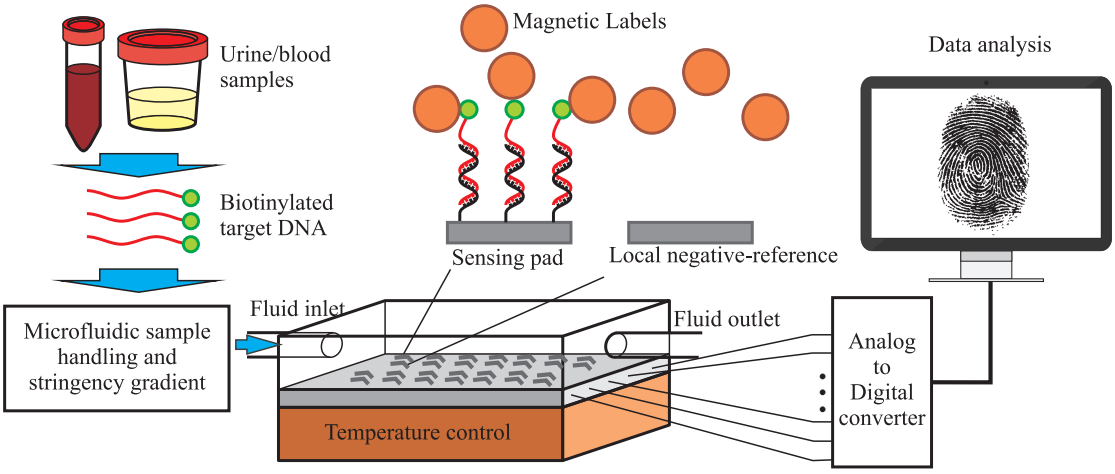

Fig. 7.2: Schematic of he proposed setup. The biotinylated target DNA and streptavidin coated magnetic labels are injected over the sensor surface in a microfluidic channel. The magnetic labels are linked to the sensor surface and give rise to a signal when the target hybridises to the surface-tethered probes. The sensor signal is measured during temperature cycles or buffer concentration gradients.

present. To be employable for cancer detection, the system should at least provide twice the amount of sensors. The measurements should be performed using a custom preamplification and a multiplexed analog-to-digital (ADC) converter. The lock-in amplification could be performed by software. Such a setup could be scalable, and provide a more flexible platform for biodetection.

Probe patterning. One of the most problematic procedure encountered during the experimental work of this thesis was the patterning of probes over the sensor surface. We used a microarray plotter to spot probes precisely over the sensor surface. The requirement for spotting was a complete coverage of only the two upper sensor arms. Often this procedure was failing due small misalignments of the machine. During the last phases of this project, it was proposed to employ hydrophobic treatment of the surface to provide well-defined areas for the probes to bind[84].

Temperature control. In Section 6.4 we saw how the absolute temperature in the melting curve was not reproducible. A possible solution to this problem is to monitor directly the temperature of the sensor. The resistivity of permalloy depends on the temperature [54]. The sensor themselves can therefore be used as thermometer, thus obtaining a measurement of the temperature near the surface tethered hybrids.

Binding kinetics. We demonstrated that PHEB biosensing has almost unique capabilities for the real time detection of surface binding events. This platform can be used to study the binding kinetics, to optimise the probes and process of surface based assays. Such application could improve also the leading technologies in biosensing, as DNA microarrays or ELISA.

Bibliography

[1] L. C. Clark and C. Lyons, "Electrode systems for continuous monitoring in cardiovascular surgery", Ann. N. Y. Acad. Sci. **102**, 29 (1962).

[2] G. Posthuma-Trumpie, J. Korf, and A. van Amerongen, "Lateral flow (immuno) assay: its strengths, weaknesses, opportunities and threats. a literature survey", Anal. Bioanal. Chem. **393**, 569 (2009).

[3] P. P. Freitas, R. Ferreira, S. Cardoso, and F. Cardoso, "Magnetoresistive sensors", Journal of Physics: Condensed Matter **19**, 165221 (2007).

[4] C. Tamanaha, S. Mulvaney, J. Rife, and L. Whitman, "Magnetic labeling, detection, and system integration", Biosens. Bioelectron. **24**, 1 (2008).

[5] S. X. Wang and G. Li, "Advances in giant magnetoresistance biosensors with magnetic nanoparticle tags: review and outlook", IEEE Trans. Magn. **44**, 1687 (2008).

[6] G. Prinz, "Magnetoelectronics", Science **282**, 1660 (1998).

[7] D. R. Baselt, G. U. Lee, M. Natesan, S. W. Metzger, P. E. Sheehan, and R. J. Colton, "A biosensor based on magnetoresistance technology", Biosens. Bioelectron. **13**, 731 (1998).

[8] D. L. Graham, H. Ferreira, J. Bernardo, P. P. Freitas, and J. M. S. Cabral, "Single magnetic microsphere placement and detection on-chip using current line designs with integrated spin valve sensors: Biotechnological applications", J. Appl. Phys. **91**, 7786 (2002).

[9] G. Li, V. Joshi, R. L. White, S. X. Wang, J. T. Kemp, C. Webb, R. W. Davis, and S. Sun, "Detection of single micron-sized magnetic bead and magnetic nanoparticles using spin valve sensors for biological applications", J. Appl. Phys. **93**, 7557 (2003).

[10] W. Shen, X. Liu, D. Mazumdar, and G. Xiao, "In situ detection of single micron-sized magnetic beads using magnetic tunnel junction sensors", Appl. Phys. Lett. **86**, 253901 (2005).

[11] E. Albisetti, D. Petti, M. Cantoni, F. Damin, A. Torti, M. Chiari, and R. Bertacco, "Conditions for efficient on-chip magnetic bead detection via magnetoresistive sensors", Biosens. Bioelectron. **47**, 213 (2013).

[12] L. Ejsing, M. F. Hansen, A. K. Menon, H. A. Ferreira, D. L. Graham, and P. P. Freitas, "Planar Hall effect sensor for magnetic micro- and nanobead detection", Appl. Phys. Lett. **84**, 4729 (2004).

[13] R. S. Gaster, D. A. Hall, C. H. Nielsen, S. J. Osterfeld, H. Yu, K. E. Mach, R. J. Wilson, B. Murmann, J. C. Liao, S. S. Gambhir, and S. X. Wang, "Matrix-insensitive protein assays push the limits of biosensors in medicine", Nat. Med. **15**, 1327 (2009).

[14] S. J. Osterfeld, H. Yu, R. S. Gaster, S. Caramuta, L. Xu, S. J. Han, D. A. Hall, R. J. Wilson, S. Sun, and R. L. White, "Multiplex protein assays based on real-time magnetic nanotag sensing", P. Natl. Acad. Sci. USA **105**, 20637 (2008).

[15] D. A. Hall, R. S. Gaster, T. Lin, S. J. Osterfeld, S. Han, B. Murmann, and S. X. Wang, "GMR biosensor arrays: A system perspective", Biosens. Bioelectron. **25**, 2051 (2010).

[16] R. Gaster, D. Hall, and S. Wang, "Autoassembly protein arrays for analyzing antibody cross-reactivity", Nano Lett. **11**, 2579 (2011).

[17] R. S. Gaster, L. Xu, S. J. Han, R. J. Wilson, D. A. Hall, S. J. Osterfeld, H. Yu, and S. X. Wang, "Quantification of protein interactions and solution transport using high-density GMR sensor arrays", Nat. Nanotechnol. **6**, 314 (2011).

[18] D. A. Hall, R. S. Gaster, S. J. Osterfeld, B. Murmann, and S. X. Wang, "GMR biosensor arrays: Correction techniques for reproducibility and enhanced sensitivity", Biosens. Bioelectron. **25**, 2177 (2010).

[19] R. S. Gaster, D. A. Hall, and S. X. Wang, "Nanolab: An ultraportable, handheld diagnostic laboratory for global health", Lab Chip **11**, 950 (2011).

[20] J. Connolly and T. G. St Pierre, "Proposed biosensors based on time-dependent properties of magnetic fluids", J. Magn. Magn. Mater. **225**, 156 (2001).

[21] W. Brown, "Thermal fluctuations of a single-domain particle", Phys. Rev. **130**, 1677 (1963).

[22] H. L. Grossman, W. R. Myers, V. J. Vreeland, R. Bruehl, M. D. Alper, C. R. Bertozzi, and J. Clarke, "Detection of bacteria in suspension by using a superconducting quantum interference device", P. Natl. Acad. Sci. USA **101**, 129 (2004).

[23] L. Tu, Y. Jing, Y. Li, and J. P. Wang, "Real-time measurement of Brownian relaxation of magnetic nanoparticles by a mixing-frequency method", Appl. Phys. Lett. **98**, 213702 (2011).

[24] A. P. Astalan, F. Ahrentorp, C. Johansson, K. Larsson, and A. Krozer, "Biomolecular reactions studied using changes in brownian rotation dynamics of magnetic particles", Biosens. Bioelectron. **19**, 945 (2004).

[25] T. Zardán Gómez de la Torre, A. Mezger, D. Herthnek, C. Johansson, P. Svedlindh, M. Nilsson, and M. Strømme, "Detection of rolling circle amplified DNA molecules using probe-tagged magnetic nanobeads in a portable AC susceptometer", Biosens. Bioelectron. **29**, 195 (2011).

[26] F. Ludwig, S. Mäuselein, E. Heim, and M. Schilling, "Magnetorelaxometry of magnetic nanoparticles in magnetically unshielded environment utilizing a differential fluxgate arrangement", Rev. Sci. Instrum. **76**, 106102 (2005).

[27] K. Enpuku, Y. Tamai, T. Mitake, T. Yoshida, and M. Matsuo, "Ac susceptibility measurement of magnetic markers in suspension for liquid phase immunoassay", J. Appl. Phys. **108**, 034701 (2010).

[28] B. T. Dalslet, C. D. Damsgaard, M. Donolato, M. Strømme, M. Strömberg, P. Svedlindh, and M. F. Hansen, "Bead magnetorelaxometry with an on-chip magnetoresistive sensor", Lab Chip **11**, 296 (2011).

[29] K. Enpuku, H. Watanabe, Y. Higuchi, T. Yoshida, H. Kuma, N. Hamasaki, M. Mitsunaga, H. Kanzaki, and A. Kandori, "Characterization of magnetic markers for liquid-phase immunoassays using brownian relaxation", Jpn. J. Appl. Phys. **51**, 023002 (2012).

[30] R. Haraszczuk, S. Yamada, M. Kakikawa, and T. Ueno, "Monitoring minute changes of magnetic markers' susceptibility by SV-GMR needle-type probe", IEEE Trans. Magn. **47**, 2584 (2011).

[31] D. Eberbeck, C. Bergemann, F. Wiekhorst, U. Steinhoff, and L. Trahms, "Quantification of specific bindings of biomolecules by magnetorelaxometry", J. Nanobiotechnology **6**, 4 (2008).

[32] F. Öisjöen, J. F. Schneiderman, A. P. Astalan, A. Kalabukhov, C. Johansson, and D. Winkler, "A new approach for bioassays based on frequency- and time-domain measurements of magnetic nanoparticles.", Biosens. Bioelectron. **25**, 1008 (2010).

[33] M. Nilsson, H. Malmgren, M. Samiotaki, M. Kwiatkowski, B. P. Chowdhary, and U. Landegren, "Padlock probes: circularizing oligonucleotides for localized DNA detection", Science **265**, 2085 (1994).

[34] D. Liu, S. L. Daubendiek, M. A. Zillman, K. Ryan, and E. T. Kool, "Rolling circle DNA synthesis: Small circular oligonucleotides as efficient templates for DNA polymerases.", J. Am. Chem. Soc. **118**, 1587 (1996).

[35] A. Fire and X. Si-Qun, "Rolling replication of short DNA circles", P. Natl. Acad. Sci. USA **92**, 4641 (1995).

[36] M. Strömberg, J. Göransson, K. Gunnarsson, M. Nilsson, P. Svedlindh, and M. Strømme, "Sensitive molecular diagnostics using volume-amplified magnetic nanobeads", Nano Lett. **8**, 816 (2008).

[37] E. Engvall and P. Perlmann, "Enzyme-linked immunosorbent assay (ELISA) quantitative assay of immunoglobulin G", Immunochemistry **8**, 871 (1971).

[38] G. MacBeath, "Protein microarrays and proteomics", Nat. Gen. **32**, 526 (2002).

[39] M. Dufva, "Fabrication of high quality microarrays", Biomol. Eng. **22**, 173 (2005).

[40] M. Dufva, in *DNA Microarrays for Biomedical Research*, Methods in Molecular Biology, Vol. 529, edited by M. Dufva (Humana Press, 2009) pp. 1–22.

[41] R. D. Canales, Y. Luo, J. C. Willey, B. Austermiller, C. C. Barbacioru, C. Boysen, K. Hunkapiller, R. V. Jensen, C. R. Knight, K. Y. Lee, Y. Ma, B. Maqsodi, A. Papallo,

E. H. Peters, K. Poulter, P. L. Ruppel, R. R. Samaha, L. Shi, W. Yang, L. Zhang, and F. M. Goodsaid, "Evaluation of DNA microarray results with quantitative gene expression platforms", Nat. Biotechnol. **24**, 1115 (2006).

[42] J. J. Chen, R. Wu, P.-C. Yang, J.-Y. Huang, Y.-P. Sher, M.-H. Han, W.-C. Kao, P.-J. Lee, T. F. Chiu, F. Chang, Y.-W. Chu, C.-W. Wu, and K. Peck, "Profiling expression patterns and isolating differentially expressed genes by cDNA microarray system with colorimetry detection", Genomics **51**, 313 (1998).

[43] J. Petersen, M. Stangegaard, H. Birgens, and M. Dufva, "Detection of mutations in the β-globin gene by colorimetric staining of DNA microarrays visualized by a flatbed scanner", Anal. Biochem. **360**, 169 (2007).

[44] L. Xu, H. Yu, M. S. Akhras, S.-J. Han, S. Osterfeld, R. L. White, N. Pourmand, and S. X. Wang, "Giant magnetoresistive biochip for DNA detection and HPV genotyping", Biosens. Bioelectron. **24**, 99 (2008).

[45] S. Auer, M. Nirschl, M. Schreiter, and I. Vikholm-Lundin, "Detection of DNA hybridisation in a diluted serum matrix by surface plasmon resonance and film bulk acoustic resonators", Anal. Bioanal. Chem. **400**, 1387 (2011).

[46] D. Wang, G. Chen, H. Wang, W. Tang, W. Pan, N. Li, and F. Liu, "A reusable quartz crystal microbalance biosensor for highly specific detection of single-base DNA mutation", Biosens. Bioelectron. **48**, 276 (2013).

[47] K. J. Breslauer, R. Frank, H. Blöcker, and L. A. Marky, "Predicting DNA duplex stability from the base sequence", P. Natl. Acad. Sci. USA **83**, 3746 (1986).

[48] N. Sugimoto, S. Nakano, M. Yoneyama, and K. Honda, "Improved thermodynamic parameters and helix initiation factor to predict stability of DNA duplexes", Nucleic Acids Res. **24**, 4501 (1996).

[49] W. M. Howell, M. Jobs, U. Gyllensten, and A. J. Brookes, "Dynamic allele-specific hybridization", Nat. Biotech. **17**, 87 (1999).

[50] M. Jobs, W. M. Howell, L. Strömqvist, T. Mayr, and A. J. Brookes, "DASH-2: Flexible, low-cost, and high-throughput SNP genotyping by dynamic allele-specific hybridization on membrane arrays", Genome Res. **13**, 916 (2003).

[51] T. Kajiyama, Y. Miyahara, L. J. Kricka, P. Wilding, D. J. Graves, S. Surrey, and P. Fortina, "Genotyping on a thermal gradient DNA chip", Genome Res. **13**, 467 (2003).

[52] M. Dufva, J. Petersen, and L. Poulsen, "Increasing the specificity and function of DNA microarrays by processing arrays at different stringencies", Anal. Bioanal. Chem. **395**, 669 (2009).

[53] C. D. Damsgaard, S. C. Freitas, P. P. Freitas, and M. F. Hansen, "Exchange-biased planar hall effect sensor optimized for biosensor applications", J. Appl. Phys. **103**, 07A302 (2008).

[54] C. Damsgaard, B. Dalslet, S. Freitas, P. Freitas, and M. Hansen, "Temperature effects in exchange-biased planar hall sensors for bioapplications", Sens. Actuators, A **156**, 103 (2009).

[55] B. T. Dalslet, M. Donolato, and M. F. Hansen, "Planar Hall effect sensor with magnetostatic compensation layer", Sens. Actuators, A **174**, 1 (2011).

[56] A. D. Henriksen, B. T. Dalslet, D. H. Skieller, K. H. Lee, F. Okkels, and M. F. Hansen, "Planar Hall effect bridge magnetic field sensors", Appl. Phys. Lett. **97**, 013507 (2010).

[57] J. Petersen, L. Poulsen, S. Petronis, H. Birgens, and M. Dufva, "Use of a multi-thermal washer for DNA microarrays simplifies probe design and gives robust genotyping assays", Nucleic Acids Res. **36**, e10 (2008).

[58] J. Petersen, L. Poulsen, H. Birgens, and M. Dufva, "Microfludic device for creating ionic strength gradients over DNA microarrays for efficient DNA melting studies and assay development", PLoS ONE **4**, e4808 (2009).

[59] V. Gehanno, P. P. Freitas, A. Veloso, J. Ferrira, B. Almeida, J. B. Soasa, A. Kling, J. C. Soares, and M. F. Da Silva, "Ion beam deposition of Mn-Ir spin valves", IEEE Trans. Magn. **35**, 4361 (1999).

[60] J. Nogués and I. K. Schuller, "Exchange bias", J. Magn. Magn. Mater. **192**, 203 (1999).

[61] S. Sun, "Recent advances in chemical synthesis, self-assembly, and applications of FePt nanoparticles", Adv. Mater. **18**, 393 (2006).

[62] T. B. G. Hansen, C. D. Damsgaard, B. T. Dalslet, and M. F. Hansen, "Theoretical study of in-plane response of magnetic field sensor to magnetic beads magnetized by the sensor self-field", J. Appl. Phys. **107**, 124511 (2010).

[63] L. Neél, "Théorie du traînage magnétique des ferromagnétiques en grains fins avec applications aux terres cuites", Ann. Géophys **5**, 99 (1949).

[64] P. Debye, "Polar molecules", Chemical Catalogue Co. (1929).

[65] K. S. Cole and R. H. Cole, "Dispersion and absorption in dielectrics I. Alternating current characteristics", J. Chem. Phys. **9**, 341 (1941).

[66] D. Sabourin, P. Skafte-Pedersen, M. J. Søe, M. Hemmingsen, M. Alberti, V. Coman, J. Petersen, J. Emnéus, J. P. Kutter, D. Snakenborg, F. Jørgensen, C. Clausen, K. Holmstrøm, and M. Dufva, "The MainSTREAM component platform: A holistic approach to microfluidic system design", J. Lab. Autom. **18**, 212 (2013).

[67] D. Sabourin, D. Snakenborg, and M. Dufva, "Interconnection blocks: a method for providing reusable, rapid, multiple, aligned and planar microfluidic interconnections", J. Micromech. Microeng. **19**, 035021 (2009).

[68] D. E. Bordelon, C. Cornejo, C. Grüttner, F. Westphal, T. L. DeWeese, and R. Ivkov, "Magnetic nanoparticle heating efficiency reveals magneto-structural differences when characterized with wide ranging and high amplitude alternating magnetic fields", J. Appl. Phys. **109**, 124904 (2011).

[69] T. Zardán Gómez de la Torre, D. Herthnek, H. Ramachandraiah, P. Svedlindh, M. Nilsson, and M. Strømme, "Evaluation of the Sulfo-Succinimidyl-4-(N-Maleimidomethyl) Cyclohexane-1-Carboxylate coupling chemistry for attachment of oligonucleotides to magnetic nanobeads", J. of Nanosci. Nanotechno. **11**, 8532 (2011).

[70] M. Donolato, B. T. Dalslet, C. D. Damsgaard, K. Gunnarsson, C. S. Jacobsen, P. Svedlindh, and M. F. Hansen, "Size-dependent effects in exchange-biased planar Hall effect sensor crosses", J. Appl. Phys. **109**, 064511 (2011).

[71] J. P. King, J. N. Chapman, M. F. Gillies, and J. C. S. Kools, "Magnetization reversal of nife films exchange-biased by irmn and femn", J. Phys. D: Appl. Phys. **34**, 528 (2001).

[72] J. Geshev, T. Dias, S. Nicolodi, R. Cichelero, A. Harres, J. J. S. Acuña, L. G. Pereira, J. E. Schmidt, C. Deranlot, and F. Petroff, "Role of the uncompensated interface spins in polycrystalline exchange-biased systems", J. Phys. D: Appl. Phys. **44**, 095002 (2011).

[73] M. Stromberg, T. Zardan Gomez de la Torre, J. Goransson, K. Gunnarsson, M. Nilsson, P. Svedlindh, and M. Strø mme, "Multiplex detection of DNA sequences using the volume-amplified magnetic nanobead detection assay", Anal. Chem. **81**, 3398 (2009).

[74] T. Zardán Gómez de la Torre, R. Ke, A. Mezger, P. Svedlindh, M. Strømme, and M. Nilsson, "Sensitive detection of spores using volume-amplified magnetic nanobeads", Small **8**, 2174 (2012).

[75] A. Engström, T. Zardán Gómez de la Torre, M. Strømme, M. Nilsson, and D. Herthnek, "Detection of rifampicin resistance in *Mycobacterium tuberculosis* by padlock probes and magnetic nanobead-based readout", PLoS ONE **8**, e62015 (2013).

[76] A. Persson, R. S. Bejhed, H. Nguyen, K. Gunnarsson, B. T. Dalslet, F. W. Østerberg, M. F. Hansen, and P. Svedlindh, "Low-frequency noise in planar Hall effect bridge sensors", Sens. Actuators, A **171**, 212 (2011).

[77] S. Fredriksson, M. Gullberg, J. Jarvius, C. Olsson, K. Pietras, S. M. Gustafsdottir, A. Ostman, and U. Landegren, "Protein detection using proximity-dependent DNA ligation assays", Nat. Biotechnol. **20**, 473 (2002).

[78] N. J. Gökemeijer, T. Ambrose, and C. L. Chien, "Long-range exchange bias across a spacer layer", Phys. Rev. Lett. **79**, 4270 (1997).

[79] T. Q. Hung, S. Oh, B. Sinha, J.-R. Jeong, D.-Y. Kim, and C. Kim, "High field-sensitivity planar Hall sensor based on NiFe/Cu/IrMn trilayer structure", J. Appl. Phys. **107**, 09E715 (2010).

[80] F. Saharil, A. Ahlford, M. Kuhnemund, M. Skolimowski, A. Conde, M. Dufva, M. Nilsson, M. Brivio, W. van der Wijngaart, and T. Haraldsson, in *Solid-State Sensors, Actuators and Microsystems (TRANSDUCERS EUROSENSORS XXVII)* (2013) pp. 357–360.

[81] P. J. Asiello and A. J. Baeumner, "Miniaturized isothermal nucleic acid amplification, a review", Lab Chip **11**, 1420 (2011).

[82] T. Konry, I. Smolina, J. M. Yarmush, D. Irimia, and M. L. Yarmush, "Ultrasensitive detection of low-abundance surface-marker protein using isothermal rolling circle amplification in a microfluidic nanoliter platform", Small **7**, 395 (2011).

[83] R. R. Serizawa, U. Ralfkiær, K. Steven, G. W. Lam, S. Schmiedel, J. Schüz, A. B. Hansen, T. Horn, and P. Guldberg, "Integrated genetic and epigenetic analysis of bladder cancer reveals an additive diagnostic value of fgfr3 mutations and hypermethylation events", Int. J. Cancer **129**, 78 (2011).

[84] R. Iino, Y. Matsumoto, K. Nishino, A. Yamaguchi, and H. Noji, "Design of a large-scale femtoliter droplet array for single-cell analysis of drug-tolerant and drug-resistant bacteria", Frontiers in Microbiology **4** (2013), 10.3389/fmicb.2013.00300.

Paper I

G. Rizzi, N. C. Lundtoft,F. W. Østerberg and M. F. Hansen
"Reversible and Irreversible Temperature-induced Changes in Exchange-biased Planar Hall Effect Bridge (PHEB) Magnetic Field Sensors"
Sensors & Transducers Journal **15**, 22 (2012)

Sensors & Transducers Journal, Vol. 15, Special Issue, October 2012, pp. 22-34

www.sensorsportal.com

Sensors & Transducers

ISSN 1726-5479

http://www.sensorsportal.com

Reversible and Irreversible Temperature-induced Changes in Exchange-biased Planar Hall Effect Bridge (PHEB) Magnetic Field Sensors

G. Rizzi, N. C. Lundtoft, F. W. Østerberg, * M. F. Hansen
Department of Micro- and Nanotechnology, Technical University of Denmark
DTU Nanotech, Building 345B, DK-2800 Kongens Lyngby, Denmark
* E-mail: Mikkel.Hansen@nanotech.dtu.dk

Received: 14 September 2012 /Accepted: 1 October 2012 /Published: 8 October 2012

Abstract: We investigate the changes of planar Hall effect bridge magnetic field sensors prepared without field annealing and with field annealing at 240 °C, 280 °C and 320 °C when these are exposed to temperatures between 25 °C and 90 °C. From analyses of the sensor response vs. magnetic field we extract the exchange bias field H_{ex}, the uniaxial anisotropy field H_K and the anisotropic magnetoresistance (AMR) of the exchange biased thin films at a given temperature. By comparing measurements carried out at elevated temperatures T with measurements carried out at 25 °C after exposure to T, we separate the reversible from the irreversible changes of the sensors. The un-annealed sample shows a significant irreversible change of H_{ex} and H_K upon exposure to temperatures above room temperature. The irreversible changes are significantly reduced but not eliminated by the low-temperature field annealing. The reversible changes with temperature are essentially the same for all samples. The results are not only relevant for sensor applications but also demonstrate the method as a useful tool for characterizing exchange-biased thin films. *Copyright © 2012 IFSA.*

Keywords: Magnetic biosensors, Planar Hall effect, Exchange bias, Anisotropic magnetoresistance.

1. Introduction

For applications of any sensor, it is important to know and correct for the effect of varying temperatures of the sensor environment. Moreover, it is important to be aware of irreversible changes of the sensor parameters induced by varying temperatures of the environment. Planar Hall effect magnetic field sensors have proven attractive for magnetic field sensing due to their low intrinsic noise

and potentially high signal-to-noise ratio [1]. We are investigating exchange-biased planar Hall effect sensors for magnetic biodetection [2, 3].

Here, we systematically study the changes of the response of planar Hall effect bridge sensors [4] upon exposure of these to temperatures between 25 °C and 90 °C. These temperatures correspond to the range typically employed in DNA based assays with amplification by polymerase chain reaction (PCR). From analyses of magnetic field sweeps of the sensor response we extract the parameters of thin film sensor stacks at all investigated temperatures and by performing measurements at 25 °C performed after all measurements at elevated temperatures we quantify and distinguish reversible and irreversible changes of each of the sensor parameters. These studies are carried out for a stack which is not exposed to any magnetic field annealing and for stacks that are field annealed at 240 °C, 280 °C and 320 °C. The results are generally relevant for applications of exchange-biased thin film sensors and demonstrate the method as a general tool for studying thin film magnetic properties vs. temperature.

2. Sensor Model

Below, we consider a material showing anisotropic magnetoresistance (AMR) with resistivities $\rho_{\|}$ and $\rho_{\perp}$ parallel and perpendicular to the magnetization vector **M**, respectively. The AMR ratio, defined as $\Delta\rho/\rho_{av}$, where $\Delta\rho \equiv \rho_{\|}-\rho_{\perp}$ and $\rho_{av} \equiv \rho_{\|}/3+2\rho_{\perp}/3$, assumes a value of 2-3 % for permalloy ($Ni_{80}Fe_{20}$). Fig. 1 shows a Wheatstone bridge consisting of four pairwise identical elements of the material of width w and length l. The resistance of a single element forming an angle α to the x-axis and with a homogeneous magnetization forming an angle θ to the x-axis is [4]

$$R(\alpha,\theta) = \frac{l}{wt}\left[\frac{1}{2}\left(\rho_{\|}+\rho_{\perp}\right)-\frac{1}{2}\Delta\rho\cos\left[2(\theta-\alpha)\right]\right], \tag{1}$$

where t is the thickness of the element. A current I injected in the x-direction results in the bridge output

$$V_y = \frac{1}{2}I\left[R(\alpha_+,\theta_+)-R(\alpha_-,\theta_-)\right], \tag{2}$$

where the orientation of magnetization of the elements forming angles α_+ and α_- to the x-axis are denoted θ_+ and θ_-. The maximum bridge output, obtained when $\alpha_+ = -\alpha_- = \pi/4$, is given by

$$V_y = \frac{1}{4}I\,\Delta\rho\frac{l}{wt}\left[\sin(2\theta_+)+\sin(2\theta_-)\right] \equiv \frac{1}{4}V_{pp}\left[\sin(2\theta_+)+\sin(2\theta_-)\right], \tag{3}$$

where we have introduced the nominal peak-to-peak sensor output voltage $V_{pp} = I\Delta\rho l/(wt)$ [4]. Equation (3) is identical to the output voltage from a cross-geometry planar Hall effect sensor multiplied by the geometrical amplification factor l/w. Therefore, we have termed the above sensors planar Hall effect bridge (PHEB) sensors [4].

Theoretically, the angles θ_+ and θ_- can be found by minimizing the single domain energy density for α_+ and α_-, respectively. We divide the volume energy density by the saturation flux density to form the normalized energy density u

$$u = -H_y\sin\theta - H_{ex}\cos\theta - \frac{1}{2}H_K\cos^2\theta - \frac{1}{2}H_s\cos^2(\alpha-\theta), \tag{4}$$

which expresses the energy density in units of the H-field. In Eq. (4), H_y is the external magnetic field applied in the y-direction, H_{ex} is the exchange field due to a unidirectional anisotropy along $\theta = 0$,

H_K is the anisotropy field due to a uniaxial anisotropy along $\theta = 0$ and H_s is the shape anisotropy field of the element (preferring a magnetization orientation with $\theta = \alpha$). Defining the demagnetization factors along and perpendicular to an element as $N_{||}$ and $N_{\perp}$, respectively, the shape anisotropy field is $H_s = (N_{\perp} - N_{||})M_s$ [5]. Our previous work [4] considered only the case of negligible shape anisotropy where $\theta_+ = \theta_- = \theta$.

We write the low-field sensor output voltage as

$$V_y = S_0 I H_y, \tag{5}$$

where we have defined the low-field sensitivity S_0. For negligible shape anisotropy, minimization of Eq. (4) for $H_s = 0$ and small values of θ yields

$$S_0 = \frac{l}{w}\frac{\Delta\rho}{t}\frac{1}{H_K + H_{ex}}. \tag{6}$$

If the shape anisotropy is significant but still small, the sensor response curve will be modified such that it flattens near zero applied field, resulting in a decrease of S_0 compared to Eq. (6), while still maintaining a peak-to-peak signal V_{pp} given by Eq. (3) (unpublished results).

3. Experimental

A batch of four wafers with top-pinned PHEB sensors was prepared on 4" silicon substrates with a 1 μm thick thermally grown oxide as follows: First, the stack Ta(3 nm)/$Ni_{80}Fe_{20}$(30 nm)/$Mn_{80}Ir_{20}$ (20 nm)/Ta(3 nm) was grown in a K. J. Lesker company CMS 18 multitarget sputter system in an Argon pressure of 3 mTorr with an RF substrate bias of 3W. The easy magnetization direction and axis of the permalloy layer were defined by applying a uniform magnetic field of $\mu_0 H_x = 20$ mT along the x-axis during the deposition. Subsequently, contacts of Ti(10 nm)/Pt(100 nm)/Au(100 nm)/Ti(10 nm) were deposited by e-beam evaporation and defined by lift-off. The negative lithography process employed a reversal baking step at 120 °C for 120 s on a hot plate in zero magnetic field.

One of the nominally identical four wafers was not given any further treatment and was labeled 'not annealed'/'un-annealed'. The other three wafers were annealed in vacuum in the sputter deposition chamber at temperatures of 240 °C, 280 °C and 320 °C for 1 hour in the presence of a saturating magnetic field $\mu_0 H_x = 20$ mT applied along the x-axis.

The dimensions of the elements of all investigated sensors were w=20 μm and l = 280 μm (Fig. 1). All sensors were surrounded by magnetic stack with a 3 μm gap to reduce the shape anisotropy of the elements. The simple theory presented in section 2 accounts for the elements but not the corners connecting the elements. The effect of corners was therefore investigated by finite element analysis of the sensor output for a single domain sensor structure. The calculations showed a sensor response that can be described by an effective sensor aspect ratio l/w = 14.87, which is 6% higher than the nominal one of l/w=14.

The magnetic properties of continuous thin films with dimensions 3×3 mm^2 were characterized for all four wafers using a LakeShore model 7407 vibrating sample magnetometer (VSM) and values of H_{ex} and H_K were extracted from easy axis hysteresis loop measurements.

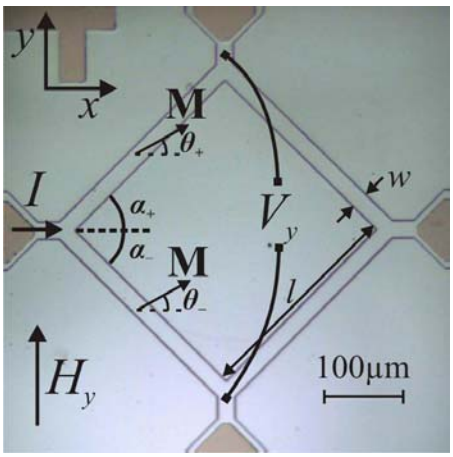

Fig. 1. Image of planar Hall effect magnetic bridge sensor with definition of geometric variables and symbols.

Values of the stack sheet resistances $\rho_{\parallel}/t$ and $\rho_{\perp}/t$ for the four wafers were obtained from electrical measurements of the resistance on transmission line test structures placed near the investigated sensor chips on the wafers in saturating magnetic fields applied parallel and perpendicular to the current, respectively.

Measurements of the sensor response vs. applied field were carried out as follows: the sensors were biased with an alternating current of root-mean-square (RMS) amplitude $I_{\mathrm{RMS}} = 1/\sqrt{2}$ mA and frequency $f = 65$ Hz provided by a Keithley 6221 precision current source. A Stanford Research Systems model SR830 lock-in amplifier was used to record the first harmonic in-phase root-mean-square (RMS) signal $V_{y,\mathrm{RMS}}$. Note, that Eq. (3) also holds for the RMS values I_{RMS} and $V_{y,\mathrm{RMS}}$. To simplify the notation below, we will therefore refer to the RMS values as V_y and I. The applied magnetic field $\mu_0 H_y$ was generated by a custom built electromagnet and monitored using commercially available Hall probes. Field sweeps were carried out by sweeping the field in both directions between $\mu_0 H_y = \pm 40$ mT. The sensor temperature was regulated to stability better than 0.1°C by use of a Peltier element, platinum RTD and a precision temperature controller. Sensor characteristics of all sensors were measured at temperatures from 25°C to 90°C in steps of 10°C. Each measurement performed at an elevated temperature was followed by a reference measurement performed at 25°C.

In addition, we also studied the effect of repeated exposure to 90 °C for an un-annealed sensor and a sensor from the wafer that was field annealed at 280 °C. These temperature cycling experiments were carried out as follows: first, the temperature was set to 25 °C and left for 10 min before a field sweep was carried out. The field sweep took about 8 min to complete. Then, the temperature was set to 90 °C and the measurement procedure was repeated. Finally, this cycle between 25 °C and 90 °C was repeated for about 7 hours.

4. Results

4.1. As Deposited Samples

In this section, we present results obtained for the samples at 25 ºC in their as-deposited state (i.e. prior to sensor characterization at elevated temperatures). We establish the model used for analyzing the field sweeps and compare to electrical and magnetic reference measurements.

The sensor signal V_y normalized with the bias current I, was measured vs. the sweeping field H_y for all four wafers. Fig. 2 shows the initial field sweeps measured for the samples with no annealing and with annealing at 280 °C. The annealing is observed to shift the peak of the sensor response towards lower field values and to increase the low-field sensitivity. The peak-to-peak value of the sensor response is found to be essentially unchanged by the annealing.

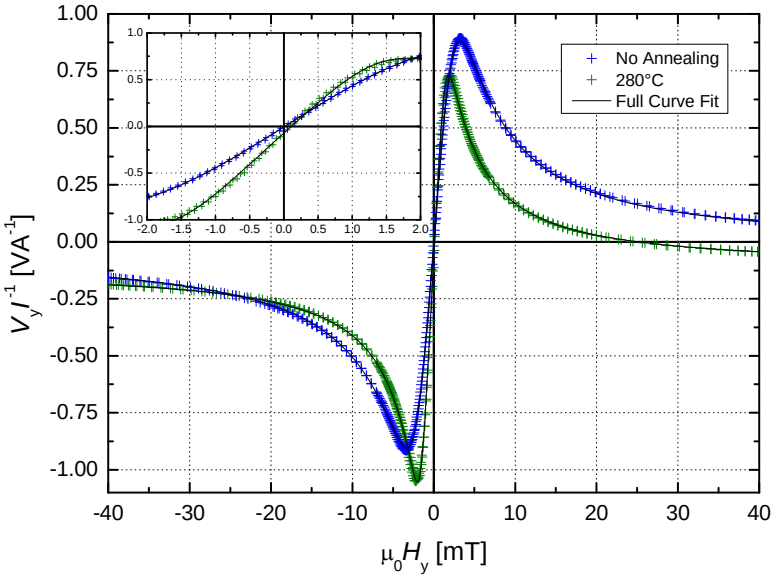

Fig. 2. Normalized sensor output (V_y/I) vs. external field (H_y) for sensors from the wafers with no annealing and with field annealing at 280°C in their initial condition. The inset shows the low-field region of the sensor response. The lines are fits to the single domain model for the sensor response described in the text.

The solid lines in Fig. 2 are least-squares fits to Eq. (3) with values of θ_+ and θ_- obtained by minimizing Eq. (4). The investigated free parameters in the fitting were V_{pp}/I , H_{ex} and H_K. The value of H_s was found to vary only marginally between the different temperature and annealing conditions and was fixed to the average value $\mu_0 H_s$ = 0.789 mT obtained from fitting data for all sensors and temperatures with this parameter set free. In the fitting we also allowed for offsets in the sensor output and the applied field. The quality of all fits was comparable to those shown in Fig. 2. Table 1 shows the values of $\mu_0 H_{ex}$ and $\mu_0 H_K$ obtained from the VSM measurements, the values of $\Delta\rho/t$ and the AMR ratio obtained from reference electrical measurements on the transmission line structure as well as the values of $\mu_0 H_{ex}$, $\mu_0 H_K$, S_0 and V_{pp}/I obtained from fits to field sweeps of the sensor response. Values reported for the low-field sensitivities S_0 were taken as the slope of the fits between ±0.15 mT.

Table 1. Parameters of the magnetic stack obtained from VSM measurements, electrical measurements on a transmission line structure and from fits to sensor field sweeps. All measurements were carried out at 25ºC on as-deposited samples (i.e. prior to any experiments at elevated temperatures). Numbers in parentheses indicate the uncertainties reported by the least squares fitting routine.

Annealing conditions	**VSM**		**Electrical ref.**		**Sensor field sweeps**			
	$\mu_0 H_{ex}$ [mT]	**$\mu_0 H_K$ [mT]**	**$\Delta\rho/t$ [Ω]**	**AMR [%]**	**$\mu_0 H_{ex}$ [mT]**	**$\mu_0 H_K$ [mT]**	**S_0 [V/(AT)]**	**V_{pp}/I [V/A]**
No annealing	2.89(5)	0.39(5)	0.1296(1)	1.88	2.66(1)	0.90(3)	465	1.779(2)
240 °C	2.02(5)	0.41(5)	0.1318(1)	2.03	1.91(1)	0.52(2)	637	1.785(3)
280 °C	1.90(5)	0.50(5)	0.1319(3)	1.95	1.60(1)	0.50(2)	699	1.764(4)
320 °C	1.39(5)	0.46(5)	0.1317(1)	2.03	1.32(1)	0.34(3)	807	1.768(7)

The values of H_{ex} obtained from VSM measurements and fits to the sensor field sweeps correspond well to each other although the values from the field sweeps are slightly lower than those obtained from the VSM measurements. The values of H_K obtained by VSM and from the sensor field sweeps are comparable for the annealed samples, but they differ about a factor of two for the un-annealed sample. The main effect of the low-temperature annealing is that H_{ex} is found to decrease monotonously with increasing annealing temperature. A decrease of about a factor of two is observed for annealing at 320 °C. The values of H_K extracted from the sensor field sweeps are found to decrease with increased annealing temperature, whereas no systematic change is found from the VSM studies. The value of $\Delta\rho/t$ remains essentially unchanged by the annealing. The low-field sensitivity is found to increase with annealing and increases almost by a factor of two for the highest annealing temperature.

4.2. Temperature Dependence of Parameters

In this section, we first present results of the experiments carried out at elevated temperatures for the un-annealed sample and show that our measurement procedure enables us to clearly distinguish reversible and irreversible changes of the sensor parameters upon exposure to a given elevated temperature. Then, we report the results of the corresponding experiments carried out on sensors from the low-temperature field annealed wafers. All parameters shown below have been obtained from fits to sensor field sweeps as described in section 4.1.

Fig. 3 shows the values of S_0, H_{ex} and H_K obtained from analysis of sensor field sweeps in a series of experiments carried out on a sensor from the wafer with no annealing at sequentially increasing temperatures T. First, the sensor response was measured at 25 °C. Then, the temperature was increased to 30 °C and the sensor response was measured after a waiting time of 2 min and finally, the temperature was reduced to 25 °C to carry out a reference measurement after a waiting time of 2 min. This procedure was repeated for temperatures increasing up to 90 °C in steps of 10 °C. The sensor parameters measured at the elevated temperature T result from the sum of reversible and irreversible changes, whereas the series of reference measurements carried out at 25 °C show only the irreversible changes. This enables us to clearly distinguish the reversible and irreversible changes of the sensor parameters as indicated by the colored areas in Fig. 3.

In Fig. 3, the value of S_0 is found to increase about 20% when the temperature is increased from 25 °C to 90 °C. Slightly more than half of this increase is irreversible. The values of H_{ex} and H_K are found to decrease approximately linearly with increasing temperature with temperature coefficients of –0.42%/°C (27% total decrease) and –0.68%/°C (44% total decrease), respectively, in good agreement with a previous study [6]. For H_{ex} about 20% of the change is irreversible and for H_K about 50 % of the change is irreversible. Thus, the irreversible changes are significant for this sample.

Corresponding series of experiments were carried out for the wafers exposed to the low-temperature field annealing.

Fig. 4(a) shows the values of V_{pp}/I for the measurements carried out on all samples. These values are proportional to $\Delta\rho/t$. The values obtained at 25 °C are close to identical and show no systematic variation with annealing conditions. Upon exposure to elevated temperatures, the values are found to decrease linearly with temperature with a temperature coefficient of –0.22 %/°C. The change is found to be fully reversible, i.e. no irreversible changes result from the increased temperature. This shows that the low-temperature field annealing and the experiments performed at elevated temperatures do not result in any detectable changes of the AMR properties of the sensor stack.

Fig. 4(b) shows the values of the low-field sensitivities S_0 normalized to the initial values obtained at 25 °C (given in Table 1) for the four investigated wafers as function of the measuring temperature T.

The data for the sample with no field annealing from Fig. 3 are shown for comparison. The field annealed samples show a much smaller temperature variation than the sample with no annealing. For the sample annealed at 240 °C the relative change of S_0 is about 7 % when the temperature is increased to 80 °C, but more than half of this change is irreversible. For the sample annealed at 280 °C, the points measured at T coincide with the reference points measured at 25 °C, indicating that the entire change of S_0 of about 3 % is irreversible. For the sample annealed at 320 °C, there is a net decrease of S_0 with T of about 2 % resulting from an irreversible increase of S_0 of about 3 % and a reversible decrease of S_0 of about 5 %.

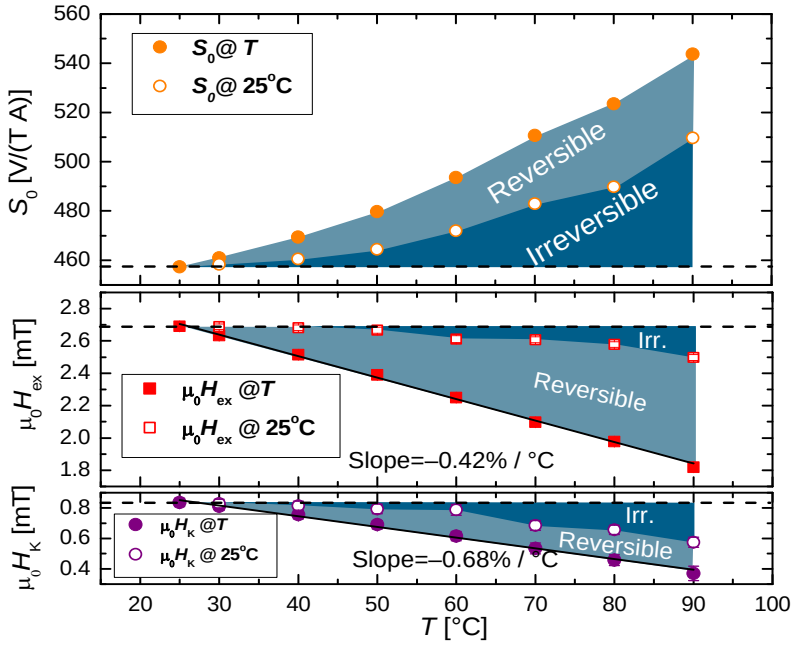

Fig. 3. Values of S_0 (top), H_{ex} (middle) and H_K (bottom) extracted from fits of the field sweeps on the un-annealed sample. Filled points are measured at temperature T, empty points are measured at the reference temperature 25°C after exposure to T. The full lines are linear fits corresponding to the indicated temperature coefficients.

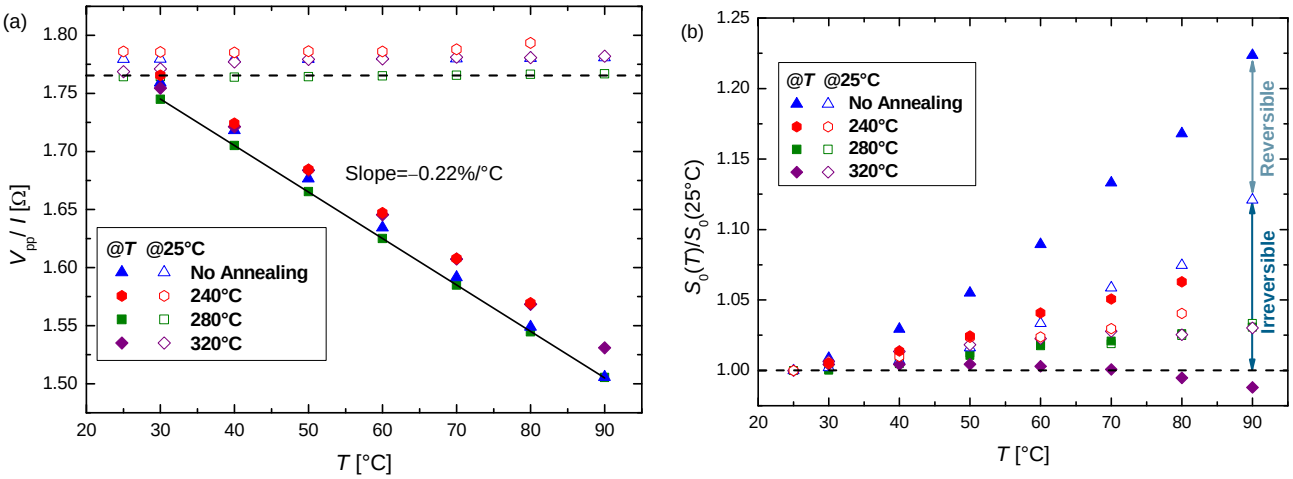

Fig. 4. Values of (a) the peak-to-peak sensor response V_{pp}/I and (b) the low-field sensitivity S_0 normalized to its initial value at 25°C obtained from field sweep fits. Different data sets are for sensors from wafers with the indicated annealing conditions. Filled points are measured at T, open points are measured at 25 °C after exposure to temperature T. The arrows to the right indicate the reversible and irreversible change for the un-annealed sample at T=90 °C.

Figs. 5(a) and (b) show the values of H_{ex} (normalized to their initial values given in Table 1) and H_K obtained for the four investigated wafers as function of the measuring temperature T, respectively. For all annealing conditions, the reversible change of H_{ex} with temperature is linear and can be described by the temperature coefficient –0.37%/°C. For the un-annealed sample the irreversible change of H_{ex} is about 8 % when the temperature is increased from 25 °C to 90 °C. The field annealed samples show a smaller, but not negligible irreversible change of H_{ex}, which appears to be independent of the annealing temperature.

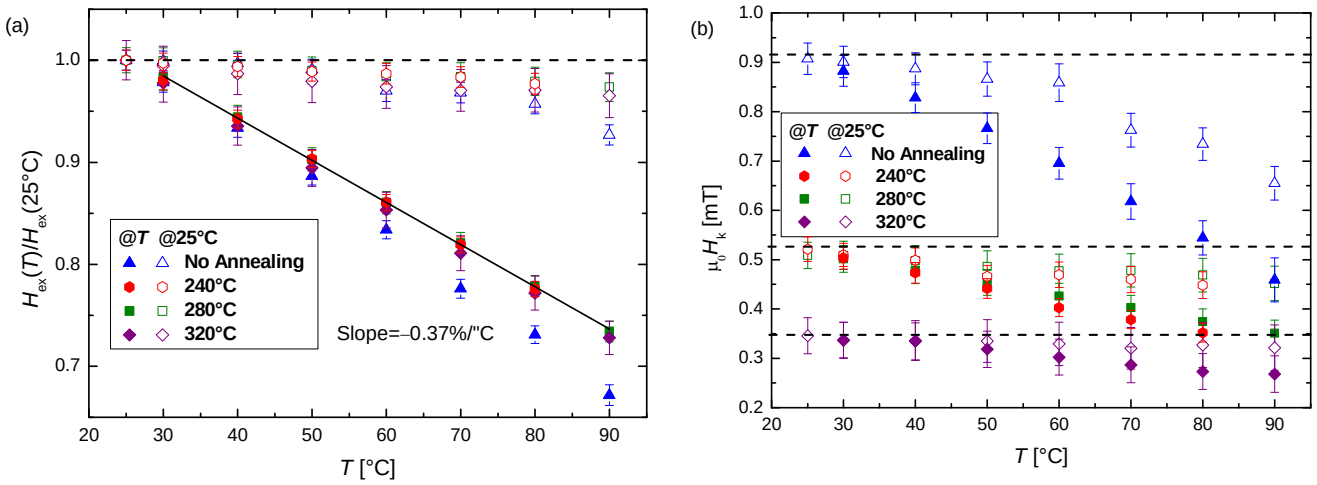

(a) (b)

Fig. 5. Values of (a) the normalized exchange bias field $H_{ex}(T)/H_{ex}(25°C)$ and (b) the anisotropy field H_K. Different data sets are for sensors from wafers with the indicated annealing conditions. Filled points are measured at T, open points are measured at 25 °C after exposure to temperature T. The dashed lines indicate the initial values of the parameters.

The initial values of H_K are found to decrease monotonically with annealing conditions. For the sample with no field annealing, the value of H_K changes almost 50 % when the temperature is increased from 25 °C to 90 °C and approximately half of this change is irreversible. The field annealed samples show a much smaller change and the irreversible change is smaller than the error on the individual points (and smallest for the sample annealed at 320 °C). The reversible decrease of H_K with temperature for these samples is about 20 %.

4.3. Temperature Cycling

Fig. 6 shows the effect of prolonged exposure at 90 °C on S_0, H_{ex} and H_K vs. the time of the temperature cycling experiment. Note, that only half of this time was spent at 90°C. Field sweeps were measured on the sensor annealed at 280 °C and on the un-annealed sensor while cycling the temperature between 25 °C and 90 °C with each temperature step taking 18 min. The lines in Fig. 6 connect points measured at the same temperature. The extracted values for the different parameters are normalized by the value reached at 90 °C after about 7 h of temperature cycling.

Fig. 6(a) shows the normalized value of S_0 vs. the time of the temperature cycling experiment. As for the results discussed above, the sensitivity of the sensor annealed at 280 °C changes little upon heating compared to the un-annealed sensor. The parameters obtained at 25 °C for the un-annealed wafer show a big change (>7 %) after first exposure at 90 °C and then slowly approach their asymptotic values.

For this sample, the sensitivity at 25 °C still changes after 7h of cycling with a total irreversible change of about 20 %. The values measured during the cycle steps at 90 °C show a similar settling over a period of hours. The chip from the wafer annealed at 280 °C shows a significant initial change in the first cycle after which the parameters slowly settle near their asymptotic values. Thus, for this sample, the irreversible change of S_0 is less than 5 % during the whole cycling experiment, and the value at 25 °C reaches 98.4 % of its final value after the first exposure to 90 °C.

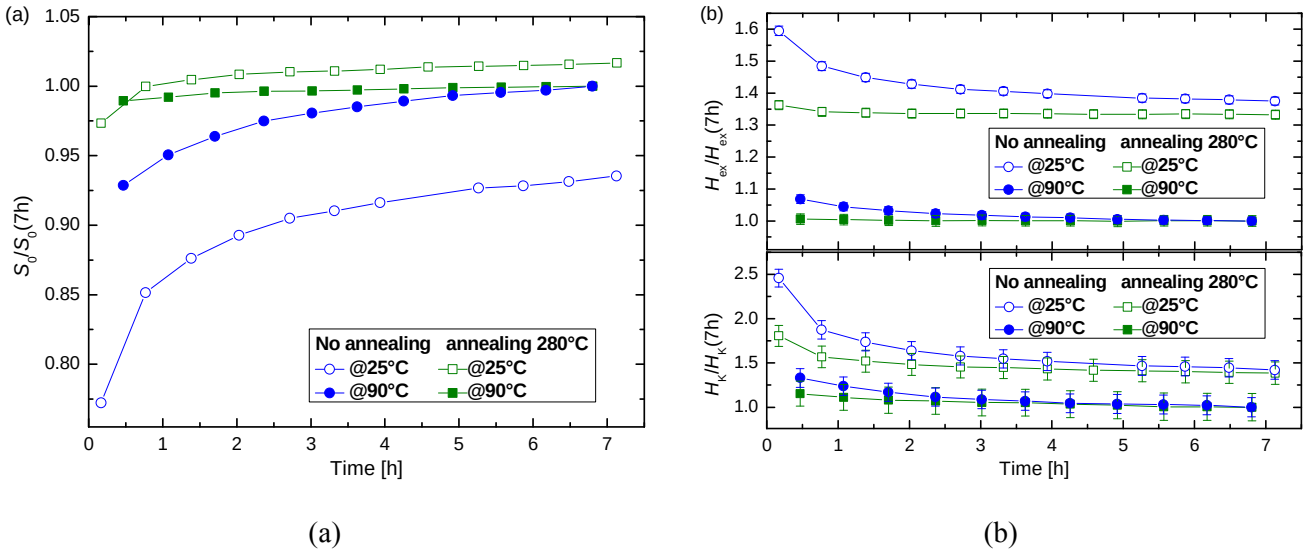

(a) (b)

Fig. 6. Values of (a) low-field sensitivity S_0 and (b) H_{ex} and H_K normalized by their value measured at 90 °C after 7 h temperature cycling between 25 °C and 90 °C. Different data sets are for sensors from wafers with the indicated annealing conditions. Filled points are measured at 90 °C open points are measured at 25 °C. The temperature was cycled between 25 °C and 90 °C, each temperature was held constant for 18 min.

Fig. 6(b) shows the corresponding normalized values of H_{ex} and H_K. The value of H_{ex} measured at 25 °C decreases for both sensors but the relative change for the annealed sensor is seven times smaller than for the un-annealed sensor. Again, the values measured at 90 °C show a similar behavior. The relative change in H_K is bigger than for H_{ex} for both sensors, although the change for the un-annealed sensor is twice as big as that for the sample annealed at 280 °C. We also notice for both H_{ex} and H_K and independent of low-temperature field annealing that the ratio between the values obtained at 90 °C and 25 °C approach the same value.

5. Discussion

5.1. Analysis Method

The presented single domain model for the sensor response provides excellent fits of all measured field sweeps. The parameters obtained from the fits are generally found to agree well with corresponding parameters obtained by VSM and on electrical reference samples although some differences appear. In section 4.1 in Table 1 that the value of H_K from the fits of the sensor measurements was about twice that obtained from the VSM measurements. This difference is in agreement with previous studies [6] and is attributed to effects of the sensor structuring.

Assuming negligible shape anisotropy, the low-field sensitivity is given by $S_0 = (l/w)(\Delta\rho/t)(H_{ex}+H_K)^{-1}$ (cf. Eq. (6)) and the peak-to-peak sensor output is given by $V_{pp}/I = (\Delta\rho/t)(l/w) = 14.87(\Delta\rho/t)$

(cf. Eq. (3)). Inserting the values for the reference samples, we find that the measured low-field sensitivities are generally about 20 % lower than the calculated values and the measured values of V_{pp}/I are about 9 % smaller than the calculated values. This is attributed to demagnetization effects due to the sensor geometry, which cause the magnetization of the sensor elements to deviate from the nominal single domain state near their edges [7]. From fits we found the shape anisotropy field $\mu_0 H_s$ = 0.789 mT, which is comparable to the values of $\mu_0 H_{ex}$ and $\mu_0 H_K$ reported in Table 1 and hence is significant.

These results indicate that the even though the results are influenced to some degree by demagnetization effects, the analysis method is robust and the parameters obtained from the fits to the single domain model reflect the variation of the physical parameters of the thin film stack. This means that field sweeps of the sensor response can be used to quantify the exchange and anisotropy fields as well as the magnetoresistive properties of the thin film stack.

5.2. Temperature Dependence of Parameters and Effect of Low-temperature Field Annealing

The studies on the as-deposited samples show that the effect of the low-temperature annealing is to decrease H_{ex} and H_K while $\Delta\rho/t$ remains essentially unchanged. The latter indicates that the microstructure of the stack is not significantly changed by the field annealing. The changes of H_{ex} and H_K indicate that the interaction between the ferromagnetic and antiferromagnetic layers is sensitive to the low-temperature field annealing. Considering the exchange bias as an interface phenomenon, the exchange bias field and the coupling energy per area J are related by $J = \mu_0 M_s t_{FM} H_{ex}$, where $\mu_0 M_s \approx 1.0$ T is the saturation flux density of permalloy and t_{FM} = 30 nm is the thickness of the permalloy layer. Inserting the values of H_{ex} from the VSM measurements in Table 1, we obtain $J_{eb} = 0.07$ mJ/m^2, which is comparable to values reported in the literature for similar stacks [8, 9].

The low-temperature annealing at 280 °C and 320 °C resulted in reductions of H_{ex} of 34 % and 52 %, respectively. Similar observations have been made in studies of similar structures with a top-pinned ferromagnet [8-11]. Previous studies have generally used measurements of the magnetic hysteresis by magnetometry [9-11], magnetooptical measurements [9] or Lorentz microscopy [8] to characterize the variation of H_{ex} and H_K with temperature, but they have not systematically studied the reversible and irreversible changes induced by exposure to elevated temperatures.

In this work we were able to separate reversible and irreversible changes of the parameters for the magnetic stack vs. temperature for samples exposed to different low-temperature field annealing conditions. We find that the temperature variation of $\Delta\rho/t$ is fully reversible. For the exchange bias field H_{ex} we find that the relative *reversible* change with temperature is the same for all samples (Fig. 5(a)). The *irreversible* change of H_{ex}, however, is sensitive to the field annealing and is significantly reduced compared to a sample without field annealing. For all field annealed samples, H_{ex} still shows irreversible change upon heating above 25 °C with a relative change that seems to be insensitive to the annealing conditions (Fig. 5(a)). For the anisotropy field H_K we find from Fig. 5(b) that both the reversible and irreversible changes upon exposure to elevated measuring temperatures are significant for the sample that was not field annealed, whereas the samples that were field annealed show significantly smaller changes with temperature. Only the sample annealed at 320 °C shows a negligible irreversible change of H_K upon exposure to 90 °C. The observed increase of the low-field sensitivity S_0 with field annealing and with exposure to elevated temperatures results from the combined effect of the reversible decrease of $\Delta\rho/t$ and the decrease of H_K+H_{ex} (cf. Eq. (6)), where the latter term dominates the temperature dependence.

To further investigate the effect of repeated exposure to elevated temperatures, we studied in Section 4.3 the samples with no annealing and with field annealing at 280 °C for repeated cycles between

90 °C and 25 °C. In Fig. 6(a), we found that for both the annealed and the un-annealed sample that the irreversible changes in the sensitivity as measured at 25 °C take place upon repeated exposure to 90 °C on a time scale of hours. Moreover, the relative change in sensitivity for the un-annealed sample is several times bigger than for the annealed sample. This change in sensitivity has to be attributed to the change in H_K and H_{ex}. Indeed, these two parameters show decay upon long exposure to 90 °C. Also, they show reduced irreversible changes in the annealed sensor compared to the un-annealed one.

For all samples, we find that even after field annealing at temperatures up to 320 °C, the values of H_{ex} and H_K still show irreversible changes upon exposure to temperatures above room temperature. These changes have to be taken into account when these stacks and sensors are used for sensing purposes in environments at elevated temperatures. The largest changes are found for the sample that was not field annealed and we have found that the field annealing significantly reduces the irreversible changes.

5.3. Possible Mechanisms

Several reports in the literature have studied the effect of annealing at low temperatures on the microstructure. King *et al.* [8] studied the magnetization reversal of NiFe/IrMn exchange bias couples by Lorentz transmission electron microscopy. For an un-annealed sample, they found that the magnetic domain structure in the ferromagnetic layer was highly complex on a microscopic scale near room temperature with no clear overall orientation. After field annealing of the sample at 300 °C, they found significantly larger magnetic domains that were essentially oriented along the cooling field. They could not detect any changes of the microstructure and therefore attributed the change of behavior to a reduction of the local pinning strength of the IrMn grains upon annealing. Thus, the IrMn grains strongly pinned the ferromagnetic layer before annealing resulting in the highly complex domain structure, but after annealing the pinning strength decreased due to relaxation in the spin structure of the IrMn grains such that the local pinning was insufficient to force the ferromagnet to orient along the local pinning field.

Geshev *et al.* [10] carefully studied the interface between Co and IrMn by high resolution cross-sectional TEM and X-ray reflectivity measurements and found no effect of annealing at 215 °C on the microstructure at the interface. Upon annealing in a magnetic field applied along the initial exchange bias direction they observed a clear reduction of H_{ex} that they attributed to relaxation of frustrated spins in the top IrMn layer. They hypothesized that the first few atomic layers of the IrMn layer show paramagnetic behavior and align themselves with the moments from the ferromagnet. When enough atomic layers of the IrMn film to sustain antiferromagnetic order are deposited, the competition between the alignment of the interface spins with those of the ferromagnetic layer and the antiferromagnetic ordering will result in high frustration of the spin structure of the IrMn layer near the interface and a high number of uncompensated spins at the interface, where the latter gives rise to the high initial exchange bias. The annealing enables relaxation of the spin structure resulting in a reduction of the pinning strength and hence of H_{ex}.

Our findings that irreversible changes of H_{ex} appear slightly above room temperature even for a sample annealed at 320 °C for one hour and that repeated exposure to elevated temperatures result in gradually decreasing values of H_{ex} indicate that a slow, thermally activated process is involved in the change of H_{ex} vs. time and temperature and that the number of uncompensated interfacial spins of the IrMn layer decreases as a result of the relaxation process. Thus, our observations are consistent with the above interpretation in terms of thermal relaxation of frustrated spins in the IrMn layer near the interface to the ferromagnet. We hope that our studies will provide further inspiration to further theoretical work on this interesting topic.

5. Conclusion

We have shown that measurements of the response vs. magnetic field of planar Hall effect Wheatstone bridges can be used to extract the exchange field H_{ex}, the anisotropy field H_K and the magnetoresistive properties of the exchange-biased stack of the sensors. We have studied the temperature variation of these parameters for a top-pinned NiFe/IrMn stack in the interval between 25 °C and 90 °C for samples that were not annealed and samples that were low-temperature field annealed at 240 °C, 280 °C and 320 °C for one hour. In our experiments we separated reversible and irreversible parameter changes. We found that the magnetoresistive effect is not significantly affected by the low-temperature field annealing and only shows reversible changes upon exposure to elevated temperatures. Both H_{ex} and H_K are sensitive to annealing as well as the exposure to elevated temperatures and the relative reversible decrease of H_{ex} with temperature can be described by a single temperature coefficient. Field annealing significantly reduces but does not eliminate the irreversible changes of both H_{ex} and H_K upon exposure to temperatures even slightly above room temperature. In experiments where both field annealed and un-annealed sensors were repeatedly exposed to 90 °C, we found a large initial change and a gradual reduction of the change upon further exposure. We take these observations as indicative of a slow thermally activated process that reduces the local pinning strength of the IrMn at the interface. The observations are consistent with previous interpretations in the literature in terms of thermal relaxation of frustrated spins in the antiferromagnet near the interface to the ferromagnet, but further work is required to firmly establish this hypothesis.

The present results have important consequences for the use of permalloy-IrMn exchange-bias couples in magnetic field sensors operating at variable temperatures. Stacks with no annealing are strongly influenced by exposure to temperatures above room temperature and these should thus be used with care in applications where the sensor is exposed to elevated temperatures and high accuracy is required. Examples of such applications could be magnetic biosensors operating at variable temperatures (e.g. for studies of biological interactions vs. temperature) and magnetic field sensors operating in variable temperature conditions. The presented method provides an attractive approach to quantitative characterization of the temperature-induced changes by exposure to given temperature conditions. We have shown that low-temperature field annealing and prolonged exposure to the highest operating temperature substantially reduces subsequent irreversible changes with increasing temperatures but also that it is difficult to completely eliminate irreversible changes of the sensor parameters. These therefore have to be considered for the use of the structures in sensing applications.

Acknowledgements

F.W. Østerberg acknowledges support by the Copenhagen Graduate School for Nanoscience and Nanotechnology (C:O:N:T) and the Knut and Alice Wallenberg (KAW) Foundation.

References

[1]. A. Persson *et al*., Low-frequency noise in planar Hall effect bridge sensors, *Sensors and Actuators A: Physical,* 171, 2011, pp. 212-218.
[2]. C. Damsgaard *et al*., Temperature effects in exchange-biased planar hall sensors for bioapplications, *Sensors and Actuators A: Physical*, 156, 2009, pp. 103-108.
[3]. B. Dalslet *et al*., Bead magnetorelaxometry with an on-chip magnetoresistive sensor, *Lab Chip,* 11, 2011, pp. 296-302.
[4]. A. Henriksen *et al.,* Planar Hall effect bridge magnetic field sensors, *Appl. Phys. Lett.,* 97, 2010, 013507.
[5]. S. Blundell, Magnetism in condensed matter, Oxford master, *Oxford University Press*, 2001.
[6]. C. Damsgaard *et al*., Exchange-biased planar Hall effect sensor optimized for biosensor applications,

J. Appl. Phys., 103, 2008, 07A302.
[7]. M. Donolato *et al*., Size-dependent effects in exchange-biased planar Hall effect sensor crosses, *J. Appl. Phys.,* 109, 2011, 064511.
[8]. J. King *et al*., Magnetization reversal of NiFe films exchange-biased by IrMn and FeMn, *J. Phys. D: Applied Physics*., 34, 2001, pp. 528-538.
[9]. J. Van Driel *et al*., Exchange biasing by $Ir_{19}Mn_{81}$: Dependence on temperature, microstructure and antiferromagnetic layer thickness, *J. Appl. Phys*., 88, 2000, pp. 975.
[10].J. Geshev *et al*. Role of the uncompensated interface spins in polycrystalline exchange-biased systems, *J. Phys. D: Applied Physics,* 44, 2011, 095002.
[11].A. Devasahayam *et al*., Magnetic, temperature, and corrosion properties of the NiFe/IrMn exchange couple, *J. Appl. Phys.,* 83, 1998, pp. 7216.

Paper II

F. W. Østerberg, G. Rizzi and M. F. Hansen
"On-chip measurements of Brownian relaxation vs. concentration of 40 nm magnetic beads"
J. Appl. Phys. **112**, 124512 (2012)

JOURNAL OF APPLIED PHYSICS **112**, 124512 (2012)

On-chip measurements of Brownian relaxation vs. concentration of 40 nm magnetic beads

Frederik Westergaard Østerberg,[a] Giovanni Rizzi, and Mikkel Fougt Hansen[b]
Department of Micro- and Nanotechnology, Technical University of Denmark, DTU Nanotech, Building 345B, DK-2800 Kongens Lyngby, Denmark

(Received 21 September 2012; accepted 16 November 2012; published online 20 December 2012)

We present on-chip Brownian relaxation measurements on a logarithmic dilution series of 40 nm beads dispersed in water with bead concentrations between 16 μg/ml and 4000 μg/ml. The measurements are performed using a planar Hall effect bridge sensor at frequencies up to 1 MHz. No external fields are needed as the beads are magnetized by the field generated by the applied sensor bias current. We show that the Brownian relaxation frequency can be extracted from fitting the Cole-Cole model to measurements for bead concentrations of 64 μg/ml or higher and that the measured dynamic magnetic response is proportional to the bead concentration. For bead concentrations higher than or equal to 500 μg/ml, we extract a hydrodynamic diameter of 47(1) nm for the beads, which is close to the nominal bead size of 40 nm. Furthermore, we study the signal vs. bead concentration at a fixed frequency close to the Brownian relaxation peak and find that the signal from bead suspensions with concentrations down to 16 μg/ml can be resolved. © *2012 American Institute of Physics*. [http://dx.doi.org/10.1063/1.4769796]

I. INTRODUCTION

Magnetic beads have proven useful for biosensing as most biological samples are non-magnetic such that magnetic beads can be manipulated and detected independently of the sample chemistry. Furthermore, magnetic biosensors rely on magnetic methods for detecting the magnetic beads, which provide an electrical signal that can be directly read out. Among the typical methods for detecting magnetic beads are inductive methods,[1] fluxgates,[2] superconducting quantum interference device (SQUID) magnetometers,[3,4] and magnetoresistive sensors.[5–7] There are pros and cons for each method; for instance, SQUID magnetometers are very sensitive but are costly, require cryogenics and are not easily integrated with a sample preparation system. Magnetoresistive sensors are not as sensitive as SQUID magnetometers but they can be operated at room temperature, they are small in dimensions, they are potentially inexpensive and they can be integrated in lab-on-a-chip systems. Thus, magnetoresistive sensors are attractive for use in lab-on-a-chip magnetic biosensing platforms.

Magnetic beads have been used for biosensing in surface-based[8] and volume-based[1,9,10] assays. In a surface-based assay, the surfaces of both the sensor and the beads are functionalized such that the presence of the analyte results in specific binding of the beads to the sensor surface. In a volume-based assay, only the beads are functionalized prior to detection and the analyte modifies the hydrodynamic size of the beads, either due to its size[11] or by inducing bead agglutination.[1] The dispersion of hydrodynamic sizes for a magnetic bead ensemble can be characterized via Brownian relaxation measurements, which were first proposed for biosensing by Connolly and St Pierre.[12]

For volume-based bioassays, the limit of detection is sensitive to the bead concentration: for a high bead concentration, only a small fraction of the beads are affected by a given amount of analyte, whereas the opposite is the case for a low bead concentration. On the other hand, a low bead concentration results in a smaller dynamic range of analyte concentrations that can be detected. Thus, the bead concentration is an important parameter for the sensitivity and dynamic range for volume-based biosensing. For any readout principle for volume-based bioassays, it is therefore important to know its dependence on the bead concentration and the range of bead concentrations for which the magnetic dynamics can be reliably characterized.

In this study, we investigate the dependence of the on-chip measurements of the dynamic magnetic bead signal on the concentration of beads with a nominal diameter of 40 nm. The study is carried out using so-called planar Hall effect bridge (PHEB) sensors[13] currently being investigating for volume-based magnetic biodetection.[10] The sensors are integrated in a microfluidic system and do not rely on any external magnetic fields. We determine the lower limit of bead concentrations required for obtaining reliable measurements of the dynamic magnetic Brownian relaxation response and we also investigate the lowest bead concentration that can be detected by the present sensors.

II. THEORY

The magnetic field sensors used in the study are based on the anisotropic magnetoresistance (AMR) effect, which causes the resistivity to be largest when the current and applied magnetic field are parallel and lowest when they are orthogonal. The sensor geometry is composed of four segments to form a Wheatstone bridge as shown in Fig. 1. Here, the potential difference V_y in the y-direction is measured upon injection of a current I in the x-direction. The sensor

[a]Electronic address: Frederik.Osterberg@nanotech.dtu.dk.
[b]Electronic address: Mikkel.Hansen@nanotech.dtu.dk.

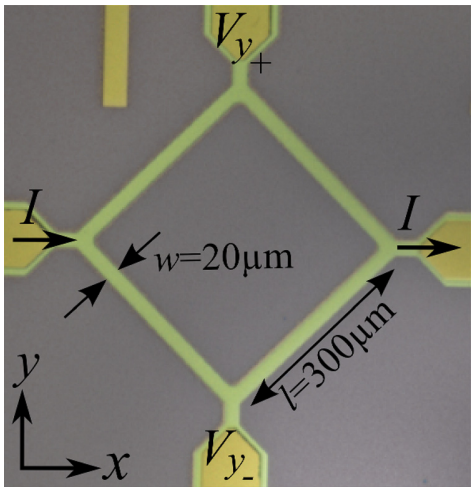

FIG. 1. Picture of sensor with definitions of dimensions. The bias current I is applied through the arms in the x-direction, while the potential difference V_y is measured across the y-direction. The length l and width w of a bridge segment are also shown.

consists of a ferromagnetic layer exhibiting the AMR effect, which is pinned along the positive x-direction by an antiferromagnetic layer. This ensures that the magnetization of the sensor is single domain and has a fixed orientation in the absence of external magnetic fields. It has recently been shown that the signal from the bridge structure shown in Fig. 1 is identical to that from a regular planar Hall effect sensor cross, except for a geometrical amplification.[13] To distinguish this particular geometry from other AMR sensor geometries, we have named sensors with this geometry planar Hall effect bridge sensors.

For low magnetic fields, the sensor signal is linear and given by[13]

$$V_y = IS_0H_y, \tag{1}$$

where S_0 is the low-field sensitivity and H_y is the magnetic field in the y-direction.

Measurements on magnetic bead suspensions are carried out without application of external magnetic fields. Instead, the magnetic beads are magnetized by the sensor self-field arising from the bias current passed through the sensor. For an alternating bias current $I(t) = I_{AC}\sin(2\pi ft)$, both the bias current and the field from the beads will oscillate at the frequency f of the bias current. As the sensor response due to the presence of magnetic beads is proportional to I^2, these will give rise to a signal oscillating at $2f$. The dynamic magnetic response of the magnetic beads is described by their complex susceptibility $\chi = \chi' - i\chi''$, where χ' and χ'' are the in-phase and out-of-phase magnetic susceptibilities of the beads, respectively. We have previously shown that the dynamic magnetic bead response for beads magnetized by the self-field can be detected using lock-in technique[10,14,15] and that the second harmonic in-phase and out-of-phase sensor signals V_2' and V_2'' for a PHEB sensor are given by[10]

$$V_2' = -2^{-3}I_{AC}^2S_0\gamma_1\chi'', \tag{2}$$

$$V_2'' = -2^{-3}I_{AC}^2S_0(\gamma_0 + \gamma_1\chi'), \tag{3}$$

where γ_0 is a constant that depends on the sensor stack and sensor geometry and γ_1 is a constant that depends on the sensor geometry and distribution of beads. Thus, the in-phase second harmonic sensor signal is proportional to the out-of-phase magnetic bead susceptibility and the out-of-phase second harmonic sensor signal depends linearly on the in-phase magnetic bead susceptibility.

A. Brownian relaxation of magnetic of beads

When a magnetic bead is placed in a magnetic field, the magnetization of the bead will align with the field either by internal flipping of the magnetic moment (Néel relaxation[16]) or by a physical rotation of the bead (Brownian relaxation[17]). For the beads used in this study, the Néel relaxation time is much longer than the Brownian relaxation time, which therefore dominates the relaxation dynamics of the beads. Brownian relaxation is characterized by the Brownian relaxation frequency,

$$f_B = \frac{k_BT}{6\pi\eta V_h}, \tag{4}$$

where k_BT is the thermal energy, η is the viscosity of the liquid in which the bead is suspended, and V_h is the hydrodynamic volume of the bead. The Brownian relaxation frequency is the frequency at which the phase-lag between the magnetic moment of the bead and the applied field is largest, meaning that a peak will appear in the out-of-phase magnetic susceptibility at $f = f_B$.

The complex susceptibility of a monodisperse ensemble of beads is described by the Debye theory.[18] The complex susceptibility of an ensemble of polydisperse beads is usually described by the empirical Cole-Cole model,[19]

$$\chi = \frac{\chi_0 - \chi_\infty}{1 + (if/f_B)^{1-\alpha}} + \chi_\infty, \tag{5}$$

where χ_0 and χ_∞ are the DC and high-frequency susceptibilities, respectively, and $0 \le \alpha \le 1$ is a measure of the polydispersity ($\alpha = 0$ for a monodisperse sample). The Cole-Cole model has been used for analyzing the data in the present work to extract f_B, α, and the DC and high-frequency susceptibilities.

III. EXPERIMENTAL

The geometric variables of the sensor are defined in Fig. 1. Each of the four branches in the sensor bridge used in the present study has a length of $l = 300$ μm and a width of $w = 20$ μm and was fabricated as follows: First, an 800 nm thick oxide was grown on a silicon wafer by wet oxidation. Then, the sensor stack Ta(3 nm)/$Ni_{80}Fe_{20}$(30 nm)/$Mn_{80}Ir_{20}$(20 nm)/Ta(3 nm) was deposited in a Kurt J. Lesker Co. CMS-18 sputter system and defined by lift-off. During deposition, a magnetic field of 20 mT was applied to define the easy direction of the magnetization along the positive x-direction in Fig. 1. Electrical contacts to the sensors of Ti(5 nm)/Au(100 nm)/Pt(100 nm)/Ti(5 nm) were deposited by e-beam evaporation and defined by lift-off. Subsequently,

a protective coating of Ormocomp (Micro Resist Technology GmbH, Germany) with a thickness of 800 nm was spin-coated and patterned by UV lithography. This coating ensured that the sensors could be operated at voltages up to 10 V without failure or bubble formation when the sensor was exposed to ionic solutions.

During measurements, the chip was mounted in a click-on fluidic system[14] providing electrical contacts to the chip and defining a fluidic channel of dimensions length × width × height = 5 mm × 1 mm × 1 mm (Fig. 2(a)). To align the chip with the channel and electrical contact, the chip was placed in an aluminum well (Fig. 2(b)). The temperature of the aluminum well was kept constant at (25.00 ± 0.01) °C during all measurements using a Peltier element. The set-up was neither magnetically nor electrically shielded.

Electrical measurements on the sensor were carried out using an HF2LI lock-in amplifier (Zurich Instruments, Switzerland) operating at a fixed voltage amplitude of 3.2 V corresponding to a current amplitude of $I_{AC} = 21$ mA. The 1st harmonic sensor response was measured vs. applied field resulting in a low-field sensor sensitivity of $S_0 = -531$ V/(T A).

Measurements were performed on nominally 40 nm magnetic beads with a COOH functional surface group (Ocean Nanotech, AR, USA). In this study, the bead concentration was varied from $c = 16$ μg/ml to $c = 4$ mg/ml in a 2-fold logarithmic dilution series. In the experiments, the bead concentration was varied in the following order: c [mg/ml] = 1, 0.25, 0.063, 0.5, 0.125, 0.031, 0.016, 4, 2.

Measurements on bead suspensions were carried out in ambient magnetic field where the 2nd harmonic sensor response was measured as a function of the frequency of the applied bias voltage. Each frequency sweep consisted of 20 points equally distributed on a log scale between $f = 986.9$ kHz and 37.7 Hz. After each measurement at f, a reference measurement was carried out at $f_{ref} = 4667$ Hz, which is near the expected Brownian relaxation frequency for the beads used in the experiments. Each of the above sweeps took a total time of 7 min and 20 s to complete. For each bead concentration, a cycle of 9 frequency sweeps, numbered 1–9, was performed. First, two sweeps (1 and 2) were performed without beads and were used as reference. At the start of sweep 3, beads were injected into the fluidic channel for 1 min at a flow rate of 30 μl/min. Then, the flow was stopped for the remaining part of sweep 3 and left stagnant in the following four sweeps (sweeps 4–7). At the start of sweep 8, the beads were washed out at a flow rate of 800 μl/min and sweep 9 was performed to confirm that the signal returned to its initial level from sweeps 1 and 2.

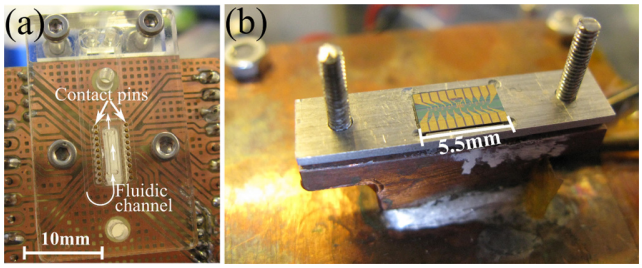

FIG. 2. (a) Fluidic system with 20 spring-loaded electrical contact pins. (b) Picture of chip in set-up prior to mounting of the fluidic system.

IV. RESULTS

A. Frequency sweeps

Figure 3 shows the in-phase (top) and out-of-phase (bottom) second harmonic sensor signals as a function of the bias current frequency for sweep 7, which is started 29 min after injection of the beads. Only measurements for the seven highest bead concentrations (63 μg/ml-4 mg/ml) are shown, as the lower concentrations are indistinguishable from $c = 63$ μg/ml on this scale. The solid lines in the figures are curve fits of the Cole-Cole model to the measured data. From Fig. 3, it is seen that the curve shape is independent of the concentration and that it scales with the bead concentration.

Figure 4 shows the Brownian relaxation frequencies f_B extracted from curve fits of the Cole-Cole model vs. bead concentration. The fits of the in-phase and out-of-phase data were carried out simultaneously with a single set of parameters. For each concentration, the values of f_B were found separately for sweeps 5–7. The error bars on each of the f_B-values in Fig. 4 correspond to the standard deviation reported by the least-squares fitting routine. It is also seen

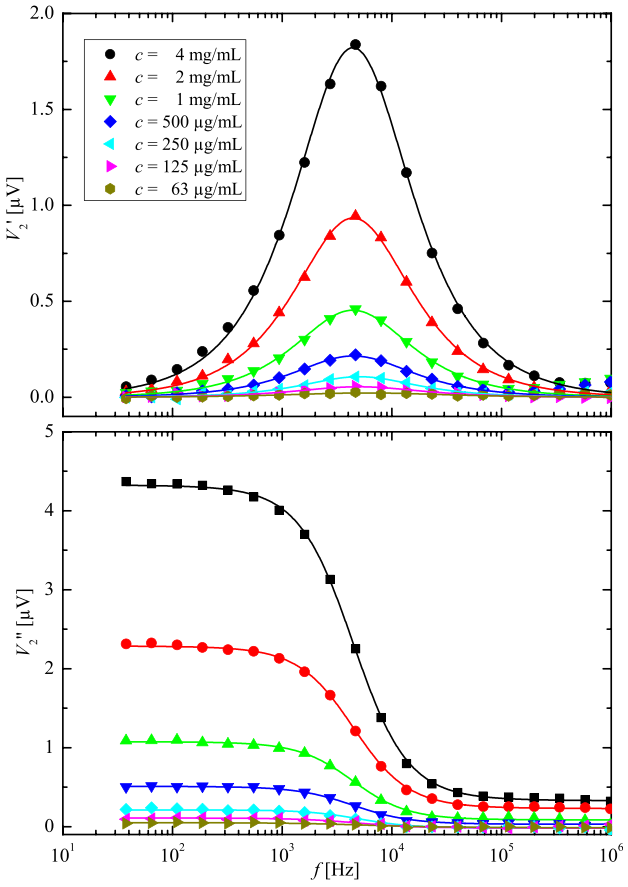

FIG. 3. In-phase (top) and out-of-phase (bottom) signals vs. bias frequency for the indicated bead suspension concentrations. The solid lines are fits of the Cole-Cole model to the measurements.

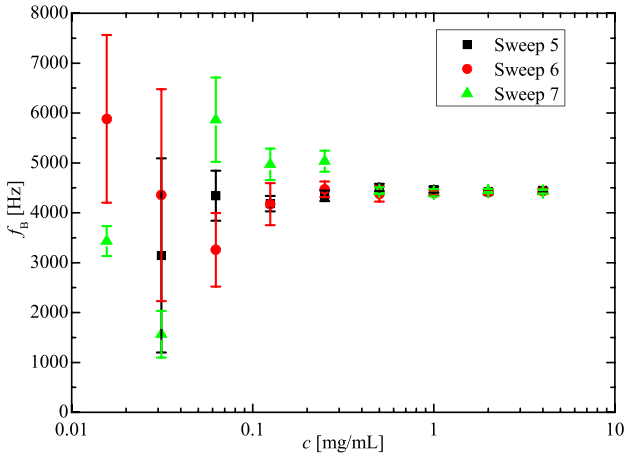

FIG. 4. Brownian relaxation frequencies extracted from sweeps 5–7 plotted against bead concentration. The length of the error bars corresponds to the standard deviations obtained from the fitting.

that for the four highest concentrations, the extracted frequencies coincide with a mean Brownian relaxation frequency of 4.4(0.1) kHz corresponding to a hydrodynamic diameter of 47(1) nm. Down to $c = 63\,\mu$g/ml the mean Brownian relaxation frequency is still 4.4 kHz, but the standard deviation increases to 0.8 kHz. The average value of the Cole-Cole parameter α was found to 0.05(0.01) for the fits shown in Fig. 4. This supports the conclusion that the curve shape is independent of the bead concentration for the investigated samples.

B. Signal at $f \simeq f_B$ vs. bead concentration

Figure 5 shows the in-phase second harmonic sensor signal of the reference points measured at $f_{ref} = 4667$ Hz normalized with c plotted vs. time t after injection of the bead suspension. The figure also shows the sweep numbers for each of the bead concentrations. Sweeps 1 and 2 are carried out without beads; the bead suspension is injected at the start of sweep 3 resulting in a signal increase and during sweeps 4–7, the signal is almost constant. During sweep 8

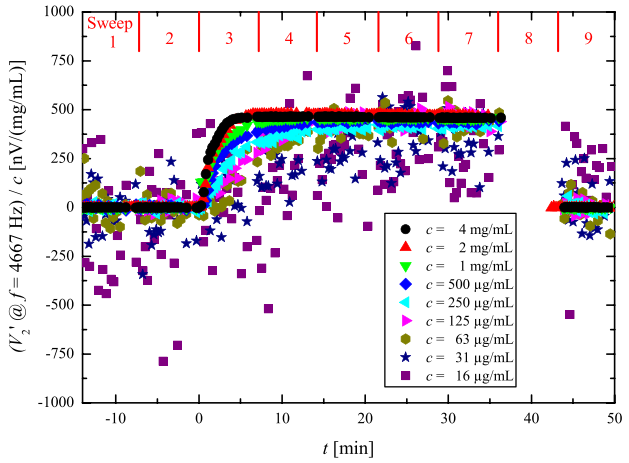

FIG. 5. In-phase 2nd harmonic sensor signal of reference points measured at $f_{ref} = 4667$ Hz normalized with bead concentration plotted as a function of the time t after injection of the bead suspension.

(not shown), the beads are washed away and the data obtained during sweep 9 shows that the signal returns to its baseline level from sweeps 1 and 2. From Fig. 5 it is observed that the signal-to-noise ratio increases with increasing bead concentration. It is also seen that a level near 460 nV/(mg/ml) is reached for all bead concentrations, except for the two lowest concentrations that are clearly at a lower level. From Fig. 5, it is also noticed that the signal rise after injection depends on the bead concentration. When the bead concentration is high, the signal reaches its steady-state value faster.

Figure 6 shows the mean values of the twenty reference points obtained during sweep 7 (last sweep before washing) as a function of the bead concentration. The error bars indicate three times the standard deviation of the mean (σ_{mean}). The line is a linear fit to the data with the intercept fixed to zero and a slope of 460(2) nV/(mg/ml). Analysis of the reference measurements obtained during sweeps 2, where the mean value defined the zero signal level in the subsequent measurements, resulted in a noise level (taken as 3 σ_{mean}) of 3.1 nV, which is shown as the horizontal dashed line in Fig. 6. It is seen that the signals from all the measured bead concentrations are significantly above the sensor noise level.

V. DISCUSSION

A. Frequency sweeps

From the frequency sweeps plotted in Fig. 3, it is seen that the shape is independent of the bead concentration, and hence that the signal scales with the concentration. This was also confirmed by the similar values of f_B and α obtained from the Cole-Cole fits for $c \geq 63\,\mu$g/ml. For the two lowest concentrations, the signal-to-noise ratio was too low to extract reliable values of f_B and α. The obtained α-value of 0.05 indicates that the bead suspension is nearly monodisperse. It is important for volume-based biodetection that the bead suspension is close to monodisperse as this results in a well defined peak in the in-phase sensor signal, which

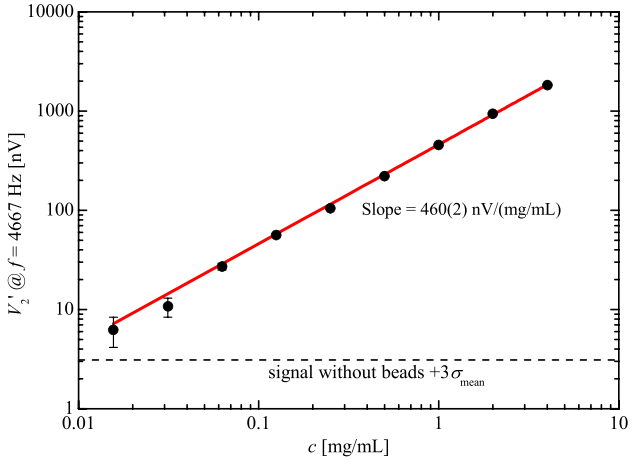

FIG. 6. Mean value of the 20 reference points measured during sweep 7 vs. bead concentration. The error bars are given as 3 σ_{mean}. The solid line is a linear fit to the data points with the intercept fixed at 0. The horizontal dashed line indicates the noise level plus 3 σ_{mean} for a measurement without any beads.

potentially allows for distinguishing the peak from isolated beads from a peak at lower frequencies due to beads bound to the target analyte.

The extracted Brownian frequencies are found to 4.4(0.8) kHz for $c \geq 63\,\mu$g/ml and 4.4(0.1) kHz for $c \geq 500\,\mu$g/ml. The mean values are identical within the uncertainties, but the standard deviation increases as the bead concentration decreases due to the lower signal-to-noise ratio. This means that if the hydrodynamic diameter needs to be extracted accurately for the present beads, a bead concentration of at least 500 μg/ml should be used.

B. Signal at $f \simeq f_B$ vs. bead concentration

Figure 5 shows the reference points measured at $f \simeq f_B$ vs. time for several bead concentrations. The values are normalized with the bead concentration and adjusted such that the injection of beads is initiated at $t = 0$ min. From this plot it is observed that the signals stabilize near 460 nV/(mg/ml) for all concentrations except for the two lowest, which do not reach this level. Figure 5 also shows that the signal returns to its baseline level after the beads are washed away, which allows for reusing the sensor.

From Fig. 5 it is seen that the rate by which the signal changes after the beads have been injected depends on the bead concentration such that a faster equilibration is found for higher bead concentrations. The equilibration arises from the fact that the bead suspension is injected into the channel containing water and that the liquid exchange near the channel wall is slower due to the parabolic velocity profile. The detailed origin of the faster equilibration for higher bead concentrations is still unknown, but we hypothesize that it could be due to cooperative phenomena, e.g., hydrodynamic interactions between the beads[20] or electrostatic repulsion between the beads due to their surface charges, which accelerate the equilibration when the bead density is high.

Figure 6 shows the average of the in-phase signal for the 20 reference points measured during sweep seven plotted vs. bead concentration. From the plot it is seen that the signal is proportional to the bead concentration with a slope of 460(2) nV/(mg/ml). It is also seen that all the measured concentrations are significantly different from reference measurement without beads on a 3 σ_{mean} level. The lowest bead mass concentration measured was 16 μg/ml, which corresponds to a particle concentration of 0.2 nM. When used in a volume-based bioassay, a lower bead concentration will increase the sensitivity and lower the dynamic range. Hence, one approach to increase the sensitivity could be to use larger magnetic beads such that the same magnetic signal can be obtained from fewer beads. However, in our system, beads that are larger than about 100 nm tend to sediment to the bottom of the fluidic channel and as the sensors are more sensitive to beads near the sensor surface, such sedimented beads will contribute significantly to the signal. The investigation of the choice of beads and optimization of the bioassay sensitivity is one focus of our future research.

VI. CONCLUSION

Based on the presented data, it is concluded that Brownian relaxation frequencies can be extracted using planar Hall effect bridge sensors for bead concentration as low as 64 μg/ml. However, a higher bead concentration results in more reliable determination of the Brownian relaxation frequency. The mean Brownian relaxation frequency for $c \geq 500\,\mu$g/ml was 4.4(0.1) kHz, which corresponds to a hydrodynamic diameter of 47(1) nm, which agrees well with the nominal size of 40 nm. The study also demonstrated that the shape of the dynamic signal is independent of the bead concentration and the amplitudes of the signals are proportional to the bead concentration once steady-state is reached. Monitoring the time dependence of the signal during bead injection showed that the signal reaches a steady state faster for higher bead concentrations. Finally, it can be concluded that the presence of beads can be detected for bead concentrations as low as 16 μg/ml.

ACKNOWLEDGMENTS

This work was supported by the Copenhagen Graduate School for Nanoscience and Nanotechnology (C:O:N:T) and the Knut and Alice Wallenberg (KAW) Foundation.

[1]A. P. Astalan, F. Ahrentorp, C. Johansson, K. Larsson, and A. Krozer, "Biomolecular reactions studied using changes in Brownian rotation dynamics of magnetic particles," Biosens. Bioelectron. **19**, 945 (2004).
[2]F. Ludwig, S. Mäuselein, E. Heim, and M. Schilling, "Magneto-relaxometry of magnetic nanoparticles in magnetically unshielded environment utilizing a differential fluxgate arrangement," Rev. Sci. Instrum. **76**, 106102 (2005).
[3]K. Enpuku, T. Minotani, T. Gima, Y. Kuroki, Y. Itoh, M. Yamashita, Y. Katakura, and S. Kuhara, "Detection of magnetic nanoparticles with superconducting quantum interference device (SQUID) magnetometer and application to immunoassays," Jpn. J. Appl. Phys., Part 2 **38**, L1102 (1999).
[4]H. Grossman, W. Myers, V. Vreeland, R. Bruehl, M. Alper, C. Bertozzi, and J. Clarke, "Detection of bacteria in suspension by using a superconducting quantum interference device," Proc. Natl. Acad. Sci. USA **101**, 129 (2004).
[5]D. R. Baselt, G. U. Lee, M. Natesan, S. W. Metzger, P. E. Sheehan, and R. J. Colton, "A biosensor based on magnetoresistance technology," Biosens. Bioelectron. **13**, 731 (1998).
[6]L. Ejsing, M. F. Hansen, A. K. Menon, H. A. Ferreira, D. L. Graham, and P. P. Freitas, "Planar Hall effect sensor for magnetic micro- and nanobead detection," Appl. Phys. Lett. **84**, 4729 (2004).
[7]S. X. Wang and G. Li, "Advances in giant magnetoresistance biosensors with magnetic nanoparticle tags: Review and outlook," IEEE T. Magn. **44**, 1687 (2008).
[8]R. S. Gaster, D. A. Hall, C. H. Nielsen, S. J. Osterfeld, H. Yu, K. E. Mach, R. J. Wilson, B. Murmann, J. C. Liao, S. S. Gambhir, and S. X. Wang, "Matrix-insensitive protein assays push the limits of biosensors in medicine," Nat. Med. **15**, 1327 (2009).
[9]A. Prieto Astalan, C. Jonasson, K. Petersson, J. Blomgren, D. Ilver, A. Krozer, and C. Johansson, "Magnetic response of thermally blocked magnetic nanoparticles in a pulsed magnetic field," J. Magn. Magn. Mater. **311**, 166 (2007).
[10]F. W. Østerberg, G. Rizzi, T. Zardán Gómez de la Torre, M. Strömberg, M. Strømme, P. Svedlindh, and M. F. Hansen, "Measurements of Brownian relaxation of magnetic nanobeads using planar Hall effect bridge sensors," Biosens. Bioelectron. **40**, 147 (2013).
[11]M. Strömberg, J. Göransson, K. Gunnarsson, M. Nilsson, P. Svedlindh, and M. Strømme, "Sensitive molecular diagnostics using volume-amplified magnetic nanobeads," Nano Lett. **8**, 816 (2008).
[12]J. Connolly and T. G. St Pierre, "Proposed biosensors based on time-dependent properties of magnetic fluids," J. Magn. Magn. Mater. **225**, 156 (2001).
[13]A. D. Henriksen, B. T. Dalslet, D. H. Skieller, K. H. Lee, F. Okkels, and M. F. Hansen, "Planar Hall effect bridge magnetic field sensors," Appl. Phys. Lett. **97**, 013507 (2010).

[14]F. W. Østerberg, B. T. Dalslet, D. Snakenborg, C. Johansson, and M. F. Hansen, "Chip-based measurements of Brownian relaxation of magnetic beads using a planar Hall effect magnetic field sensor," AIP Conf. Proc. **1311**, 176–183 (2010).
[15]B. T. Dalslet, C. D. Damsgaard, M. Donolato, M. Strømme, M. Strömberg, P. Svedlindh, and M. F. Hansen, "Bead magnetorelaxometry with an on-chip magnetoresistive sensor," Lab Chip **11**, 296 (2011).
[16]L. Neél, "Théorie du traînage magnétique des ferromagnétiques en grains fins avec applications aux terres cuites," Ann. Géophys. **5**, 99 (1949).
[17]W. Brown, "Thermal fluctuations of a single-domain particle," Phys. Rev. **130**, 1677 (1963).
[18]P. Debye, *Polar Molecules* (Chemical Catalogue Co. 1929).
[19]K. S. Cole and R. H. Cole, "Dispersion and absorption in dielectrics I. Alternating current characteristics," J. Chem. Phys. **9**, 341 (1941).
[20]C. Mikkelsen, M. F. Hansen, and H. Bruus, "Theoretical comparison of magnetic and hydrodynamic interactions between magnetically tagged particles in microfluidic systems," J. Magn. Magn. Mater. **293**, 578 (2005).

Paper III

F. W. Østerberg, G. Rizzi and M. F. Hansen
"On-chip measurements of Brownian relaxation of magnetic beads with diameters from 10 nm to 250 nm "
J. Appl. Phys. **113**, 154507 (2013)

JOURNAL OF APPLIED PHYSICS **113**, 154507 (2013)

On-chip measurements of Brownian relaxation of magnetic beads with diameters from 10 nm to 250 nm

Frederik Westergaard Østerberg,[a] Giovanni Rizzi, and Mikkel Fougt Hansen[b]
Department of Micro- and Nanotechnology, Technical University of Denmark, DTU Nanotech, Building 345 East, DK-2800 Kongens Lyngby, Denmark

(Received 16 January 2013; accepted 4 April 2013; published online 19 April 2013)

We demonstrate the use of planar Hall effect magnetoresistive sensors for AC susceptibility measurements of magnetic beads with frequencies ranging from DC to 1 MHz. This wide frequency range allows for measuring Brownian relaxation of magnetic beads with diameters ranging from 10 nm to 250 nm. Brownian relaxation is measured for six different magnetic bead types and their hydrodynamic diameters are determined. The hydrodynamic diameters are found to be within 40% of the nominal bead diameters. We discuss the applicability of the different bead types for volume-based biosensing with respect to sedimentation, magnetic trapping, and signal per bead. Among the investigated beads, we conclude that the beads with a nominal diameter of 80 nm are best suited for future on-chip volume-based biosensing experiments using planar Hall effect sensors. © *2013 AIP Publishing LLC* [http://dx.doi.org/10.1063/1.4802657]

I. INTRODUCTION

Magnetic beads have proven to be a promising ingredient in future biosensors.[1–4] Since most biological samples are non-magnetic, the readout will not be disturbed by chemical or biological components of the sample. Magnetic beads also have the advantage that they can be manipulated magnetically and are generally well dispersed in a liquid sample such that diffusion times can be significantly reduced. Finally, the presence and properties of magnetic beads can be detected by magnetic field sensors to directly provide an electrical signal.

Connolly and St Pierre[5] first proposed to use Brownian relaxation measurements of magnetic beads for biosensing. Brownian relaxation is the physical rotation of a bead in response to an oscillating magnetic field and it is characterized by the Brownian relaxation frequency, which is inversely proportional to the hydrodynamic volume of the bead. Using functionalized magnetic beads, it is possible to bind a target analyte to the beads to obtain a detectable increase of their hydrodynamic size.

The simplest assay is to directly detect a hydrodynamic size change of the free beads in suspension due to bound analytes. However, as most analytes are typically much smaller than the beads, this will only give rise to a limited change of hydrodynamic size.[6] Moreover, the change may be difficult to resolve due to the inevitable bead size distribution. A more effective assay strategy is to use the target analyte to form clusters of beads and hence induce bead agglutination.[7] Yet another strategy is to use amplification of the target analyte to form substantially larger entities, e.g., by forming large DNA coils by a rolling circle amplification.[8,9] Such coils have the advantage of both changing the hydrodynamic size of single beads significantly and that each coil can bind multiple beads.[10] The drawback is that the rolling circle amplification requires additional sample preparation.

Brownian relaxation of magnetic beads can be measured with various techniques including inductive methods,[6] fluxgates,[11] superconducting quantum interference device (SQUID) magnetometers,[12] and magnetoresistive sensors.[13,14] Particularly magnetoresistive sensors are promising in future lab-on-chip devices as they are small, potentially inexpensive, require small sample volumes, and can be integrated with sample preparation in a microfluidic device.

The frequency range in which a given technique operates determines the bead sizes for which Brownian relaxation can be measured. Thus, it is advantageous to have a detection system that can operate at frequencies spanning many orders of magnitude.

Here, we demonstrate on-chip measurements of Brownian relaxation of magnetic beads with diameters ranging from 10 nm to 250 nm using so-called planar Hall effect bridge (PHEB) sensors[15,16] and that these sensors are feasible for dynamic magnetic measurements up to MHz frequencies. Finally, we discuss the best choice of bead type and size for future on-chip volume-based bioassays employing these sensors.

II. THEORY

A. Brownian relaxation of magnetic beads

When a magnetic bead is placed in an external magnetic field, the magnetic moment will align with the direction of the applied field. The moment of the bead may relax by an internal flipping of the moment (Néel relaxation[17]) and by a physical rotation (Brownian relaxation[18]). The Néel relaxation may be relevant for magnetic nanograins smaller than about 10–20 nm, when these form either a single magnetic core or being part of a multigrain core. In this work, we will for simplicity assume that Néel relaxation can be neglected, i.e., that the Brownian relaxation mechanism dominates. Thus, when a bead is placed in a magnetic field oscillating at

[a]Electronic mail: Frederik.Osterberg@nanotech.dtu.dk.
[b]Electronic mail: Mikkel.Hansen@nanotech.dtu.dk.

frequency f, the dynamic behavior is characterized by the Brownian relaxation frequency

$$f_B = \frac{k_B T}{6\pi\eta V_h}, \quad (1)$$

where $k_B T$ is the thermal energy, η is the dynamic viscosity of the liquid in which the bead is suspended and V_h is the hydrodynamic volume of the bead. The dynamic magnetic behavior of a magnetic bead ensemble in response to an applied magnetic field is described by the complex magnetic susceptibility $\chi = \chi' - i\chi''$, where χ' and χ'' denote the in-phase and out-of-phase magnetic susceptibilities, respectively. For $f \ll f_B$, the beads rotate in phase with the applied field and for $f \gg f_B$ the field is oscillating too fast for the beads to respond. When $f = f_B$, the component of the bead moment lagging behind the applied field assumes its maximum, resulting in a peak in the out-of-phase magnetic susceptibility. Cole and Cole[19] have shown empirically that the complex magnetic susceptibility due to Brownian relaxation for a polydisperse ensemble of beads is often well described by

$$\chi = \frac{\chi_0 - \chi_\infty}{1 + (if/f_B)^{1-\alpha}} + \chi_\infty, \quad (2)$$

where χ_0 and χ_∞ are the DC and high-frequency susceptibilities, respectively. The parameter α is a measure of the polydispersity of the bead ensemble and can assume values between 0 and 1. For a monodisperse sample, $\alpha = 0$ and the Cole-Cole model reduces to the Debye model.[20]

B. Sensor signal

The sensors used in this study are based on the anisotropic magnetoresistance (AMR) effect.[21] The sensors are structured in a bridge geometry as shown in Fig. 1. A bias current I is applied in the x-direction and the potential difference V_y is measured across the y-direction. The signal from the sensor bridge is the same as for cross-shaped planar Hall effect sensors except for a geometrical amplification.[15] To distinguish them from other AMR bridge geometries, we have therefore named them PHEB sensors.[15]

For low magnetic fields, the sensor signal is linear and given by[15]

$$V_y = IS_0 H_y, \quad (3)$$

where S_0 is the low-field sensitivity and H_y is the average magnetic field acting on the sensor area in the y-direction.

Our measurements of the magnetic bead susceptibility are performed in nominally zero externally applied magnetic field and the beads are magnetized by the magnetic field arising from the alternating bias current $I(t) = I_{AC}\sin(2\pi ft)$ passed through the sensors. We have previously shown[16] that the in-phase and out-of-phase components of the complex second harmonic sensor signal $V_2 = V_2' + iV_2''$ measured using lock-in technique can be written as

$$V_2' = -2^{-3} I_{AC}^2 S_0 \gamma_1 \chi'', \quad (4)$$

$$V_2'' = -2^{-3} I_{AC}^2 S_0 (\gamma_0 + \gamma_1 \chi'). \quad (5)$$

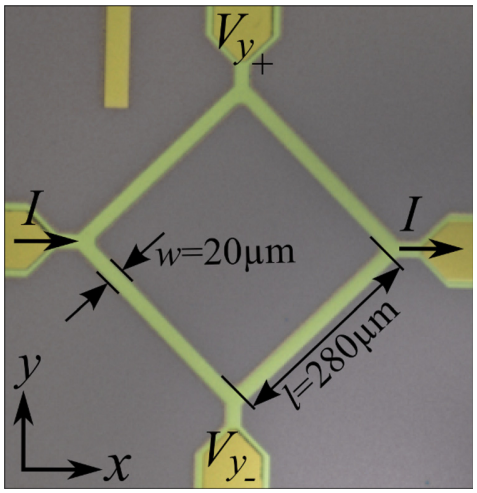

FIG. 1. Picture of a sensor with definition of dimensions. The bias current I is applied through the arms in the x-direction, while the potential difference V_y is measured across the y-direction.

Here, γ_0 is a constant depending on the sensor stack and geometry that describes the sensor self-biasing and γ_1 is a parameter depending on the sensor geometry and distribution of beads that describes the magnetic field acting on the sensor from magnetic beads magnetized by the sensor self-field. The value of γ_1 is positive in the presence of beads and zero in the absence of beads.[22] Thus, the in-phase second harmonic sensor signal is proportional to the out-of-phase magnetic bead susceptibility and the out-of-phase second harmonic sensor signal depends linearly on the in-phase magnetic bead susceptibility. The term γ_0 can be found from a measurement without beads and subtracted from the out-of-phase sensor signal. The resulting corrected value $V_{2,cor}''$ is proportional to the in-phase magnetic bead susceptibility. In the data presentation and analysis, it is convenient to use this to relate the corrected second harmonic sensor signal $V_{2,cor} = V_2' + iV_{2,cor}''$ to the Cole-Cole expression, Eq. (2), as

$$-iV_{2,cor} = V_{2,cor}'' - iV_2' = \frac{V_0 - V_\infty}{1 + (if/f_B)^{1-\alpha}} + V_\infty, \quad (6)$$

where V_0 and V_∞ are defined as

$$V_0 = -2^{-3} I_{AC}^2 S_0 \gamma_1 \chi_0, \quad (7)$$

$$V_\infty = -2^{-3} I_{AC}^2 S_0 \gamma_1 \chi_\infty. \quad (8)$$

We note that the value of γ_1 cannot be determined unless the bead distribution is known and that it is sensitive to changes of the bead distribution and concentration near the sensor surface over the duration of an experiment. Thus, the method provides relative and not absolute values of the complex magnetic susceptibility and care should be taken if beads tend to sediment.

III. EXPERIMENTAL

The planar Hall effect bridge sensor used for the following experiment consists of four segments arranged in a Wheatstone bridge configuration as shown in Fig. 1, each

bridge segment has a length of $l = 280\,\mu$m and a width of $w = 20\,\mu$m. The exchange-biased sensor stack consisting of Ta(3 nm)/$Ni_{80}Fe_{20}$(30 nm)/$Mn_{80}Ir_{20}$(20 nm)/Ta(3 nm) has been sputter-deposited in an applied magnetic field of 20 mT to define an easy direction of magnetization along the positive x-direction. For further details on the fabrication, see Ref. 16. The low-field sensitivity for this sensor was found to $S_0/\mu_0 = -581\,\mathrm{V/(T\,A)}$, where μ_0 is the permeability of free space. The bridge resistance along the current was found to 151.5 Ω.

Electrical contact to the sensor was made with a click-on fluidic system,[14] which also defined the fluidic channel on top of the sensor. The channel dimensions were length × width × height = 5 mm × 1 mm × 0.1 mm. During all measurements, the temperature of the sensor mount was kept constant at (25.00 ± 0.01)°C using a proportional integral differential (PID) controlled Peltier element. The sensor was neither electrically nor magnetically shielded.

A. Brownian relaxation measurements

The second harmonic sensor signals were measured using two different lock-in amplifiers depending on the investigated interval of frequencies.

Frequency sweeps below 50 kHz were carried out using a Stanford Research Systems model SR830 lock-in amplifier. The alternating sensor bias current of amplitude $I_{AC} = 20$ mA was supplied by a Keithley model 6221 AC current source. The two instruments were synchronized via a trigger link. The frequency of the current was swept from $f = 43.7$ kHz to $f = 1.88$ Hz in 29 logarithmically equidistant steps. After each measurement at frequency f, a reference measurement was performed at a reference frequency f_{ref} near the expected Brownian relaxation frequency of the beads under investigation. A full frequency sweep consisting of the measurements at 30 different frequencies and the 30 reference measurements took 3 min and 45 s.

Frequency sweeps extending up to 5 MHz were carried out using a Zurich Instruments HF2LI lock-in amplifier. The internal voltage output of the lock-in amplifier was used to bias the sensors corresponding to a current of amplitude 20 mA. The frequency was swept from $f = 5$ MHz to $f = 37.7$ Hz in 30 logarithmically equidistant steps. Also for these measurements, reference points were measured between each frequency. A full frequency sweep took 5 min and 20 s.

Brownian relaxation measurements were performed for six different bead types with nominal diameters D_{nom} ranging from 10 nm to 250 nm. The following bead types were studied: (1)–(3) iron oxide nanoparticles with nominal diameters of $D_{nom} = 10$ nm, 25 nm, and 40 nm and carboxylic acid surface groups (cat. SHP) from Ocean Nanotech, USA, suspended in MilliQ water; (4) plain bionized nano ferrite (BNF)-starch beads with a nominal diameter of $D_{nom} = 80$ nm (cat. 10-00-801) from Micromod, Germany, suspended in phosphate buffered saline (PBS); (5)-(6) plain Nanomag-D beads with nominal diameters of $D_{nom} = 130$ nm (cat. 09-00-132) and 250 nm (cat. 09-00-252) from Micromod, Germany, suspended in PBS. Beads with nominal diameters from 10 nm to 40 nm were characterized using the high-frequency set-up, and beads with nominal diameters from 80 nm to 250 nm beads were characterized using the low-frequency set-up. The bead concentration was kept constant at 1 mg/ml for all six bead types.

For measurements with both lock-ins, reference frequency sweeps without beads were measured with liquid in the fluidic channel to correct for γ_0 before injection of the bead suspension. Then, 20 μl of bead suspension was injected into the liquid channel on the chip at a flow rate of 13.3 μl/min for 1.5 min. This volume corresponds to 40 times the channel volume. After injection of the bead suspension, the beads were left for characterization in the fluidic channel for about 60 min (Ocean Nanotech beads) or 240 min (Micromod beads) before being washed out at flow rate of 300 μl/min. Measurements were also performed after washing to verify that the signals returned to their initial values. Measurements on the same bead suspension using both set-ups were found to give identical results in the overlapping intervals, although with a slightly lower data noise at low frequencies using the set-up for low frequencies (data not shown).

B. Data treatment

First, the data were corrected for instrumental phase shifts and offsets due to γ_0 using the reference sweeps measured without beads. Then, the data recorded at different frequencies were corrected for the variation of the signal amplitude due to bead sedimentation over the duration of a frequency sweep. This was done by normalizing the measurement at each frequency f with the in-phase second harmonic sensor data recorded at $f = f_{ref}$. Finally, all data in the frequency sweep were multiplied with the average value of the measurements at $f = f_{ref}$ obtained during the frequency sweep. Bead sedimentation over a single frequency sweep was mainly an issue for the 250 nm beads from Micromod. Subsequently, the modified Cole-Cole model, Eq. (6), was fitted to the corrected data with f_B, α, V_0, and V_∞ as the four free fitting parameters. The model was fitted to the in-phase and out-of-phase sensor data simultaneously with a single set of parameters. The hydrodynamic diameters were calculated from the obtained Brownian relaxation frequency using Eq. (1) assuming that the beads are spherical and that PBS has the dynamic viscosity of water. The hydrodynamic diameters will be reported instead of the Brownian relaxation frequencies.

IV. RESULTS

A. Signal vs. time at $f = f_{ref}$

The in-phase signals measured at $f = f_{ref}$ chosen near the Brownian relaxation frequencies are plotted vs. time t after injection of the bead suspension in Fig. 2 for all bead types. The value of f_{ref} is indicated in the figure and listed in Table I for each bead type. The signals from the Ocean Nanotech beads (Fig. 2(a)) show a steep increase over the first few minutes and become stable after ~5–15 min. The signals from the Micromod beads (Fig. 2(b)) show a steep initial increase followed by a slow linear increase with time for at

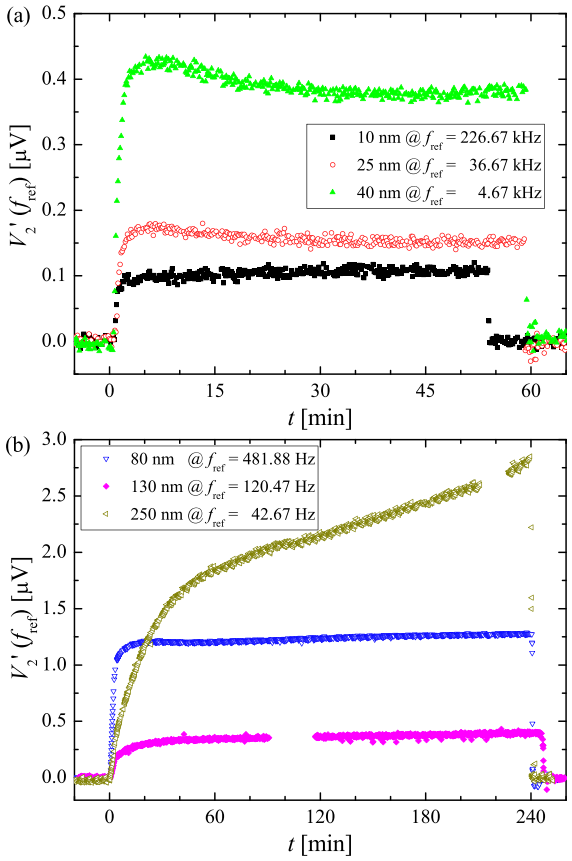

FIG. 2. In-phase second harmonic signal measured at the indicated values of f_{ref} vs. time t after injection of the bead suspension for (a) Ocean Nanotech beads with nominal diameters of 10 nm, 25 nm, and 40 nm and (b) Micromod beads with nominal diameters of 80 nm, 130 nm, and 250 nm. In the final part of each experiment, the bead suspension is washed out of the channel.

least several hours. The initial signal increase takes place at a higher rate for smaller beads than for larger beads. The transition to the region with a linearly increasing signal occurs at $t \sim 10$ min, ~15 min, and ~45 min for the Micromod beads with $D_{nom} = 80$ nm, 130 nm, and 250 nm, respectively, and the linear increase is significantly larger for the 250 nm beads than for the other two bead sizes. From the figure it is also seen that, except for the 130 nm beads, the signal magnitude increases with increasing bead size. It is also noted that all signals return to their baseline level after washing.

From the reference measurements, the standard deviation of the baseline in-phase sensor signal is estimated for each of the six reference frequencies. This is done by finding the standard deviation of the points measured without beads present in the fluidic system ($\sigma_{NoBeads}$). This number represents the combined effect of the sensor and amplifier noise and fluctuations of the ambient conditions (temperature, magnetic, and electric fields) during an experiment and defines the smallest signal change that can be resolved under our experimental conditions. The six values are listed in Table I. It is seen that the values of $\sigma_{NoBeads}$ are constant at 5–6 nV for the frequencies between 226.67 kHz and 4.67 kHz measured with the HF2LI lock-in amplifier, whereas they increase from 4 nV to 10.9 nV when decreasing the frequency from 481.88 Hz to 42.67 Hz for the SR830 lock-in amplifier.

TABLE I. Standard deviation $\sigma_{NoBeads}$ of baseline in-phase sensor signal at $f = f_{ref}$ for the six values of f_{ref} used for the different bead types.

D_{nom} (nm)	Lock-in	f_{ref}	$\sigma_{NoBeads}$ (nV)
10	HF2LI	226.67 kHz	5.1
25	HF2LI	36.67 kHz	5.6
40	HF2LI	4.67 kHz	5.6
80	SR830	481.88 Hz	4.0
130	SR830	120.47 Hz	7.6
250	SR830	42.67 Hz	10.9

B. Brownian relaxation measurements with PHEB

In Fig. 3 the in-phase (top) and out-of-phase (bottom) second harmonic sensor signals are plotted as function of frequency for measurements initiated at $t = 20$ min. The solid lines are least squares curve fits of the Cole-Cole model to the data. The model generally provides good fits to the data. In order to better illustrate the shape of the curves and the quality of the fits, the second harmonic signals have been normalized to their maximum values and plotted in Fig. 4. From the normalized plots, it is seen that the peaks in the in-phase signals are comparatively narrow for the 10 nm, 40 nm, and 80 nm beads and wide for 25 nm, 130 nm, and 250 nm beads.

The values of the fitting parameters are shown in Table II. The height of the peak in the V_2' data depends only

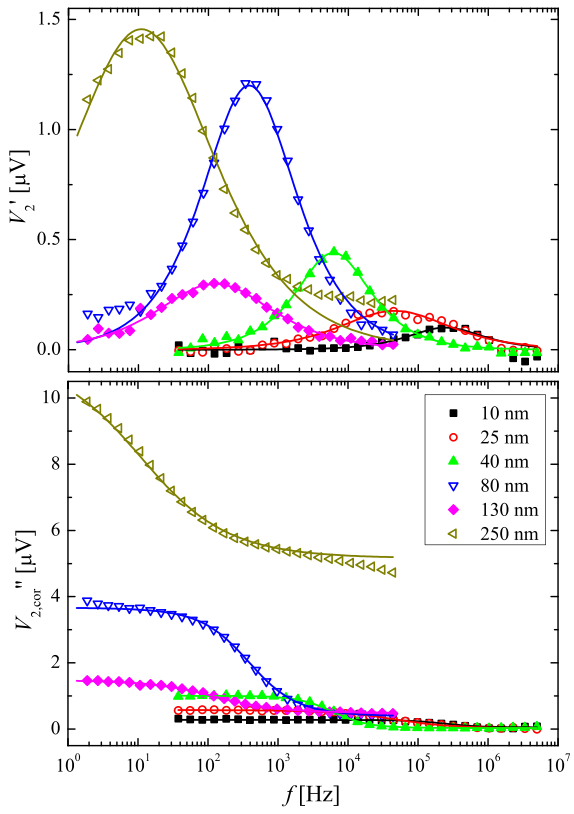

FIG. 3. In-phase (top) and out-of-phase (bottom) corrected second harmonic sensor signals. The solid lines are fits of the Cole-Cole model to the data.

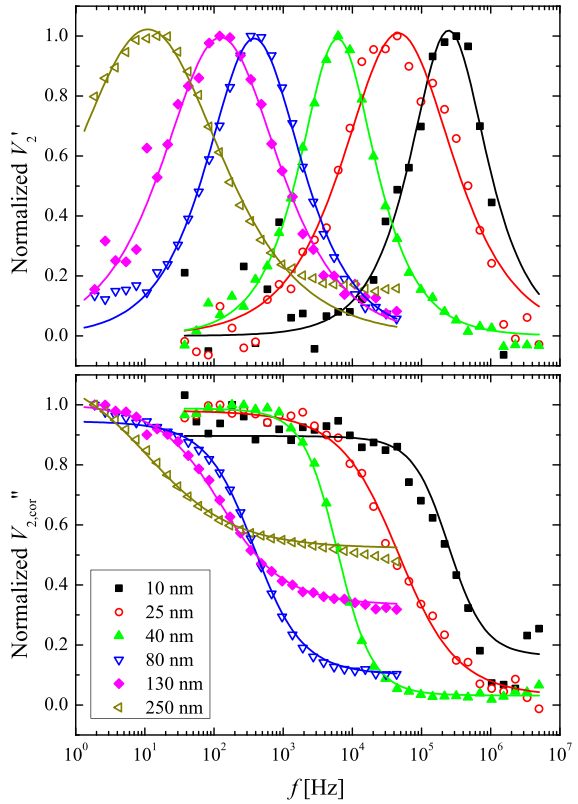

FIG. 4. In-phase (top) and out-of-phase (bottom) corrected second harmonic sensor signal from Fig. 3 normalized to their respective maximum values. The solid lines are fits of the Cole-Cole model to the data.

on $V_0 - V_\infty$ and α and is given by $V'_{2,\text{peak}} = -\text{Im}[(V_0 - V_\infty)/(1+\text{i}^{1-\alpha})]$. For $\alpha = 0$, $V'_{2,\text{peak}} = \frac{1}{2}(V_0 - V_\infty)$. From the table, it is observed that the hydrodynamic diameters obtained from the fits are all within 40% of the nominal bead sizes. It is also seen that for the 10 nm-80 nm beads the value of $V_0 - V_\infty$ increases with the bead diameter. V_∞ is found to be close to zero for the beads from Ocean Nanotech.

1. Sensor signal vs. nominal bead concentration

From the measurements, it is possible to estimate the signal normalized with the bead molar concentration for the six different bead types. This number is important when estimating the suitability of each bead type for volume-based biosensing. The signal per bead molar concentration is calculated by dividing the in-phase peak signal $V'_{2,\text{peak}}$ with the molar concentration c of beads. The in-phase peak signal per concentration is listed in Table II. From this table it is seen that, although the bead concentration by mass is the same for all samples, the samples with larger beads provide more signal. Obviously, when the signal is normalized with the molar concentration of the bead suspension, the larger beads provide substantially higher signals. For example, the normalized signal for the 250 nm beads is found to be 5 orders of magnitude larger than that for the 10 nm beads. If the bead magnetizations were the same, this difference would be anticipated to be $25^3 = 15\,625$, which is one order of magnitude smaller than the observed ratio. However, it should be noted that the larger beads also sediment such that the actual bead concentration near the sensor surface is higher than the nominal one.

V. DISCUSSION

A. Brownian relaxation measurements

It is seen from the results that the planar Hall effect sensor can be used to measure Brownian relaxation over the frequency range 1 Hz–1 MHz. With this frequency range it is shown that Brownian relaxation can be measured for beads ranging in diameters from 10 nm to 250 nm and meaningful hydrodynamic diameters can be extracted from the measurements. The hydrodynamic diameters for the small beads from Ocean Nanotech are within a few nanometers of their nominal values. This is consistent with the assumption that Brownian relaxation dominates for these particles. These differences can be due to batch to batch variations. The hydrodynamic diameters found for the beads from Micromod are found to be significantly larger than their nominal values. It is expected that the hydrodynamic diameters are larger than their nominal values, because the nominal diameters are determined from transmission electron microscopy (TEM), which measures the core size. However, the hydrodynamic size obtained for the 250 nm beads is too large to be explained by differences in measuring techniques alone. Effects that could contribute to a higher measured hydrodynamic size are trapping of beads by the magnetostatic field from the sensor stack, interactions between the bead and the sensor surface, and bead-bead interactions.

B. Signal vs. time at $f = f_{\text{ref}}$

In the experiments, we found a steep initial increase of the signal followed by either a stable signal for the beads that are smaller than 100 nm or a slowly increasing signal for the beads that are larger than about 100 nm (cf. Fig. 2).

TABLE II. Values of D_h, α, $V_0 - V_\infty$, and V_∞ obtained from Cole-Cole fits to the frequency sweeps initiated 20 min after injection of the bead suspensions. The numbers in parenthesis after the fitting parameter are 95% uncertainties. The last two columns list the molar concentration c of each bead type in nM and the peak sensor signal normalized with the bead molar concentration $V'_{2,\text{peak}}/c$. $\text{LOD}_{\text{theory}}$ is the theoretical limit of detection calculated by $\sigma_{\text{NoBeads}}/(V'_{2,\text{peak}}/c)$.

D_{nom} [nm]	Producer	D_h [nm]	α	$V_0 - V_\infty$ [μV]	V_∞ [μV]	c [nM]	$V'_{2,\text{peak}}/c$ [nV/nM]	$\text{LOD}_{\text{theory}}$ [pM]
10	Ocean Nanotech	12.4(3)	0.08(5)	0.23(2)	0.05(18)	860	0.1	5.1×10^4
25	Ocean Nanotech	21.6(4)	0.28(2)	0.56(2)	0.02(17)	58	3.0	1.9×10^3
40	Ocean Nanotech	42.4(2)	0.06(1)	0.97(1)	0.03(15)	14	31.4	1.8×10^2
80	Micromod	107.0(9)	0.20(1)	3.29(4)	0.4(7)	2.0	602	6.6
130	Micromod	155(2)	0.31(1)	0.99(2)	0.5(2)	0.48	622	12.2
250	Micromod	349(3)	0.43(1)	6.01(7)	5.2(5)	0.08	17.9×10^3	0.6

The steep initial signal increase is due to the injection of the bead suspension in the already liquid-filled fluidic system; due to the parabolic velocity profile of the liquid during injection, the liquid near the channel walls is replaced more slowly than that in the center of the channel. This results in an equilibration process, where the bead concentration at the sensor surface increases due to continued injection of the bead suspension as well as due to gravitational sedimentation and diffusion of the beads.

The beads are subject to gravitational sedimentation at a velocity $u = D^2(\rho_b - \rho_f)g/(18\eta)$,[23] where D is the bead diameter, ρ_f and ρ_b are the densities of the fluid and beads, respectively, and g is the gravitational acceleration. Taking $D = D_{nom}$, we can find the characteristic time t_{sed} for sedimentation of the beads in the channel as h/u, where $h = 0.1$ mm is the channel height. For the Micromod beads, $\rho_b \approx 3\,g/cm^3$ and we find $t_{sed}[min] \simeq 25$, 90, and 240 for the beads with $D_{nom}[nm] = 250$, 130, and 80, respectively.

The corresponding characteristic time t_{dif} for diffusion over the height of the liquid channel is estimated from the Stokes-Einstein diffusivity $D_{dif} = k_B T/(3\pi\eta D_{nom})$ using that $D_{dif} \sim h^2/t_{dif}$. For the Micromod beads with $D_{nom}[nm] = 250$, 130, and 80, we obtain $t_{dif}[min] \simeq 96$, 50, and 31, respectively. These simple arguments show that bead sedimentation dominates over the random thermal motion of the beads for the 250 nm beads that sedimentation and thermal motion are comparable for the 130 nm beads and that thermal motion dominates for beads with sizes of 80 nm and below.

Experimentally, we have observed an initial steep increase of the signal measured vs. time at $f = f_{ref}$ in Fig. 2 upon injection of the bead suspension. As previously mentioned, due to the parabolic velocity profile and that liquid without beads is already present in the channel during injection, the bead concentration near the bottom of the channel, where the sensor is located, is therefore initially lower than in the bulk of the bead suspension. This concentration increases due to exchange of liquid in the channel, sedimentation and equilibration of the bead concentration by diffusion. For the 250 nm beads, this equilibration is dominated by sedimentation and the estimated sedimentation time of about 25 min is consistent with the observed time of about 45 min in Fig. 2(b). For the beads with sizes below 130 nm, the equilibration time is mainly attributed to diffusion of the beads. The beads from Ocean Nanotech are so small that the equilibration takes place while the bead suspension is injected. After the initial equilibration, the signals from all bead types stabilize and remain essentially constant except for the 250 nm Micromod beads, where the signal shows a significant increase with time. We attribute this increase to accumulation of beads near the sensor edges due to the magnetostatic field from the sensor stack. This accumulation was clearly visible in micrographs of the sensor during the experiments and was also visible in the frequency sweeps as a signal occurring at a lower frequency than that due to freely rotating beads. For the other bead types, no bead accumulation near the sensor edges could be observed visually and the signal tail at low frequencies in the sensor measurements due to immobilized or partially immobilized beads was significantly smaller or negligible. Thus, the sedimentation and trapping of the 250 nm beads results in a time dependence of the signal due to the bead suspension itself, i.e., prior to introduction of biomolecules, which is clearly undesirable. These beads are, therefore, not suited for biosensing with the present sensors.

1. Sensor signal vs. nominal bead concentration

From the value of signal per bead concentration listed in Table II, it is clear that the choice of bead type will be very important for the sensitivity of a volume-based biosensor. For the beads investigated here, the peak signal normalized with the nominal bead molar concentration varies over 5 orders of magnitude, which means that the choice of bead type has a high impact on the sensitivity and dynamic range of concentrations that can be detected. For instance, the bead concentration of the 10 nm beads is 860 nM, which means that, at least in principle, it will be possible to detect analyte concentrations up to this value. The downside is a low signal per bead which for the 10 nm beads is only 0.1 nV/nM. Comparing to the baseline resolution from Table I of 5.1 nV, it implies that the theoretical limit of detection LOD_{theory} is expected to be higher than ~51 nM. On the other hand, for the 250 nm beads the theoretical dynamic range is 0.6–81 pM, the drawback of these beads is that they sediment, which will make them difficult to use for biosensing. The sedimentation of the 80 nm beads is limited and the signal is large. Thus, these beads will be the best compromise for biosensing to achieve a low detection limit. The theoretical dynamic range for the 80 nm beads is 6 pM-2 nM. The upper sensitivity limit can be moved to higher concentrations by increasing the bead concentration, but this will also increase the background signal and potentially make it more difficult to measure low concentrations. The lower limit of detection can be decreased further by decreasing the bead concentration and/or increasing the signal-to-noise ratio of the measurement system. Currently most of the noise is induced by the lock-in amplification, which means increasing the sensor signal will increase the signal-to-noise ratio. This can be achieved by using lower noise amplification electronics, increasing the measurement time to reduce the effect of the noise or improving the sensor design. One way of increasing the sensor signal is to increase the length of each bridge segment, which is the focus of future studies.

VI. CONCLUSION

It has been demonstrated that planar Hall effect bridge sensors can be used to measure AC susceptibility of magnetic beads for frequencies spanning from DC to 1 MHz. This wide frequency span allows for measuring Brownian relaxation of beads with nominal diameters ranging from 10 nm to 250 nm. The hydrodynamic diameters obtained from the measurement are all within 40% of the nominal diameter supplied by the manufacturer. From the measurements, it is also concluded that among the investigated beads the 80 nm beads are most promising for volume-based biosensing, because they provide the largest signal per bead among the bead types that do not suffer from sedimentation and magnetic trapping issues on the sensors.

ACKNOWLEDGMENTS

This work was supported by the Copenhagen Graduate School for Nanoscience and Nanotechnology (C:O:N:T) and the Knut and Alice Wallenberg (KAW) Foundation.

[1]I. Koh and L. Josephson, "Magnetic nanoparticle sensors," Sensors **9**, 8130 (2009).
[2]S. X. Wang and G. Li, "Advances in giant magnetoresistance biosensors with magnetic nanoparticle tags: Review and outlook," IEEE Trans. Magn. **44**, 1687 (2008).
[3]N. Jaffrezic-Renault, C. Martelet, Y. Chevolot, and J.-P. Cloarec, "Biosensors and bio-bar code assays based on biofunctionalized magnetic microbeads," Sensors **7**, 589 (2007).
[4]J. Göransson, T. Zardán Gómez De La Torre, M. Strömberg, C. Russell, P. Svedlindh, M. Strømme, and M. Nilsson, "Sensitive detection of bacterial DNA by magnetic nanoparticles," Anal. Chem. **82**, 9138 (2010).
[5]J. Connolly and T. G. St Pierre, "Proposed biosensors based on time-dependent properties of magnetic fluids," J. Magn. Magn. Mater. **225**, 156 (2001).
[6]A. P. Astalan, F. Ahrentorp, C. Johansson, K. Larsson, and A. Krozer, "Biomolecular reactions studied using changes in Brownian rotation dynamics of magnetic particles," Biosens. Bioelectron. **19**, 945 (2004).
[7]C. Hong, C. Wu, Y. Chiu, S. Yang, H. Horng, and H. Yang, "Magnetic susceptibility reduction method for magnetically labeled immunoassay," Appl. Phys. Lett. **88**, 212512 (2006).
[8]A. Fire and X. Si-Qun, "Rolling replication of short DNA circles," Proc. Natl. Acad. Sci. U.S.A. **92**, 4641 (1995).
[9]D. Liu, S. L. Daubendiek, M. A. Zillman, K. Ryan, and E. T. Kool, "Rolling circle DNA synthesis: Small circular oligonucleotides as efficient templates for DNA polymerases," J. Am. Chem. Soc. **118**, 1587 (1996).
[10]M. Strömberg, J. Göransson, K. Gunnarsson, M. Nilsson, P. Svedlindh, and M. Strømme, "Sensitive molecular diagnostics using volume-amplified magnetic nanobeads," Nano Lett. **8**, 816 (2008).
[11]F. Ludwig, S. Mäuselein, E. Heim, and M. Schilling, "Magnetorelaxometry of magnetic nanoparticles in magnetically unshielded environment utilizing a differential fluxgate arrangement," Rev. Sci. Instrum. **76**, 106102 (2005).
[12]H. Grossman, W. Myers, V. Vreeland, R. Bruehl, M. Alper, C. Bertozzi, and J. Clarke, "Detection of bacteria in suspension by using a superconducting quantum interference device," Proc. Natl. Acad. Sci. U.S.A. **101**, 129 (2004).
[13]B. T. Dalslet, C. D. Damsgaard, M. Donolato, M. Strømme, M. Strömberg, P. Svedlindh, and M. F. Hansen, "Bead magnetorelaxometry with an on-chip magnetoresistive sensor," Lab Chip **11**, 296 (2011).
[14]F. W. Østerberg, B. T. Dalslet, D. Snakenborg, C. Johansson, and M. F. Hansen, "Chip-based measurements of Brownian relaxation of magnetic beads using a planar Hall effect magnetic field sensor," AIP Conf. Proc. **1311**, 176–183 (2010).
[15]A. D. Henriksen, B. T. Dalslet, D. H. Skieller, K. H. Lee, F. Okkels, and M. F. Hansen, "Planar Hall effect bridge magnetic field sensors," Appl. Phys. Lett. **97**, 013507 (2010).
[16]F. W. Østerberg, G. Rizzi, T. Zardán Gómez de la Torre, M. Strömberg, M. Strømme, P. Svedlindh, and M. F. Hansen, "Measurements of Brownian relaxation of magnetic nanobeads using planar Hall effect bridge sensors," Biosens. Bioelectron. **40**, 147 (2013).
[17]L. Néel, "Théorie du traînage magnétique des ferromagnétiques en grains fins avec applications aux terres cuites," Ann. Géophys. **5**, 99 (1949).
[18]W. Brown, "Thermal fluctuations of a single-domain particle," Phys. Rev. **130**, 1677 (1963).
[19]K. S. Cole and R. H. Cole, "Dispersion and absorption in dielectrics. I. Alternating current characteristics," J. Chem. Phys. **9**, 341 (1941).
[20]P. Debye, *Polar Molecules* (Chemical Catalogue Co., 1929).
[21]W. Thomson, "On the electro-dynamic qualities of metals: Effects of magnetization on the electric conductivity of nickel and of iron," Proc. R. Soc. London **8**, 546 (1856).
[22]T. B. G. Hansen, C. D. Damsgaard, B. T. Dalslet, and M. F. Hansen, "Theoretical study of in-plane response of magnetic field sensor to magnetic beads magnetized by the sensor self-field," J. Appl. Phys. **107**, 124511 (2010).
[23]F. W. Østerberg, B. T. Dalslet, C. D. Damsgaard, S. C. Freitas, P. P. Freitas, and M. F. Hansen, "Bead capture on magnetic sensors in a microfluidic system," IEEE Sens. J. **9**, 682 (2009).

Paper IV

F. W. Østerberg, G. Rizzi and M. F. Hansen
"On-chip Brownian relaxation measurements of magnetic nanobeads in the time domain"
J. Appl. Phys. **113**, 234508 (2013)

JOURNAL OF APPLIED PHYSICS **113**, 234508 (2013)

On-chip Brownian relaxation measurements of magnetic nanobeads in the time domain

Frederik Westergaard Østerberg,[a] Giovanni Rizzi, and Mikkel Fougt Hansen[b]
Department of Micro- and Nanotechnology, Technical University of Denmark, DTU Nanotech, Building 345 East, DK-2800 Kongens Lyngby, Denmark

(Received 27 March 2013; accepted 3 June 2013; published online 19 June 2013)

We present and demonstrate a new method for on-chip Brownian relaxation measurements on magnetic nanobeads in the time domain using magnetoresistive sensors. The beads are being magnetized by the sensor self-field arising from the bias current passed through the sensors and thus no external magnetic fields are needed. First, the method is demonstrated on Brownian relaxation measurements of beads with nominal sizes of 40, 80, 130, and 250 nm. The results are found to compare well to those obtained by an already established measurement technique in the frequency domain. Next, we demonstrate the time and frequency domain methods on Brownian relaxation detection of clustering of streptavidin coated magnetic beads in the presence of different concentrations of biotin-conjugated bovine serum albumin and obtain comparable results. In the time domain, a measurement is carried out in less than 30 s, which is about six times faster than in the frequency domain. This substantial reduction of the measurement time allows for continuous monitoring of the bead dynamics vs. time and opens for time-resolved studies, e.g., of binding kinetics. © *2013 AIP Publishing LLC*. [http://dx.doi.org/10.1063/1.4811462]

I. INTRODUCTION

Magnetic beads have been demonstrated as a useful component for the read-out in future biosensors.[1–4] A major advantage of using magnetic beads is that most biological samples are nonmagnetic and, therefore, there is nominally no background signal from the sample. Magnetic beads are also easy to functionalize such that they bind specifically to, e.g., antibodies, proteins, or DNA.

Traditionally, biosensing with a read-out based on magnetic beads is either surface-based or volume-based. In surface-based sensing, both the sensor surface and the beads are functionalized such that the target analyte will be sandwiched between the beads and the surface and result in beads being bound to the sensor surface.[2,5,6] In volume-based sensing, only the beads are functionalized and the presence of the target analyte is detected as a change of the hydrodynamic size of the magnetic beads either by adding to the size of the beads or by inducing bead agglutination. The use of Brownian relaxation measurements for volume-based biosensing was first proposed by Connolly and St Pierre.[7]

Brownian relaxation of magnetic beads is often measured in the frequency domain by AC susceptibility measurements with either inductive methods,[8] fluxgates,[9] SQUID magnetometers,[10] or magnetoresistive sensors.[11,12] However, Brownian relaxation can also be measured in the time domain.[13–15] The advantage of time domain measurements is that they can be performed much faster and a single measurement may take less than a second, whereas frequency domain measurements require a sequence of measurements at different frequencies typically resulting in measurement times on the order of minutes or longer. Thus, time domain measurements result in a much shorter analysis time and therefore also enable time-resolved studies. Disadvantages of time domain measurements compared to frequency domain measurements are that more noise are picked up in a DC measurement compared to the lock-in technique used in the frequency domain, and the time resolution of the data acquisition will set a limit for how fast changes can be detected.

Recently, we have demonstrated the possibility of performing Brownian relaxation measurements in the frequency domain on so called planar Hall effect bridge sensors without the need for any external magnets.[16,17] Here, we present and demonstrate a new approach that enables the use of the same sensors for Brownian relaxation measurements in the time domain and we show that this new approach substantially reduces the measuring time. We first compare measurements in the frequency and time domains on a series of four nanobead samples with diameters ranging from 40 nm to 250 nm. Next, we present initial results of biodetection experiments, where the two methods are employed to detect the clustering of streptavidin beads in the presence of biotin-conjugated bovine serum albumin.

II. THEORY

A. Brownian relaxation of magnetic beads

We consider an ensemble of magnetic beads placed in an applied magnet field with an equilibrium magnetization M_0. For convenience, the measured magnetization M is defined to be positive when it is parallel to the applied field, i.e., the magnetization M equals $+M_0$ and $-M_0$ when the magnetic moments are parallel and antiparallel to the applied field, respectively. The bead magnetic moments align with the applied magnetic field either by internal flipping of the

[a]Electronic mail: Frederik.Osterberg@nanotech.dtu.dk
[b]Electronic mail: Mikkel.Hansen@nanotech.dtu.dk

magnetization (Néel relaxation[18]) or by a physical rotation (Brownian relaxation[19]). For the beads used in this study, we assume that the Néel relaxation time is much longer than the Brownian relaxation time, which therefore dominates the relaxation dynamics of the beads.[17] The Brownian relaxation of magnetic beads can be measured in both the time and the frequency domains. The theory for both domains is described below.

1. Time domain

The Brownian relaxation of magnetic beads suspended in a liquid is characterized by the characteristic Brownian relaxation time

$$\tau_B = \frac{3\eta V_h}{k_B T}, \tag{1}$$

where η is the viscosity of the liquid, V_h is the hydrodynamic volume of the bead, and $k_B T$ is the thermal energy.

In this study, the measurements in the time domain are performed by passing a square wave current $I(t)$ with an amplitude of I_0 and period T_I though the sensor. The current through the sensor generates a magnetic self-field (H) around the sensor, which is proportional to the current, such that the sign of the magnetic field changes with the sign of the current. The beads rotate to align their magnetic moments with the magnetic field. This means that just after flipping of the current from $+I_0$ to $-I_0$, the magnetization of the beads will be antiparallel with the sensor self-field and then relax to being parallel. This is repeated when the current changes sign from $-I_0$ to $+I_0$, where it is noted that M again has an initial value of $-M_0$ as it is antiparallel to the magnetic field generated by the current. This is illustrated in Fig. 1.

The relaxation of the beads is described by an exponential decay with the Brownian relaxation time as the exponential time constant. As the magnetization of the beads relaxes from being antiparallel ($-M_0$) to being parallel ($+M_0$) with the magnetic field, we assume it to be described by

$$M(t) = M_0[1 - 2\exp(-t/\tau_B)], \tag{2}$$

where t is the time after the sign change of the magnetic field.

2. Frequency domain

The traditional method of measuring Brownian relaxation with planar Hall effect sensors is to pass an alternating current through the sensor

$$I(t) = \sqrt{2} I_{RMS} \sin(2\pi f t), \tag{3}$$

where I_{RMS} is the root mean square value of the current and f is the frequency of the current.

Measurements in the frequency domain are characterized by the complex magnetic susceptibility $\chi = \chi' - i\chi''$ with the in-phase component χ' and out-of-phase component χ''. The Brownian relaxation is characterized by the Brownian relaxation frequency

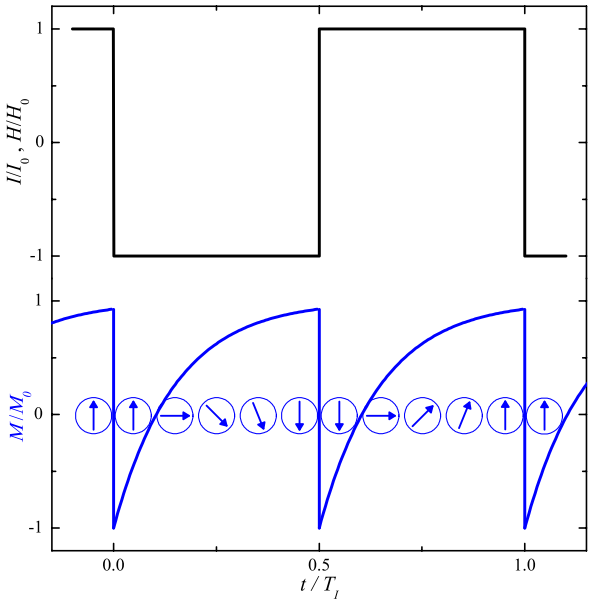

FIG. 1. Schematic of how a magnetic bead relaxes in a flipping magnetic field. The magnetic field changes direction when the current changes direction. Before flipping of the magnetic field, the magnetization of the bead will be parallel with the field. Immediately after flipping of the magnetic field, the magnetization of the bead will be anti-parallel, meaning the magnetization along the applied field is $M = -M_0$. The bead will then relax by rotation to become parallel with the field ($M = M_0$).

$$f_B = \frac{1}{2\pi\tau_B} = \frac{k_B T}{6\pi\eta V_h}. \tag{4}$$

At this characteristic frequency, the phase-lag between the magnetic moment of the bead and the applied field is largest, meaning that a peak will appear in the out-of-phase magnetic susceptibility at $f = f_B$.

According to Debye theory,[20] the complex magnetic susceptibility for an ensemble of beads with a single relaxation time is given by

$$\chi(f) = \frac{\chi_0 - \chi_\infty}{1 + (if/f_B)} + \chi_\infty, \tag{5}$$

where χ_0 and χ_∞ are the DC and high-frequency susceptibilities, respectively.

3. Size distribution

The equations for the magnetization in the time domain and the magnetic susceptibility in the frequency domain are only valid for a monodisperse ensemble of beads. Hence, the equations need to be averaged over a bead distribution. The size distribution of magnetic beads is often well described by the log-normal distribution given by

$$f_{LN}(D_h)dD_h = \frac{1}{D_h \sigma\sqrt{2\pi}} \exp\left(-\frac{(\ln D_h - \mu)^2}{2\sigma^2}\right) dD_h, \tag{6}$$

where μ is the logarithm to the median hydrodynamic diameter D_{hm}, $D_{hm} = \exp(\mu)$, and σ is the logarithmic standard deviation. We define the size distribution function to be volume-weighted, i.e., the volume fraction of the particles

with hydrodynamic diameters between D_h and $D_h + dD_h$ is $f_{LN}(D_h; \mu, \sigma)dD_h$. The definition of the size distribution therefore takes directly into account that the signal from a single bead is proportional to the bead volume.

B. Sensor signals

The magnetic beads are magnetized by the self-field arising from the bias current passed through the sensor. Figure 2 shows the contours of the magnetic field $\mu_0 H$ calculated using the Biot-Savart law for a total bias current of 14.1 mA, which is the current relevant for our experimental studies. The bias current is distributed between the two sensor branches that each has the width $w = 20\,\mu$m. The calculations show that the maximum value of $\mu_0 H$ found near the sensor edge is about 0.25 mT. This value is well below typical values applied in Brownian relaxation measurements in commercial set-ups.

For low magnetic fields, the sensor signal is linear and given by[21]

$$V = S_0 I H_y + R_{off} I, \tag{7}$$

where S_0 is the low-field sensitivity, H_y is the average magnetic field acting on the sensor area in the y-direction, and R_{off} accounts for a possible sensor offset. The value of H_y can be written as

$$H_y = \gamma_0 I + H_{y,beads} + H_{y,ext}. \tag{8}$$

Here, γ_0 is a constant that describes the effect of the self-field and which depends on the sensor stack and geometry;[22] $H_{y,beads}$ and $H_{y,ext}$ are magnetic fields acting on the sensor in the y-direction from the beads and external sources, respectively. The expression for $H_{y,beads}$ will be written slightly differently for measurements in the time domain and the frequency domain. In the time domain, we write

$$H^{time}_{y,beads} = \gamma_{1t} M(t) I \tag{9}$$

and in the frequency domain, we write

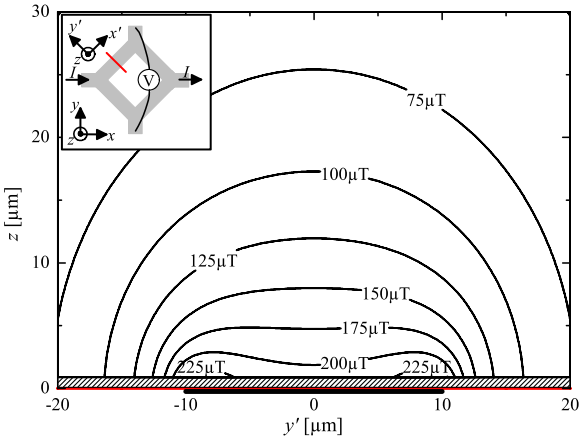

FIG. 2. Contour plot of the magnetic self-field ($\mu_0 H$) from the bias current through the sensor. The black line from $y' = -10\,\mu$m to $y' = 10\,\mu$m represents the sensor. The inset shows a sketch of the sensor, where the red line through the upper left branch represents the cross section where the self-field is calculated.

$$H^{freq}_{y,beads} = \gamma_1 \chi(f) I, \tag{10}$$

where γ_{1t} and γ_1 are constants that depend on the sensor geometry and bead distribution. Hansen *et al.*[22] have shown that magnetic beads magnetized by the self-field always contribute with a positive sign to the average magnetic field experienced by the sensor and that 85% of the sensor signal for a homogeneous bead dispersion arises from a volume centered on the sensor stripe with a width of about 2 w and height of about 1.5 w. For the sensors in the present study, where each branch has a length $l = 280\,\mu$m, this corresponds to a total probing volume of about 1.3 nl.

1. Time domain

When measurements are performed in the time domain, the current is alternating between $+I_0$ and $-I_0$ with the corresponding signals $V_+(t)$ and $V_-(t)$ given by

$$V_+(t) = S_0 I_0^2(\gamma_0 + \gamma_{1t} M(t)) + I_0(S_0 H_{y,ext} + R_{off}), \tag{11}$$

$$V_-(t) = S_0 I_0^2(\gamma_0 + \gamma_{1t} M(t)) - I_0(S_0 H_{y,ext} + R_{off}), \tag{12}$$

where t is defined as zero at the instance where the current changes sign. From this, it is seen that R_{off} and $H_{y,ext}$ can be eliminated by calculating the average of the two measurements and that $\gamma_0 + \gamma_{1t} M(t)$ can be eliminated by calculating the difference of the two measurements

$$V_{ave}(t) = \frac{1}{2}[V_+(t) + V_-(t)] = S_0 I_0^2(\gamma_0 + \gamma_{1t} M(t)), \tag{13}$$

$$V_{diff}(t) = \frac{1}{2}[V_+(t) - V_-(t)] = I_0(S_0 H_{y,ext} + R_{off}). \tag{14}$$

The offset due to γ_0 in V_{ave} can be corrected for by subtracting a measurement performed without beads. After this correction, $V_{ave}(t)$ is proportional to the time-dependent magnetization. It is seen that $V_{diff}(t)$ is linearly dependent on $H_{y,ext}$.

The function that is fitted to the measurements is the theoretical signal integrated over the volume-weighted log-normal distribution of hydrodynamic diameters

$$V_{fit,t} = -V_{0t}\left(1 - 2\int_0^\infty \exp[-t/\tau_B(D_h)] f_{LN}(D_h) dD_h\right) + V_{off}, \tag{15}$$

where $V_{0t} \equiv -S_0 I_0^2 \gamma_{1t} M_0$ is the amplitude of the decay and V_{off} is correcting for possible offsets. With these definitions, V_{0t} is positive (as $S_0 < 0$) and $V_{fit,t}/V_{0t}$ equals $+1$ for $t = 0$ and -1 for $t \to \infty$. The free fitting parameters are V_{0t}, V_{off}, D_{hm}, and σ, where the two last parameters account for the distribution of hydrodynamic diameters.

2. Frequency domain

For measurement in the frequency domain using lock-in detection, we have previously shown[16] that the complex magnetic susceptibility can be obtained from the complex

second harmonic sensor signal $V_2 = V_2' + iV_2''$ with in-phase and out-of-phase components

$$V_2' = -2^{-2} I_{\mathrm{RMS}}^2 S_0 \gamma_1 \chi'', \tag{16}$$

$$V_2'' = -2^{-2} I_{\mathrm{RMS}}^2 S_0 (\gamma_0 + \gamma_1 \chi'). \tag{17}$$

Thus, the in-phase second harmonic sensor signal is proportional to the out-of-phase magnetic bead susceptibility and the out-of-phase second harmonic sensor signal depends linearly on the in-phase magnetic bead susceptibility. Again, the offset due to γ_0 can be corrected for by subtracting a measurement without beads.

The function used for fitting to the measurements in the frequency is again the sensor signal averaged over the volume-weighted lognormal distribution of hydrodynamic diameters

$$V_{\mathrm{fit},f} = V_2' + iV_2'', \tag{18}$$

$$= i\int_0^\infty \frac{V_0 - V_\infty}{1 + \left(if/f_{\mathrm{B}}(D_{\mathrm{h}})\right)} f_{\mathrm{LN}}(D_{\mathrm{h}}) \mathrm{d}D_{\mathrm{h}} + iV_\infty, \tag{19}$$

with $V_0 = -2^{-2} I_{\mathrm{RMS}}^2 S_0 \gamma_1 \chi_0$ and $V_\infty = -2^{-2} I_{\mathrm{RMS}}^2 S_0 \gamma_1 \chi_\infty$. In addition to V_0 and V_∞, the free fitting parameters are the median hydrodynamic diameter D_{hm} and the logarithmic standard deviation σ.

III. EXPERIMENTAL

A. Sensor fabrication and mounting

The magnetic field sensor used is a so called planar Hall effect bridge sensor based on the anisotropic magnetoresistance of permalloy.[16,21] The sensor stack Ta(3 nm)/$Ni_{80}Fe_{20}$(30 nm)/$Mn_{80}Ir_{20}$(20 nm)/Ta(3 nm) was deposited in a field of 20 mT applied along the positive x-direction to define an easy magnetization direction. The stack was patterned in a Wheatstone bridge geometry consisting of four segments each with a length of $l = 280\,\mu$m and a width of $w = 20\,\mu$m. For a more detailed description of the sensor fabrication and design, see Ref. 16. The low-field sensitivity of the sensor was measured to $S_0/\mu_0 = -591$ V/(T A) and the resistance along the current direction was measured to 161.7 Ω.

In order to allow for electrical contact to the sensor, a click-on fluidic system[12,16] was used, which also defined the fluidic channel with dimensions length × width × height = 5 mm × 1 mm × 0.1 mm. The temperature of the sensor mount in good thermal contact to the sensor was kept constant at $(25.00 \pm 0.01)^\circ$C by a Peltier element. The sensor was neither electrically nor magnetically shielded.

B. Measurement equipment

The current through the sensor was supplied by a 6221 AC and DC Current Source (Keithley Instruments, USA). For time domain measurements, it delivered a square wave with a current amplitude of $I_0 = 14.1$ mA at a frequency of 8 Hz, which allowed $T_I/2$ =62.5 ms between each flipping of the current. For measurements in the frequency domain, a sine wave with a current amplitude of 20 mA ($I_{\mathrm{RMS}} = 14.1$ mA) was used with a frequency varying in 29 logarithmically equidistant steps from 43.69 kHz to 1.88 Hz. For both domains, a trigger signal was sent from the power supply, such that the measurements in the time domain were started exactly at the point when the current was flipped and, in the frequency domain, to get accurate information on the phase.

Measurements in the time domain were recorded using a NI USB-6281 data acquisition card (National Instruments, USA) with 18 bits of resolution on a range ±0.1 V. This corresponds to a voltage resolution of 0.8 μV. The sample rate was set to 600 000 samples per second, and in addition, a low pass filter of 3 kHz was applied to reduce the impact of high-frequency noise. To improve the signal-to-noise ratio, the signal was averaged over 192 periods. Thus, the time used for each measurement in the time domain was 24 s. For the data analysis, the measurement data were combined and averaged in 500 "bins" of widths increasing logarithmically with time.

Measurements of the second harmonic sensor signal in the frequency domain were recorded using a SR830 lock-in amplifier (Stanford Research Systems, USA). A frequency sweep consisting of measurements at 30 frequencies took 2 min and 21 s.

The data acquisition card and the lock-in amplifier were connected in parallel such that measurements with both instruments were performed immediately after one another. The measurement time in the time domain of 24 s is about a factor of six smaller than the measurement time in the frequency domain of 2 min and 21 s.

C. Procedure

1. Bead sizes

The Brownian relaxation has been measured in both the time and frequency domains for four different bead types with nominal diameters of 40 nm, 80 nm, 130 nm, and 250 nm. The 40 nm beads were SHP Iron oxide nanoparticles with carboxylic acid groups (Ocean Nanotech, USA), the 80 nm beads were BNF-starch with a plain surface (Micromod, Germany), and the 130 nm and 250 nm were Nanomag-D also with plain surfaces (Micromod, Germany).

All bead suspensions were diluted to a bead concentration of 1 mg/ml with milliQ water for the 40 nm beads and a phosphate buffered saline (PBS) solution for the remaining three bead types. Prior to the first experiment, the fluidic channel was rinsed and filled with milliQ water. An experiment was carried out by first injecting 20 μl of the sample into the fluidic channel at a flow rate of 13.3 μl/min for 1.5 min. Then, the beads were left in the channel for 10 min to allow for a steady state and the measurements were recorded. Finally, the beads were washed out with PBS at a flow rate of 300 μl/min for 1–2 min. Reference measurements with no beads were performed between measurements on the four samples. These measurements were used to correct for γ_0 and an instrumental phase-shift.

2. Bead clustering

Measurements of bead clustering were carried out by mixing 15 μl of PBS containing varying concentrations of

biotin-conjugated bovine serum albumin (bBSA) (A8549, Sigma-Aldrich, USA) with 15 μl of a 2 mg/ml suspension of streptavidin coated 80 nm BNF-starch beads (Micromod, Germany). Each bBSA has 8-16 biotin molecules available for binding to a streptavidin molecule. Since each bBSA molecule is able to bind more than two streptavidin molecules, adding bBSA to streptavidin coated beads will allow for the formation of dimers or clusters. All concentrations given below are the bead and bBSA concentrations after mixing. Immediately after mixing, the suspension was placed in a magnetic field of 45 mT for 10 min to enhance formation of bead clusters after which it was injected into the fluidic system at a flow rate of 13.3 μl/min for 1.5 min. The sample was left stagnant in the fluidic system for 20 min, allowing time for five repeated measurements in the time and frequency domains. The first measurement in the frequency domain was performed during the sample injection and was not used for the analysis. When a series of measurements was completed, the bead suspension was washed out with PBS at a flow rate of 300 μl/min for 1–2 min and a reference measurement (used to correct for γ_0) was performed before a new sample was injected.

Five different samples were investigated with final bBSA concentrations of 0 nM, 0 nM, 2.5 nM, 5 nM, and 10 nM, respectively.

IV. RESULTS

A. Time domain signal vs. bias current

Figure 3 shows equilibrium values of V_{ave} and V_{diff} obtained from time domain measurements vs. current amplitude I_0. The values of V_{ave} in Fig. 3(a) have been corrected for γ_0 using the average of the two measurements without beads recorded before and after beads were on the sensor. The figure shows corrected data obtained with and without a suspension of 80 nm magnetic beads in the fluidic channel. In the absence of the magnetic beads, the data are scattered around zero, and in the presence of the bead suspension, the data are proportional to I_0^2 in accordance with Eq. (13). This shows that the data correction procedure works as intended and that the measurements are stable over time. Fig. 3(b) shows the corresponding values of V_{diff}. These are found to depend linearly on I_0 in accordance with Eq. (14) with a slope that has no systematic dependence on the measurement conditions. The observed slope change can be due to a variation of the background external field and/or a change of the sensor offset between the measurements. Assuming the former, it corresponds to field changes on the order of 0.5 μT and the latter, it corresponds to sensor offset changes on the order of 0.5 mΩ. Given that the sensor operates with no magnetic shielding, field variations on the order of 0.5 μT are quite likely over a period of hours. As long as the field and offset are stable over the duration of a period in the current cycle (125 ms in the present experiments), it will not affect the measurements of V_{ave}.

1. Bead sizes

Figure 4 shows the time domain Brownian relaxation measurements obtained for the four different bead sizes. The

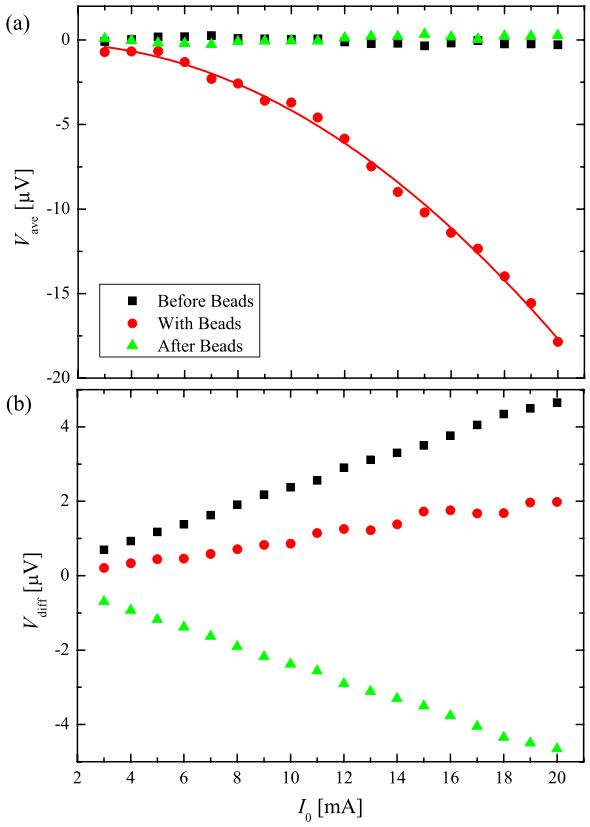

FIG. 3. Equilibrium values of V_{ave} and V_{diff} obtained from time domain measurements vs. current amplitude I_0. Panel (a) shows corrected equilibrium values of V_{ave} vs. I_0 with and without 80 nm magnetic beads. The solid line is a parabolic fit to the measurements with beads. Panel (b) shows values of V_{diff} vs. I_0.

measurements have been normalized with V_{0t} such that the signals for the different bead sizes can be easily compared. It is seen that the relaxation time increases with the bead size. The points measured for the 40 nm and 130 nm beads, where the absolute signal is lower, are more scattered on this normalized scale. The lines plotted through each data set are least squares curve fits of Eq. (15) to the data prior to normalization. The parameters obtained from the fits are shown in

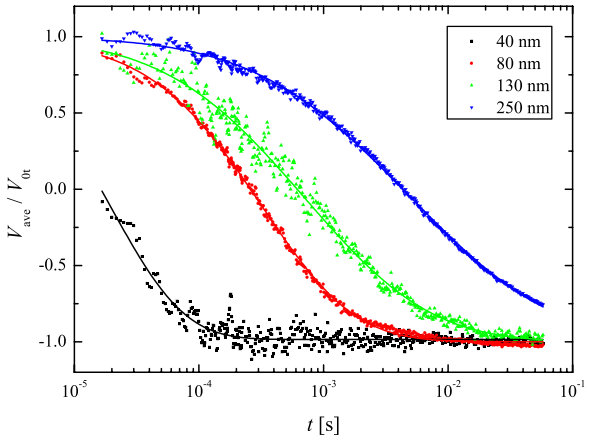

FIG. 4. Brownian relaxation measurements in the time domain. V_{ave} normalized with the fitting parameter V_{0t} vs. time for four different bead sizes. The lines are curve fits of Eq. (15) to the data. The signals have all been corrected for offsets found from fitting.

TABLE I. Parameters obtained from least squares fitting of Eq. (15) to the time domain measurements and of Eq. (19) to the frequency domain measurements for the four different bead sizes. The 40 nm beads are from Ocean Nanotech and suspended in MilliQ water, while the remaining three types are from Micromod and suspended in PBS. The numbers in parentheses are the errors for the 95 % confidence interval obtained from the least squares curve fits.

	Time domain				Frequency domain			
D_{nom} [nm]	D_{hm} [nm]	σ	V_{0t} [μV]	V_{off} [μV]	D_{hm} [nm]	σ	$V_0 - V_\infty$ [μV]	V_∞ [μV]
40	41(2)	0.22(5)	1.8(3)	−0.4(3)	42.5(3)	0.18(2)	0.95(2)	0.1(2)
80	108(1)	0.35(1)	4.81(2)	0.48(2)	107(2)	0.32(2)	3.16(5)	0.4(8)
130	152(2)	0.45(2)	1.36(2)	1.85(1)	159(4)	0.50(2)	0.97(2)	0.5(3)
250	299(4)	0.60(1)	7.68(6)	8.15(5)	350(7)	0.64(2)	5.66(7)	5.5(5)

Table I. For the 40 nm beads from Ocean Nanotech, the median hydrodynamic diameter is found to match its nominal value within the experimental uncertainty. For the Micromod beads, the median hydrodynamic diameters are found to be significantly larger than their nominal values. The values of σ are also found to increase with the bead size.

Figure 5 shows the Brownian relaxation measurements on the same samples in the frequency domain. As for the time domain measurements (Table I), the signal amplitude varies significantly with the bead type. The lines are least squares curve fits of Eq. (19) to the measurements. It is seen that the fits match the measured data well except for the 250 nm beads. The parameters obtained from the fits are listed in Table I. For beads with nominal sizes below 250 nm, the median hydrodynamic diameters and values of σ obtained by the two methods agree within the experimental uncertainty. However, for the 250 nm beads, the hydrodynamic diameter obtained from the frequency domain measurement is significantly larger than that obtained from the time domain measurement.

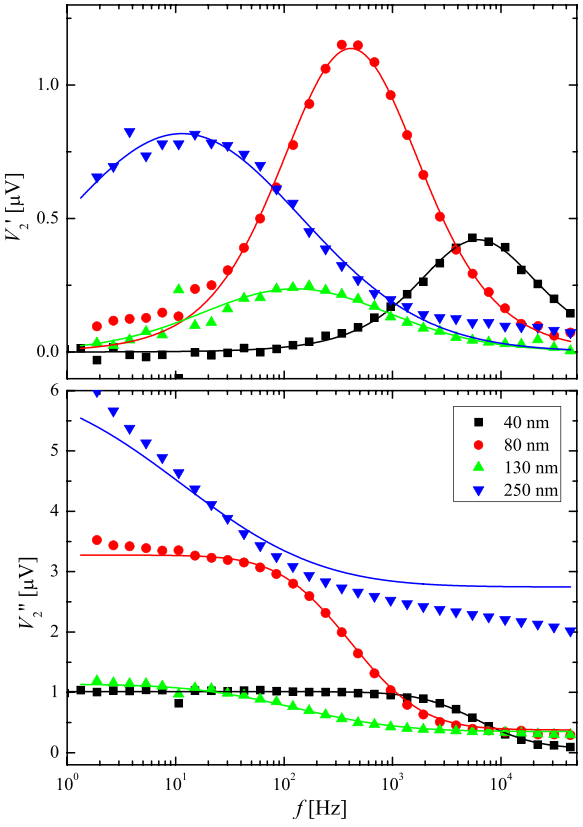

FIG. 5. Brownian relaxation measurements in the frequency domain. Second harmonic in-phase (top) and out-of-phase (bottom) signal vs. frequency for 5 different bead sizes. The sweep is performed from high to low frequencies. The lines are curve fits of Eq. (19) to the data.

B. Bead clustering

Figure 6 shows time domain measurements for bead clustering with bBSA. The measurements shown are the last performed in the series of five repeated measurements and have been corrected for offsets. The lines are least squares curve fits of Eq. (15) to the data. Data from seven different measurements are shown: Two measurements with beads but without bBSA; three measurements with beads and with varying bBSA concentrations; and finally two reference measurements with neither beads nor bBSA. It is seen that the two measurements without bBSA almost coincide. When the bBSA concentration is increased, both the signal amplitude and the signal slope for $t \geq 10^{-2}$ s increase.

Figure 7 shows the corresponding measurements in the frequency domain. Again, the measurements on the two samples without bBSA are found to be very similar. For the samples with bBSA, the peak in the in-phase sensor signal (corresponding to the out-of-phase magnetic susceptibility) is found to increase in intensity and it is shifted towards lower frequencies upon increasing bBSA concentration. Least squares curve fits of Eq. (19) are plotted as solid lines.

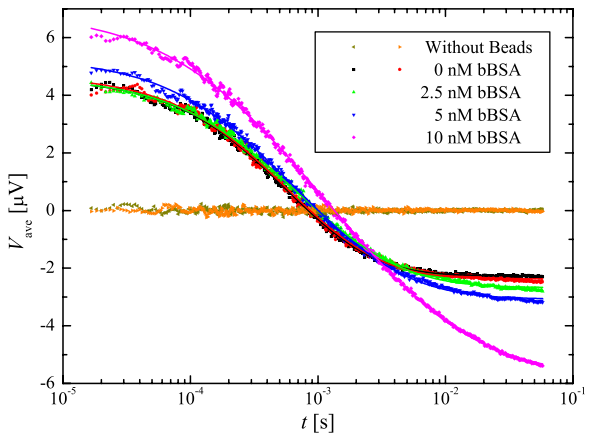

FIG. 6. Time domain measurements of clustering of streptavidin coated bead by binding to bBSA. V_{ave} is plotted vs. time. The lines are curve fits of Eq. (15) to the data.

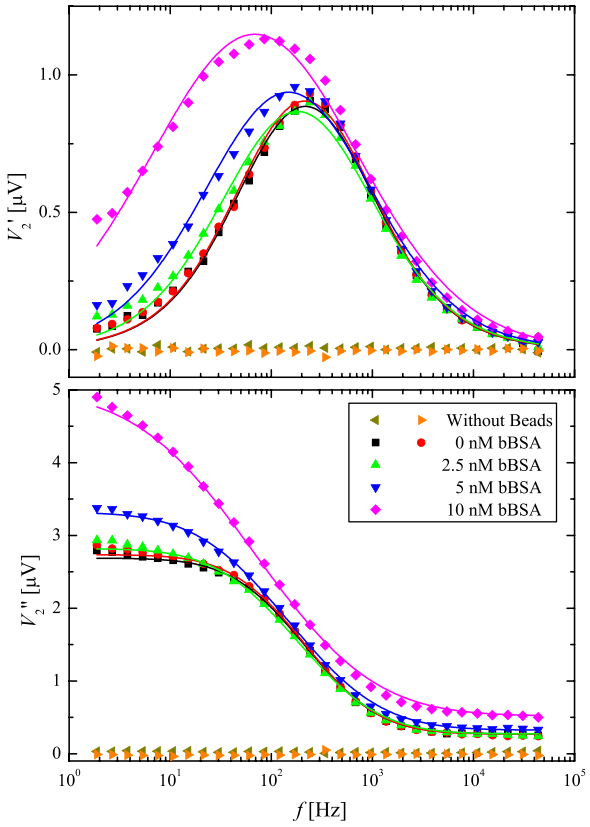

FIG. 7. Frequency domain measurements of clustering of streptavidin coated beads by bBSA. The in-phase (top) and out-of-phase (bottom) second harmonic sensor signals are plotted vs. bias current frequency. The lines are curve fits of Eq. (19) to the data.

The median hydrodynamic diameters D_{hm} and lognormal standard deviations σ obtained from analyses of the time and frequency domain measurements are listed in Table II. In general, it is seen that both D_{hm} and σ increase with increasing concentration of bBSA. However, the values of D_{hm} obtained in the time domain do not differ significantly for bBSA concentrations of 2.5 nM and 5 nM (although the values of σ do).

Figure 8 shows the values of D_{hm} extracted from fits of the measurements with 0 nM and 10 nM bBSA as function of time after sample injection. It is seen that in both the time and frequency domains, the sample without bBSA has a value of D_{hm} that increases slightly with time. In the presence of bBSA, the value of D_{hm} increases faster with time. It

TABLE II. Parameters obtained from least squares fitting to the measurement in the time and frequency domains for five different bBSA concentrations. The numbers in parentheses are the errors for the 95 % confidence interval obtained from the least squares curve fits.

	Time domain		Frequency domain	
c_{bBSA} [nm]	D_{hm} [nm]	σ	D_{hm} [nm]	σ
0	127.1(6)	0.31(1)	129(2)	0.34(2)
0	128.9(8)	0.33(1)	130(2)	0.34(2)
2.5	139.0(8)	0.40(1)	137(2)	0.40(3)
5	138.8(8)	0.43(1)	147(3)	0.47(3)
10	172.7(9)	0.62(1)	190(4)	0.65(3)

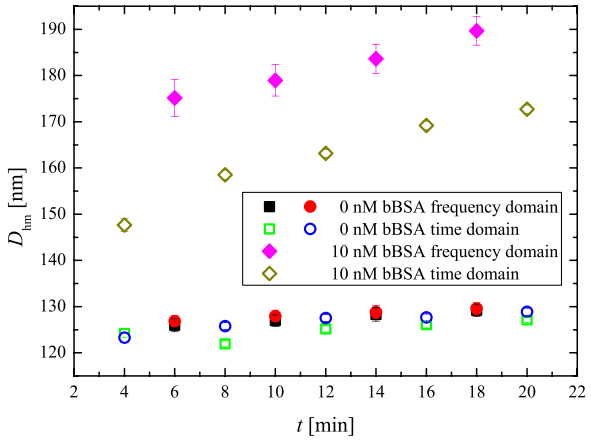

FIG. 8. Median hydrodynamic diameters obtained in the time and frequency domains vs. time after injection. Results are plotted for samples with 0 nM and 10 nM of bBSA.

is also seen that the values of D_{hm} obtained from frequency domain measurements are generally larger than those obtained from time domain measurements.

V. DISCUSSION

A. Bead size

For the beads with nominal sizes below 250 nm, the hydrodynamic sizes found by the two methods agree within the experimental uncertainty. For the 250 nm beads, there are several possible explanations for the observed significant difference between the time and frequency domain measurements: The 250 nm bead suspension does not reach steady-state over the duration of the experiment and hence the signal continuously increases with time due to bead sedimentation. This means that the signal measured during a sweep in the frequency domain increases during the sweep such that the signal level is higher towards the end of the sweep. As the frequency is swept from high to low frequencies, this may skew the spectrum towards lower values, i.e., towards larger hydrodynamic diameters. In the time domain, each measurement is carried out over a much shorter time interval (125 ms) and is thus not affected by bead sedimentation. However, if not all beads can achieve equilibrium during a half-period, which is consistent with the observation for the 250 nm beads in Fig. 4, this will give a relatively larger weight to the small beads in the measurements and hence shift the result towards smaller bead dimensions.

The Brownian relaxation measurements of the 40 nm beads are almost on the limit of what can be resolved with the data acquisition card used for the time domain measurements, both in terms of signal level and time resolution. The signal relaxes in around 100 μs and due to the low pass filter, the first measurement is obtained after 17 μs and the time resolution of the data acquisition card is only 1.6 μs. This results in only 60 measurement points to define the relaxation signal. From the scattering of the points for the measurements on 40 nm beads, it is also seen that the signal change due to relaxation is only a few times the resolution of the data acquisition card. Note that a signal in these measurements of 1 μV

corresponds to an average magnetic field of 120 nT. Hence, at present, the time domain measurements are limited by the resolution and noise of the data acquisition card. Low-noise signal amplification can significantly improve this as the sensors have a very low intrinsic noise level.[23] For example, the present sensors have a calculated thermal noise on the order of 1 nV under the present measurement conditions. The time domain measurements can also be improved by magnetic and electrical shielding of the set-up and the inclusion of gradiometer-like sensor configurations. Such improvements are the focus of our ongoing studies.

B. Bead clustering

Both time and frequency domain measurements can be used to detect the presence of bBSA by measuring an increase in the hydrodynamic diameters. However, with the present setup and preliminary set of data, measurements in the frequency domain measurements are found to be more sensitive to bBSA. Again, this can likely be improved with lower noise electronics for the signal treatment and/or longer measuring times to avoid a skewing of the bead size distribution towards lower values.

It was found that for samples containing bBSA, the median hydrodynamic diameter increases with time, whereas without bBSA, it is nearly constant. This is because bead clusters sediment due to their larger size and they thereby increase the ratio between clustered and free beads near the sensor surface. This effect will potentially make the planar Hall effect bridge sensors more sensitive if longer time is waited before performing the measurement. Hence, an optimum condition can be defined from the stability of the free beads, the sedimentation time for the bead clusters, and the desired analysis time. Moreover, it can also be envisioned to use active bead manipulation, where the cluster sedimentation is accelerated using an externally applied magnetic field gradient.

VI. CONCLUSION

We have shown that hydrodynamic sizes can be measured in a microfluidic channel with planar Hall effect bridge sensors in both the time and frequency domains without need for externally applied magnetic fields. We have also demonstrated that both methods can be used to detect clustering of streptavidin coated beads in the presence of biotin-conjugated bovine serum albumin. In this study, the time domain measurements take only a sixth of the time of the measurements in the frequency domain and they provide results of similar quality. This time can potentially be further reduced by optimizing the electronics and measurement times on the order of seconds are therefore within reach. Such short measurement times will allow for quick diagnostic tests as well as for real-time monitoring of the binding kinetics of magnetic beads and biological samples.

ACKNOWLEDGMENTS

This work was supported by the Copenhagen Graduate School for Nanoscience and Nanotechnology (C:O:N:T) and the Knut and Alice Wallenberg (KAW) Foundation.

[1]I. Koh and L. Josephson, "Magnetic nanoparticle sensors," Sensors **9**, 8130 (2009).
[2]S. X. Wang and G. Li, "Advances in giant magnetoresistance biosensors with magnetic nanoparticle tags: Review and outlook," IEEE Trans Magn. **44**, 1687 (2008).
[3]N. Jaffrezic-Renault, C. Martelet, Y. Chevolot, and J.-P. Cloarec, "Biosensors and bio-bar code assays based on biofunctionalized magnetic microbeads," Sensors **7**, 589 (2007).
[4]J. Göransson, T. Zardán Gómez De La Torre, M. Strömberg, C. Russell, P. Svedlindh, M. Strømme, and M. Nilsson, "Sensitive detection of bacterial DNA by magnetic nanoparticles," Anal. Chem. **82**, 9138 (2010).
[5]J. Schotter, P. Kamp, A. Becker, A. Pühler, G. Reiss, and H. Brückl, "Comparison of a prototype magnetoresistive biosensor to standard fluorescent DNA detection," Biosens. Bioelectron. **19**, 1149 (2004).
[6]R. S. Gaster, D. A. Hall, C. H. Nielsen, S. J. Osterfeld, H. Yu, K. E. Mach, R. J. Wilson, B. Murmann, J. C. Liao, S. S. Gambhir, and S. X. Wang, "Matrix-insensitive protein assays push the limits of biosensors in medicine," Nat. Med. **15**, 1327 (2009).
[7]J. Connolly and T. G. St Pierre, "Proposed biosensors based on time-dependent properties of magnetic fluids," J. Magn. Magn. Mater. **225**, 156 (2001).
[8]A. P. Astalan, F. Ahrentorp, C. Johansson, K. Larsson, and A. Krozer, "Biomolecular reactions studied using changes in Brownian rotation dynamics of magnetic particles," Biosens. Bioelectron. **19**, 945 (2004).
[9]F. Ludwig, S. Mäuselein, E. Heim, and M. Schilling, "Magnetorelaxometry of magnetic nanoparticles in magnetically unshielded environment utilizing a differential fluxgate arrangement," Rev. Sci. Instrum. **76**, 106102 (2005).
[10]H. Grossman, W. Myers, V. Vreeland, R. Bruehl, M. Alper, C. Bertozzi, and J. Clarke, "Detection of bacteria in suspension by using a superconducting quantum interference device," Proc. Natl. Acad. Sci. U.S.A. **101**, 129 (2004).
[11]B. T. Dalslet, C. D. Damsgaard, M. Donolato, M. Strømme, M. Strömberg, P. Svedlindh, and M. F. Hansen, "Bead magnetorelaxometry with an on-chip magnetoresistive sensor," Lab Chip **11**, 296 (2011).
[12]F. W. Østerberg, B. T. Dalslet, D. Snakenborg, C. Johansson, and M. F. Hansen, "Chip-based measurements of Brownian relaxation of magnetic beads using a planar hall effect magnetic field sensor," AIP Conf. Proc. **1311**, 176–183 (2010).
[13]R. Kötitz, P. Fannin, and L. Trahms, "Time domain study of Brownian and Néel relaxation in ferrofluids," J. Magn. Magn. Mater. **149**, 42 (1995).
[14]D. Eberbeck, C. Bergemann, F. Wiekhorst, U. Steinhoff, and L. Trahms, "Quantification of specific bindings of biomolecules by magneto-relaxometry," NanoBiotechnology **6**, 4 (2008).
[15]F. Öisjöen, J. F. Schneiderman, A. P. Astalan, A. Kalabukhov, C. Johansson, and D. Winkler, "A new approach for bioassays based on frequency- and time-domain measurements of magnetic nanoparticles," Biosens. Bioelectron. **25**, 1008 (2010).
[16]F. W. Østerberg, G. Rizzi, T. Zardán Gómez de la Torre, M. Strömberg, M. Strømme, P. Svedlindh, and M. F. Hansen, "Measurements of Brownian relaxation of magnetic nanobeads using planar hall effect bridge sensors," Biosens. Bioelectron. **40**, 147 (2013).
[17]F. W. Østerberg, G. Rizzi, and M. F. Hansen, "On-chip measurements of Brownian relaxation of magnetic beads with diameters from 10 nm to 250 nm," J. Appl. Phys. **113**, 154507 (2013).
[18]L. Neél, "Théorie du traînage magnétique des ferromagnétiques en grains fins avec applications aux terres cuites," Ann. Géophys. **5**, 99 (1949).
[19]W. Brown, "Thermal fluctuations of a single-domain particle," Phys. Rev. **130**, 1677 (1963).
[20]P. Debye, *Polar Molecules* (Chemical Catalogue Co., 1929).
[21]A. D. Henriksen, B. T. Dalslet, D. H. Skieller, K. H. Lee, F. Okkels, and M. F. Hansen, "Planar Hall effect bridge magnetic field sensors," Appl. Phys. Lett. **97**, 013507 (2010).
[22]T. B. G. Hansen, C. D. Damsgaard, B. T. Dalslet, and M. F. Hansen, "Theoretical study of in-plane response of magnetic field sensor to magnetic beads magnetized by the sensor self-field," J. Appl. Phys. **107**, 124511 (2010).
[23]A. Persson, R. S. Bejhed, H. Nguyen, K. Gunnarsson, B. T. Dalslet, F. W. Østerberg, M. F. Hansen, and P. Svedlindh, "Low-frequency noise in planar Hall effect bridge sensors," Sens. Actuators, A **171**, 212 (2011).

Paper V

F. W. Østerberg, G. Rizzi, T. Zardán Gómez de la Torre, M. Strömberg, M. Strømme, P. Svedlindh and M. F. Hansen
"Measurements of Brownian relaxation of magnetic nanobeads using planar Hall effect bridge sensors"
Biosens.Bioelectron. **40**, 147-152 (2013)

Biosensors and Bioelectronics 40 (2013) 147–152

Contents lists available at SciVerse ScienceDirect

Biosensors and Bioelectronics

journal homepage: www.elsevier.com/locate/bios

Measurements of Brownian relaxation of magnetic nanobeads using planar Hall effect bridge sensors

F.W. Østerberg [a], G. Rizzi [a], T. Zardán Gómez de la Torre [b], M. Strömberg [b], M. Strømme [b], P. Svedlindh [b], M.F. Hansen [a,*]

[a] Department of Micro- and Nanotechnology, Technical University of Denmark, DTU Nanotech, Building 345B, DK-2800 Kongens Lyngby, Denmark
[b] Department of Engineering Sciences, Uppsala University, The Ångström Laboratory, Box 534, SE-751 21 Uppsala, Sweden

ARTICLE INFO

Available online 20 July 2012

Keywords:
Brownian relaxometry
Magnetorelaxometry
Lab-on-a-chip
Magnetic sensor
Biosensor
Magnetic nanobeads

ABSTRACT

We compare measurements of the Brownian relaxation response of magnetic nanobeads in suspension using planar Hall effect sensors of cross geometry and a newly proposed bridge geometry. We find that the bridge sensor yields six times as large signals as the cross sensor, which results in a more accurate determination of the hydrodynamic size of the magnetic nanobeads. Finally, the bridge sensor has successfully been used to measure the change in dynamic magnetic response when rolling circle amplified DNA molecules are bound to the magnetic nanobeads. The change is validated by measurements performed in a commercial AC susceptometer. The presented bridge sensor is, thus, a promising component in future lab-on-a-chip biosensors for detection of clinically relevant analytes, including bacterial genomic DNA and proteins.

1. Introduction

In recent years, the interest in using magnetic particle-based biosensors has increased (Göransson et al., 2010; Jaffrezic-Renault et al., 2007; Koh and Josephson, 2009; Wang and Li, 2008). One of the main reasons for this is the lack of magnetic background in most biological samples. Furthermore, magnetic particles of dimension in the sub-micrometer range, so called nanobeads, have high physical and chemical stability, are inexpensive to produce, and can easily be made biocompatible.

Brownian relaxation was first proposed for biosensing by Connolly and St Pierre (2001). The principle behind using Brownian relaxation for biodetection is that a naked magnetic particle will have a smaller hydrodynamic diameter than the same particle bound to a biomolecule. This means that the naked particle will relax faster than a particle bound to a biomolecule. Brownian relaxation has been demonstrated to work for both detection of DNA (Strömberg et al., 2008) and proteins (Astalan et al., 2004; Öisjöen et al., 2010; Zardán Gómez de la Torre et al., 2012). Traditionally, Brownian relaxation is measured in a SQUID magnetometer, which is expensive and requires cryogenic liquids for cooling; other methods include inductive setups and fluxgates (Ludwig et al., 2005). None of these methods are easily integrated into a lab-on-a-chip system, thus there is a need for a sensor suited for integration onto a lab-on-chip platform. We have previously demonstrated that Brownian relaxation can be measured using a cross-shaped planar Hall effect (PHE) sensor without the need for any externally applied field since the beads are magnetized by the field generated by the alternating sensor bias current (Dalslet et al., 2011; Østerberg et al., 2010).

In the present work, we compare results obtained from measurements of Brownian relaxation of 40 nm magnetic beads using two different PHE sensor geometries; the traditional cross geometry and the newly proposed bridge (PHEB) geometry (Henriksen et al., 2010; Persson et al., 2011). We first show that the two sensor types yield the same frequency dependence of the measured signal from magnetic nanobeads and that the signals measured by the bridge sensor are six times as large as those measured by the cross-shaped sensor. We then present results of the first on-chip experiments, where functionalized magnetic nanobeads are mixed and hybridized to DNA coils formed in a rolling circle amplification (RCA) process. These results are found to compare well with those obtained in experiments carried out using a commercial AC susceptometer. The presented findings open up for the development of inexpensive on-chip magnetic read-out devices for detection of clinically relevant analytes including bacterial genomic DNA and proteins.

2. Theory

Below, the theoretically expected signals from magnetic beads when they are magnetized by the sensor self-field for both the

* Corresponding author. Tel.: +45 45256338.
E-mail addresses: frederik.osterberg@nanotech.dtu.dk (F.W. Østerberg), Mikkel.Hansen@nanotech.dtu.dk (M.F. Hansen).

0956-5663/$ - see front matter © 2012 Elsevier B.V. All rights reserved.
http://dx.doi.org/10.1016/j.bios.2012.07.002

cross and bridge geometries of planar Hall effect sensors are derived. It is also described how the dynamic magnetic bead response can be extracted using lock-in technique.

2.1. Low-field sensor response

The sensors rely on the anisotropic magnetoresistance (AMR) effect measured in the cross and bridge geometries shown in Fig. 1. The cross consists of two orthogonal arms each of width w. The bridge consists of four arms of width w and length l that form angles $\pm\pi/4$ to the x-axis as illustrated in Fig. 1. The sensors consist of a ferromagnetic layer exhibiting the AMR effect, which is exchange pinned along the positive x-direction in zero external magnetic field by an antiferromagnet. The sensors are connected in series and are biased by a current I applied in the positive x-direction. The resulting sensor output voltages V_C and V_B of the cross and the bridge, respectively, are measured along the y-direction. In zero magnetic field both sensors will ideally give zero output voltage. Upon application of a small magnetic field H_y in the y-direction, the magnetization of the ferromagnetic layer will rotate resulting in non-zero values of V_C and V_B due to the AMR effect. The cross sensor is usually termed planar Hall effect sensor because it shares the geometry with ordinary Hall sensors. The bridge sensor presented here has recently been shown to have exactly the same response as the cross sensor except for a geometrical amplification factor and hence this particular class of AMR sensors was termed planar Hall effect bridge sensors (Henriksen et al., 2010). For both sensors, the output for low applied magnetic fields can be written as

$$V_C = IS_{C,0}H_y, \tag{1}$$

$$V_B = IS_{B,0}H_y, \tag{2}$$

where $S_{C,0}$ and $S_{B,0}$ are the low-field sensitivities of the cross and bridge sensors, respectively. When the two sensors have the same value of w, the two sensitivities are ideally related as $S_{B,0} = (l/w)S_{C,0}$ (Henriksen et al., 2010).

2.2. Response to sensor self-field and magnetic beads

We consider the self-field H_{sf} acting on the sensor in the directions indicated in Fig. 1 due to the applied sensor bias current. For the present sensors, part of the sensor bias current is shunted in the antiferromagnetic layer. This gives rise to an effective in-plane magnetic field acting on the ferromagnetic layer aligned perpendicular to the direction of the current I_c through the conductor. We write this effective field as $I_c\gamma_0$, where γ_0 is a constant that depends on the sensor stack and sensor geometry. Likewise, magnetic beads that are present on and near the conductor will be magnetized by the field from the sensor bias

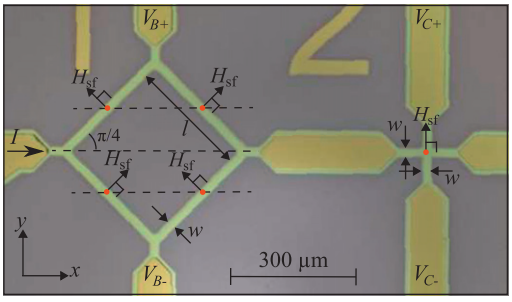

Fig. 1. Picture of a bridge and a cross sensor connected in series with definition of geometric variables and the orientation of self-fields acting on the sensor. The current is applied in the x-direction, while sensor signals are measured across the sensors in the y-direction.

current and give rise to a net positive field acting on the conductor. This we write as $I_c\gamma_1\chi$, where γ_1 depends on the sensor geometry and bead distribution and χ is the magnetic bead susceptibility (Hansen et al., 2010). Hence, we write the total self-field acting on the sensor due to the applied bias current as

$$H_{sf} = I_c\gamma_0 + I_c\gamma_1\chi. \tag{3}$$

For the cross sensor, the entire current passes through the sensor and the self-field acts in the positive y-direction. Inserting $I_c = I$ and $H_y = H_{sf}$ in Eq. (1) yields the expected self-field signal:

$$V_C = I^2 S_{C,0}(\gamma_0 + \gamma_1\chi). \tag{4}$$

For the bridge sensor, only half of the bias current passes through each branch and the sensor is sensitive only to the y-component of the self-field. Inserting $I_c = I/2$ and $H_y = H_{sf}/\sqrt{2}$ in Eq. (2) yields the expected self-field signal:

$$V_B = 2^{-3/2} I^2 S_{B,0}(\gamma_0 + \gamma_1\chi), \tag{5}$$

where we have implicitly assumed that γ_0 and γ_1 are the same for the two sensor types. Combining Eqs. (4) and (5), we find that the ratio of the self-field signals for the two sensors is

$$V_B/V_C = 2^{-3/2}(S_{B,0}/S_{C,0}) \tag{6}$$

and that, ideally, $V_B/V_C = 2^{-3/2}(l/w)$.

2.3. Dynamic magnetic susceptibility measurements

To probe the dynamic magnetic properties of magnetic nanobeads, we apply an alternating sensor bias current $I(t) = I_{AC}\sin(2\pi ft)$, where I_{AC} is the current amplitude, f is the frequency and t is the time. The response of a bead ensemble to the alternating magnetic field is described by the complex magnetic susceptibility:

$$\chi = \chi' - i\chi'' \equiv |\chi|\cos\phi - i|\chi|\sin\phi, \tag{7}$$

where χ' and χ'' are the components of χ in-phase and out-of-phase with the magnetic field, respectively, and ϕ is the phase lag of the magnetic response with respect to the magnetic field. As the self-field signals are proportional to I^2, the signals must be detected at twice the frequency ($2f$) of the bias current. This can be achieved by measuring the 2nd harmonic signal $V_2 = V_2' + iV_2''$ using lock-in technique, where V_2' and V_2'' are the in-phase and out-of-phase signals, respectively. We have previously shown (Dalslet et al., 2011; Østerberg et al., 2010) that the 2nd harmonic signals for the cross sensor are

$$V_{C,2}' = -2^{-3/2} I^2 S_{C,0}\gamma_1\chi'', \tag{8}$$

$$V_{C,2}'' = -2^{-3/2} I^2 S_{C,0}(\gamma_0 + \gamma_1\chi'). \tag{9}$$

Hence, $V_{C,2}'$ is directly proportional to the out-of-phase susceptibility χ'' and $V_{C,2}''$ depends linearly on the in-phase susceptibility χ'. The corresponding expressions for the bridge sensor can be found using Eq. (6).

2.4. Brownian relaxation of magnetic beads

We consider a magnetic bead, where the superparamagnetic relaxation time due to internal flipping of the magnetic moment of the bead is much longer than the Brownian relaxation time due to a physical rotation of the bead (Brown, 1963). Hence, we assume that Brownian relaxation is the dominating relaxation mechanism in the investigated frequency window. Brownian relaxation is characterized by the Brownian relaxation frequency

f_B given by

$$f_B = \frac{k_B T}{6\pi\eta V_h}, \tag{10}$$

where T is the absolute temperature, k_B is Boltzmann's constant, η is the dynamic viscosity of the liquid and V_h is the hydrodynamic volume of the relaxing entity.

For an ensemble of monodisperse non-interacting particles the complex susceptibility χ is described by the Debye (1929) theory. To account for a possible polydispersity, Cole and Cole (1941) have later provided the empirical expression:

$$\chi = \frac{\chi_0 - \chi_\infty}{1 + (if/f_B)^{1-\alpha}} + \chi_\infty, \tag{11}$$

where α ($0 \le \alpha < 1$) is the Cole–Cole parameter, which equals zero for a monodisperse sample, and χ_0 and χ_∞ are the DC and high-frequency susceptibilities. It should be noted that the DC susceptibility χ_0 in a Brownian relaxation sense is strongly sensitive to whether the beads are dynamically active or not whereas the high-frequency susceptibility χ_∞ depends only on the amount of beads.

3. Material and methods

3.1. Sensor fabrication

The sensors were fabricated on a silicon wafer with a 1 μm thick thermal oxide. The sensor stack Ta(3 nm)/$Ni_{80}Fe_{20}$(30 nm)/$Mn_{80}Ir_{20}$(20 nm)/Ta(3nm) was deposited in a Kurt J. Lesker CMS-18 magnetron sputter system and defined by liftoff. During deposition, a magnetic field of 20 mT was applied to define an easy magnetization direction along the positive x-direction (Henriksen et al., 2010). The contact stack Ti(10 nm)/Pt(100 nm)/Au(100 nm)/Ti(10 nm) was deposited in a Wordentech QLC 800 metal evaporator and also defined by liftoff. Finally, a 900 nm thick layer of Ormocomp (Micro resist technology GmbH, Germany) was spun on to the wafer and patterned by photo lithography, to leave the sensors covered and the contact pads uncovered. The Ormocomp layer prevents electrical contact between the sensors and the liquids during measurements, such that the sensors can be operated at voltages up to at least 10 V during measurements without formation of bubbles or sensor corrosion. For this study the bridge sensor has the dimensions $l = 280$ μm and $w = 20$ μm and the cross sensor has the dimension $w \times w = 20$ μm × 20 μm, for definitions see Fig. 1.

3.2. Measurement setup

Electrical contact to the chip was made using a click-on fluidic system with integrated spring-loaded electrical contacts. The click-on fluidic system has a polydimethylsiloxane (PDMS) gasket, which defines the sidewalls and the top of the fluidic channel of which the chip forms the bottom. The channel height, width and length are 1 mm, 1 mm and 5 mm, respectively. For further details on the click-on system, see Østerberg et al. (2010). During measurements, the chip was placed in a measurement set-up where the temperature was held constant at 25 °C using a PID Peltier temperature control system.

Measurements of the 2nd harmonic sensor signal vs. frequency were carried out using an HF2LI lock-in amplifier (Zurich Instruments, Switzerland). The bias current was provided by the built-in function generator of the lock-in amplifier. The two sensors tested in this study were connected in series, which means that the same current was passed through the two sensors. The resistance of the two sensors in series was 222.9 Ω. Three different voltage amplitudes were applied corresponding to the bias current amplitudes $I_{AC} = 12.4$ mA, 18.6 mA and 24.8 mA.

The low-field sensor sensitivities were found measuring the 1st harmonic sensor response vs. magnetic field applied in the y-direction as described by Henriksen et al. (2010). For the cross and bridge sensors, we obtained $S_{C,0} = -90$ V/(AT) and $S_{B,0} = -616$ V/(AT), respectively.

3.2.1. Brownian relaxation measurements using cross and bridge sensors

The relaxation measurements were performed by measuring the 2nd harmonic signals as a function of bias current frequency. All frequency sweeps comparing the bridge and cross were performed with 18 equally spaced points on a log scale from 338.2 kHz down to 37.7 Hz. After each of the 18 points in the frequency sweep, a reference point was recorded at 4667 Hz, which is near the expected Brownian relaxation frequency of the studied beads. The total time for such a sweep with 18 different frequencies and 18 reference points was 7 min and 15 s. The sweeps were set to run continuously, such that when a sweep ended, a new sweep started automatically.

Prior to introduction of magnetic nanobeads in the fluidic system, three background sweeps were performed with MilliQ water in the fluidic channel. These sweeps were used to correct for an instrumental phase shift at high frequencies and to subtract the offset due to the self-field from the current shunted through the antiferromagnetic layer. Hence, all data shown below have been corrected for γ_0 (cf. Eq. (9)).

At the beginning of the fourth frequency sweep, a suspension of 1 mg/mL 40 nm SHP beads with COOH surface (Ocean Nanotech, AR, USA) was injected into the fluidic channel at a flow rate of 30 μL/min and the nanobead suspension was left stagnant in the fluid channel for the subsequent four frequency sweeps (sweeps number 5–8). When the 9th frequency sweep started, the fluid channel was flushed with MilliQ water for 3 min at a flow rate of 800 μL/min. Finally, a tenth sweep was measured to verify that the sensors were back to their initial state.

3.2.2. Brownian relaxation measurements on samples containing DNA coils and oligonucleotide-tagged magnetic nanobeads

The samples for the DNA coil detection experiments were prepared as described in Zardán Gómez de la Torre et al. (2011a) using amine-functionalized magnetic nanobeads with a nominal diameter of 50 nm (Micromod Partikeltechnologie GmbH, Germany). Briefly, single-stranded detection oligonucleotides (5′-SH-TTT TTT TTT TTT TTT TTT TTG TTG ATG TCA TGT GTC GCAC-3′-FAM) complementary to the repeating sequence of the DNA coils were conjugated to the beads (10 oligonucleotides per nanobead) using the sulfo-succinimidyl-4-(*N* -maleimidomethyl) cyclohexane-1-carboxylate (sulfo-SMCC) chemistry as described in Zardán Gómez de la Torre et al. (2011b) and suspended in 1 × PBS pH 7.5 to a concentration of 1 mg/mL. A 4 nM suspension of DNA coils was produced through the padlock probe target recognition (Nilsson et al., 1994) and the RCA technology (Fire and Si-Qun, 1995; Liu et al., 1996) using an RCA-time of 60 min. This resulted in long single-stranded DNA coils containing about 1000 repetitions of the complement of the padlock probe sequence. The DNA coils were suspended in hybridization buffer (4 mM Tris–HCl, 4 mM EDTA, 0.02 v/v% Tween-20 and 0.1 M NaCl). The sequences of the target and padlock probes were 5′-CCC TGG GCT CAA CCTAGG AAT CGC ATT TG-3′ and 5′-TAG GTT GAG CCC AGG GAC TTC TAG AGT GTA CCG ACC TCA GTA GCC GTG ACT ATC GAC TTG TTG ATG TCA TGT GTC GCA CCA AAT GCG ATT CC-3′, respectively.

Detection experiments were carried out by first diluting the DNA coil suspension with hybridization buffer to a DNA coil

concentration of 400 pM. Then, a 30 μL solution of oligonucleotide-tagged beads was added to a 30 μL solution of hybridization buffer (reference sample) or 400 pM of DNA coils (200 pM after addition of oligonucleotide-tagged beads). The mixture was gently homogenized and thereafter incubated for 30 min at 70 °C. Immediately after, 30 μL of the incubated sample was injected into the chip system and characterized using the planar Hall effect bridge sensor. Another 30 μL sample was diluted to 200 μL with 1 × PBS and characterized in a DynoMag commercial AC susceptometer (Imego, Sweden).

4. Results

4.1. Brownian relaxation measurements using cross and bridge sensors

Fig. 2 shows the in-phase (top) and out-of-phase (bottom) 2nd harmonic sensor signals vs. frequency obtained from measurements of the Ocean Nanotech beads with a nominal diameter of 40 nm for the three indicated amplitudes of the bias current. The data for the cross sensor have been scaled by a factor of 6. All data have been corrected for an instrumental phase shift and the data measured on MilliQ water have been subtracted. Hence, the corrected in-phase sensor response is proportional to the out-of-phase magnetic susceptibility and the corrected out-of-phase sensor response is proportional to the in-phase magnetic susceptibility. The figure shows that the signals, as expected from Eqs. (4) and (5), are quadrupled when the current amplitude is doubled and that the signal from the bridge sensor is close to six times that from the cross sensor.

The solid lines in Fig. 2 are curve fits to the Cole–Cole model, Eq. (11). The nanobead suspension was injected during the fourth frequency sweep and the signal was stable during sweeps number 5–8. These frequency sweeps were analyzed in terms of the Cole–Cole model and the resulting Brownian relaxation frequencies are shown in Table 1. The errors on the values of f_B in Table 1 are the standard deviations found from the four repeated measurements. The results show that f_B increases slightly with the bias current for measurements on the bridge sensor, whereas no clear trend is observed for measurements on the cross sensor. Furthermore, Table 1 shows that the uncertainties in f_B decrease significantly when the bias current is increased and also that the uncertainties are substantially smaller for the bridge than for the cross. For example, for the highest bias current, the relative error on the determination of f_B is 0.1% for the bridge and 5% for the cross. The obtained Brownian relaxation frequencies correspond to hydrodynamic diameters in the range 42–45 nm.

The reference points measured at $f=4667$ Hz after each point in the frequency sweep are plotted in Fig. 3 vs. the time t after initiation of the experiment for the indicated amplitudes of the current. The figure also indicates the frequency sweeps in chronological order. Again the data for the cross sensor have been scaled by a factor of 6.

For all measurements, a constant signal is observed until the nanobead suspension is injected at $t=22$ min. Then, the signal increases to an approximately constant level, which is reached at

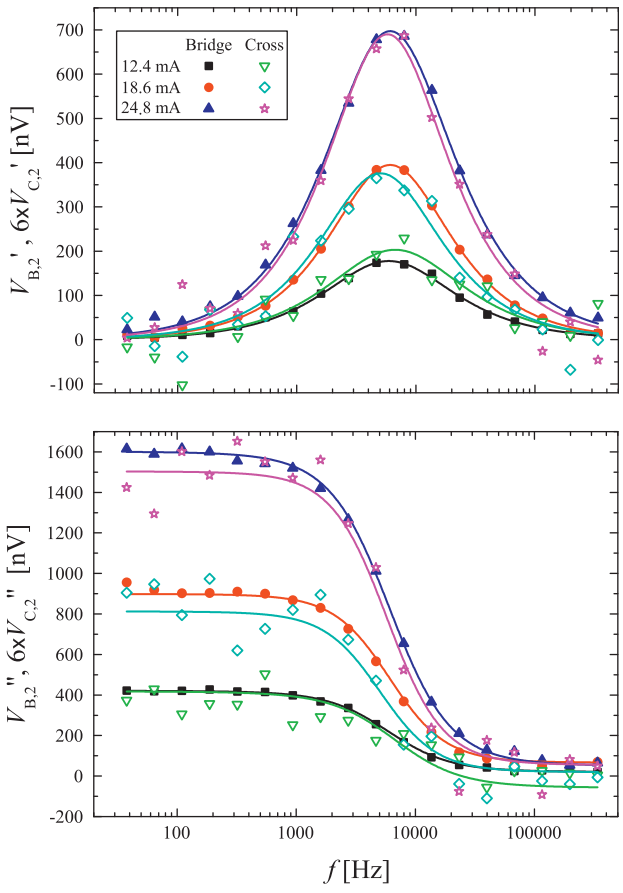

Fig. 2. In-phase (top) and out-of-phase (bottom) 2nd harmonic signal vs. frequency for the indicated bias currents measured for cross and bridge shaped sensors. The signals measured for the cross are multiplied by 6. The data shown are from the last frequency sweep with nanobeads (sweep number 8). The solid lines are curve fits to the Cole–Cole model.

Table 1
Average Brownian relaxation frequencies and α-parameters obtained from Cole–Cole fits to the frequency sweeps number 5–8 for cross and bridge sensors. The numbers in parentheses indicate the standard deviations (σ) of the four measurements.

I (mA)	f_B (kHz)		α	
	Bridge	Cross	Bridge	Cross
12.4	6.0(0.1)	6.5(0.9)	0.068(0.006)	0.16(0.06)
18.6	6.05(0.06)	5.3(0.3)	0.054(0.015)	0.04(0.02)
24.8	6.097(0.006)	6.1(0.3)	0.063(0.006)	0.04(0.03)

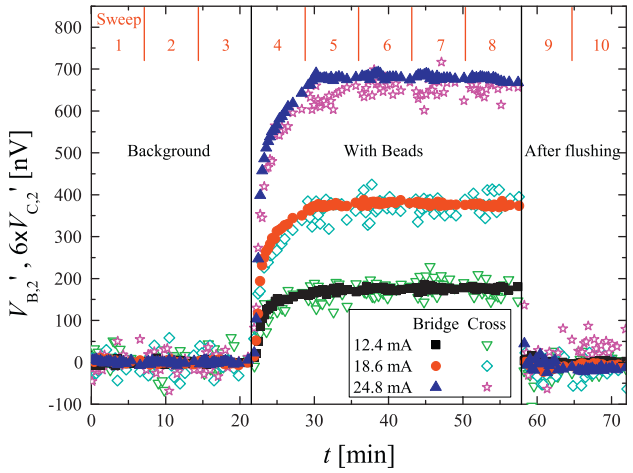

Fig. 3. In-phase signal of reference measurements ($f=4667$ Hz) plotted vs. time for the indicated bias currents. Signals from the cross sensor are multiplied by a factor of six. The graph is separated into three regions by two vertical lines: background (prior to nanobead injection), with nanobeads and after flushing. The numbers from 1 to 10 at the top show the number of the frequency sweep where the points were obtained.

$t \approx 29$ min corresponding to the initiation of frequency sweep number 5. After frequency sweep number 8 is completed at $t \approx 58$ min, the fluidic system is rinsed with water and the signal returns to the background level. The scaled signal levels for both sensor types show the same behavior with nearly identical signal levels. However, the data noise for the cross sensor is significantly higher than for the bridge sensor. Table 2 shows the average value and standard deviation for the measurements in Fig. 3 obtained during sweeps number 5–8. The average values for the bridge sensor are close to six times as large as those for the cross, whereas the standard deviations for the bridge sensor are less than two times those for the cross sensor. The standard deviation varies only little with the bias current and hence the relative standard deviation decreases approximately as the inverse signal, i.e., as the inverse square of the bias current. The lowest relative standard deviation of 0.9% is obtained for the bridge sensor with a bias current amplitude of $I_{AC} = 24.8$ mA.

4.2. Brownian relaxation measurements on samples containing DNA coils and oligonucleotide-tagged magnetic nanobeads

Fig. 4 shows the dynamic magnetic measurements on oligonucleotide-tagged nanobeads incubated with a suspension of DNA coils with a concentration of 200 pM as well as corresponding reference measurements on a sample containing no DNA coils. The measurements have been carried out simultaneously in both the DynoMag AC susceptometer (top panel) and in the chip system using the bridge sensor (bottom panel). The Brownian relaxation frequency of the individual nanobeads was measured to $f_B \approx 297$ Hz. To obtain data values that are independent of the nanobead concentration, all data have been normalized with the in-phase susceptibility measured well above f_B that approximates χ_∞. This normalization procedure was recently validated by Zardán Gómez de la Torre et al. (2011a) by comparing results obtained in the DynoMag AC susceptometer normalized with the high-frequency value of χ' with those obtained in a SQUID AC susceptometer normalized with the saturation magnetic moment. Nanobeads that are bound to DNA coils relax at a frequency of the order of 1 Hz (Strömberg et al., 2008), which is outside the investigated frequency window. Therefore, nanobeads that are bound to DNA coils will be dynamically inactive for the investigated frequencies and will not contribute to the peak in χ'' but still contribute to the high-frequency value of χ'. The binding of nanobeads to DNA coils is therefore detected as a reduction of the height of the peak in χ'' as well as in the low-frequency value of χ'.

The results displayed in Fig. 4 show that the same Brownian relaxation frequencies are obtained in the DynoMag system and by the bridge sensor in the chip system. In both cases the intensity of the peak in the normalized out-of-phase magnetic susceptibility (χ'' for the DynoMag system and V_2' for the bridge sensor) is reduced when the nanobeads are immobilized to the DNA coils. The observations in the DynoMag system are consistent with previously reported results (Zardán Gómez de la Torre et al., 2011a). The relative reduction of the peak height for the bridge sensor is larger than that observed in the DynoMag system.

Table 2
Average in-phase signal for cross and bridge sensors at three different bias currents for the 4×18 reference points from sweeps number 5 to 8. The numbers in parentheses indicate the standard deviations. The relative standard deviations are also calculated.

I (mA)	V_2' (nV)		$\sigma_{V_2'}/V_2' \times 100\%$ (%)	
	Bridge	Cross	Bridge	Cross
12.4	174(5)	29(3)	2.9	10.3
18.6	377(5)	62(4)	1.3	6.5
24.8	679(6)	108(4)	0.9	3.7

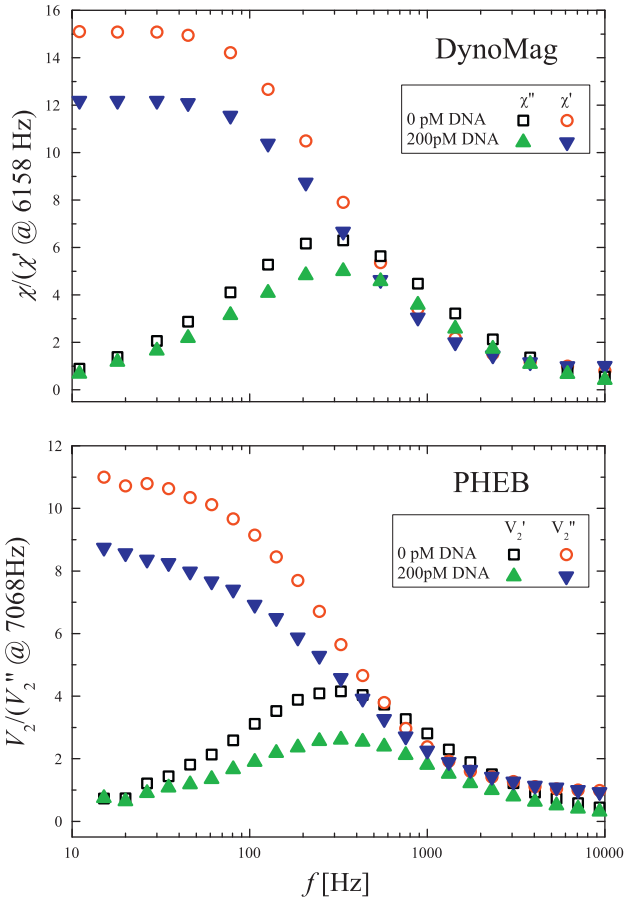

Fig. 4. Top: complex susceptibility vs. frequency measured with the DynoMag AC susceptometer. Measurements are normalized to the in-phase susceptibility at 6158 Hz. Bottom: in-phase and out-of-phase 2nd harmonic signal vs. frequency measured with a planar Hall effect bridge sensor. Measurements are normalized to the out-of-phase signal at 7068 Hz.

5. Discussion

5.1. Brownian relaxation measurements using cross and bridge sensors

First, we note that the ratio between the measured low-field sensitivities for the bridge and cross sensor is $S_{B,0}/S_{C,0} = 6.8$, which is considerably lower than the ratio of 14 expected solely from the sensor geometry. We attribute this to demagnetization effects of the sensor, which reduce the sensitivity of the bridge sensor and increase the sensitivity of the cross sensor (Donolato et al., 2011). Using the ratio between the low-field sensitivities, we estimate from Eq. (6) that the nanobead signals should have a ratio of $V_B/V_C = 2.4$, which is significantly lower than the experimentally observed ratio of about six. This deviation is likely caused by a combination of demagnetization effects and the simplifying assumption that the current through the cross sensor is uniformly distributed over the sensor width w, also in the central part of the cross. The detailed origin of the differences will be topic of our continued studies.

In all measurements, we have found that the highest signal is obtained for the bridge sensor with the highest applied bias

current. Part of the observed noise in the measurements originates from electrical noise in the measurement set-up as the signals are small. However, we have chosen not to use a pre-amplifier as they typically induce significant instrumental phase shifts at high frequencies. Higher values of the sensor bias current than those employed here can be used, but they will result in non-negligible self-heating of the sensor, which is undesirable.

The extracted Brownian relaxation frequencies shown in Table 1 increase slightly with bias current. This increase could be due to self-heating of the sensor, which would correspond to a temperature increase of 0.6 °C when taking the temperature dependence of the viscosity of water into consideration. However, the increase is within the uncertainty limits of the measurements and thus, it cannot be concluded to be due to temperature changes. In general the extracted values are more stable for measurements performed on the bridge sensor than on the cross sensor. This shows that the higher signal-to-noise ratio results in smaller variations of the parameters extracted from the fits and hence that the measurements are robust and reproducible.

The results from measurements at the reference frequency in Fig. 3 show the time dependence of the dynamic bead signal. It is observed that the signal for 40 nm beads stabilizes 7 min after injection of the nanobead suspension. This time dependence originates from the time needed to equilibrate the bead concentration after the bead suspension is injected into the water-filled channel where the initial bead concentration near the sensor is lower due to the parabolic flow profile. Fig. 3 also shows that after flushing nanobeads away with 800 μL/min for 3 min, the signal returns to the background level, which allows for reusing the sensor.

5.2. Brownian relaxation measurements on samples containing DNA coils and oligonucleotide-tagged magnetic nanobeads

The results from relaxation measurements on nanobeads with and without DNA coils shown in Fig. 4 in general indicate the same trends whether measured with the bridge sensor or the DynoMag. In both cases the normalized peak levels become smaller in the presence of DNA coils. This was also the effect of DNA coils demonstrated by Zardán Gómez de la Torre et al. (2011a), where the DynoMag results were compared to SQUID results. A reason why the responses are not completely identical could be that the DynoMag AC susceptometer measures on the entire sample volume, whereas the bridge sensor is more sensitive to beads near to the sensor surface. The latter can in fact prove useful for detecting DNA coils since nanobeads bound to DNA coils will sediment faster than free nanobeads. Therefore, the ratio between bound and free nanobeads near the sensor surface will become larger and this will make it easier to detect smaller DNA coil concentrations.

6. Conclusion

We have compared on-chip Brownian relaxation measurements carried out using planar Hall effect sensors with cross and bridge geometries with the same sensor width. For the investigated geometries we found that the bead signal from the bridge sensor is six times that from the cross. Moreover, the Brownian relaxation frequencies were determined with significantly less variation for the bridge sensor than for the cross.

The bridge sensor was also used to measure the difference between two samples of nanobeads with 0 pM and 200 pM of DNA coils produced by RCA. For comparison, equivalent samples were measured in a commercial AC susceptometer, and the differences between 0 pM and 200 pM samples were found to be very similar in the two systems. The presented bridge sensor may, thus, open up for new possibilities to build inexpensive biosensors for detecting pathogens and other clinically relevant analytes that can be amplified using RCA, including DNA sequences and proteins.

Acknowledgments

This work was supported by the Copenhagen Graduate School for Nanoscience and Nanotechnology (C:O:N:T), The Royal Swedish Academy of Sciences and the Knut and Alice Wallenberg (KAW) Foundation. Also we would like to acknowledge Anja Mezger for functionalization of beads with oligonucleotides, Camilla Russell for preparing the DNA coils, and Rebecca Stjernberg Bejhed for assisting during the DNA coil measurements.

References

Astalan, A.P., Ahrentorp, F., Johansson, C., Larsson, K., Krozer, A., 2004. Biosensors and Bioelectronics 19, 945–951.
Brown, W., 1963. Physical Review 130, 1677–1686.
Cole, K.S., Cole, R.H., 1941. The Journal of Chemical Physics 9, 341.
Connolly, J., St Pierre, T.G., 2001. Journal of Magnetism and Magnetic Materials 225, 156–160.
Dalslet, B.T., Damsgaard, C.D., Donolato, M., Strømme, M., Strömberg, M., Svedlindh, P., Hansen, M.F., 2011. Lab on a Chip 11, 296–302.
Debye, P., 1929. The Chemical Catalogue Co. New York.
Donolato, M., Dalslet, B.T., Damsgaard, C.D., Gunnarsson, K., Jacobsen, C.S., Svedlindh, P., Hansen, M.F., 2011. Journal of Applied Physics 109, 064511.
Fire, A., Xu, S.-Q, 1995. Proceedings of the National Academy of Sciences of the USA 92, 4641–4645.
Göransson, J., Zardán Gómez De La Torre, T., Strömberg, M., Russell, C., Svedlindh, P., Strømme, M., Nilsson, M., 2010. Analytical Chemistry 82, 9138–9140.
Hansen, T.B.G., Damsgaard, C.D., Dalslet, B.T., Hansen, M.F., 2010. Journal of Applied Physics 107, 124511.
Henriksen, A.D., Dalslet, B.T., Skieller, D.H., Lee, K.H., Okkels, F., Hansen, M.F., 2010. Applied Physics Letters 97, 013507.
Jaffrezic-Renault, N., Martelet, C., Chevolot, Y., Cloarec, J.P., 2007. Sensors 7, 589–614.
Koh, I., Josephson, L., 2009. Sensors 9, 8130–8145.
Liu, D., Daubendiek, S.L., Zillman, M.A., Ryan, K., Kool, E.T., 1996. Journal of the American Chemical Society 118, 1587–1594.
Ludwig, F., Mäuselein, S., Heim, E., Schilling, M., 2005. Review of Scientific Instruments 76, 106102.
Nilsson, M., Malmgren, H., Samiotaki, M., Kwiatkowski, M., Chowdhary, B.P., Landegren, U., 1994. Science 265, 2085–2088.
Öisjöen, F., Schneiderman, J.F., Astalan, A.P., Kalabukhov, A., Johansson, C., Winkler, D., 2010. Biosensors and Bioelectronics 25, 1008–1013.
Østerberg, F.W., Dalslet, B.T., Snakenborg, D., Johansson, C., Hansen, M.F., 2010. AIP Conference Proceedings, 176–183.
Persson, A., Bejhed, R.S., Nguyen, H., Gunnarsson, K., Dalslet, B.T., Østerberg, F.W., Hansen, M.F., Svedlindh, P., 2011. Sensors and Actuators A: Physical 171, 212–218.
Strömberg, M., Göransson, J., Gunnarsson, K., Nilsson, M., Svedlindh, P., Strømme, M., 2008. Nano Letters 8, 816–821.
Wang, S.X., Li, G., 2008. IEEE Transactions on Magnetics 44, 1687–1702.
Zardán Gómez de la Torre, T., Mezger, A., Herthnek, D., Johansson, C., Svedlindh, P., Nilsson, M., Strømme, M., 2011a. Biosensors and Bioelectronics 29, 195–199.
Zardán Gómez de la Torre, T., Herthnek, D., Ramachandraiah, H., Svedlindh, P., Nilsson, M., Strømme, M., 2011b. Journal of Nanoscience and Nanotechnology 11, 8532–8537.
Zardán Gómez de la Torre, T., Ke, R., Mezger, A., Svedlindh, P., Strømme, M., Nilsson, M., 2012. Small, 2174–2177.

Paper VI

F. W. Østerberg, G. Rizzi, M. Donolato, R. S. Bejhed, A. Mezger, M. Strömberg, M. Nilsson, M. Strømme, P. Svedlindh and M. F. Hansen
"On-chip detection of rolling circle amplified DNA molecules from *Bacillus globigii* spores and *Vibrio cholerae*"
Small (2014)

NANO MICRO small

Biosensors

On-Chip Detection of Rolling Circle Amplified DNA Molecules from *Bacillus Globigii* Spores and *Vibrio Cholerae*

*Frederik W. Østerberg, Giovanni Rizzi, Marco Donolato, Rebecca S. Bejhed, Anja Mezger, Mattias Strömberg, Mats Nilsson, Maria Strømme, Peter Svedlindh, and Mikkel F. Hansen**

For the first time DNA coils formed by rolling circle amplification are quantified on-chip by Brownian relaxation measurements on magnetic nanobeads using a magnetoresistive sensor. No external magnetic fields are required besides the magnetic field arising from the current through the sensor, which makes the setup very compact. Limits of detection down to 500 Bacillus globigii spores and 2 pM of Vibrio cholerae are demonstrated, which are on the same order of magnitude or lower than those achieved previously using a commercial macro-scale AC susceptometer. The chip-based readout is an important step towards the realization of field tests based on rolling circle amplification molecular analyses.

1. Introduction

Infectious and parasitic diseases rank second among the "top killers" of the world.[1] The countrywide economic loss due to infectious diseases is immense, cementing poverty and underdevelopment in many regions of the world. Early detection, high sensitivity and rapid identification with high specificity of emerging and reemerging pathogens are absolute requirements today in both human and veterinary medicine.

The two standard methods employed for the detection of pathogenic bacteria in hospitals and medical centers are culture followed by colony counting or nucleic acid tests based on the polymerase chain reaction (PCR). Culture based methods are time consuming, up to several days, while PCRs require expensive equipment and trained personnel. Thus, there is a need for novel microbiological detection methods with a high sensitivity to pathogens in relevant biological media that can provide results within a short time and at low cost.

Figure 1a schematically illustrates an alternative approach to the detection pathogenic bacteria based on rolling circle amplification (RCA) that enables both nucleic acid and immunoassay based testing. (i) First, circularized reporter molecules are generated in an antibody based proximity ligation assay (PLA)[2] or the circularized DNA is formed from a DNA target by padlock probe recognition.[3] (ii) The circularized DNA is then amplified by rolling circle amplification (RCA) to form RCA coils.[2] (iii) Finally, the RCA coils are detected.

The padlock probe assay is based on a strictly target DNA dependent circularization reaction, while the PLA utilizes DNA modified antibodies to template circularization of probe strands upon coincident binding of two or more PLA probes to a target protein.[4] The circular DNA molecules

Dr. F. W. Østerberg, G. Rizzi, Dr. M. Donolato
Dr. M. F. Hansen
Department of Micro- and Nanotechnology
Technical University of Denmark
DTU Nanotech, Building 345 East
DK-2800, Kongens Lyngby, Denmark
E-mail: Mikkel.Hansen@nanotech.dtu.dk

R. S. Bejhed, Dr. M. Strömberg, Prof. M. Strømme, Prof. P. Svedlindh
Department of Engineering Sciences
Uppsala University
Ångström Laboratory, Box 534
SE-751 21, Uppsala, Sweden

A. Mezger, Prof. M. Nilsson
Science for Life Laboratory
Department of Biochemistry and Biophysics
Stockholm University, Box 1031
SE-171 21, Solna, Sweden

DOI: 10.1002/smll.201303325

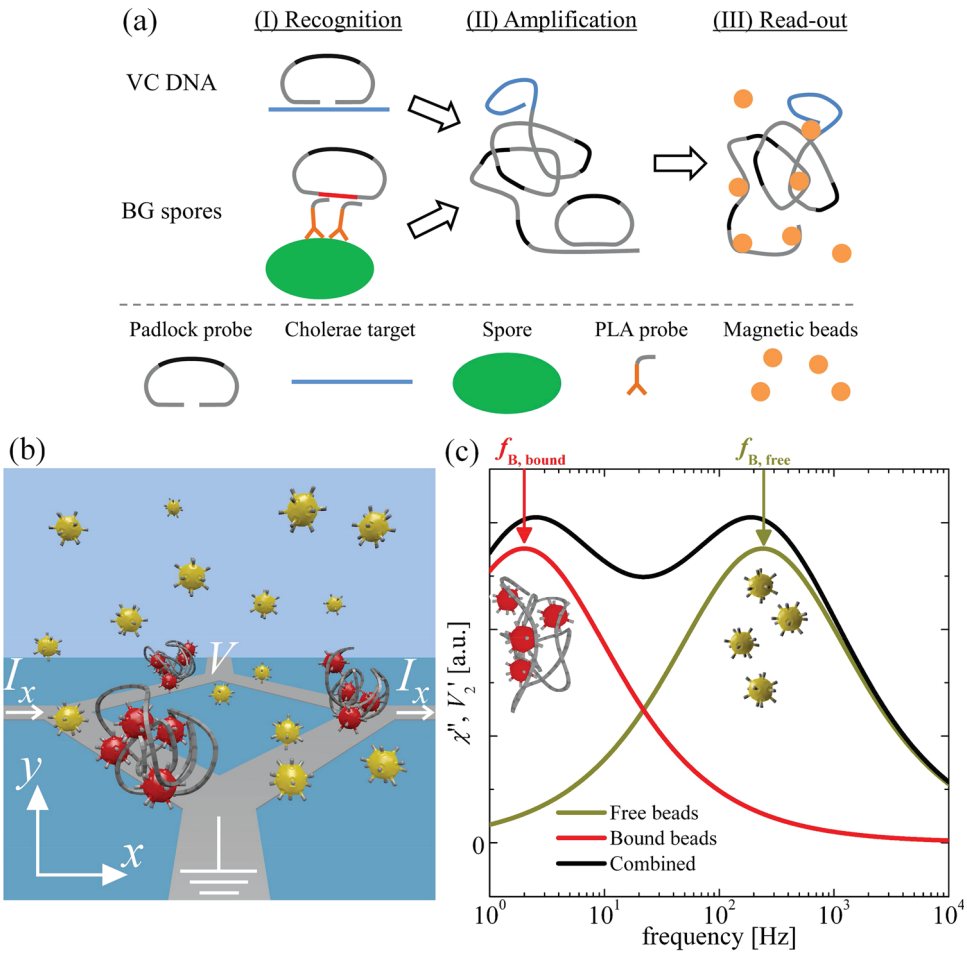

Figure 1. **(a)** Simplified schematic of the bioassay scheme for the detection of *Vibrio cholerae* (VC) DNA and *Bacillus globigii* (BG) bacterial spores. **(b)** Sketch of planar Hall effect bridge (PHEB) sensor with free beads (yellow) and beads bound to RCA coils (red) distributed over the sensor. The sensor bias current I is applied in the x-direction, while the voltage V is measured in the y-direction. **(c)** Calculated out-of-phase magnetic susceptibility (in-phase second harmonic signal of the PHEB sensor) for free and bound beads as well as the two combined.

formed by these assays are copied in an isothermal DNA polymerization reaction that due to the endless nature of the circular template proceeds until the polymerase dies, creating a very long DNA polymer (10–100 kilobases depending on the polymerization time) consisting of tandem repeated copies of the sequence of the DNA circle.[5] These long DNA polymers spontaneously coil into 500–1000 nm diameter blobs of DNA in solution due to Brownian motion of the flexible DNA chain.[6,7] Compared to PCR amplification, padlock probe recognition followed by RCA results in a highly specific detection that, for example, can robustly resolve mutant sequence variants with no need for bacterial culture.[8] Moreover, RCA is less sensitive to contaminants than PCR and requires only two temperature steps near room temperature.[7]

Currently, the optimal method for detecting RCA coils is by fluorescent microscopy, which requires high-power lasers and fast and sensitive line-cameras resulting in detection limits down to the fM range.[9] However, this instrument is expensive, and unsuitable to be used as the readout in a portable lab-on-a-chip device.

Another method for detecting the RCA coils relies on the change of the Brownian relaxation response of magnetic nanobeads functionalized with detection oligonucleotides when the nanobeads bind to the RCA coils. The principle behind this detection scheme is that the Brownian relaxation frequency f_B of a magnetic nanobead is inversely proportional to its hydrodynamic volume. Thus, when analytes bind to a magnetic nanobead, its hydrodynamic volume increases resulting in a decrease of f_B.[10] Strömberg et al.[11] demonstrated the use of a Brownian relaxation detection scheme for the detection of RCA coils down to pM concentrations as magnetic nanobeads bound to micrometer-sized coils show a substantially different Brownian relaxation than free magnetic nanobeads.[11–14] The Brownian relaxation response was characterized via measurements of the frequency spectrum of the complex magnetic susceptibility (χ) using a superconducting quantum interference device (SQUID) magnetometer. However, a SQUID magnetometer is a bulky instrument that requires cryogenic liquids, which makes it unsuitable for the readout in a lab-on-a-chip biosensor. Zardán Gómez de la Torre et al.[15] later showed that RCA coils can also be detected with a portable AC susceptometer operated at room temperature.[15–18] Such a device is more compact than a SQUID, but it is still not suitable for the readout in a lab-on-a-chip biosensor.

small 2014,
DOI: 10.1002/smll.201303325

Recently, it has been shown that magnetoresistive planar Hall effect bridge (PHEB) sensors can be used to measure the hydrodynamic size of magnetic nanobeads with no need for externally applied magnetic fields.[19] The sensors are sub-millimeter in size and can be operated at room temperature. Due to their small size, they require only small sample volumes and are easily integrated as the readout in a complete lab-on-a-chip system with integrated sample preparation. In our previous work,[19] we demonstrated the feasibility of measuring the dynamic response of magnetic nanobeads dispersed in a biological buffer and observed a qualitative change of the dynamic magnetic signal when functionalized magnetic beads were incubated with a high concentration of RCA coils.

Here, we demonstrate for the first time that RCA coils can be precisely quantified on-chip using PHEB sensors and an analysis approach based on the ratio of the in-phase sensor signals at low and intermediate frequencies. Two types of pathogenic target entities, a DNA target sequence originating from *Vibrio cholerae* (VC) and spores produced by *Bacillus globigii* (BG), are quantitatively detected to illustrate the versatility of the assay.

The sensors used for this study are based on the anisotropic magnetoresistance of permalloy and are patterned in a Wheatstone bridge configuration as illustrated in Figure 1b, where a bias current I is forced through the sensor in the x-direction, while the sensor voltage V is measured across the sensor in the y-direction. Details on the sensor geometry, operation and mounting are given in the Supporting Information.

The beads are magnetized by the magnetic field due to the bias current passed through the sensor, i.e., no external magnetic field sources are needed. By using an alternating bias current with frequency f, it is possible to measure the complex magnetic susceptibility $\chi = \chi' - \mathrm{i}\chi''$ using lock-in technique.[20] The in-phase and out-of-phase second harmonic sensor signals V_2' and V_2'' are proportional to the out-of-phase and in-phase components χ'' and χ' of the magnetic susceptibility, respectively.[21] The Brownian relaxation dynamics of the beads gives rise to a peak in χ'' or equivalently in V_2' at the Brownian relaxation frequency f_B. Figure 1c illustrates the readout principle of the volume-based assay. Free magnetic beads will have a high Brownian relaxation frequency $f_{B,free}$, whereas beads bound to RCA coils have a much larger hydrodynamic size and hence a significantly lower Brownian relaxation frequency, $f_{B,bound}$. The fraction of beads bound to RCA coils depends on the concentration of RCA coils and can be estimated from analyses of frequency sweeps such as those illustrated in Figure 1c.

2. Results and Discussion

Figure 2a shows the normalized in-phase second harmonic sensor signal vs. frequency for the samples containing concentrations c = 4–256 pM of RCA coils formed from VC DNA and a negative reference sample (c = 0 pM). Spectra measured for c = 1 pM and 2 pM are omitted, because on this scale they are indistinguishable from the spectrum for the sample with c = 0 pM. The spectra shown in Figure 2a were all recorded 30 min after sample injection into the microfluidic readout system. From the figure it is seen that the Brownian relaxation peak of the free beads (0 pM) is near 240 Hz, which corresponds to a hydrodynamic size of 125 nm. This size is significantly larger than the nominal bead size of 80 nm reported by the manufacturer. This deviation may be caused by batch-to-batch variation of the bead size, an increase of the bead size due to the functionalization, bead clustering, and a possible positive selection of larger beads during bead washing steps.

In previous studies by Strömberg et al.[11,12,22] and Zardán Gómez de la Torre et al.,[13] the measured AC susceptibility for each sample was normalized with the saturation magnetic moment of the sample or the high-frequency value of χ', which are both proportional to the number of nanoparticles in the sample. As the signals in these techniques are obtained from the entire sample volume, such normalization can be used to quantify the fraction of beads that are bound to coils solely from the reduction of the peak due to free beads in the normalized spectrum. A magnetoresistive sensor, however, is primarily sensitive to magnetic nanoparticles near the sensor surface[23] implying that the amount of beads contributing to the signal may vary over time. Moreover, the out-of-phase 2nd harmonic sensor signal is subject to a small variable offset, which renders analyses using V_2'' data less reliable. In the Supporting Information we present a detailed comparison of different analysis approaches and show that the analysis of the measurement results based on only the V_2' data presented below gives the optimum result. Moreover, in section 1.1 of the Supporting Information we show that the area under the V_2' vs. log(f) spectra is proportional to the total amount of beads contributing to the sensor signal. To facilitate evaluation of the frequencies where the signal decreases and increases with the concentration of RCA coils, we have normalized the frequency spectra with the average value of V_2' (which is proportional to the area of the V_2' vs. log(f) curve). Figure 2a shows the normalized V_2' spectra obtained for the indicated concentrations of RCA coils formed from VC.

From Figure 2a, it is seen that the normalized signals can be split into three regions: At low frequencies (f < 35 Hz), the normalized in-phase signal increases with RCA coil concentration; at medium frequencies (35 Hz < f < 2.7 kHz), the normalized signal decreases with RCA coil concentration; and at high frequencies (f > 2.7 kHz), the normalized signal increases slightly with RCA coil concentration. The explanation for the behavior of the normalized signal in these regions connects to the facts that the beads not bound to RCA coils have a Brownian relaxation peak near 240 Hz and that the beads bound to RCA coils have a Brownian relaxation peak below 1 Hz. When the RCA coil concentration increases, the relative amount of free beads and hence the normalized signal at medium frequencies decreases. Correspondingly, the relative amount of beads bound to RCA coils increases, which is seen as an increase of the normalized signal at low frequencies. In order to quantify the RCA coil concentration, we propose to calculate the ratio $R(c)$ between the total signal measured at low and medium frequencies as described in detail in the

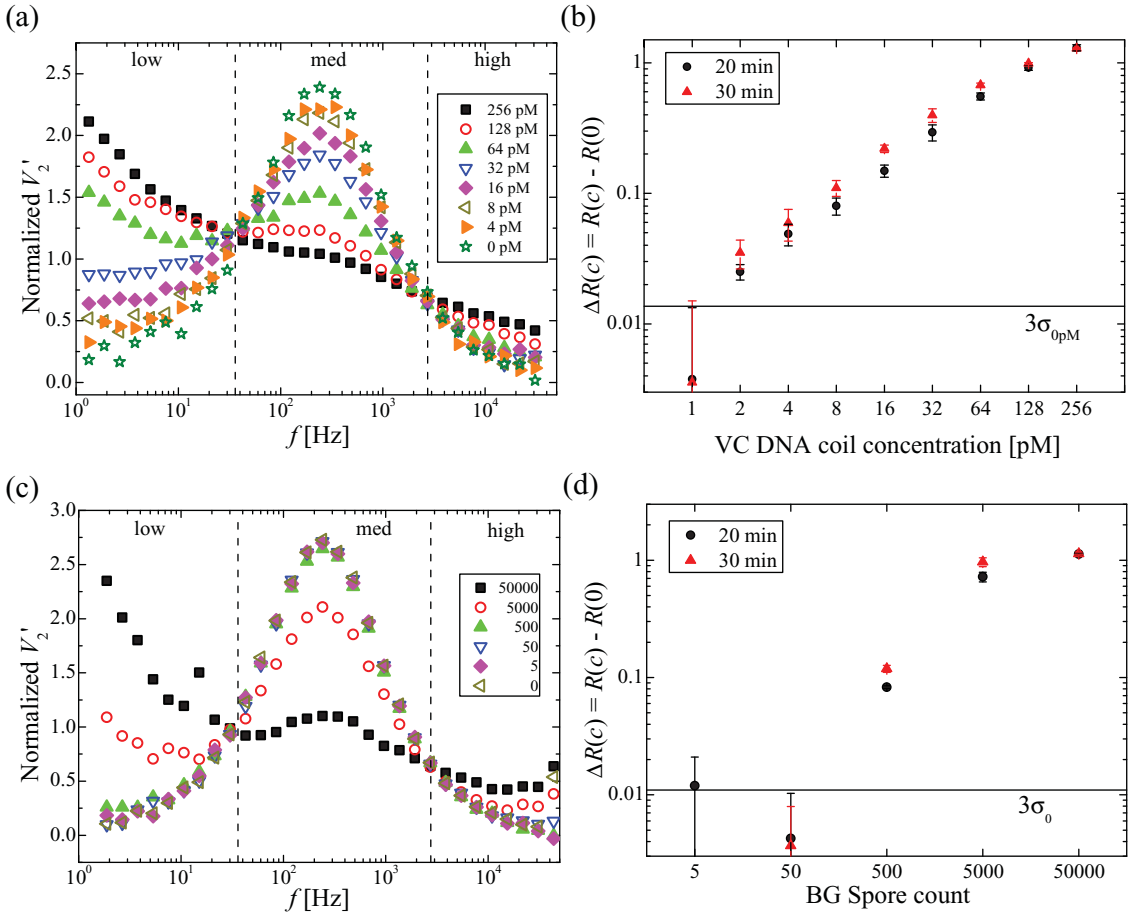

Figure 2. In-phase second harmonic sensor signal vs. frequency for samples with (a) 4–256 pM RCA coils formed from *Vibrio cholerae* (VC) DNA and (c) RCA coils formed from 5 – 50000 *Bacillus globigii* (BG) spores. All spectra are normalized with their average signal. The measurements were recorded 30 min after sample injection into the microfluidic readout system. The two vertical lines divide the frequency range into low, medium and high frequencies. Panels (b) and (d) show $\Delta R(c) \equiv R(c) - R(0)$ vs. concentration c of RCA coils formed from VC and BG spore samples, respectively. $R(c)$ is the ratio of the total signal measured at low frequencies to that measured at medium frequencies over four frequency sweeps (10 min total measuring time) ending at the indicated times. The values of $\Delta R(c)$ are plotted 20 and 30 min after sample injection. The horizontal lines indicate the 3σ levels for the samples without RCA coils. The error bars are standard deviations ($n = 3$).

Supporting Information. Figure 2b shows $\Delta R(c) \equiv R(c) - R(0)$ vs. concentration of RCA coils formed from *Vibrio cholerae* obtained 20 and 30 min after sample injection into the microfluidic readout system. The values plotted are averages of triplicate experiments carried out on separate days, and the error bars represent the corresponding standard deviations (σ). The horizontal line corresponds to three standard deviations of the samples containing no RCA coils ($3\sigma_{0pM}$). This line determines the limit of detection (LOD). It is noted that the signal ratio for samples with RCA coils increases with time after injection into the microfluidic system. This is due to sedimentation of beads bound to RCA coils (see Supporting Information). Thus, the ratio of bound to free beads near the sensor surface increases for longer analysis time. Therefore, the LOD also improves with longer time. After both 20 min and 30 min, Figure 2b shows that samples with 2 pM RCA coil concentrations are clearly different from the negative control samples whereas those with 1 pM are indistinguishable from the negative control. Hence, the LOD is between 1 and 2 pM. Both curves in Figure 2b show a linear trend although with beginning saturation appearing for the highest investigated RCA coil concentration of 256 pM. Thus, the dynamic range is about two orders of magnitude. Saturation appears when most or all of the magnetic nanobeads are bound to RCA coils. It should be noted that the LOD and dynamic range can be tuned by varying the magnetic bead concentration. The LOD can be shifted towards lower values by using a lower magnetic bead concentration at the expense of a smaller signal to noise ratio.

Figure 2c shows the normalized spectra obtained from measurements on RCA coils produced from BG spores by PLA. They show the same behavior as in Figure 2a with the same splitting into low, medium and high frequency regions. Figure 2d shows $\Delta R(c)$ vs. number of BG spores. Again, it is seen that the LOD decreases with time and that the ratios increase with time. For these measurements, the samples with 500 spores are significantly different from the negative control sample both 20 min and 30 min after sample injection. It is also noted that the ratio for the sample with 50,000 spores did not change over time. This is likely because these samples contained an excess of RCA coils, such that almost all beads became bound to RCA coils. From Figure 2c it is

small 2014,
DOI: 10.1002/smll.201303325

observed that a small peak is left near 240 Hz for the sample containing 50,000 spores. This peak may be due to beads that were not successfully functionalized with detection oligonucleotides such that they did not bind to RCA coils.

Previously, RCA coils formed from VC DNA have been characterized using a commercial AC magnetic susceptometer by Zardán Gómes de la Torre et al.[15] using the analysis strategy presented in the Supporting Information. They found an LOD of 4 pM and a similar dynamic range using an analysis time of about 30 min. The same authors studied RCA coils formed from BG spores, where they also found a detection limit of 500 spores for samples prepared in the same way as in the present study.[17] Thus, the present results have shown that the LOD and dynamic range in the microfluidic readout system are similar to or better than those obtained in a commercial AC susceptibility system. The microfluidic readout system has the advantages that it is compact and suited for integration with upstream sample processing and that it measures on much smaller sample volumes. Thus, the presented assays may actually perform better with a microfluidic-based readout than using a bulky commercial instrument.

The present work has focused on the detection of coils formed using an RCA time of 60 min. These coils are so large, ≈1 μm in diameter, that the signal due to magnetic beads bound to coils is well separated from that of free magnetic beads in the frequency spectra. This has enabled the presented straightforward analysis. However, to reduce the total assay time a shorter RCA time could potentially be used. This would result in smaller RCA coils and hence shift the signal from beads bound to coils to higher frequencies. This could facilitate observation of more of the low-frequency peak from magnetic beads bound to RCA coils but it would also result in larger overlap between the low-frequency peak and the peak from free magnetic beads, which could make the analysis more challenging. Moreover, smaller RCA coils are not able to bind as many magnetic beads as larger coils and they also sediment more slowly. These factors reduce the sensitivity to a given coil concentration when the RCA time is reduced. An optimization of the assay for a given application would involve varying both the magnetic bead size and concentration as well as the RCA time to identify the best compromise between LOD, dynamic range and total assay time. The method could also be envisioned to directly detect small molecules such as short DNA strands. In this case, the change of the hydrodynamic size of the individual magnetic beads due to the molecular binding is typically small compared to the magnetic bead size resulting in only a small change of the Brownian relaxation time spectrum.[10,24] For such applications, it is therefore advantageous to pursue different assay strategies where the presence of the target results in agglutination of the magnetic beads[25,26] or binding of the magnetic beads to a solid support.[27] The exploration of such assay strategies will be topic of future studies.

3. Conclusion

In this paper, we have for the first time shown that magnetoresistive sensors integrated in a microfluidic readout system can be used for the on-chip quantification of coils of DNA formed by RCA with no need for externally applied magnetic fields. We have demonstrated that RCA coils formed off-chip from *Vibrio cholerae* can be detected in concentrations down to 2 pM with an analysis time of 20 min. Furthermore, we have demonstrated that the magnetoresistive sensor readout combined with off-chip proximity ligation assay and RCA can detect down to 500 *Bacillus globigii* spores. These results are as good as—or better—than those obtained in commercial AC susceptometers on much larger sample volumes. This shows that magnetoresistive sensors are promising for a chip-based readout of volume-based assays for detection of DNA and spores based on RCA coil formation. Thus, a significant barrier towards a lab-on-a-chip implementation of such assays has been removed. Our future work aims at integrating the chip-based readout with on-chip sample preparation and amplification.

4. Experimental Section

Below, we describe the on-chip detection experiments of RCA coils formed from VC target using padlock probe recognition and RCA and from BG spores using a proximity ligation assay (PLA) followed by circle-to-circle amplification (C2CA), i.e., RCA in several steps (in this case two). Details of the RCA coil preparation are given in the Supporting Information. In both cases, the RCA time was 1 hour (for the spore protocol this was the time for the final RCA step) resulting in coil lengths ~90 kbp.

The RCA coils formed from VC DNA were produced in an initial concentration of 4 nM and subsequently diluted with hybridization buffer to form a two-fold serial dilution of samples with final RCA coil concentrations between 1 pM and 256 pM. Thus, measurements on these RCA coils only tested the chip readout and not the whole assay. For the RCA coils formed from BG spores, the PLA was applied to starting mixtures with 50,000 to 5 spores in a ten-fold serial dilution series. Hence, for these, the whole assay including the chip readout was tested.

The magnetic beads chosen for the readout should have a remanent magnetic moment such that the Brownian relaxation mechanism dominates (i.e., superparamagnetic relaxation is negligible). Moreover, the magnetic beads should be small enough to minimize bead sedimentation on the sensor surface and large enough to enhance the sensitivity of the sensor signal to a low number of binding events.[21] In this study we used streptavidin coated magnetic beads with a nominal diameter of 80 nm (BNF-starch beads, Product no. 10–19–801, Micromod Partikeltechnologie GmbH, Germany). These beads showed the best properties in our previous comparative study of six different bead types.[21] The beads were functionalized with biotinylated single stranded detection oligonucleotides complementary to the repeating RCA coil sequences (see Supporting Information) and diluted in phosphate buffered saline (PBS) to a concentration of 1 mg/mL.

The samples were prepared for analysis by gently mixing the functionalized bead suspension (15 μL) with RCA coil solution (15 μL), followed by incubation at 55°C for 30 min. After incubation, the mixture was injected into the microfluidic readout system and the second harmonic sensor signal was recorded as function

of frequency. The experiments were carried out in triplicate on separate days.

Supporting Information

Supporting Information is available from the Wiley Online Library or from the author.

Acknowledgements

This work was supported by the Knut and Alice Wallenberg (KAW) Foundation, Copenhagen Graduate School for Nanoscience and Nanotechnology (C:O:N:T), the Carl Trygger Foundation, the Swedish Research Council and FORMAS (BioBridges, Dnr. 221–2012–444).

[1] World Health Organization. The global burden of disease: 2004 update. WHO Press **2008** (ISBN 978 92 4 156371 0).
[2] S. Fredriksson, M. Gullberg, J. Jarvius, C. Olsson, K. Pietras, S. M. Gustafsdottir, A. Ostman, U. Landegren, *Nat. Biotechnol.* **2002**, *20*, 473–477.
[3] M. Nilsson, H. Malmgren, M. Samiotaki, M. Kwiatkowski, B. P. Chowdhary, U. Landegren, *Science* **1994**, *265*, 2085–2088.
[4] O. Söderberg, M. Gullberg, M. Jarvius, K. Ridderstrale, K. J. Leuchowius, J. Jarvius, K. Wester, P. Hydbring, F. Bahram, L. G. Larsson, U. Landegren, *Nat. Methods* **2006**, *3*, 995–1000.
[5] J. Banér, M. Nilsson, M. Mendel-Hartvig, U. Landegren, *Nucleic Acids Res.* **1996**, *26*, 5073–5078.
[6] G. A. Blab, T. Schmidt, M. Nilsson, *Anal. Chem.* **2004**, *76*, 495–498.
[7] J. Jarvius, J. Melin, J. Göransson, J. Stenberg, S. Fredriksson, C. Gonzalez-Rey, S. Bertilsson, M. Nilsson, *Nat. Methods* **2006**, *3*, 725–727.
[8] P. Hardenbol, J. Banér, M. Jain, M. Nilsson, E. A. Namsaraev, G. A. Karlin-Neumann, H. Fakhrai-Rad, M. Ronaghi, T. D. Willis, U. Landegren, R. W. Davis, *Nat. Biotechnol.* **2003**, *21*, 673–678.
[9] J. Göransson, R. Ke, R. Y. Nong, W. M. Howell, A. Karman, J. Grawé, J. Stenberg, M. Granberg, M. Elgh, D. Herthnek, P. Wikström, J. Jarvius, M. Nilsson, *PLoS ONE* **2012**, *7*(2): e31068
[10] J. Connolly, T. G. St Pierre, *J. Magn. Magn. Mater.* **2001**, *225*, 156.
[11] M. Strömberg, J. Göransson, K. Gunnarsson, M. Nilsson, P. Svedlindh, M. Strømme, *Nano Lett.* **2008**, *8*(3), 816–821.
[12] M. Strömberg, T. Zardán Gómez de la Torre, J. Göransson, K. Gunnarsson, M. Nilsson, P. Svedlindh, M. Strømme, *Anal. Chem.* **2009**, *81*, 3398–3406.
[13] T. Zardán Gómez de la Torre, M. Strömberg, C. Russell, J. Göransson, M. Nilsson, P. Svedlindh, M. Strømme, *J. Phys. Chem. B* **2010**, *114*, 3707–3713.
[14] J. Göransson, T. Zardán Gómez de la Torre, M. Strömberg, C. Russell, P. Svedlindh, M. Strømme, M. Nilsson, *Anal. Chem.* **2010**, *82*, 9138–9140.
[15] T. Zardán Gómez de la Torre, A. Mezger, D. Herthnek, C. Johansson, P. Svedlindh, M. Nilsson, M. Strømme, *Biosens. Bioelectron.* **2011**, *29*, 195–199.
[16] T. Zardán Gómez de la Torre, D. Herthnek, H. Ramachandraiah, P. Svedlindh, M. Nilsson, M. Strømme, *J. Nanosci. Nanotechnol.* **2011**, *11*, 8532–8537.
[17] T. Zardán Gómez de la Torre, R. Ke, A. Mezger, P. Svedlindh, M. Strømme, M. Nilsson, *Small* **2012**, *8*, 2174–2177.
[18] A. Engström, T. Zardán Gómez de la Torre, M. Strømme, M. Nilsson, D. Herthnek, *PLoS ONE* **2013**, *8*, e62015.
[19] F. W. Østerberg, G. Rizzi, T. Zardán Gómez de la Torre, M. Strömberg, M. Strømme, P. Svedlindh, M. F. Hansen, *Biosens. Bioelectron.* **2013**, *40*, 147.
[20] F. W. Østerberg, B. T , Dalslet, D. Snakenborg, C. Johansson, M. F. Hansen, *AIP Conf. Proc.* **2010***1311*, 176.
[21] F. W. Østerberg, G. Rizzi, M. F. Hansen, *J. Appl. Phys.* **2013**, *113*(15), 154507.
[22] M. Strömberg, T. Zardán Gómez de la Torre, J. Göransson, K. Gunnarsson, M. Nilsson, M. Strømme, P. Svedlindh, *Biosens. Bioelectron.* **2008**, *24*, 696–703.
[23] T. B. G. Hansen, C. D. Damsgaard, B. T. Dalslet, M. F. Hansen, *J. Appl. Phys.* **2010**, *107*, 124511.
[24] A. P. Astalan, F. Ahrentorp, C. Johansson, K. Larsson, A. Krozer, *Biosens. Bioelectron.* **2004**, *19*, 945.
[25] C.-Y. Hong, C. C. Wu, Y. C. Chiu, S. Y. Yang, H. E. Horng, H. C. Yang, *Appl. Phys. Lett.* **2006**, *88*, 212512.
[26] R. Kötitz, W. Weitschies, L. Trahms, W. Brewer, W. Semmler, *J. Magn. Magn. Mater.* **1999**, *194*, 62.
[27] D. Eberbeck, C. Bergemann, F. Wiekhorst, U. Steinhoff, L. Trahms, *J. Nanobiotechnol.* **2008**, *6*, 4.

Received: October 23, 2013
Revised: January 10, 2014
Published online:

DOI: 10.1002/smll.201303325

Paper VII

G. Rizzi, F. W. Østerberg, M. Dufva and M. F. Hansen
"Magnetoresistive sensor for real-time single nucleotide polymorphism genotyping"
Biosens.Bioelectron. **52**, 445 (2014)

Biosensors and Bioelectronics 52 (2014) 445–451

Contents lists available at ScienceDirect

Biosensors and Bioelectronics

journal homepage: www.elsevier.com/locate/bios

Magnetoresistive sensor for real-time single nucleotide polymorphism genotyping

Giovanni Rizzi, Frederik Westergaard Østerberg, Martin Dufva, Mikkel Fougt Hansen *

Department of Micro- and Nanotechnology, Technical University of Denmark, DTU Nanotech, Building 345 East, DK-2800 Kongens Lyngby, Denmark

ARTICLE INFO

Article history:
Received 8 July 2013
Received in revised form
15 August 2013
Accepted 3 September 2013
Available online 19 September 2013

Keywords:
Biosensor
Magnetoresistive sensor
Single nucleotide polymorphism
Microfluidics
DNA genotyping

ABSTRACT

We demonstrate a magnetoresistive sensor platform that allows for the real-time detection of point mutations in DNA targets. Specifically, we detect point mutations at two sites in the human beta globin gene. For DNA detection, the present sensor technology has a detection limit of about 160 pM and a dynamic range of about two orders of magnitude. The sensors are based on a new geometry for biological sensing that detects the difference between the amount of beads bound to a sensing pad and a local integrated negative reference pad. The magnetic beads are magnetised by the magnetic field arising from the sensor bias current such that no external magnetic fields are needed. The sensors are integrated in a microfluidic system with temperature control. The local negative reference integrated in the sensor geometry efficiently compensates for sensor offsets, external magnetic fields and a uniform background of magnetic beads, which enables real-time quantification of the specific binding of magnetic beads to the sensor surface under varying experimental conditions.

1. Introduction

Genotyping has wide application in diagnostics of genetic diseases, cancers, and viral and bacterial infections. There is an ever-increasing need for rapid, specific and sensitive methods to detect particular DNA sequences in a sample. Several diseases are related to alternative forms (alleles) of a given gene. For cancer and genetic diagnostics, the assays must be able to distinguish DNA species differing in only one base to perform so called single nucleotide polymorphism (SNP) genotyping. In some cases the SNP is known and specific probes against that particular SNP can be designed. In other cases, the SNP is unknown and must be screened for. Allele specific hybridisation is a rapid method for SNP genotyping that employs probes specific for the wild type (WT) and mutant type (MT) sequences. A simple hybridisation and dehybridisation reaction, most often with an end-point fluorescence readout, can then be used to obtain specificity. Multiplexing allele specific reactions is a substantial optimisation process and sequence dependent variation around each respective SNP makes it difficult to obtain fully optimised SNP calling at a given assay condition (Poulsen et al., 2011). The efficacy of SNP calling can be increased by treating the hybridisation at different stringencies by varying the salt concentration or the temperature (Howell et al., 1999; Poulsen et al., 2011; Petersen et al., 2008, 2009). The SNP calling can be performed after a given time point or in real time (Howell et al., 1999; Poulsen et al., 2011; Petersen et al., 2008, 2009). Studying real-time dehybridisation is preferable since far more conditions can be investigated as compared to post washing analysis. However, real-time fluorescence monitoring is hampered by high background signals from the fluorochromes used to detect the hybrids. Real-time investigation of hybridisation and dehybridisation can also be used to obtain high resolution melting curves for screening of unknown mutations in a sample (Er and Chang, (2012)). Such analyses are mostly performed in solution phase using intercalating fluorescent dyes. A corresponding analysis is possible using DNA microarrays (Nørholm et al., 2004), but it requires specialised and bulky instrumentation, and it is still hampered by high background signals from fluorochromes present in the sample.

Biosensors with a readout based on the binding of magnetic beads to the surface of a magnetoresistive field sensor based on the giant magnetoresistance (GMR) or tunnelling magnetoresistance effects have been proposed for the detection of DNA or proteins by a number of authors and are reviewed by Freitas et al. (2007), Tamanaha et al. (2008) and Wang and Li (2008). Common for most of these approaches is that the magnetic beads are excited by an oscillating applied magnetic field resulting in a signal detectable by the magnetic field sensor. The studies have focused on the end-point detection by comparing the signal level after a washing step to that before the sample was introduced. Recently, Gaster et al. (2009) demonstrated the first real-time measurements of the magnetic bead-binding to a GMR sensor surface due to protein interactions. These measurements were

* Corresponding author. Tel.: +45 45 25 63 38.
E-mail address: Mikkel.Hansen@nanotech.dtu.dk (M. Fougt Hansen).

0956-5663/$ - see front matter © 2013 Elsevier B.V. All rights reserved.
http://dx.doi.org/10.1016/j.bios.2013.09.026

carried out in a background of magnetic beads and thus the need for washing was eliminated. Although the magnetoresistive sensing technology is promising, real-time measurements of the binding due to specific biological interactions have been limited to protein interactions.

In the present work, we demonstrate a novel magnetoresistive-based sensor architecture that allows for real-time detection of microarray-based DNA hybridisation and dehybridisation without the issues of washing steps and measurement of the background signal.

Previously, we have presented the design of magnetic field sensors in a planar Hall effect cross-geometry (Ejsing et al., 2004) and a Wheatstone bridge geometry based on the anisotropic magnetoresistance effect (Henriksen et al., 2010). The particular Wheatstone bridge configuration studied by Henriksen et al. (2010) gave the same response as the planar Hall effect sensor cross geometry except for a geometrical amplification factor and was hence named planar Hall effect bridge (PHEB) geometry. It has been demonstrated that sensors based on this geometry are well suited for dynamic measurements on magnetic beads in a liquid volume near the sensor surface using only the magnetic field from the sensor bias current as excitation (Østerberg et al., 2013a). Here, we present a new Wheatstone bridge sensor geometry, which integrates a local negative reference. We show that this enables the real-time quantification of beads that are *specifically* bound to the sensor surface due to biomolecular recognition, even in a background of magnetic beads in suspension and when the environmental conditions of the sensor are changed. Subsequently, we evaluate the sensitivity of the present sensors when used for DNA analysis and demonstrate their applicability for SNP detection.

2. Material and methods

2.1. Sensor designs

The PHEB sensors are based on the anisotropic magnetoresistance of a thin film of permalloy ($Ni_{80}Fe_{20}$) of the Wheatstone bridge geometry shown in Fig. 1a, which is exchange-pinned along the x-direction using an antiferromagnetic layer (Henriksen et al. (2010)). When biased with an AC voltage $V_x = \sqrt{2}\, V_{RMS} \sin(2\pi f t)$, a magnetic field H_y acting on the sensor area along the y-axis gives rise to a sensor voltage output along the y-axis, which can be measured by lock-in detection in the first harmonic in-phase signal. For small fields, the response is linear and given by $V_1' = (V_{RMS}/R) S_0 H_y$, where R is the bridge resistance and $S_0 (< 0)$ is the low-field sensitivity (see Supplementary Material). The current running in the sensor also generates a small inhomogeneous magnetic field in the proximity of the sensor surface (Hansen et al., 2010; Østerberg et al., 2013b). This self-field is used to magnetise the magnetic beads near the surface allowing for their detection with no need for external magnetic fields. The signal from magnetic beads over the sensor surface can be measured by lock-in detection in the second harmonic out-of-phase signal (Østerberg et al., 2013a), which can be written as

$$V_2'' = -\frac{1}{4} S_0 \left(\frac{V_{RMS}}{R}\right)^2 (\gamma_0 + \gamma_1) \tag{1}$$

A detailed derivation of this expression is given in the Supplementary Material. Here, γ_0 is a constant describing a sensor self-biasing due to current shunting in other layers than the magnetoresistive layer and γ_1 is a parameter accounting for the signal due to magnetic beads, which depends on the sensor width, the bead diameter, the bead magnetic susceptibility and the bead number density distribution in the volume over the sensor (including both beads on the sensor surface and in the volume over the sensor) (Hansen et al., 2010). The value of γ_1 is zero in the absence of magnetic beads and positive in the presence of magnetic beads.

Here, we propose a new sensor geometry termed differential PHEB (dPHEB) with identical top and bottom halves of the bridge as illustrated in Fig. 1b. This symmetry makes the sensor nominally insensitive to uniform magnetic fields. Moreover, since the self-field acts identically on the top and bottom parts, the second harmonic out-of-phase signal depends *only* on differences in the amount of beads on and over the top and bottom halves of the bridge, respectively. The second harmonic out-of-phase signal of the dPHEB sensor can be expressed as

$$V_2'' = -\frac{1}{8} S_0 \left(\frac{V_{RMS}}{R}\right)^2 (\gamma_{top} - \gamma_{bottom}) \tag{2}$$

where S_0 is the low-field sensitivity of a PHEB sensor with identical dimensions and γ_{top} and γ_{bottom} depend on the amount of beads on and over the top and bottom halves of the bridge. If the bead concentration in the liquid over the sensor surface is the same for the two sensor halves, only a difference in the amount of surface-bound magnetic beads is anticipated to give rise to a difference between γ_{top} and γ_{bottom}. A full derivation of Eq. (2) is given in the Supplementary Material. In this work, only the top half of the differential sensor is functionalised to allow for cancellation of the signal from the beads in suspension.

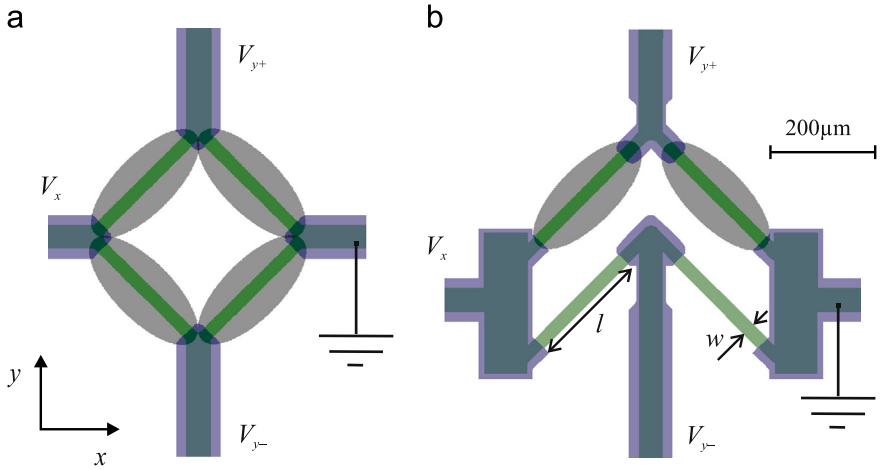

Fig. 1. Schematic illustration of sensor geometries: (a) PHEB sensor (b) Differential PHEB (dPHEB) sensor. The sensors are voltage-biased along the x-axis and the sensor signal V_y is measured along the y-axis. The arms of the sensor bridges are functionalised with surface-linked probes as indicated by the grey areas.

2.2. Sensor fabrication

The magnetic field sensors with the geometries in Fig. 1 with $l = 250\ \mu m$ and $w = 25\ \mu$m were fabricated as described previously by Henriksen et al. (2010). Briefly, the top-pinned magnetic stack Ta(15)/$Ni_{80}Fe_{20}$(30)/$Mn_{80}Ir_{20}$(10)/Ta(5) (all thicknesses in nm) was deposited by sputtering in a saturating magnetic field applied along the *x*-direction. Compared to our previous studies, the stack was slightly modified to have a thicker bottom tantalum layer and a thinner Mn–Ir layer to reduce the sensor self-biasing (γ_0). The electrical contacts consisting of Ti(10)/Pt(100)/Au(100)/Ti (10) were deposited by electron beam evaporation and defined by lift-off. The sensors were passivated with a layer of Ormocomp (Micro resist technology GmbH, Berlin, Germany) hybrid polymer of thickness 900 nm. The polymer, diluted 1:2 in Ma-T 1050, was spin coated over the sensors at 3000 rpm for 60 s. The coating geometry was defined by UV lithography and after development, the polymer was hard baked for 3 h at 150 °C. Finally, the wafer was diced into chips, each comprising six sensors.

2.3. Surface chemistry and patterning

A silanisation of the sensor surface was used to covalently couple amino-labelled oligonucleotides to the sensor coating. Briefly, this was carried out by: (1) surface activation for 20 min in 45% H_2O_2 followed by rinsing in MilliQ water and drying; (2) washing in acetone and dipping in 10% v/v solution of 3-Aminopropyltriethoxysilane (APTS) in acetone for 30 min; (3) rinsing in acetone and drying followed by immersion in 5% v/v solution of Glutaraldehyde (GA) in MilliQ water for 30 min; (4) rinsing in MilliQ water and drying.

Solutions of 20 μM capture probe oligonucleotides in 3 × saline-sodiumcitrate (SSC) (Invitrogen, Auckland, New Zealand) were spotted on the sensor surface to cover the sensor arms as depicted in Fig. 1 using a Nanoplotter™ with a NanoTip™ (both from GeSim GmbH, Grosserkmannsdorf, Germany) and incubated overnight.

In this work we used allele-specific DNA probes (Supplementary Table S2) designed for SNP genotyping in the human beta globin (*HBB*) gene by Petersen et al. (2008). Two mutation sites were investigated: CD 8/9 and CD 17. The wild type (WT) and mutant type (MT) probes differ by a single base insertion (CD 8/9) and by a single base substitution (CD 17), respectively. In addition, a biotinylated probe was used as a direct binding site for magnetic labels to function as a positive reference. All probes were purchased from DNA Technology A/S, Risskov, Denmark.

Prior to use, the sensors were rinsed in MilliQ water and the surface was blocked in a solution of 1 mg/mL bovine serum albumin (BSA) in 1 × phosphate buffered saline (PBS) for 20 min.

2.4. Measurement platform

The chip was mounted in a click-on microfluidic system (Østerberg et al., 2010) ensuring electrical contacts to the sensors, and defining a fluidic channel ($1 \times 1 \times 5\ mm^3$) over the chip surface. The sensors were connected in parallel and a voltage $V_{RMS} = 1.6$ V at a frequency $f = 167$ Hz was applied by the lock-in amplifier via a commercial audio amplifier. This frequency was chosen low enough to ensure that the magnetic response of the beads was in-phase with the field excitation and high enough to facilitate low-noise measurements at a rate of about 3 data points per second. The resistance of a single sensor bridge was $R = 89\ \Omega$, such that the *RMS* bridge current was 18 mA. The corresponding *RMS* value of the magnetic excitation field at the surface of the sensor was about 0.25 mT (see Supplementary Material).

The sensor signals were amplified using SR552 bipolar preamplifiers and measured with SR830 lock-in amplifiers from Stanford Research Systems Inc, Sunnyvale, CA, USA. The temperature of the chip holder was measured with a Pt1000 thermoresistor and controlled using a Peltier element with an accuracy of 0.1 °C via an LFI3751 temperature controller (Wavelength Electronics, Inc., Bozeman, MT, USA).

The response of the two sensor designs to a homogeneous external applied magnetic field was measured in the first harmonic in-phase sensor voltage V_1'. The magnetic field, provided by a custom built Helmholtz coil, was swept in steps from +11 mT to −11 mT and back. These measurements were used to obtain the low-field sensitivity for the PHEB sensor and to test the immunity of the dPHEB sensor to a homogeneous external applied magnetic field.

The response of the sensor designs to magnetic beads magnetised by the sensor self-field was measured in the second harmonic out-of-phase signal V_2'' in zero external applied magnetic field. To compensate for small offsets in the V_2'' signals, the experimental results are plotted as the variations $\Delta V_2''$ of the V_2'' signals with respect to their values at the initiation of the experiment.

2.5. Experimental procedure

2.5.1. Target oligonucleotides and magnetic labels

The target oligonucleotides (Supplementary Table S2) were 120 bases long synthetic sequences from the human *HBB* gene (DNA Technology A/S, Risskov, Denmark). Probes towards the CD 8/9 and CD 17 mutation sites (Supplementary Table S2) were biotinylated in the 5' end to allow for binding to the streptavidin coated magnetic labels.

The magnetic beads used for this work were Miltenyi Streptavidin MicroBeads (Cat. 130-048-102, Miltenyi Biotec Norden AB, Lund, Sweden) with a nominal diameter of 50 nm. According to Gaster et al., 2011, each bead comprises on the order of ten iron oxide nanoparticles with a diameter of about 10 nm.

2.5.2. Sensitivity to magnetic beads

Here, we linked biotinylated DNA probes directly to the sensor surface and studied the sensor output change for the two sensor types upon exposure to streptavidin magnetic beads as function of the number of functionalised sensor arms (see Supplementary Fig. S4a for a schematic illustration).

In the experiments, 15 μL of stock solution of streptavidin magnetic beads was injected over the functionalised sensor by means of a syringe pump and the variation of the second harmonic signal ($\Delta V_2''$) after 20 min of incubation was recorded. Subsequently, the sensors were washed with 1 × PBS at a flow rate of 200 μL/min for 1 min and the sensor signals were measured again.

2.5.3. DNA hybridisation and dose-response

Here, we formed a sandwich between DNA capture probes immobilised on the sensor surface, the biotinylated DNA target and streptavidin magnetic beads and studied the time response vs. the DNA target concentration (see Supplementary Fig. S4b for a schematic illustration).

In the experiments, we used a dPHEB sensor functionalised on the top two arms with CD 8/9 WT capture probes. The biotinylated WT target was diluted in 2 × SSC + 0.05% SDS in a five-fold dilution series and mixed 1:1 v/v with the stock magnetic bead suspension to final DNA target concentrations ranging from 40 nM to 0.156 nM. Immediately after, 20 μL of sample was injected into the microfluidic sensor at a flow rate of 30 μL/min and incubated for 60 min at 37 °C under stagnant conditions. The change of the

second harmonic out-of-phase signal ($\Delta V_2''$) was monitored vs. time during the incubation.

2.5.4. Real-time SNP genotyping

Here, we studied the response of dPHEB sensors functionalised with DNA capture probes upon exposure to DNA target–bead mixtures during incubation under low stringency conditions and subsequently under higher stringency washing (see Supplementary Fig. S4c for a schematic illustration).

The top arms of two sensors on the same chip were functionalised with WT and MT capture probes, respectively. The two mutation sites were investigated on separate chips. Solutions of 10 nM WT, MT or 1:1 mixture of MT/WT DNA were prepared in 1 × SSC+0.025% SDS. 10 μL of the target solution was mixed with 10 μL of the stock bead solution and immediately injected into the microfluidic sensor system at a flow rate of 30 μL/min. The final concentration of the target was 5 nM and the buffer was 0.5 × SSC+0.012% SDS. The sample was incubated over the sensor for 30 min at 37 °C. After hybridisation, the sensors were washed with 0.05 × SSC+0.05% SDS for 80 s at a flow rate of 30 μL/min and left stagnant. Three repetitions of the procedure were performed for each target combination. The sensor signals were monitored real-time during the process.

To compare the signals from the two sensors, we define the normalised ratio (*NR*) of the sensor signals as

$$NR = \frac{\Delta V_2''[WT]}{\Delta V_2''[WT] + \Delta V_2''[MT]}, \quad (3)$$

where $\Delta V_2''[WT]$ and $\Delta V_2''[MT]$ are the second harmonic out-of-phase signal variations for the sensors functionalised with WT and MT capture probes, respectively.

3. Results

3.1. Sensitivity to external fields and magnetic beads

First, the response of the two sensor designs in Fig. 1 to external magnetic fields was compared. The inset of Fig. 2 shows the first harmonic in-phase signal (V_1') measured as function of homogeneous external applied magnetic fields $\mu_0 H_y$ in the range ± 11 mT. The standard PHEB sensor showed the behaviour described previously (Henriksen et al., 2010) with a linear low-field region with a slope corresponding to a low-field sensitivity of $S_0/\mu_0 \cong -300$ V/(AT). The response of the differential sensor (dPHEB) was about 50 times smaller. This shows that the differential sensor efficiently cancelled out homogeneous externally applied magnetic fields as well as the sensor self-bias field.

Subsequently, the response of the two sensor designs was investigated as function of the number of sensor arms functionalised with a biotinylated capture probe upon exposure to streptavidin coated magnetic beads.

The squares in Fig. 2 show the signal measured for PHEB sensors as function of the number of arms functionalised with biotinylated capture probes before and after washing, respectively. Note, that the measurements before washing were carried out with the magnetic bead suspension in the liquid channel over the sensor. The signal was found to increase linearly with the number of functionalised arms. This shows that the signals from the arms are additive in accordance with the theory presented in the Supplementary Material. Moreover, before washing a significant signal was observed from the arms with no functionalisation. Washing was found to significantly reduce but not eliminate this signal. The signal vs. number of functionalised arms was observed to follow a straight line with the same slope but different non-zero offsets both before and after washing.

The triangles in Fig. 2 show the corresponding signals measured for dPHEB sensors when zero to two of the upper sensor arms were functionalised as illustrated in Fig. 1b. In this case, no offset of the sensor response vs. number of functionalised arms was observed and the points measured before and after washing (i.e., with and without beads in the fluid channel) were perfectly overlapping with the same slope as observed for the PHEB sensors. Moreover, the standard deviations on the measurements on the dPHEB sensors were found to be about four times smaller than those obtained for the PHEB sensors.

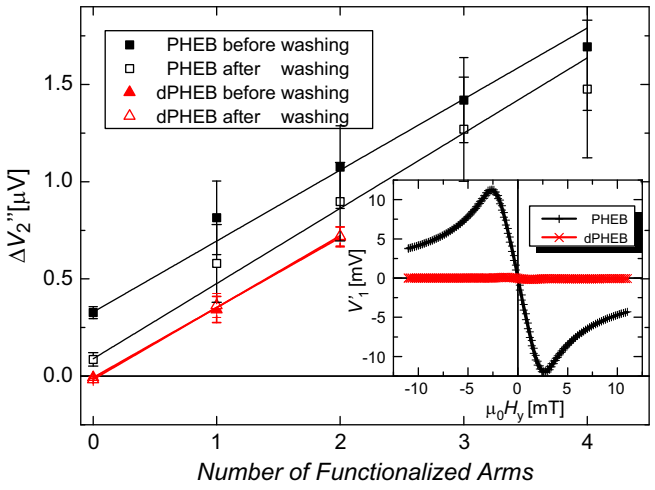

Fig. 2. Second harmonic out-of phase signal $\Delta V_2''$ vs. number of sensor arms functionalised with biotinylated positive reference probes. The signals before washing were measured with the magnetic bead suspension in the microfluidic channel over the sensor. The signals after washing were obtained with no beads in the liquid channel after washing with 1 × PBS. Error bars are standard deviations obtained from repeated experiments ($n=3$). *Inset*: First harmonic in-phase signal vs. external applied magnetic field $\mu_0 H_y$ in the range ± 11 mT.

3.2. DNA hybridisation and dose-response curve

A dPHEB sensor was functionalised on the two top arms with CD 8/9 WT capture probe oligonucleotides as illustrated in the inset of Fig. 3. In the assay, the biotinylated WT target of different concentrations was mixed with the streptavidin magnetic beads and introduced into the fluidic system to form the WT capture probe – biotinylated WT target – streptavidin magnetic bead sandwich on the sensor

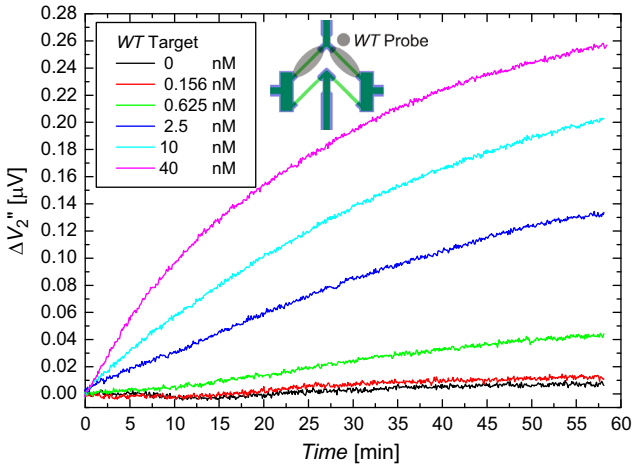

Fig. 3. Second harmonic out-of-phase signal variation measured during incubation of biotinylated WT target of the indicated concentrations and streptavidin coated magnetic beads with dPHEB sensors functionalised with CD 8/9 WT capture probe oligonucleotides as illustrated in the inset. The target and beads entered the fluidic system at time $t=0$ min.

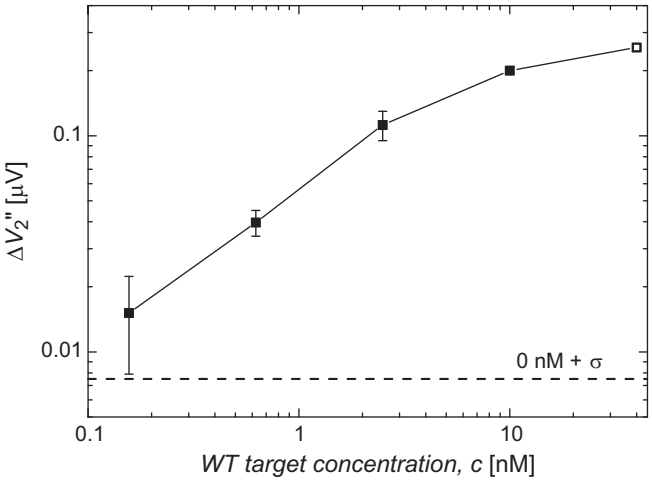

Fig. 4. Signal variation vs. WT target concentration from dPHEB sensors functionalised with CD 8/9 WT capture probe oligonucleotides after about 60 min of hybridisation with the WT target and streptavidin magnetic beads. Error bars are standard deviations obtained from repeated experiments ($n=3$), except for c=40 nM ($n=1$). The dashed line indicates the negative control result plus one standard deviation ($n=3$).

surface. Fig. 3 shows the measured signal variation $\Delta V_2''$ vs. time t during incubation with the bead-WT target mixture.

The dPHEB geometry allowed us to follow the hybridisation reaction in real-time. After sample injection, the signal increased for all tested target concentrations with a tendency to level off for long times (this was most pronounced for the highest tested concentration). The no DNA target sample showed only a small variation of the signal around 0 μV (Fig. 3). These small signal fluctuations were around two times the noise of the sensor signal, and determined our limit of detection. The smallest investigated concentration ($c=156$ pM) gave a signal still discernible from the negative reference. Fig. 4 shows the relationship between the target concentration and the signal measured after about 60 min of hybridisation. The dashed line indicates the mean value of three reference experiments with no DNA ($\Delta V_2''=4.5$ nV) plus one standard deviation ($\sigma=3.1$ nV). The signal for the lowest tested concentration was above this threshold level. The signal for the sample with the highest target concentration ($c=40$ nM) reached $\Delta V_2'' = 0.25\ \mu V$ corresponding to about one third of the value obtained when the biotinylated DNA was directly linked to the sensor surface (Fig. 2). This difference may be due to the higher affinity of the streptavidin–biotin bond and the more complex reaction dynamics when both the target and the beads are in suspension compared to when only the beads are in suspension. The signal in Fig. 4 starts to saturate when the target concentration exceeds about 10 nM and hence the readout has a dynamic concentration range of about two orders of magnitude.

3.3. Real-time SNP genotyping

In these experiments, the arms of two different dPHEB sensors on the same chip were functionalised with WT and MT capture probes as illustrated in the inset of Fig. 5. The two mutation sites (CD 8/9 and CD17) were investigated on separate chips. Real-time measurements of the sensor signals were performed during incubation with the streptavidin bead—biotinylated DNA mixtures (compositions given in the figure) as well as during subsequent washing with a higher stringency buffer. The target concentration was chosen to 5 nM to ensure that the signal was close to but below saturation such that dehybridisation events could be maximally resolved. The measured signals for the individual sensors are shown vs. time in Supplementary Fig. S5. The resulting normalised ratios NR given by Eq. (3) for three repetitions of the

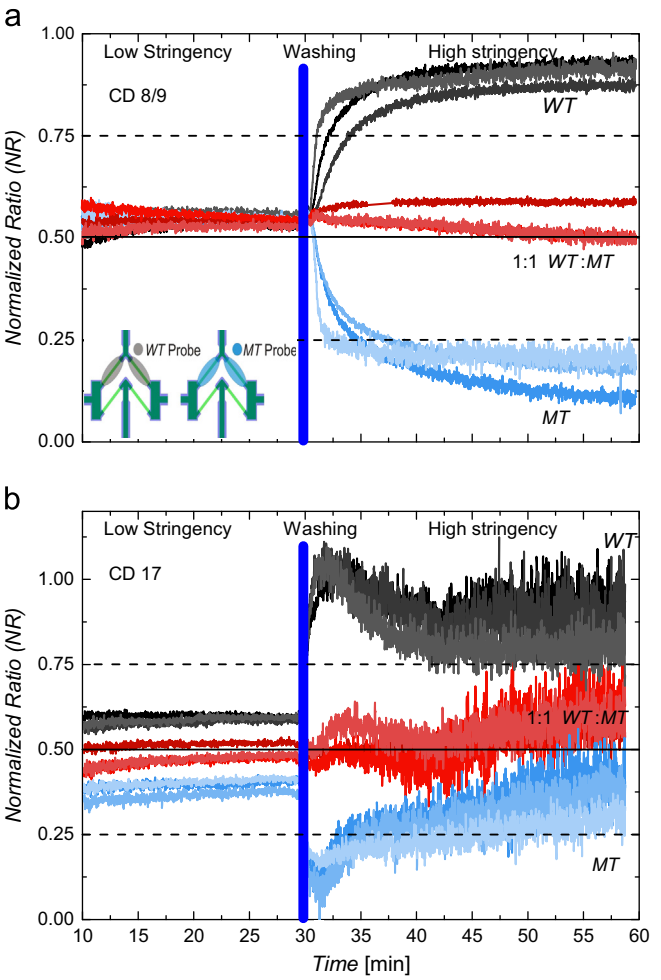

Fig. 5. Normalised signal ratio (NR) vs. time for experiments with the indicated target combinations. The sensors were functionalised with WT and MT capture probes as depicted in the inset for (a) the CD 8/9 mutation site and (b) the CD 17 mutation site in the human HBB gene, respectively. Samples were injected at $t=0$ min. The normalised ratio was not meaningful for the first 10 min due to low signals.

indicated target compositions are shown in Fig. 5a and b for the CD 8/9 and CD 17 mutation sites, respectively. Values of NR of 1 and 0 correspond to hybridisation to only the WT and MT capture probes, respectively, and $NR=0.5$ corresponds to identical hybridisation to the two probes.

For the CD 8/9 mutation site, after approximately 15 min of hybridisation under low stringency condition (0.5 × SSC+0.012% SDS), the normalised ratio approached 0.5 for all target combinations, corresponding to identical hybridisation of all targets to WT and MT capture probes (Figs. 5a and 6a). For all target combinations, we found $NR \cong 0.54(1)$.

For the CD 17 mutation site, the value of the normalised ratio prior to washing was found to differ for the three target combinations (Figs. 5b and 6a) and the signal level was generally lower than for the CD 8/9 mutation (Supplementary Fig. S5). For the three targets we found $NR \cong 0.39(2)$ (MT target), $NR \cong 0.49(2)$ (1:1 WT:MT target) and $NR \cong 0.591(6)$ (WT target), respectively.

Under higher stringency conditions (0.05 × SSC+0.05% SDS), the mismatched duplexes denatured at a faster rate than the perfectly matched counterparts. Approximately 10 min after initiation of the washing, the NR values for the CD 8/9 mutation site (Figs. 5a and 6b) stabilised above 0.8 and below 0.2 for the WT and MT targets, respectively. For the 1:1 mixed MT:WT target, the normalised ratio remained close to the value of 0.54 obtained before

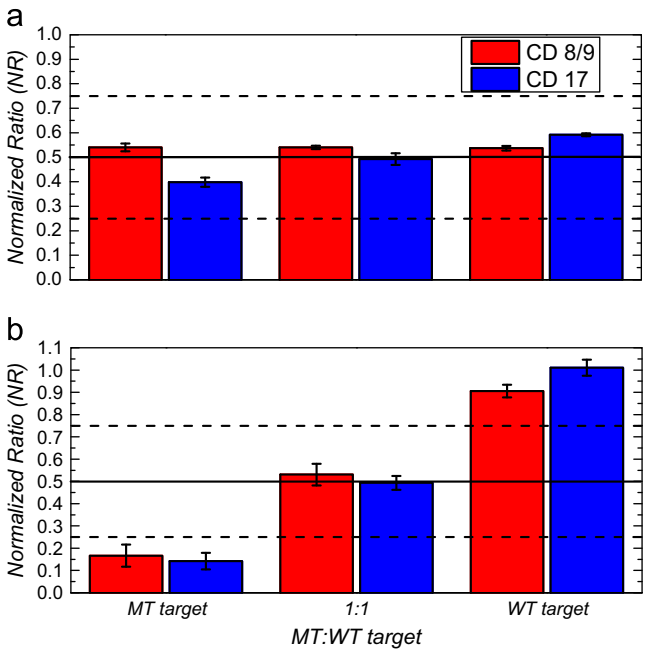

Fig. 6. Normalised ratio (*NR*) of sensors signals measured for different WT and MT target ratios. The experiments were performed with capture probes for the CD 8/9 and CD 17 mutation sites in the human HBB gene. The signals were measured (a) after 30 min incubation of the target and bead suspension on the sensor; and (b) 25 min (CD 8/9) or 2 min (CD 17) after washing in stringent buffer. Error bars are standard deviations obtained from repeated experiments ($n=3$).

washing. For the CD 17 mutation site (Figs. 5b and 6b), the maximum separation of the normalised ratios for the different targets was observed 2 min after initiation of the washing. For longer times, the separation was reduced and the standard deviation of the normalised ratio increased because of denaturation of both the mismatching and matching DNA duplexes, which resulted in a decrease of the sensor signals. For this mutation, the normalised ratio for the 1:1 mixed MT: WT target after washing assumed a value of $NR \cong 0.49(3)$.

4. Discussion

4.1. Characterisation of differential sensor

The study on the biotin-streptavidin bound beads on sensor surface showed the strengths and weaknesses of the two sensor designs. For both sensor designs, the signal due to bound beads was found to depend linearly on the number of functionalised sensor arms. The maximum signal from the dPHEB design was only half of the maximum signal from a PHEB design, because only half the sensor was used for sensing as the other sensor half was used as a local negative reference. However, the signals from the dPHEB design showed no offset both before and after washing when the sensor arms were not functionalised and the standard deviations of the sensor signals were about four times smaller than for the corresponding data for the PHEB sensors (Fig. 4). We speculate that due to the nearness of the sensing and reference arms of the dPHEB sensors, the two parts of the sensor are exposed to the nearly identical temperature, background bead concentration, external magnetic field and hybridisation conditions and that this results in the lower offset and variance of the signals. Therefore, the *environmental* parameters affecting the sensor are efficiently cancelled out in dPHEB sensors and these can be used to measure the amount of beads that are *specifically* bound to the top half of the sensor. For these reasons, the dPHEB sensors are the best choice for surface-based assays.

4.2. DNA hybridisation and dose-response curve

The design of the dPHEB sensors, and in particular the local reference, allowed for target detection in concentrations down to 156 pM, with a dynamic range of about two orders of magnitude and a low background. The obtained detection limit and dynamic range is well suited for analysis of DNA products from an amplification process such as polymerase chain reaction (PCR). Other research groups have been using magnetic labels for this purpose. In particular, Xu et al. (2008) demonstrated the detection of 10 nM of PCR products by adding magnetic particles to a spin valve sensor onto which the target was hybridised outside the measurement system. Our system offers a microfluidic liquid control as well as control of the sensor temperature during real-time measurements. These are key elements to carry out the hybridisation procedure on-chip. The integration of these control systems with the sensor allows for a real-time measurement of the hybridisation reaction.

The closest comparable method to the present one is DNA microarrays. Microarrays based on end-point fluorescence readout in a commercial microarray reader typically have detection limits of 1–10 pM. The detection limit depends on hybridisation time, surface chemistry, slide material, and the probes used. The fluorescence readout typically has several orders of magnitude of dynamic range. Non-fluorescent readouts, such as colorimetric enzymatic readouts, have detection limits similar to fluorescence (10–30 pM) but with only one or at most two orders of magnitude of dynamic range (Chen et al., 1998; Petersen et al., 2007). The present method has a higher detection limit and a dynamic range similar to colorimetric detection methods. Dynamic ranges of one to two orders of magnitude are sufficient for SNP genotyping (Petersen et al., 2007). As the detection limit for the presented method is high at present, it is better suited for analysis of targets prepared by an amplification process, such as PCR. The advantages of the presented method over optical detection are the integration in a compact microfluidic system with flexible reaction conditions and the ability to perform real-time measurements of the DNA hybridisation and dehybridisation.

Other chip-based methods to measure hybridisation in real-time includes surface plasmon resonance (SPR) (Auer et al., 2011), quartz crystal microbalance (QCM) (Wang et al., 2013), and film bulk acoustic resonators (FBAR) (Auer et al., 2011). These methods do not use a labelling of the targets and have detection limits of about 1 nM. This limit is set by the unspecific binding of the sample matrices to the sensor surface (Auer et al., 2011, Wang et al., 2013). Since there is virtually no magnetic signal from biological material, magnetic label detection is insensitive to the sample matrix. Moreover dPHEB sensors, via their integrated local negative reference, are effective in cancelling the signals from unspecifically bound targets and labels in suspension.

4.3. Real-time SNP genotyping

Stringent washing was employed to denature mismatched duplexes from the CD 8/9 and CD 17 mutations of the *HBB* gene. The same mutation sites were previously investigated by Petersen et al. (2009) under varying washing stringency conditions. In their work, an optimal washing buffer composition of $0.25 \times$ SSC + 0.1% SDS was identified for genotyping of the CD 8/9 mutation, but acceptable discrimination was obtained down to salt concentrations of $0.035 \times$ SSC. Here, we utilised $0.05 \times$ SSC + 0.05% SDS, which is within their working buffer range. For the CD 17 mutation site, Petersen et al. found that the optimal washing stringency was lower than that for the CD 8/9 mutation site, and that higher stringency conditions (i.e. washing at a lower salt concentration) led to lower reproducibility of the *NR* values due to loss of signal.

This agrees well with the results presented here, where the washing buffer was found to induce a fast denaturation of also the matched duplexes for the CD 17 mutation site. Nevertheless, with the dPHEB sensors, it was possible to perform real-time measurements during incubation and washing in contrast to the end-point detection employed in a standard microarray-based approach with fluorescence readout (Petersen et al., 2008, 2009; Poulsen et al., 2011). The real-time data can be used to obtain kinetic data and to optimise, for example, the timing of SNP genotyping. For both mutation sites, the value of *NR* changed rapidly after the washing was initiated (Fig. 5). For the CD 8/9 mutation site, the normalised ratio approached its equilibrium value after about 10 min and a clear distinction between a homozygote WT target (100% WT target) and a homozygote MT target (100% MT target) could be made using cut-off values of >0.75 and <0.25, respectively. For the CD 17 mutation site, the cut-off values were reached 2 min after initiation of the washing, after which the total signal decreased resulting in lower reliability of the values of *NR*. Considering the rapid signal change in Fig. 5, it is possible to perform a robust genotyping for the present samples just a few minutes after the high stringency buffer is introduced while longer washing times may reduce the total signal. Real-time data allows for genotyping of multiple SNPs even when the optimal washing time varies between different probe sets. Moreover, rapid SNP detection may be feasible using the presented approach.

5. Conclusions

A system for real-time hybridisation assays using magnetic labels and integrated magnetoresistive field sensors was described. The system comprised integrated microfluidic sample handling and temperature control. Each sensor included a local negative reference close to the active sensing area. Therefore, the influence of the sensor environment (temperature, external magnetic field, magnetic bead background) was strongly reduced. These features enabled real-time studies of the *specific* binding of magnetic beads to the upper part of the sensor in a background of magnetic beads under changing environmental conditions and strongly improved the reliability of the quantification of the specific binding of magnetic beads. In the system, we demonstrated the detection of DNA targets down to a concentration of about 160 pM. This number is anticipated to be further improved by optimising the sensor stack and geometry to achieve a higher sensitivity to surface-bound magnetic beads. Moreover, we demonstrated the strengths of the system in real-time SNP genotyping experiments on two mutation sites in the human *HBB* gene, where the hybridisation of WT, MT and a 1:1 mixture of WT and MT targets were monitored during incubation and stringent washing. The results showed data of high quality and reproducibility with a clear distinction between the three investigated targets for both investigated mutations.

The presented system provides a flexible tool for investigations of the real-time specific binding of magnetic beads to a functionalised sensor surface as function of biological target, the liquid composition and the temperature. Our future work aims at using this tool for studies of DNA hybridisation kinetics and for the optimisation of hybridisation conditions for SNP genotyping.

Acknowledgements

Frederik W. Østerberg acknowledges support from the Copenhagen Graduate School for Nanoscience and Nanotechnology (C:O:N:T) and the Knut and Alice Wallenberg (KAW) Foundation.

Appendix A. Supplementary material

Supplementary data associated with this article can be found in the online version at http://dx.doi.org/10.1016/j.bios.2013.09.026.

References

Auer, S., Nirschl, M., Schreiter, M., Vikholm-Lundin, I., 2011. Analytical and Bioanalytical Chemistry 400 (5), 1387–1396.
Chen, J.J.W., Wu, R., Yang, P.-C., Huang, J.-Y., Sher, Y.-P., Han, M.-H., Kao, W.-C., Lee, P.-L., Chiu, T.F., Chang, F., Chu, Y.-W., Wu, C.-W., Peck, K., 1998. Genomics 51 (3), 313–324.
Ejsing, L., Hansen, M.F., Menon, A.K., Ferreira, H.A., Graham, D.L., Freitas, P.P., 2004. Applied Physics Letters 84, 4729.
Er, T.-K., Chang, J.-G., 2012. Clinica Chimica Acta 414, 197–201.
Freitas, P.P., Ferreira, R., Cardoso, S., Cardoso, F., 2007. Journal of Physics: Condensed Matter 19, 165221.
Gaster, R.S., Hall, D.A., Nielsen, C.H., Osterfeld, S.J., Yu, H., Mach, K.E., Wilson, R.J., Murmann, B., Liao, J.C., Gambhir, S.S., Wang, S.X., 2009. Nature Medicine 15, 1327–1333.
Gaster, R.A., Hall, D.A., Wang, S.X., 2011. Nano Letters 11, 2579–2583.
Hansen, T.B.G., Damsgaard, C.D., Dalslet, B.T., Hansen, M.F., 2010. Journal of Applied Physics 107, 124511.
Henriksen, A.D., Dalslet, B.T., Skieller, D.H., Lee, K.H., Okkels, F., Hansen, M.F., 2010. Applied Physics Letters 97, 013507.
Howell, W.M., Jobs, M., Gyllensten, U., Brookes, A.J., 1999. Nature Biotechnology 17, 87–88.
Nørholm, M., Bruus, H., Jakobsen, M.H., Telleman, P., Ramsing, N.B., 2004. Lab-on-a-Chip 4, 28–37.
Østerberg, F.W., Dalslet, B.T., Snakenborg, D., Johansson, C., Hansen, M.F., 2010. AIP Conference Proceedings 1311, pp. 176–183.
Østerberg, F.W., Rizzi, G., de la Torre, Zardán Gómez, Strömberg, T., Strømme, M., Svedlindh, M., Hansen, M.F., P., 2013a. Biosensors and Bioelectronics 40 (1), 147–152.
Østerberg, F.W., Rizzi, G., Hansen, M.F., 2013b. Journal of Applied Physics 113, 234508.
Petersen, J., Stangegaard, M., Birgens, H., Dufva, M., 2007. Analytical Biochemistry 360 (1), 169–171.
Petersen, J., Poulsen, L., Petronis, S., Birgens, H., Dufva, M., 2008. Nucleic Acids Research 36, e10.
Petersen, J., Poulsen, L., Birgens, H., Dufva, M., 2009. PLoS One 4, e4808.
Poulsen, L., Søe, M.J., Møller, L.B., Dufva, M., 2011. PLoS One 6 (3), e14777.
Tamanaha, C.R., Mulvaney, S.P., Rife, J.C., Whitman, L.J., 2008. Biosensors and Bioelectronics 24, 1–13.
Wang, S.X., Li, G., 2008. IEEE Transactions on Magnetics 44, 1687–1702.
Wang, D., Chen, G., Wang, H., Tang, W., Pan, W., Li, N., Liu, F., 2013. Biosensors and Bioelectronics 48, 276–280.
Xu, L., Yu, H., Akhras, M.S., Han, S., Osterfeld, S., White, R.L., Pourmand, N., Wang, S.X., 2008. Biosensors and Bioelectronics 24 (1), 99–103.